UNIVERSITY OF OKLAHOMA

GRADUATE COLLEGE

A NOVEL POLYSACCHARIDE-BASED SURFACE ENGINEERING STRATEGY FOR NANOMEDICINES

A DISSERTATION

SUBMITTED TO THE GRADUATE FACULTY

in partial fulfillment of the requirements for the

Degree of

DOCTOR OF PHILOSOPHY

By

WEN YANG
Norman, Oklahoma
2022

Downloaded from SHAREOK. Persistent Handle URL: https://hdl.handle.net/11244/335970

A NOVEL POLYSACCHARIDE-BASED SURFACE ENGINEERING STRATEGY

FOR NANOMEDICINES

A DISSERTATION APPROVED FOR THE
STEPHENSON SCHOOL OF BIOMEDICAL ENGINEERING

BY THE COMMITTEE CONSISTING OF

Dr. Stefan Wilhelm, Chair

Dr. Zhibo Yang

Dr. Handan Acar

Dr. Qinggong Tang

© Copyright by WEN YANG 2022
All Rights Reserved.

Acknowledgments

I began my Ph.D. adventure at the University of Oklahoma as an international student and woman in engineering after graduating from medical school. This decision was driven by my internship in the hospital and encouraged by Prof. Yanlin Wang, the director of the clinical medicine department, where I got my medical degree. The Ph.D. journey is replete with both delights and challenges. Without the support and encouragement of Dr. Wilhelm, family in China and the United States, and lab friends, I would not be able to complete all of these challenges and attain the current achievements. Thank you so much for believing in me and supporting me throughout this crucial chapter of my life.

First and foremost, I would like to convey my heartfelt gratitude to my Ph.D. advisor, Prof. Stefan Wilhelm, for his endless patience and step-by-step mentoring in helping me develop professional progress in science. Thank you so much for mentoring me with improvements in knowledge and skills in scientific research, planning, communication, and organization that positively impacted my life. Thank you very much for accepting me to your research group, supporting me as an international student, and embracing cultural differences across countries. I am grateful for the consistent assistance and support I have gotten over the past several years. I am fortunate and honored to be a member in the name of Wilhelm lab.

I would like to thank Dr. DeAngelis Paul and Mrs. Dixy E. Green, thanks for your insightful advice, efficient responses, and excellent editing over our long-term collaborative projects and manuscripts. Although the graduate college does not officially assign Dr. DeAngelis to maintain mentoring obligations in my committee, I appreciate Dr. DeAngelis' excellent mentoring in my professional growth as a researcher.

I appreciate my committee members, Dr. Qinggong Tang, Dr. Handan Acar, and

Dr. Zhibo Yang. Dr. Qinggong Tang provides me with sincere suggestions on my program's progress and thoughtful guidance on my career. Thanks Dr. Handan Acar offered professional advice on my academic projects and encouraging me as a woman in engineering. Thanks to Dr. Zhibo Yang's advice on becoming a competent graduate student and sharing his secret to superb scientific writing.

I have been fortunate to work with great labmates Dr. Lin Wang, Vinit Sheth, Alyssa M. Holden, Alex N. Frickenstein, Dr. Nathan D. Donahue, and Evan M. Mettenbrink offered me tremendous support and help. I have been significantly aided by Dr. Si Wu and Mulin Fang, Dr. Yushan Zhang, Dr. Priyabrata Mukherjee, Dr. Qing He, and Dr. Binbin Weng, who provided excellent support for LC/MS analysis, material synthesis, and manuscript revision, respectively. I would like to thank all the individuals I met at the University of Oklahoma, Dr. Mengmeng Zhai, Dr. Binrui Cao, and Dr. Kegan Sunderland, for their friendships, science guidance, and cheering for me when I first arrived in the United States. Additionally, I wish to express my gratitude to all the individuals whose names I do not include here but in my published works for their invaluable contributions to my projects.

Finally, I must thank my family in China and host family in the United States for their unconditional love, giving, and support. I am so proud of my sister for her brave and contribution in standing in the first line for defending the COVID-19 when the disease first spreads in my hometown Wuhan. Thanks to my host family, Mr. and Mrs. Burrus, for their love, encouragement, and inclusion. Thanks to the Friends with International Students program of the University of Oklahoma for offering me opportunities to meet with friends coming from all over the world, including Korea, Japan, Columbia, Bolivia, Germany, United Kingdom, Denmark, Italy, France, Spain, Norway, Finland, etc. All those great days colored my Ph.D. life outside of laboratories.

Table of Contents

Acknowledgments....iv
Table of Contents....vi
List of Figures....xi
List of Tables....xv
Abstract....xvi

Chapter 1 Introduction....1
1.1 Nanoparticle Classification and Physicochemical Properties....1
1.2 Nanotoxicology....6
1.3 Nanotoxicity Mechanisms....13
1.4 Nanotoxicity Assessment....19
1.5 Strategies to Mitigate Nanotoxicity....21
1.6 Perspective and Conclusion....22

Chapter 2 Nanoparticle Surface Engineering with Heparosan Polysaccharide Reduces Serum Protein Adsorption and Enhances Cellular Uptake....24
2.1 Introduction....24
2.2 Materials and Methods....26
2.2.1 Nanoparticle synthesis (15-nm, 55-nm, or 100-nm AuNPs; 55-nm AgNPs; and liposomes)....26
2.2.2 Heparosan synthesis and characterization of OPSS-HEP conjugation....28
2.2.3 Saturation curve of gold nanoparticles....31
2.2.4 Saturation curve of heparosan coated liposomes....31
2.2.5 HEP-AuNPs prepared by the salt aging method....32
2.2.6 HEP-AuNPs and HEP-AgNPs prepared by the pH method....33
2.2.7 HEP-AuNPs prepared by the vortex method....34
2.2.8 Quantification of HEP-coatings 15-nm and 55-nm AuNPs using a radiolabeling strategy....35
2.2.9 TEM characterization of HEP- and citrate-AuNPs....36
2.2.10 TEM characterization of AuNPs inside of cells....37
2.2.11 Agarose gel electrophoresis....38
2.2.12 Quantifying HEP desorption upon exposure of HEP-coated nanoparticles to human plasma....39
2.2.13 Protein corona formation upon nanoparticle incubation in FBS....40

2.2.14 Protein isolation 41
2.2.15 Protein cleanup 42
2.2.16 SDS-PAGE for protein corona characterization 43
2.2.17 Liquid Chromatography Tandem Mass Spectrometry (LC-MS/MS) 44
2.2.18 BCA-based protein quantification assays 46
2.2.19 Cell viability tests 47
2.2.20 Hemolysis assays 48
2.2.21 Cytokine release assay 49
2.2.22 Nanoparticle cell uptake studies 50
2.2.23 Confocal laser scanning microscopy studies 51
2.2.24 UV-Vis spectrophotometry-based depletion assay 52
2.3 Results and Discussion 53
2.3.1 Surface modification of nanoparticles with the polysaccharide heparosan 53
2.3.2 Ability of heparosan to reduce ability protein adsorption on nanoparticle surface 58
2.3.3 Protein analysis of nanoparticle protein corona 61
2.3.4 Biological interaction of nanoparticles with cells 63
2.4 Conclusion 67

Chapter 3 Controlling Nanoparticle Uptake in Innate Immune Cells with Heparosan Polysaccharides 68

3.1 Introduction 68
3.2 Materials and Methods 70
3.2.1 Gold nanoparticle synthesis (15-nm or 55-nm AuNPs) 70
3.2.2 Heparosan synthesis 72
3.2.3 HEP-AuNPs prepared by the pH assisted method 74
3.2.4 Nanoparticle cell uptake study 75
3.2.5 Real time confocal characterization of nanoparticle cellular uptake 76
3.2.6 Confocal characterization of nanoparticle cellular uptake in fixed cells 77
3.2.7 Transmission electron microscopy (TEM) imaging of AuNPs inside of cells 78
3.2.8 Energy dependent temperature and transport inhibition experiment 79
3.2.9 HEP structural analog competition experiment 80
3.2.10 Multivalent nanoparticle cell interaction 81
3.3 Results and Discussion 82
3.3.1 Uptake behavior of heparosan (HEP) modified nanoparticles over time 82
3.3.2 HEP-AuNPs cellular internalization through the energy-dependent endocytic pathways 85

3.3.3 HEP-AuNPs cellular internalization through clathrin-mediated endocytosis and macropinocytosis/phagocytosis 88
3.3.4 Controlling HEP-AuNPs cellular uptake by structural analogs of HEP 91
3.3.5 Controlling HEP-AuNPs cellular uptake by varying surface HEP density 96
3.4 Conclusion 98

Chapter 4 Summary and future directions 99

References 100

Appendix A: List of Supporting Figures 122
Figure S1. Chemical structure of OPSS-HEP, and OPSS-PEG. 122
Figure S2. Characterization of the OPSS-HEP conjugation. 123
Figure S3. Agarose gel electrophoresis images of 15-nm HEP-AuNPs. 124
Figure S4. Nanoparticle colloidal stability of 15-nm HEP-AuNPs. 125
Figure S5. Physicochemical characterization of 55-nm HEP-AuNPs. 126
Figure S6. Nanoparticle colloidal stability of 55-nm HEP-AuNPs. 127
Figure S7. Characterization of 100-nm HEP-AuNPs and summary of HEP-AuNPs. 128
Figure S8. Optimized pH method for maintaining colloidal stability of 100-nm AuNPs modified with low HEP densities. 129
Figure S9. FBS incubation of 15-nm, 55-nm, or 100-nm HEP-AuNPs by salt aging. 130
Figure S10. Agarose gel electrophoresis images of HEP-AuNPs upon FBS incubation. 131
Figure S11. Heparosan coating reduces protein corona formation on silver nanoparticles and liposomes. 132
Figure S12. Heparosan coating reduces protein corona formation on 15-nm AuNPs. 133
Figure S13. Physicochemical characterization of PEG-AuNPs. 134
Figure S14. Assessment of cytokine release levels. 135
Figure S15. Cytotoxicity and hemolysis tests using HEP- or PEG-AuNPs. 136
Figure S16. Light micrographs of different cell types after incubation with 55-nm HEP-AuNPs. 137
Figure S17. Quantification of the light scattering intensity of nanoparticles in cells. 138
Figure S18. Cell uptake quantification of 15-nm HEP-AuNPs and PEG-AuNPs by ICP/MS in RAW 264.7 macrophages and 4T1 breast cancer cells with and without AuNPs etching. 139

Figure S19. Transmission electron microscopy imaging of the subcellular distribution of 55-nm gold nanoparticles.....140
Figure S20. Cellular uptake of silver nanoparticles, liposomes, or gold nanoparticles with various coatings. 141
Figure S21. Cell uptake of polymer-coated 55-nm AuNPs in HUVEC endothelial cells. 142
Figure S22. The effect of FBS incubation on cellular uptake. 143
Figure S23: Cellular uptake of HEP-coated 55-nm AuNPs in J774A.1 macrophages, RAW 264.7 macrophages, and DC 2.4 dendritic cells. 144
Figure S24: Light micrographs of HEP-AuNPs uptake over time. 145
Figure S25: The cellular uptake kinetics of heparosan (HEP) modified gold nanoparticles (AuNPs) in DC 2.4 dendritic cells. 146
Figure S26: Confocal laser scanning micrographs of HEP-AuNPs uptake in real-time via live cell imaging.....147
Figure S27: Internalization of heparosan (HEP) modified gold nanoparticles (AuNPs) in RAW 264.7 macrophages. 148
Figure S28: Internalization of heparosan (HEP) modified gold nanoparticles (AuNPs) in DC 2.4 dendritic cells. 149
Figure S29: HEP-AuNPs escape from intracellular vesicles. 150
Figure S30: Light micrographs of HEP-AuNP cellular uptake at low temperature, with sodium azide, or with various other endocytic inhibitors. 151
Figure S31: The lack of an inhibition effect of EIPA on 55-nm HEP-AuNP cellular internalization. 152
Figure S32: Light micrographs showing the effect of chlorpromazine on HEP-AuNPs cellular internalization. 153
Figure S33: Light micrographs showing the inhibition effect of cytochalasin D on HEP-AuNPs cellular internalization. 154
Figure S34: Light micrographs and ICP-MS results of the endocytosis inhibitor effect on DC 2.4 cells.....155
Figure S35: Light micrographs and ICP-MS results of the endocytosis inhibitor effect on RAW 264.7 cells. 156
Figure S36: Cell viability of chlorpromazine and cytochalasin D in DC 2.4 and RAW 264.7 cells. 157
Figure S37: Light micrographs and ICP-MS results of GAG structural analogs for competition experiments using RAW 264.7 cells. 158
Figure S38: ICP-MS quantification of HEP-AuNPs cellular uptake in the presence of HEP or GlcNAc. 159

Figure S39: Light micrographs of 55-nm HEP-AuNPs uptake in RAW 264.7 cells in the presence of various GAG competitors. 160
Figure S40: Cell viability of RAW 264.7 macrophages in the presence of CS A or heparin. 161
Figure S41: Light micrographs and ICP-MS results of CS A competition experiment using DC 2.4 cells 162
Figure S42: Effect of CS A on cell viability of DC 2.4 dendritic cells (1 mg/mL; 3.5 h). 163
Figure S43: Effect of CS A on cell viability of DC 2.4 dendritic cells (2 mg/mL; 25 h). 164
Figure S44: Effect of CS A on cell viability of DC 2.4 dendritic cells (2 mg/mL; 4.5 h). 165
Figure S45: Light micrographs of CS A competition effect on HEP-AuNPs cellular uptake over time. 166
Figure S46: Light micrographs of CS A competition effect on HEP-AuNPs cellular uptake. 167
Figure S47. The physical characterization of HEP- or PEG-coated AuNPs. 168
Figure S48: Light micrographs of RAW 264.7 cells incubated with AuNPs possessing different heparosan (HEP) coating densities. 169
Figure S49: Effect of HEP coating density on AuNP physical parameters and RAW cell uptake. 170

Appendix B: List of Supporting Figures 171
Table S1. Summary of proteins identified from LC/MS-MS. 171
Table S2. LC-MS/MS analysis of surface adsorbed proteins from 55-nm HEP-AuNPs. 172
Table S3. LC-MS/MS analysis of surface adsorbed proteins from 55-nm PEG-AuNPs. 173

Appendix C: Abbreviations 174

Appendix D: List of Copyrights and Permissions 176
No permission is needed from Annual Reviews as an author for Chapter 1 176
Reuse permission for Chapter 2 177

List of Figures

Figure 1.1 Nanoparticle classification and physicochemical properties.....4
Figure 1.2 Schematic representation of nanoparticle adverse effects and nanotoxicity.....5
Figure 1.3 Anti-PEG immunogenicity induced mechanisms of nanoparticle pseudoallergic infusion reaction cascade and accelerated blood clearance (ABC) phenomenon.....18
Figure 2.1 Schematic of gold nanoparticle (AuNP) surface modification with heparosan (HEP) polymers. 54
Figure 2.2 Characterization of heparosan (HEP) surface modification using 15-nm AuNPs. 56
Figure 2.3 Nanoparticle surface engineering with heparosan reduces protein corona formation.....60
Figure 2.4 Proteomic analysis of nanoparticle protein corona by LC-MS/MS 62
Figure 2.5 Cytotoxicity, hemolysis, and cell uptake of HEP- and PEG-modified 55-nm AuNPs.....66
Figure 3.1 The cellular uptake of heparosan (HEP) modified gold nanoparticles (AuNPs) is time-dependent. 84
Figure 3.2 HEP-coated nanoparticles enter cells through endocytosis. 86
Figure 3.3 HEP-coated nanoparticles enter cells through clathrin-mediated endocytosis and macropinocytosis/phagocytosis.....90
Figure 3.4 Evaluation of structural HEP analogs as competitors for HEP-coated nanoparticle uptake. 93
Figure 3.5 Surface coating of HEP provides multivalent ligands for strong nanoparticles and cell interaction.....97
Figure S1 Chemical structure of OPSS-HEP, and OPSS-PEG.....122
Figure S2 Characterization of the OPSS-HEP conjugation. 123
Figure S3 Agarose gel electrophoresis images of 15-nm HEP-AuNPs. 124
Figure S4 Nanoparticle colloidal stability of 15-nm HEP-AuNPs. 125
Figure S5 Physicochemical characterization of 55-nm HEP-AuNPs. 126
Figure S6 Nanoparticle colloidal stability of 55-nm HEP-AuNPs. 127
Figure S7 Characterization of 100-nm HEP-AuNPs and summary of HEP-AuNPs 128

Figure S8 Optimized pH method for maintaining colloidal stability of 100-nm AuNPs modified with low HEP densities. 129
Figure S9 FBS incubation of 15-nm, 55-nm, or 100-nm HEP-AuNPs by salt aging 130
Figure S10 Agarose gel electrophoresis images of HEP-AuNPs upon FBS incubation 131
Figure S11 Heparosan coating reduces protein corona formation on silver nanoparticles and liposomes. 132
Figure S12 Heparosan coating reduces protein corona formation on 15-nm AuNPs 133
Figure S13 Physicochemical characterization of PEG-AuNPs 134
Figure S14 Assessment of cytokine release levels 135
Figure S15 Cytotoxicity and hemolysis tests using HEP- or PEG-AuNPs 136
Figure S16 Light micrographs of different cell types after incubation with 55-nm HEP-AuNPs 137
Figure S17 Quantification of the light scattering intensity of nanoparticles in cells 138
Figure S18 Cell uptake quantification of 15-nm HEP-AuNPs and PEG-AuNPs by ICP/MS in RAW 264.7 macrophages and 4T1 breast cancer cells with and without AuNPs etching. 139
Figure S19 Transmission electron microscopy imaging of the subcellular distribution of 55-nm gold nanoparticles. 140
Figure S20 Cellular uptake of silver nanoparticles, liposomes, or gold nanoparticles with various coatings. 141
Figure S21 Cell uptake of polymer-coated 55-nm AuNPs in HUVEC endothelial cells. 142
Figure S22 The effect of FBS incubation on cellular uptake. 143
Figure S23 Cellular uptake of HEP-coated 55-nm AuNPs in J774A.1 macrophages, RAW 264.7 macrophages, and DC 2.4 dendritic cells. 144
Figure S24 Light micrographs of HEP-AuNPs uptake over time. 145
Figure S25 The cellular uptake kinetics of heparosan (HEP) modified gold nanoparticles (AuNPs) in DC 2.4 dendritic cells. 146
Figure S26 Confocal laser scanning micrographs of HEP-AuNPs uptake in real-time via live cell imaging. 147

Figure S27 Internalization of heparosan (HEP) modified gold nanoparticles (AuNPs) in RAW 264.7 macrophages. 148
Figure S28 Internalization of heparosan (HEP) modified gold nanoparticles (AuNPs) in DC 2.4 dendritic cells. 149
Figure S29 HEP-AuNPs escape from intracellular vesicles. 150
Figure S30 Light micrographs of HEP-AuNP cellular uptake at low temperature, with sodium azide, or with various other endocytic inhibitors. 151
Figure S31 The lack of an inhibition effect of EIPA on 55-nm HEP-AuNP cellular internalization 152
Figure S32 Light micrographs showing the effect of chlorpromazine on HEP-AuNPs cellular internalization. 153
Figure S33 Light micrographs showing the inhibition effect of cytochalasin D on HEP-AuNPs cellular internalization. 154
Figure S34 Light micrographs and ICP-MS results of the endocytosis inhibitor effect on DC 2.4 cells 155
Figure S35 Light micrographs and ICP-MS results of the endocytosis inhibitor effect on RAW 264.7 cells. 156
Figure S36 Cell viability of chlorpromazine and cytochalasin D in DC 2.4 and RAW 264.7 cells 157
Figure S37 Light micrographs and ICP-MS results of GAG structural analogs for competition experiments using RAW 264.7 cells 158
Figure S38 ICP-MS quantification of HEP-AuNPs cellular uptake in the presence of HEP or GlcNAc 159
Figure S39 Light micrographs of 55-nm HEP-AuNPs uptake in RAW 264.7 cells in the presence of various GAG competitors. 160
Figure S40 Cell viability of RAW 264.7 macrophages in the presence of CS A or heparin 161
Figure S41 Light micrographs and ICP-MS results of CS A competition experiment using DC 2.4 cells. 162
Figure S42 Effect of CS A on cell viability of DC 2.4 dendritic cells (1 mg/mL; 3.5 h). 163
Figure S43 Effect of CS A on cell viability of DC 2.4 dendritic cells (2 mg/mL; 25 h) 164

Figure S44 Effect of CS A on cell viability of DC 2.4 dendritic cells (2 mg/mL; 4.5 h). 165
Figure S45 Light micrographs of CS A competition effect on HEP-AuNPs cellular uptake over time. 166
Figure S46 Light micrographs of CS A competition effect on HEP-AuNPs cellular uptake. 167
Figure S47 The physical characterization of HEP- or PEG-coated AuNPs. 168
Figure S48 Light micrographs of RAW 264.7 cells incubated with AuNPs possessing different heparosan (HEP) coating densities. 169
Figure S49 Effect of HEP coating densities on AuNP physical parameters and RAW cell uptake. 170

List of Tables

Table 1.1 Examples of nanoparticle toxicity in human subjects. 8
Table 1.2 Examples of nanoparticle toxicity assessment tools. 20
Table 3.1 Summary of endocytosis inhibitors 87
Table 3.2 Summary of structural analogs of HEP for competition experiments 94
Table S1 Summary of proteins identified from LC/MS-MS 171
Table S2 LC-MS/MS analysis of surface adsorbed proteins from 55-nm HEP-AuNPs. 172
Table S3 LC-MS/MS analysis of surface adsorbed proteins from 55-nm PEG-AuNPs. 173

Abstract

This dissertation presents the development and evaluation of a novel polysaccharide-based surface engineering strategy for nanomedicines.

Chapter one summaries the current status of nanoparticle toxicology. Nanoparticles from natural and anthropogenic sources are abundant in the environment, thus human exposure to nanoparticles is inevitable. Due to this constant exposure, it is critically important to understand the potential acute and chronic adverse effects that nanoparticles may cause to humans. In this chapter, we explore and highlight the current state of nanotoxicology research with a focus on mechanistic understanding of nanoparticle toxicity at organ, tissue, cell, and biomolecular levels. We discuss nanotoxicity mechanisms, including generation of reactive oxygen species, nanoparticle disintegration, modulation of cell signaling pathways, protein corona formation, and poly(ethylene glycol)-mediated immunogenicity. We conclude with a perspective on potential approaches to advance current understanding of nanoparticle toxicity. Such improved understanding may lead to mitigation strategies that could enable safe application of nanoparticles in humans. Advances in nanotoxicity research will ultimately inform efforts to establish standardized regulatory frameworks with the goal of fully exploiting the potential of nanotechnology while minimizing harm to humans. (**Chapter 1**)

Chapter two introduces the use of polysaccharide heparosan (HEP) surface modification on nanoparticles as an alternative to poly(ethylene glycol) (PEG) and showed the investigation of the biological interaction of HEP coated nanoparticles with cells. Nanoparticle modification with PEG is a widely used surface engineering strategy in nanomedicine. However, since the artificial PEG polymer may adversely impact nanomedicine safety and efficacy, alternative surface modifications are needed. Here,

we explored the 'self' polysaccharide HEP to prepare colloidally stable HEP-coated nanoparticles, including gold and silver nanoparticles and liposomes. We found that the HEP-coating reduced the nanoparticle protein corona formation as efficiently as PEG coatings upon serum incubation. Liquid chromatography-mass spectrometry revealed the protein corona profiles. Heparosan-coated nanoparticles exhibited up to 230-fold higher uptake in certain innate immune cells, but not in other tested cell types, than PEGylated nanoparticles. No noticeable cytotoxicity was observed. Serum proteins did not mediate the high cell uptake of HEP-coated nanoparticles. Our work suggests that HEP polymers may be an effective surface modification technology for nanomedicines to safely and efficiently target certain innate immune cells. (**Chapter 2**)

Chapter three describes the HEP-AuNPs uptake behavior and pathways in immune cells and established controlling strategies for nanoparticle cellular uptake. Our findings indicate that HEP-coated nanoparticles were endocytosed in a time-dependent manner by innate immune cells via both clathrin-mediated and macropinocytosis/phagocytosis pathways. Upon endocytosis, HEP-coated nanoparticles were found in intracellular vesicles as well as in the cytoplasm, demonstrating the potential for nanoparticle escape from these intracellular vesicles. Competition with other glycosaminoglycan types inhibited the endocytosis of HEP-coated nanoparticles only partially. We further found that nanoparticle uptake into innate immune cells can be controlled by more than 3 orders of magnitude via systematically varying the HEP surface density. Our results suggest there exists substantial potential for HEP-coated nanoparticles to target innate immune cells for efficient intracellular delivery, including into the cytoplasm. This HEP nanoparticle surface engineering technology may be broadly used to develop efficient nanoscale devices for drug and gene delivery as well as gene editing and immuno-engineering applications. (**Chapter 3**)

Chapter 1 Introduction

1.1 Nanoparticle Classification and Physicochemical Properties

Nanoparticles comprise a class of materials with dimensions in the 1 to 100 nm range that exhibit unique physical, chemical, and biological properties making them distinct from their corresponding bulk materials or small molecule [1,2]. Owing to their unique material characteristics, nanoparticles are broadly used in a range of applications, including industrial catalytic processes, energy conversion and storage, display technologies, as well as cosmetics, medical devices, and therapeutics and diagnostics [3–5]. In addition to such rationally designed nanoparticles, we are constantly surrounded by substantial amounts of naturally and incidentally formed particles, such as corrosion and erosion derived nanoparticles in water and airborne nanoparticles from traffic and industrial combustion [6,7]. The abundance of nanoparticles in the environment and everyday consumer products makes human exposure inevitable. However, the potential acute and chronic health risks that nanoparticles may pose to humans are poorly investigated and understood.

In this article, we introduce the major nanoparticle classes and explore how their corresponding physicochemical properties affect toxicity. Our discussion of the main nanotoxicity mechanisms provides an overview of how nanoparticles interact with the body at organ, tissue, cell, and biomolecular levels. Such mechanistic understanding is enabled by diverse experimental and theoretical methods that have been developed and applied for assessment and evaluation of nanotoxicity. We conclude our discussion with a perspective on potential strategies to mitigate nanotoxicity with the goal to exploit the full potential of nanotechnology for safe application in humans. We hope that our article serves as a valuable resource that covers the current landscape of nanotoxicity research,

and that it will inspire new studies focused on expanding our understanding of nanoparticle toxicity. Improved understanding of nanotoxicity may ultimately inform the development of regulatory frameworks to minimize potential harm to humans

Nanoparticles can be grouped into three main classes: (i) natural, (ii) incidental, and (iii) engineered nanoparticles (**Figure 1.1 A-C**). The first class is comprised of natural nanoparticles that are ubiquitous in the environment and generated during naturally occurring physical, chemical, and biological processes. Examples of such natural nanoparticles include inorganic metal-based nanoparticles, e.g., naturally formed silver nanoparticles, and organic nanoparticles, e.g., virus nanoparticles and exosomes (**Figure 1.1 A**). The second class includes incidental nanoparticles that are generated unintentionally as byproducts of industrial and non-industrial processes, such as corrosion, combustion, or cooking. Examples include inorganic and organic combustion products, such as metal- and carbon-based nanoparticles, respectively (**Figure 1.1 B**). In the third class, engineered nanoparticles are intentionally designed and fabricated for specific industrial and/or medical applications. Examples include zinc oxide and titanium dioxide nanoparticles in sunscreen and liposomes for drug delivery applications (**Figure 1.1 C**) [8–10]. An alternative terminology for natural and incidental nanoparticles is ultrafine particles (UFPs). These UFPs are airborne particulates of less than 100 nm in aerodynamic diameter. While incidental and engineered nanoparticles are typically of anthropogenic origin, i.e. caused and/or prepared by human activity, natural nanoparticles are generated without human intervention [1,6].

Beyond the classification by different sources of origin, the various nanoparticle types can be further differentiated by their physicochemical properties (**Figure 1.1 D**). Physicochemical properties, such as nanoparticle composition, size, surface chemistry, and shape, are key factors that govern nanoparticle interactions with biological systems

and biomolecules. These interactions can affect biomolecular and cellular signaling, biological kinetics and transport, nanoparticle biodistribution, immunogenicity, and toxicity (**Figure 1.2**) [11]. Compared to samples of engineered nanoparticles, natural and incidental nanoparticles tend to exhibit more heterogeneous physicochemical properties with substantial variations in nanoparticle composition, size, surface chemistry, and shape (**Figure 1.1 A-C**). This heterogeneity complicates assessment and understanding of nanoparticle biological interactions, adverse effects, and toxicity.

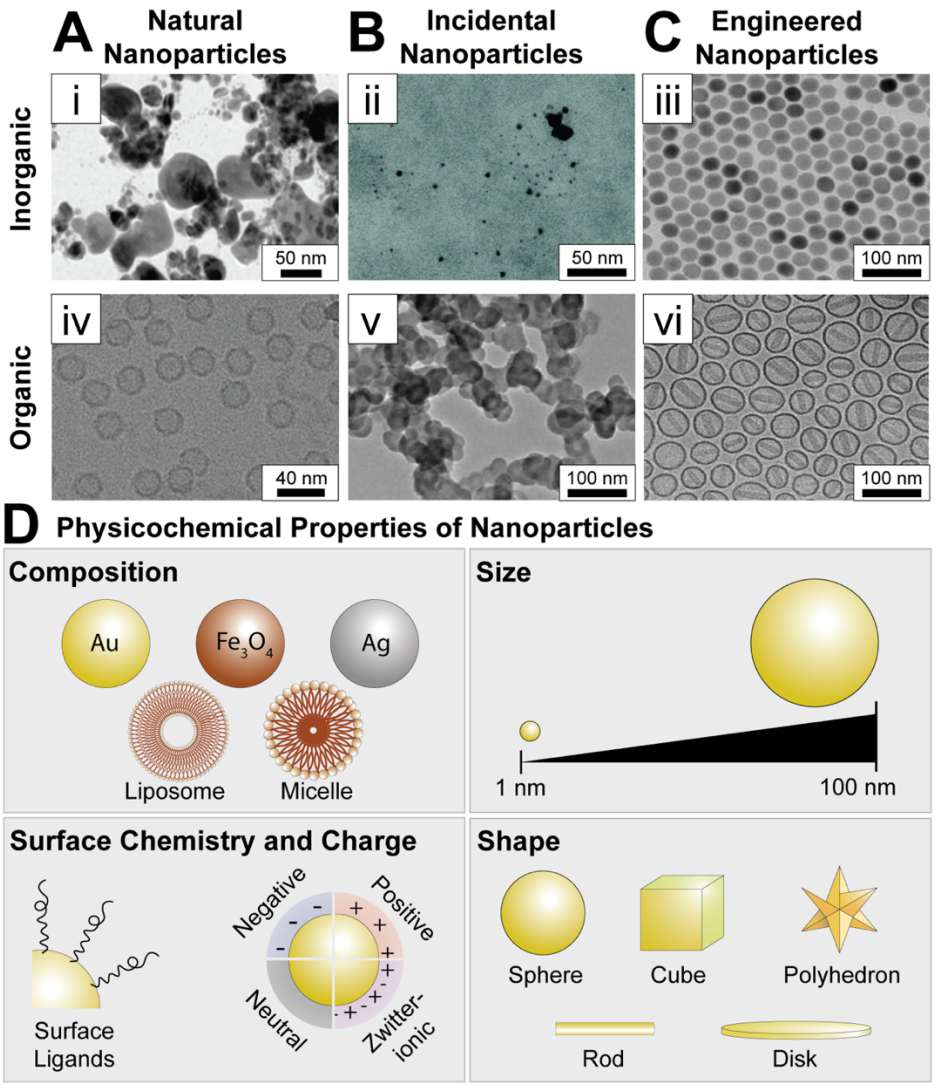

Figure 1.1: Nanoparticle classification and physicochemical properties

Nanoparticles can be broadly organized into three different classes: **(A)** natural, **(B)** incidental, and **(C)** engineered nanoparticles. Nanoparticles from all of these classes can be made from inorganic (i-iii) or organic (iv-vi) materials. In contrast to natural and incidental nanoparticles, engineered nanoparticles typically exhibit narrow size distributions as well as defined shape and surface properties. Panels A-C display transmission electron micrographs of different inorganic nanoparticles (i. and ii. silver nanoparticles; iii. upconversion ($NaYF_4$/Yb,Er) nanoparticles) and organic (iv. cowpea mosaic virus-like nanoparticles; v. carbon black nanoparticles; vi. doxorubicin-loaded liposomes). Adapted with permission: (i) Refs [12], American Chemical Society, 2011; (ii) Refs [13], American Chemical Society, 2011; (iii) Refs [14], Ivyspring International Publisher, 2013; (iv) Refs [15], American Chemical Society, 2019; (v) Refs [16], BioMed Central; 2009; (vi) Refs [17], PLOS, 2014. **(D)** Schematic of various nanoparticle physicochemical properties, including different nanoparticle compositions, sizes, surface chemistries, and shapes.

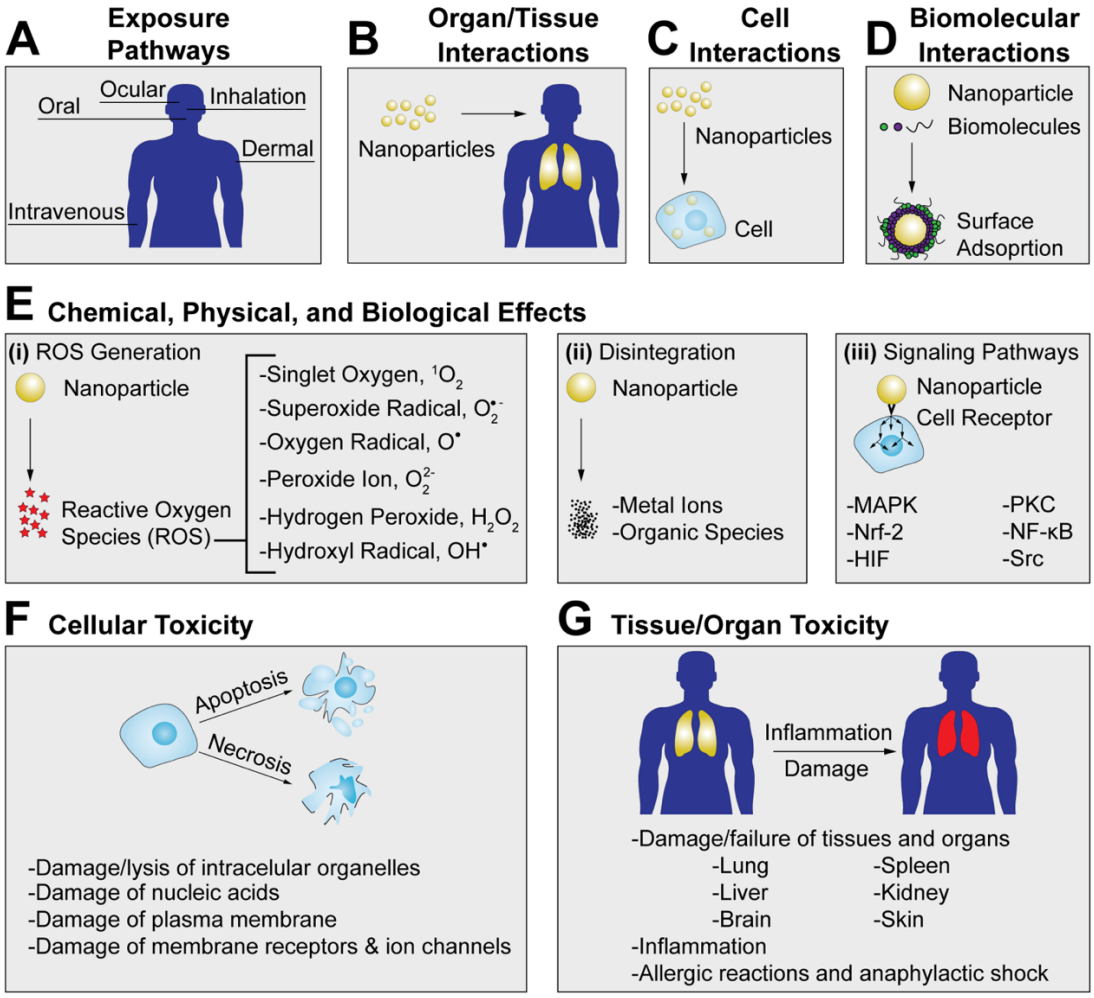

Figure 1.2: Schematic representation of nanoparticle adverse effects and nanotoxicity

(A) Nanoparticle exposure pathways. Upon exposure, nanoparticles can interact with organs/tissues **(B)**, cells **(C)**, and biomolecules **(D)**. Major nanoparticle toxicity mechanisms include: **(E,i)** the generation of reactive oxygen species (ROS); **(E,ii)** nanoparticle disintegration and release of metal ions and organic species; and **(E,iii)** nanoparticle-mediated activation of cell signaling pathways. Nanoparticle adverse effects and toxicity can lead to cell apoptosis and necrosis **(F)**, tissue/organ damage, inflammation, and anaphylactic shock **(G)**.

1.2 Nanotoxicology

The study of nanoparticle adverse effects and toxicity is commonly referred to as nanotoxicology [18]. Upon exposure, all three classes of nanoparticles, i.e. natural, incidental, and engineered nanoparticles, may interact with organs, tissues, cells, and biomolecules (**Figure 1.2**). In consequence, nanoparticle exposure may induce undesirable and harmful nano-bio interactions and other downstream mechanisms that can potentially result in adverse effects and nanotoxicity.

Nanoparticle toxicity may occur as a function of exposure route, dose, concentration, exposure time, and frequency. Traditionally, these fundamental toxicity factors are relevant for assessment of small molecule drugs and other compounds. In the evaluation of nanotoxicology, these parameters are also widely used. However, beyond these classical toxicology parameters, other important factors that may affect nanoparticle toxicity need to be considered, including nanoparticle physicochemical properties, such as material composition, size, surface chemistry, and shape (**Figure 1.1 D**). Compared to small molecules, these additional physicochemical variables make nanotoxicity assessment complex, and evaluation of nanoparticle toxicity on a case-by-case level may be required. For example, slight variations in nanoparticle surface chemistry can result in significantly different toxicity, biodistribution, and elimination profiles even if the nanomaterial core is the same [19–21].

To fully evaluate nanoparticle toxicity, nanoparticle structure and corresponding physicochemical properties need to be completely understood and characterized. This way observed toxic effects can be better attributed to certain nanoparticle properties for establishing specific nanoparticle “structure-activity/toxicity” functional relationships. As nanoparticle structural properties affect toxicity significantly, it is even more

challenging to evaluate the safety of nanoparticles that exhibit large variations in physicochemical properties as seen often for natural and incidental nanoparticles (**Figure 1.1 A-B**). It is therefore challenging to draw general conclusions about nanoparticle toxicity, as nanotoxicity is dependent on complex interactions between different physicochemical properties and the corresponding biological environment. Based on this complexity, it is important to establish well defined standardized methodologies for the systematic evaluation of nanotoxicity under relevant conditions to achieve comparable toxicological data sets. However, this level of standardization has not been achieved yet, which makes it difficult to provide general trends of nanotoxicity for acute (<14 days) and chronic (>4 months) exposure regimens [22] .

To provide examples of the broad range of potential nanoparticle adverse effects and toxicity, we have summarized reported studies that assessed nanotoxicity of different nanoparticle classes and types in human subjects (**Table 1.1**). Table 1 also includes studies that evaluated the toxicity of relevant engineered nanoparticles, such as Ag and ZnO nanoparticles, on human subjects but without any reported clinical or pathological findings, implying that the tested nanoparticles were safe and without noticeable adverse effects under the specific testing conditions. For context, Ag and ZnO nanoparticles are used in over-the-counter consumer products, such as anti-viral, antibacterial, and anti-inflammatory products and compounds, as well as sunscreen [23–25]. We want to emphasize that detailed reports and systematic clinical studies of nanoparticle toxicity in humans for various different nanoparticle types are limited. Most published reports focus on the assessment of nanoparticle toxicity at cell culture and animal model levels. However, these models do not fully recapitulate nanoparticle toxicity responses in humans and are therefore limited in their predictive power of possible hazards to humans [26].

Table 1.1: Examples of nanoparticle toxicity in human subjects.

Adverse Effect	Nanoparticle Class and Type	Exposure Route, Dose, Duration, Number of Human Subjects	Toxicity Mechanism	Toxicity Assessment	Ref.
Neurotoxicity	Natural Fe_3O_4 (<20 nm)	n/a n/a Chronic (many years) 22 human subjects	Abnormal, age-associated biomineralization of Fe_3O_4 in the brain	Quantitative magnetometry; correlation between Fe_3O_4 nanoparticle concentration in the human brain and Alzheimer's disease	[27]
Neurotoxicity	Incidental Fe_3O_4 and Fe_2O_3 (up to 150 nm)	Inhalation n/a Chronic (many years) 37 human subjects	Inhalation of airborne pollutant nanoparticles; potentially enhanced ROS generation leading to neurodegenerative diseases	High-resolution TEM, EELS, and EDX analysis of human brain samples	[28]
Pulmonary toxicity	Incidental Chemically complex mixtures (10-80 nm)	Inhalation 30,000 NPs/cm^3 (>10 times than background levels) Acute (6 h per day for 3 days) 17 human subjects	Upper airway inflammation and systemic oxidative stress with generation of pro-inflammatory cytokines	Analysis of 14 cytokines in nasal lavage samples and analysis of 8-OH-dG and creatinine in human urine samples	[29]
Vascular dysfunction	Incidental Diesel exhaust nanoparticles (<100 nm)	Inhalation $1.2 \cdot 10^6$ NPs/cm^3 Acute (up to 14 days) 16 human subjects	Increased systolic blood pressure and attenuated vasodilation due to nanoparticle induced vascular oxidative stress	Measurement of forearm blood flow, blood pressure, and biomarker analysis of human blood samples	[7]
Genotoxicity	Incidental Silver	Inhalation n/a Chronic 76 human subjects	DNA damage in mononuclear leukocytes due to oxidative stress induced by silver nanoparticles	Blood analysis for DNA damage using alkaline comet assay and analysis of total antioxidant status, total oxidant status, total thiol, and ceruloplasmin in human blood plasma samples	[30]
Immunotoxicity	Engineered PEGylated liposomes (Doxil, ~100 nm)	I.v. 40-306 mg Acute (infusion for 1 h) 29 human subjects	Hypersensitivity reaction and anaphylatoxin release due to complement	Analysis of human blood samples for complement terminal	[31]

			activation of PEGylated liposomes	complex (SC5b-9) to correlate complement activation with hypersensitivity reaction	
None reported	Engineered Silver (A: 5-10 nm, and B: 25-40 nm)	Ingestion A: 100 µg/day; B: 480 µg/day Acute (up to 14 days) 60 human subjects	No clinically important changes in weight, BMI, blood pressure, heart rate, and laboratory findings in blood and urine samples	Analysis of human blood and urine samples, including hematology, ELISA for ROS and pro-inflammatory cytokines, MRI	[32]
None reported	Engineered ZnO w/ and w/o silane coating (up to 74 nm)	Topical dermal application Up to 100 mg/mL daily Acute (up to 5 days) 5 human subjects	No nanoparticle penetration through stratum corneum; no morphological or redox changes	Analysis of nanoparticle skin penetration using multiphoton tomography and fluorescence lifetime imaging microscopy	[10]

To emphasize the importance of composition and other physicochemical properties on nanoparticle adverse effects and toxicity, we highlight a study by Mills et al. that assessed adverse vascular side effects in 16 healthy human subjects exposed to combustion-derived nanoparticles from diesel exhaust over an acute exposure duration of 14 days [7]. Impaired vascular function in study subjects was observed due to oxidative stress caused by inhalation of diesel exhaust nanoparticles. In contrast, when study subjects were exposed to filtered exhaust, i.e. exhaust without nanoparticles, or air containing pure carbon nanoparticles, vascular impairment was not observed. These findings indicate that nanoparticle composition along with other physicochemical properties play key roles in nanotoxicity.

Other important nanoparticle physicochemical properties that affect nanotoxicity include size, surface chemistry, and shape (**Figure 1.1 D**). For more detailed information on how nanoparticle physicochemical properties affect nano-bio interactions, adverse effects, and toxicity, we refer interested readers to excellent review articles by Chan and Howard groups, respectively [11,18].

Nanoparticle size is a physicochemical parameter that has been reported to affect cellular uptake efficiency and cytotoxicity [33]. A study by Pan et al. reported size-dependent cytotoxicity of gold nanoparticles with identical surface chemistry on fibroblasts, epithelial cells, macrophages, and melanoma cells in cell culture [34]. The researchers reported that nanoparticles with a diameter of 1.4 nm exhibited the highest cytotoxicity, while nanoparticles with a diameter of 15 nm had no reported toxicity. The esearchers listed size-dependent nanoparticle cell uptake kinetics and interactions with the cell plasma membrane promoting cell apoptosis and necreosis as potential reasons for the observed differences in cytotoxicty.

In addition to nanoparticle size, surface chemistry is another important parameter that directly affects nanotoxicity. For example, a study by Bozich and coworkers concluded that gold nanoparticles with an overall positive surface charge exhibited a greater extent of toxicity on

Daphina magna model organisms compared to negatively charged gold nanoparticles of the same core size [35]. Similarly, Lee and coworkers reported enhanced cytotoxicity of positively charged gold nanoparticles upon evaluation of mouse breast cancer 4T1 cells in cell culture [36]. In comparison to neutral nanoparticles, there was a substantial reduction in cell viability of ~50% for positively charged nanoparticles. Potential reasons for the increased toxicity of positively charged nanoparticles include a higher electrostatic attraction of nanoparticles to negatively charged cell surfaces and overall increased nanoparticle cellular uptake, potentially leading to increases in oxidative stress and reactive oxygen species [37,38]. As the nanoparticle surface interacts directly with biomolecules and biological systems, it is a driver of cellular uptake and intracellular transport kinetics [33]. In addition, surface chemistry and surface charge are key factors of nanoparticle agglomeration and aggregation, which are additional variables that need to be considered in the assessment of nanotoxicity [39,40].

Besides size and surface chemistry, nanoparticle shape may significantly affect nanotoxicity [38]. For example, a study by Zhao and coworkers reported increased cytotoxicity of needle- and plate-shaped nanosized hydroxyapatite compared to sphere- and rod-shaped nanoparticles in human lung BEAS-2B epithelial cells [41]. A potential reason for the increased cytotoxicity may be that needle- and spike-like nanoparticle shapes potentially puncture cellular membranes leading to compromised cellular integrity and cell death. The shape properties of micro- and nanoparticles can also induce physical activation of innate immunity. As reported by Wang et al., TiO_2 microparticles exhibiting nanospikes can exert mechanical stress on cells which can lead to potassium efflux and inflammasome activation in macrophages and dendritic cells [42]. These findings highlight the potential of nanoparticle shape to tune nanoparticle immunogenicity by physical cues which could potentially be attractive for vaccination and immunotherapy approaches.

Nanoparticle physicochemical properties not only affect cellular interactions but may

also determine biodistribution, clearance, and elimination [43–45]. For example, nanoparticles with sizes smaller than 5.5 nm will be eliminated rapidly via kidneys into urine [46]. Nanoparticles larger than the renal cutoff size are often efficiently sequestered by cells in the liver and spleen, including Kupffer cells, B cells, T cells, and endothelial cells [45], and may be eliminated to various extent via the hepatobiliary pathway [21]. Understanding how nanoparticle physicochemical properties affect nano-bio interactions will provide an opportunity to control nanoparticle fate and toxicity inside the body. Such control may ultimately lead to more potent nanoparticle-based medical treatments and diagnostics with reduced side effects and toxicity for patients. An example for this is the use of liposomes that encapsulate the small molecule cancer drug doxorubicin. Compared to treatment with free drug, FDA-approved doxorubicin liposomes (i.e. Doxil®) can reduce cardiotoxicity to improve the quality of life for cancer patients [47].

1.3 Nanotoxicity Mechanisms

There are a number of different pathways how nanoparticles can enter the body. These pathways include, inhalation, oral ingestion, ocular exposure, skin deposition, and intravenous administration (**Figure 1.2 A**) [10,48–51]. The inhalation of airborne nanoparticles is a major exposure pathway and allows nanoparticles to enter and deposit in lung tissues and the alveolar region (**Figure 1.2 B**) [52]. Accumulation of nanoparticles in the lung can lead to oxidative-stress mediated lung inflammation at both acute and chronic stages [53,54]. Maher and coworkers reported that magnetite nanoparticles can enter the brain via the olfactory bulb [28]. Brain accumulation of magnetite nanoparticles that are abundant in airborne particulate matter pollution can lead to enhanced production of reactive oxygen species which is causally linked to neurodegenerative diseases, such as Alzheimer's disease [28,55] .

After entering the body, nanoparticles may interact with the initially encountered organ or tissue. Nanoparticles may also translocate and enter the bloodstream (for example in the lung) to access distant organs/tissues via systemic transport (**Figure 1.2 B**) [56,57]. Within organs, tissues, and the blood, nanoparticles can interact with cells and intracellular organelles to potentially cause toxicity at cellular and subcellular levels (**Figure 1.2 C**). It is important to point out that upon entry into the body nanoparticles interact with a variety of different biomolecules, including proteins, sugars, lipids, and nucleic acids (**Figure 1.2 D**). These interactions result in the formation of a biomolecular nanoparticle surface corona, often referred to as protein corona. Protein corona (or biomolecular corona) formation may change nanoparticle surface chemistry substantially and ultimately affect nanotoxicity. The binding of proteins to nanoparticle surfaces may also lead to protein unfolding [58,59]. This process may induce the loss of protein function and may cause immunotoxicity [60,61] . In addition, the protein configuration change can lead to adverse effects and toxicity via cell signaling pathway activation [59], enzyme function loss [62], nanoparticle aggregation [58], new antigenic site formation

[63], and protein fibrillation [64].

At the cellular level, direct interaction between nanoparticles and cells may result in physical damage of cell membrane structures [65,66]. For example, graphene nanoparticles have been reported to cause physical damage, cytoskeletal dysfunction, and abnormal morphological stretching in different cell types as a result of the blade-like shape of these materials [65,66]. In addition, nanoparticles may be able to block cell membrane receptors and membrane ion channels, which may interrupt normal cellular biofunctions and homeostasis [67]. Leifert et al. reported that 1.4-nm gold nanoparticles were able to block voltage-gated potassium channels in vitro, which may lead to unwanted cardiac malformation in mice [67].

A major nanotoxicity mechanism is the generation of reactive oxygen species (ROS), such as singlet oxygen, superoxide anion radical, oxygen radical, peroxide ion, hydrogen peroxide and hydroxyl radical (**Figure 1.2. E**). ROS generation can occur in different ways. One way is through one-electron oxidative reactions with transition metals or nanoparticle surface groups [68,69]. It is important to note that a nanoparticle exhibits a relatively large surface area compared to the particle volume. An increase in surface area is typically accompanied by an increase in chemical reactivity potentially leading to increased ROS production. Another ROS generation mechanism is via mitochondrial respiration and subsequent ROS release into the cytoplasm through pores in mitochondrial membranes created by nanoparticles [68]. In healthy cells, an equilibrium is maintained between intracellular antioxidants and ROS. However, intracellular nanoparticles can directly damage mitochondria, causing an increase in intracellular ROS and oxidative stress [70]. Enhanced intracellular ROS levels may stimulate further ROS release from mitochondria through a process called ROS-induced ROS release (RIRR). This process can substantially increase intracellular ROS levels and amplify the oxidative imbalance [71]. High levels of ROS can cause oxidative stress and damage to cellular organelles, DNA, cell membranes, ion channels and cell surface receptors leading to adverse effects and toxicity.

Metal or metal oxide nanoparticles are used in preclinical and clinical applications, such as imaging, photothermal therapy, and biosensors [72]. However, corrosive tissue microenvironments and lysosomal degradation may disintegrate nanoparticles to release potentially harmful metal ions (**Figure 1.2 E**). For many nanoparticles, including Ag, CdSe, ZnO, and Fe_3O_4 nanoparticles, released metal ions may generate high levels of oxidative stress and are main sources of nanotoxicity. For example, Ag(I) ions released from silver nanoparticles can cause DNA damage, ROS generation and cell membrane destruction as reported from cell culture studies [73]. We want to emphasize that nanotoxicity results obtained in cell culture studies do not necessarily recapitulate the nanoparticle toxicity potential in animal models or human subjects. For example, CdSe quantum dots were found to be toxic in cell culture, but there was no reported toxicity in animal models [74–77].

The generation of high levels of ROS and the release of harmful metal ions from nanoparticles have been reported to affect a variety of cell signaling pathways, such as nuclear factor kappa-light-chain enhancer of activated B cell (NF-kB), mitogen activated protein kinase (MAPK), Akt, and Src (**Figure 1.2 E**) [78–81]. Activation and modulation of these signaling pathways can affect cell proliferation, differentiation, and cell survival. Nyga et al. reported that cobalt nanoparticles can stabilize hypoxia-inducible factor (HIF) protein and upregulate HIF gene expression. HIF pathway activation can affect cell growth, cell survival, apoptosis, and metabolic adaptation [82,83]. Importantly, there can be interplay and synergistic effects between ROS generation, cell signaling modulation, and nanoparticle disintegration. For example, nanoparticle disintegration may lead to modulation of signaling pathways and/or induce ROS generation [84]; ROS generation can activate numerous signaling pathways or cause nanoparticle disintegration; and in turn, different cell signaling pathways can induce ROS generation [85]. These mechanisms may cause damage of cell membranes, intracellular organelles and nucleic acids and eventually lead to cell apoptosis or necrosis (**Figure 1.2 F**). Loss of functional cells

may compromise organ function and result in organ damage or inflammatory responses (**Figure 1.2 G**). Moreover, cell apoptosis, necrosis, and pyroptosis may lead to the release of large amount of intracellular content to potentially cause local inflammation or systemic immune responses (**Figure 1.2 G**) [86–88].

In addition to the toxicity caused by nanoparticle core materials, surface components may also contribute significantly to nanoparticle adverse effects and toxicity. For example, researchers coat nanoparticle surfaces with polymers, such as dextran and poly(ethylene glycol), PEG, to reduce adsorption of proteins and other biomolecules and to prolong nanoparticle blood circulation times [89,90]. Thus, PEG is widely used in preclinical and clinical studies for surface modification of nanomedicines. However, PEG may induce hypersensitivity reactions and anaphylaxis in human subjects mediated by anti-PEG antibodies [31,91,92].

Upon an initial systemic administration of PEGylated nanoparticles, anti-PEG IgM may be generated by marginal zone spleen B cells (**Figure 1.3 A-B**). The anti-PEG IgM then target PEGylated nanoparticles during subsequent administrations causing complement activation via the classical pathway (**Figure 1.3 C**) [93–96]. Upon activation of the complement system, anaphylatoxins will be released, including platelet-activating factor, histamine, or cytokines, resulting in hypersensitivity reactions [97]. Kozma and coworkers documented the causal relationship between complement activation by anti-PEG IgM and hypersensitivity reactions in pig models. Although the study was conducted in pigs, it provides valuable insights into potential PEG-related toxicity mechanisms in humans [98]. Other studies reported that hypersensitivity to nanoparticles surface components may be induced by complement activation via alternative pathway. This pathway does not dependent on anti-PEG antibodies and is not limited to PEGylated nanoparticles [99,100]. More in-depth studies are needed to fully elucidate the underlying mechanisms of hypersensitivity reactions. In addition to complement activation-related pseudoallergy (CARPA) reactions, complement independent pseudoallergy (CIPA) is

caused by anti-PEG IgG (**Figure 1.3 C**). Mechanistically, a nanoparticle binds to anti-PEG IgG forming the nanoparticle-IgG complex. This complex can bind to the Fcγ receptors on mast cells, basophils, and neutrophils resulting in the release of platelet-activating factor, histamine, or cytokines, to induce hypersensitivity reactions [101–103].

Hypersensitivity reactions often occur during second and later stage administration of PEGylated nanoparticles. However, hypersensitivity reactions have also been observed during the first dosage in human subjects. A potential explanation for this is the abundance of pre-existing anti-PEG IgG in humans [102]. It has been reported that humans who had never received PEGylated materials and drugs exhibit pre-existing anti-PEG IgG in various amounts [104,105]. According to a study by Yang et al., anti-PEG antibodies were detected in 72% of contemporary human samples, while 56% of historical samples from the past 30 years exhibited anti-PEG antibodies. A large number of humans exhibit detectable levels of anti-PEG IgG and IgM and these numbers are expected to increase in the future as a result of human exposure to products that contain PEG, such as over-the-counter medication, cosmetics, and other everyday consumer products [97,112]. Besides hypersensitivity reactions, complement activation can also directly attack the lipid membrane of drug-carrying nanoparticles, such as doxorubicin liposomes, to release encapsulated chemotherapy drugs prematurely. Such premature drug release may affect the therapeutic effect of nanomedicines and could potentially contribute to additional nanotoxicity concerns [113]. Anti-PEG immunity may also contribute to the so-called accelerated blood clearance (ABC) phenomenon (**Figure 1.3 C**) [114,115]. Upon repeated administration of PEGylated nanoparticles, anti-PEG IgM opsonization may trigger efficient nanoparticle phagocytosis. As a result, nanoparticles may accumulate to a large extent in cells and organs of the mononuclear phagocyte system, including the liver, after their first administration. Besides the observed decrease in nanoparticle therapeutic efficacy upon ABC, acute and chronic nanotoxicity of sequestered nanoparticles are of substantial concern.

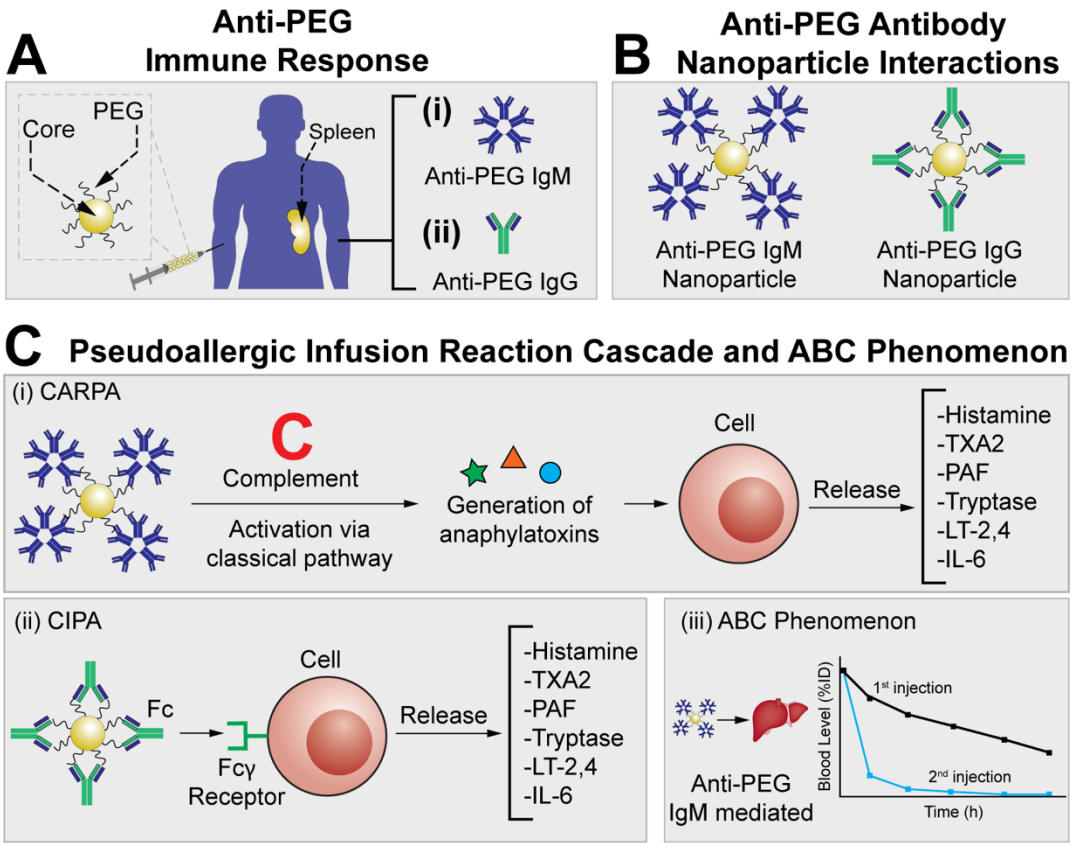

Figure 1.3: Anti-PEG immunogenicity induced mechanisms of nanoparticle pseudoallergic infusion reaction cascade and accelerated blood clearance (ABC) phenomenon

(A) Anti-PEG immune responses can be stimulated by intravenous administration of PEGylated nanoparticles. These nanoparticles can stimulate spleen marginal zone B cells and plasma B cells to produce anti-PEG IgM and IgG, respectively. **(B)** Anti-PEG IgM and IgG can bind efficiently to PEGylated nanoparticles. **(C,i)** The complement (*C*) activation-related pseudoallergy (CARPA) mechanism is initiated by anti-PEG IgM binding to the nanoparticle surface. In a subsequent step, the complement system is activated via the classical pathway. This activation leads to generation of anaphylatoxins that stimulate different types of innate immune and blood cells, including macrophages, mast cells, basophils, and granulocytes, to release secondary mediators of pseudoallergy, such as histamine, TXA2, PAF, Tryptase, LT2-4, and IL-6. **(C,ii)** The complement independent pseudoallergy (CIPA) is characterized by anti-PEG IgG binding to nanoparticles. The anti-PEG IgG Fc fragment can bind to Fcg receptors on macrophages, mast cells, and basophils, to release secondary mediators of pseudoallergy. **(C,iii)** The rapid blood clearance of PEGylated nanoparticles upon repeated administration is referred to as the ABC phenomenon and is mediated in part by anti-PEG IgM opsonization leading to efficient nanoparticle phagocytosis and accumulation in cells and organs of the mononuclear phagocyte system, including the liver.

1.4 Nanotoxicity Assessment

Toxicity assessments are used to evaluate the safety of nanoparticles. In **Table 1.2**, we have summarized examples of commonly used cell culture and animal toxicity tests used for nanotoxicity assessment. Cell culture studies enable the nanotoxicity evaluation for various model animal and human cell lines and are beneficial due to their simplicity, scalability, low cost, and throughput. However, cell culture studies, in contrast to animal models, lack complex physiology and are limited in their predictive power of nanotoxicity for other species and humans. Animal model testing allows to account for complex physiological environments during nanotoxicity assessment but may be limited in predicting toxic responses and adverse effects in humans. Computational nanotoxicity methods can help to bridge the gaps between cell culture, animal models, and human subjects and will substantially impact nanotoxicity modelling and prediction in the future [116]. Computational studies can reduce the need, cost, and time required for animal and cell nanotoxicity testing [117–119]. However, due to the lack of standardized protocols for nanotoxicity testing, published studies exhibit substantial heterogeneities in term of nanoparticle characterization, dose metrics, experimental methods, data completeness, reducing the overall statistical power and accuracy of computational models for nanotoxicity predictions [120,121].

Table 1.2: Examples of nanoparticle toxicity assessment tools.

	Assessment tools	Ref.
Cell culture level toxicity tests		
Cell membrane integrity	LDH assay	122
Cell morphology	Microscopy	123
Cell necrosis and apoptosis	Flow cytometry	124
Cell viability and cell death	MTT assay, live/dead assay, flow cytometry, trypan blue, WST	125
DNA damage and gene expression	Comet assay with formamidopyrimidine-DNA glycosylase (Fpg) treatment; gene expression levels monitored by qPCR	126
Hemoglobin release	Hemolysis assay	127
Inflammation and immune responses	ELISA	128
Ion channel disruption	Patch-clamp experiment	129
Mitochondrial damage	Mitochondrial membrane potential (MMP) measurements	130
Protein structure	CD, DSC, FTIR, cryo-EM	131
ROS generation	DCFH assay, fluorescence lifetime imaging microscopy	132,133
Animal and human level toxicity tests		
Biochemistry	Tissue-damaging enzymes (ALP, LDH, ALAT), cytokine analysis	134
Hematology	Hemoglobin content, total protein, total erythrocytes and leukocytes counts	135
Histopathology	Tissue sections (hematoxylin/eosin, immunohistochemistry)	134,136
Pharmacokinetics and pharmacodynamics	MRI, PET, SPECT, CT, ICP-MS, fluorescence, biodistribution, clearance, and elimination	51,137
Skin test	Skin penetration and skin allergic reactions	10
Survival studies	Kaplan-Meier analysis, survival curves, median survival, LC_{50}, LD_{50}	135
Clinical trials (phase I-IV)	Safety and toxicity data on human subjects	138

1.5 Strategies to Mitigate Nanotoxicity

By understanding the underlying toxicity mechanisms, researchers can start to devise strategies for mitigating nanoparticle adverse effects and nanotoxicity. While few studies focus on manipulating the nanoparticle core composition, the majority of reported approaches center around the modification of nanoparticles surface chemistry and surface properties. For example, silica coating and polymer encapsulation strategies can be used to control nanoparticle disintegration and ion release kinetics of metal and metal oxide nanoparticles to mitigate metal ion induced toxicities and ROS production [14,139–142]. Another popular approach is to passivate the nanoparticle surface with PEG for reducing biomolecular corona formation and for camouflaging nanoparticles. However, due to the immunogenic potential of PEG, other nanoparticle surface coating technologies are urgently needed that provide similar camouflaging properties as PEG but without side effects for patients, including hypersensitivity, allergic reactions, and anaphylactic shock. A creative approach to addressing this challenge is to wrap nanoparticles in cell plasma membranes, such as membranes derived from erythrocytes [143]. Red blood cell membrane coated nanoparticles exhibit minimal protein corona formation, toxicity, and immunogenicity. These strategies can be effective in mitigating the nanotoxicity potential of engineered nanoparticles to provide safer and more potent nanomedicines in the future and to use nanoparticles for safe applications in consumer products and industrial processes. However, it is difficult to apply such strategies to natural and incidental nanoparticles. The nanotoxicity of these nanoparticles may be mitigated by antioxidant therapy or by reducing human exposure to these nanoparticles via respiratory protection, including masks and other protective equipment [139,144].

1.6 Perspective and Conclusion

One of the most pressing questions in conversations about nanoparticles it whether nanoparticles are toxic. The answer to this question is not straightforward as nanotoxicity depends on many parameters. Great caution is required to not generalize nanoparticle safety and toxicity concerns. At current state, the evaluation of nanoparticle toxicity requires careful case-by-case assessment, because biological and pathological effects are determined by a number of variables, including nanoparticle physiochemical properties, exposure route, dose, duration, and others. This is in line with recent thoughtful editorials, viewpoints, and correspondences on nanoparticle risk assessment and nanosafety [145–150]. Nanotoxicity is a highly important and timely research area, as human exposure to different nanoparticle classes and types will continue to increase in the future.

One of the main barriers to advancing progress in nanotoxicology is the lack of unified and standardized procedures of nanoparticle characterization, risk assessment methods, and reporting [121,145,151]. For example, nanoparticle dose metrics are used and reported differently in different research studies, including mass-, surface area-, or nanoparticle number-based metrics [18]. It will be important to standardize nanoparticle dose metrics in experimental design and data reporting to facilitate data mining and computational approaches, such as the NanoSolveIT project, that use multi-scale physics-based and data-driven models, including toxicogenomics and biokinetics, for integrated in silico nanoparticle risk assessment [116]. Modeling and prediction of nanotoxicity require harmonized and integrated datasets to train the computational models.

These datasets are typically obtained from conventional nanotoxicity studies that are based on in vitro cell culture studies and/or in vivo animal model experiments. There are ongoing debates within the research community about the potential and power of these models for predicting nanotoxicity in humans [117,119,120,134]. A limitation for assessment of potential

nanoparticle risks in those simplified models is that it is difficult to model chronic long-term exposure in laboratory animals that exhibit significantly shorter lifespans than humans do. However, data on chronic low dose nanoparticle exposure might provide valuable new insights on the long-term toxic effects of nanoparticles. Great attention and care should be placed on evaluating and understanding the mechanisms of nanotoxicity in biologically and physiologically relevant models. This may require new models of toxicity evaluation that exploit high throughput screening methods [152,153], machine learning approaches [117], and the development of new 3D microfluidic based tissue chips and organoids aimed at better recapitulating human physiology [154–156]. Such advanced tissue models combined with advanced optical imaging [157–160] and single-cell analytical methods, such as single-cell RNA sequencing and single-cell elemental quantification could provide powerful tools to assess nanotoxicity at an individual cell level [161].

As nanoparticles may trigger immunogenicity and immunotoxicity, as observed in some cases with PEGylated nanomedicines, the formulation of non-immunogenic nanoparticles is required. This may be achieved by coating nanoparticles with PEG-alternatives, such as zwitterionic polymers or cell derived plasma membranes [162,163]. Recently, Lazarovits and coworkers reported a method to create a new class of size- and shape tunable nanoparticles that are made entirely from patient-derived proteins. These nanoparticles are biodegradable and do not activate innate or adaptive immunity following systemic administration in animal models [164].

Nanotoxicology research will greatly benefit from the convergence of disciplines, such as materials science, chemistry, engineering, biology, medicine, and toxicology, to answer the pressing questions if nanoparticles are safe for applications in humans and if yes, under which conditions. Ultimately, such concerted research will inform regulatory agencies and catalyze the generation of frameworks to exploit the full potential of safe nanoparticles in humans.

Chapter 2 Nanoparticle Surface Engineering with Heparosan Polysaccharide Reduces Serum Protein Adsorption and Enhances Cellular Uptake

2.1 Introduction

Nanoparticles provide flexible platforms for the development of drug delivery technologies, disease diagnostics, and vaccines[8,9,44,165–167]. Yet, upon exposure to physiological fluids, proteins adsorb onto the nanoparticle surface to form a layer termed the protein corona[168,169]. This protein corona can alter the biological fate and immunogenicity of nanoparticles[168–171]. For example, certain proteins can undergo configurational changes upon adsorption to nanoparticle surfaces, potentially resulting in nanoparticle aggregation or the presentation of novel antigenic sites [58,63]. To address this challenge, nanoparticle surface modifications with synthetic polymers are commonly used in nanomedicine to enhance colloidal stability and reduce the non-specific protein adsorption [14,36,162,172,173].

While the FDA has approved the clinical use of nanoparticles with polymer coatings, such as poly(ethylene glycol) (PEG) and dextran, these coating agents have been reported in some cases to impact nanomedicine safety and efficacy adversely [174–176]. These reports have raised growing clinical concern about anti-PEG immunogenicity, which may be amplified by the widespread use of PEG in cosmetics, health care products, and over-the-counter medications [104,177]. Recently, the PEG-coated nanoparticles have been developed as COVID vaccines. The U.S. Centers for Disease Control and Prevention reported an allergic rate of 11.1 per million administered doses of Pfizer/BioNTech's COVID vaccine, and a boosted injection indicated a mean of 1.78-fold increase of anti-PEG antibodies [106–111]. The allergic reaction of PEG to the vaccines carried the high risk of anaphylaxis. Anti-PEG antibodies can bind to PEGylated nanoparticles, which may induce undesired immune responses, including premature clearance

of nanomedicines, allergic reactions, and anaphylaxis [98,101,104,108,111,178–180]. There is a need to investigate alternative nanoparticle surface modifications that can address the shortcomings of PEGylated nanomedicines [181].

Here, we explored the polysaccharide heparosan (HEP) as a biocompatible nanoparticle surface modification agent. The HEP polysaccharide is a biosynthetic precursor in the anticoagulant polysaccharides pathway in animals [182,183]. In a previous report, no immunogenicity was observed when HEP was used as a surface coating agent for drug delivery liposomes in vivo [184]. While some reported studies used HEP-coated liposomes and micelles [184–187], we demonstrate here the broad applicability of HEP surface modifications for various inorganic and organic nanomaterials (i.e. gold nanoparticles (AuNPs), silver nanoparticles (AgNPs), and synthetic liposomes). Using AuNPs as a model system, we systematically characterized HEP-based surface modifications and quantitatively assessed the associated biological interactions.

First, we adopted two different methods, salt aging and pH reduction, to efficiently functionalize the negatively charged HEP on the surface of AuNPs of various sizes. Then, AuNPs with various HEP surface densities were exposed to serum-containing media, and we compared the protein corona characteristics to PEGylated nanoparticles. Next, we performed label-free liquid chromatography tandem mass spectrometry (LC-MS/MS) to study the protein corona profiles of HEP- or PEG- functionalized AuNPs. We quantified the cytotoxicity, cytokine release profiles, and the cellular uptake of these HEP- or PEG-coated AuNPs upon exposure to various cell types. Additionally, we assessed the cellular uptake profiles of HEP- or PEG-coated AgNPs and liposomes. Our results indicate that HEP polymers may be an effective surface modification technology for nanomedicines.

2.2 Materials and Methods

2.2.1 Nanoparticle synthesis (15-nm, 55-nm, or 100-nm AuNPs; 55-nm AgNPs; and liposomes)

A redox reaction-based bottom-up synthesis approach was used for the synthesis of 15-nm, 55-nm, or 100-nm AuNPs. Aqua Regia was used to clean the reaction flasks before synthesis. Aqua Regia is prepared as a 3:1 ratio of hydrochloric acid (Sigma-Aldrich, ACS reagent, 37%) and nitric acid (Sigma-Aldrich, ACS reagent, 70%).

Based on a protocol published by Turkevich *et al.*, we synthesized 15-nm gold nanoparticles [188]. Briefly, 98.9 mL nanopure water and 1.0 mL of 0.102M sodium citrate tribasic dihydrate (Sigma-Aldrich) were prepared in aqua regia-cleaned 250 mL Erlenmeyer flask. This flask was then placed on a hot plate with settings of 300 °C and ~200 rpm. When the mixture solution in this flask started boiling, 100 µl of 0.25 M aqueous gold (III) chloride trihydrate (Sigma-Aldrich) was added rapidly, and the stirring speed was increased to ~ 400 rpm. Next, a 7 min timer was set. During this 7 min of reaction, the color of the solution changed from purple to cherry red. After 7 min, the flask was placed on ice to quench the reaction and then stored at 4°C. To prevent nanoparticle aggregation, Tween 20 (Sigma-Aldrich, Molecular Biology, Grade) was added with a final concentration of 0.01% (v/v) Tween20. To concentrate and wash, nanoparticles were centrifuged at 15,000 x*g* for 90 minutes using a ThermoFisher Heraeus Multifuge X3R centrifuge. Both DLS and UV-Vis spectrophotometry measurements were performed for nanoparticle quality assessment.

To synthesize larger nanoparticles, a seed-mediated synthesis protocol from Perrault *et al*. was adopted [189]. The 15-nm seed gold nanoparticles were prepared by the previously described protocol; these 'seed' particles were transferred to a new clean flask to synthesize 55-nm AuNPs. The solutions were added and mixed in the following order at room temperature and 400 rpm: 93.7 mL of nanopure water, 0.967 mL of 15-mM aqueous sodium citrate tribasic dihydrate, 0.967 mL of 25-mM aqueous gold (III) chloride trihydrate, 3.35 mL of citrate-stabilized 2.4-nM 15 nm gold nanoparticles (without the addition of Tween 20), and 0.967 mL 25-mM aqueous hydroquinone (Sigma-Aldrich, ReagentPlus, ≥ 99.0%). The solution turned from light pink into dark wine-red right after the addition of hydroquinone. After the overnight reaction, 1 mL, 10% Tween 20 (v/v) was added to this mixture to get a final Tween 20 concentration around 0.1% (v/v). Nanoparticles were centrifuged at 2,000 x*g* for 120 minutes, and then the supernatant was discarded. Pellets were washed with 0.1% (v/v) Tween 20 and 0.01% (w/v) sodium citrate tribasic dihydrate solution for 3 times following centrifugation at 2,000 x*g* for 30 minutes. Nanoparticles were dispersed in 0.1% (v/v) Tween 20 and 0.01% (w/v) sodium citrate tribasic dihydrate solution, and then both concentration and hydrodynamic diameter were measured by UV-Vis spectrophotometry and DLS, respectively. The nanoparticle dispersion was stored at 4 °C until further use.

A modified one-pot method was adopted for the synthesis of 55-nm citrate-capped silver nanoparticles (AgNPs) [190]. Briefly, tannic acid and sodium citrate tribasic dihydrate were added into 100 mL of boiling nanopure water for final concentrations of 5 mM and allowed to stir vigorously for 15 minutes. Then, 0.1 mL of 250 mM silver(I) nitrate was immediately added to the reaction and boiled for 15 minutes.

Uncoated liposomes and PEG-coated liposomes were prepared based on a published paper [154]. Briefly, uncoated liposomes with a fluorescent tag for imaging were prepared by adding a stock of 0.44 mg/mL DiO'; DiOC18 (3) (3,3'-Dioctadecyloxacarbocyanine Perchlorate) in chloroform to solid 1,2-distearoyl-sn-glycero-3-phosphocholine (DSPC) and cholesterol (final molar ratio of 1:1.3:0.9, respectively). PEG-liposomes were prepared by using 0.44 mg/mL DiO'; DiOC18(3) (3,3'-Dioctadecyloxacarbocyanine Perchlorate) (solvent is chloroform) dissolved 1,2-distearoyl-sn-glycero-3-phosphocholine (DSPC), cholesterol, and phosphatidylethanolamine modified with 2-kDa polyethylene glycol (DSPE-PEG2000) (final molar ratio of 1:1.3:0.9:0.3). After mixing lipids in the desired ratio, the chloroform was evaporated by a rotary evaporator. The lipid films were suspended in 600 μL of 37ºC warmed 1x phosphate buffered saline using bath sonication (ultrasonic cleaner Branson CPX8800H at 25ºC) for approximately 20 min. The mixture was then extruded through a 100-nm polycarbonate filter at 60ºC for 21 cycles. The hydrodynamic diameter was measured by DLS.

2.2.2 Heparosan synthesis and characterization of OPSS-HEP conjugation

A quasi-monodisperse 13 kDa-heparosan (HEP) polysaccharide (polydispersity *Mw/Mn* 1.038 +/- 0.005) with a reducing end amino group (HEP-NH2) was synthesized by synchronized, stoichiometrically controlled chemoenzymatic reaction using an amine-containing acceptor, UDP-sugar donors, and PmHS enzyme as described previously.[191] This starting material was employed to create two derivatives: (a) a HEP with a thiol-reactive group (HEP-OPSS) at the reducing terminus, and (b) a radioactive version of the same polymer tagged at the non-reducing terminus ([^{3}H]HEP-OPSS). HEP polymers were quantified using the carbazole assay with a glucuronic acid standard [192].

The thiol-reactive dithiol-pyridyl (OPSS) group was introduced into the reducing end of various HEP-NH_2 polymers using a 31- to 42-fold molar excess of *N*-succinimidyl 3-(2-

pyridyldithio)propionate (SPDP) (ThermoFisher) added as 2 or 4 additions in neat DMSO; the reaction was performed with 6-6.7 mg/mL HEP-NH_2 and 30-37% DMSO solvent final in 0.1 M HEPES, pH 7.2, 5 mM EDTA, at room temperature overnight. The HEP-OPSS target was precipitated by the addition of NaCl (0.1 M final) and 4.8 volumes of isopropanol on ice for 2 hours. The resulting pellet was harvested by centrifugation (1,800 x *g*, 30 min), the supernatant was aspirated, and the pellet was dried (3 min under vacuum or air-dried for 2.25 hours) before re-suspension in water at 4°C overnight. The HEP-OPSS was purified from small MW compounds via either strong anion exchange chromatography or by ultrafiltration.

The HEP-OPSS (~100 mg synthesis scale) was applied to a HiTrap Q strong anion exchange column (5 mL bed; GE Healthcare) equilibrated in Buffer A (10 mM NaOAc, pH 5.8) at 2 mL/min and washed with 4 column volumes (cv) of 100% buffer A. A series of linear gradient steps with NaCl elution (using B buffer = A + 1 M NaCl in steps of 10 cv of 90A:10B, 4 cv of 60A:40B, and then 1 cv of 40A:60B) removed traces of OPSS from the target. The 0.21-0.5 M NaCl fractions containing the HEP-OPSS target were pooled, precipitated with 2.5 volumes of ethanol (similar process to isopropanol employed above), the pellet suspended in water, and stored at -20°C. Alternatively, the HEP-OPSS (~200 mg synthesis scale) target was purified by repeated ultrafiltration (6 cycles with 3 kDa MWCO membrane; Amicon) against water at room temperature to desalt the sample and to remove any residual SPDP. The presence of the OPSS group on the sugar chain was verified by reaction with SAMSA (a fluorescent thiol activated with base per the manufacturer's instructions; ThermoFisher) and then PAGE analysis [193]. A fluorescent band at the appropriate MW was detected, thus indicating the successful installation of the OPSS moiety onto the sugar chain as described later.

Radioactive forms of the HEP-OPSS were created by first end-labeling 100-200 μg HEP-NH_2 with 1.1-9 μCi of UDP-[^{3}H]-GlcNAc (PerkinElmer) and PmHS under reactions conditions similar to nonradioactive HEP-NH_2 synthesis. The radioactive research was done by

Dixy Green in Dr. DeAngelis's lab at the department of biochemistry and molecular biology in the University of Oklahoma Health Sciences Center [191]; under these conditions only ~1-2% of the HEP chains (~65 monosaccharide units long) are tagged with a single radioactive sugar thus not significantly altering the overall MW of the preparation. The purified material was then reacted with OPSS as above except: (*i*) a 2,000 to 3,555 molar excess of OPSS was used for 3-4 hrs, (*ii*) the final concentration of HEP-NH_2 was 0.2 mg/mL, and (*iii*) the target was precipitated by the addition of NaCl (0.3 M final) and 3 volumes of ethanol at -20°C for 2 hours. The resulting pellet was harvested by centrifugation (18,000 x*g* for 0.5-1 hr), the supernatant was aspirated, and the pellet was then washed in 70% ethanol/0.1 M NaCl and centrifuged again. The pellet was air-dried, resuspended in water, and then purified by repeated ultrafiltration (6 cycles with 3 kDa MWCO; Amicon) against water. The specific activity of the final [^{3}H]HEP-OPSS product was measured by liquid scintillation counting and determined to be 93-360 mCi/mmol (7-27 nCi/µg).

Polyacrylamide gel electrophoresis was conducted to ensure the successful conjugation of OPSS to heparosan molecules. In these tests, 13-kDa OPSS-HEP were reacted with a fluorescent probe with either (i) a free thiol (activated SAMSA Fluorescein; Cat# A685; Invitrogen) or (ii) a thiol-reactive group (Fluorescein-5-Maleimide; Cat# 62245; Thermo Scientific) overnight at room temperature. The 13-kDa HEP-NH_2 without OPSS conjugation was used for control. SAMSA was activated by 0.1 M NaOH at room temperature for 15 min, then neutralized with HCl. Samples of the reaction (2 µg of HEP/lane) were compared to control lanes (13-kDa HEP-NH_2 without OPSS modification) with free probes on 6% polyacrylamide gels (1x TBE, 250 V for 15 min). The gel was first imaged for fluorescence (ChemDoc MP imager; BioRad) to observe the probes (indicating if the OPSS was still reactive or the OPS had been lost after processing, etc.) and then was stained with Alcian Blue (cat# A9186; Sigma-Aldrich) to detect the presence of heparosan.

2.2.3 Saturation curve of gold nanoparticles

This protocol was based on a published paper [194]. Briefly, a constant surface area to volume ratio was maintained for every desired PEG (MW 10 kDa, Laysan Bio) surface density (PEG/nm^2); only the surface modification density conditions were varied. The addition ratios of PEG polymer to nanoparticle surface area were 0, 0.1, 0.25, 0.5, 1, 2 PEG/nm^2 for 15-nm AuNPs. Samples were prepared in triplicate by mixing the DI water, PEG solution, and 15-nm citrate-stabilized AuNPs in order. The vials were vortexed a second time and then left to incubate at room temperature for 30 minutes. After the incubation period passed, the PEG was then fully conjugated to the surface of the nanoparticles, which was verified with the Malvern ZetaSizer using dynamic light scattering (DLS). The DLS measured hydrodynamic diameter, which consists of the gold core diameter and the layer of hydration from the surface-bound molecules. Additionally, the success of the effect of the PEG density on the surface charge of the nanoparticles was qualitatively observed through gel electrophoresis, as described below in the gel electrophoresis section. The heparosan saturation curve was obtained by a similar procedure with the use of the salt aging or pH methods as described below.

2.2.4 Saturation curve of heparosan coated liposomes

Naked liposomes were coated with lipid-modified heparosan polymers using post-insertional modification as in a published paper [187]. Briefly, 13-kDa heparosan-dipalmitate polymers were mixed with uncoated liposomes, then incubated for 90 min at 37 ºC; these conditions result in efficient incorporation of a HEP-coating on the outer leaflet of the bilayer. The saturation curve was obtained by mixing 9.71 mg/mL heparosan polymer with uncoated liposome at the percentage of molar ratio of HEP polymer to lipids.

2.2.5 HEP-AuNPs prepared by the salt aging method

The coating of heparosan by salt aging on 15-nm gold nanoparticles was based on the Hurst/Zhang method [195,196]. This method entails increasing the concentration of sodium chloride (Sigma) to help the heparosan conjugate attach to the gold nanoparticle surface. Briefly, citrate stabilized AuNPs were obtained that had been prepared as described above. A constant surface area to volume ratio was maintained for every desired heparosan surface density (HEP/nm^2); only the surface modification density conditions were varied. The addition ratios of HEP polymer to nanoparticle surface area were 0, 0.25, 0.5, 1, or 2 HEP/nm^2 for 15-nm AuNPs. According to a published protocol, different HEP coating density conditions were performed for 55-nm and 100-nm gold nanoparticles [194]: the range was 0, 0.01, 0.1, 0.5, 1, or 2 HEP/nm^2. Triplicates were performed for each condition. Nanoparticle and heparosan solution were mixed together in DI water and incubated at room temperature for 20 min. NaCl was added in 0.1 M NaCl increments until the final NaCl concentration reached 0.7 M. Each increment was followed by a 20 min incubation at room temperature before the next addition of NaCl. DLS was performed after the final incubation. Agarose gel electrophoresis was performed as described below in the gel electrophoresis section.

2.2.6 HEP-AuNPs and HEP-AgNPs prepared by the pH method

The protocol was adapted and modified from a published paper from Liu's lab [196]. In a different process from the salt aging method described above, pH 3.0 Citrate·HCl buffer or pH 3.0 HCl without citrate was used as a solvent for the heparosan and gold nanoparticle mixture instead of using DI water. A constant surface area was maintained for every target heparosan surface density (HEP/nm^2); only the surface modification density conditions were varied. The addition of HEP polymer to nanoparticle surface reactions were 0, 0.25, 0.5, 1, 2 HEP/nm^2 for 15-nm AuNPs. HEP surface coating density of 55-nm AuNPs were 0, 0.1,0.25, 0.5, 1, or 2 HEP/nm^2. The calculated HEP was added and mixed with acid water, then followed by adding nanoparticles. After a brief vortex, NaCl solution was added in 0.3-M NaCl increments until the final NaCl concentration reached 0.6-M. Each increment was followed by a 20 min incubation at room temperature. DLS was measured after final incubation. Agarose gel electrophoresis was performed as described below in the gel electrophoresis section. The optimized pH method shared the same procedure without the addition of citrate to the acid water. The colloidal stability of the low coating density of HEP was maintained over 390 days with the pH method without citrate addition.

The pH method without citrate addition was used for coating HEP on AgNPs. To attach HEP-OPSS or PEG-OPSS to silver nanoparticles, these reagents were first reduced to HEP-SH or PEG-SH by incubation with Tris(2-carboxyethyl)phosphine hydrochloride (TCEP; Sigma-Aldrich) at a molar ratio of 1:50 for 2 h. This reduction step was employed as the OPSS group does not react efficiently with AgNPs in comparison to AuNPs. The hydrodynamic diameter changes were measured by DLS. Based on the maximum saturation curve we obtained from 55-nm AuNPs by DLS, we added over 5 polymers per nm^2 in the silver nanoparticle coating.

2.2.7 HEP-AuNPs prepared by the vortex method

For comparison, instead of using salt aging and pH routes, an experiment was done to modify 15-nm nanoparticles with heparosan-OPSS without the salt aging method or pH, similar to the PEGylation method described above. The main objective of this experiment was to showcase the effectiveness of heparosan coating without salt aging by comparison of the amount of heparosan bound to the nanoparticle surface. For this, conditions for heparosan surface coating reactions were chosen to be 0, 0.1, 0.25, 0.5, 0.75, 1, 1.5, or 2 HEP/nm^2. DLS and gel electrophoresis were performed.

2.2.8 Quantification of HEP-coatings 15-nm and 55-nm AuNPs using a radiolabeling strategy

Radioactive heparosan and versions of heparosan-OPSS were mixed in a mass ratio of 1 to 4. This heparosan mixture was used to modify 15-nm or 55-nm AuNPs. By using the salt aging method mentioned above, different densities of heparosan mixture as input surface densities (HEP/nm^2) were used to modify 15-nm and 55-nm AuNPs. The input surface HEP densities for 15 nm were 0.2, 0.5, 1.0, 2.0, or 3.0 HEP/nm^2. For 55-nm AuNPs, the input surface coating reactions were 0.1, 0.25, 0.5, 1.0, or 2.0 HEP/nm^2. After the conjugation process, heparosan-modified AuNPs were centrifuged at 4°C for 30 min and centrifuged at either 15,000 xg for 15-nm or 2,000 xg for 55-nm. To remove free heparosan, the pellet volume after centrifugation was carefully loaded on 25% Percoll (Amersham) and followed by centrifugation at 4°C (1 h at 15,000 xg for 15-nm or 2,000 xg for 55-nm AuNPs). The radioactivity was measured by liquid scintillation counting on a Packard Tricarb 2300TR.

2.2.9 TEM characterization of HEP- and citrate-AuNPs

Samples were loaded and prepared with negative staining by 2% uranyl acetate (Ted Pella, Inc) on a TEM grid (Ted Pella, Inc) [197]. TEM images were taken by a 200-kV field emission JEOL2010F analytical transmission electron microscope with a DE-12 camera. ImageJ (NIH) was used to analyze TEM images [198].

2.2.10 TEM characterization of AuNPs inside of cells

RAW 264.7 macrophage cells (~1 million) were seeded in each well of a 6-well-plate overnight. Dispersions of 0.3-nM PEG- or HEP-AuNPs were then incubated with the cells for 6 h. Any uninternalized AuNPs were removed by washing the cells thrice with 1X PBS. Cells were scraped and collected by centrifugation (500 x*g*, 5 min, 25ºC) into a 1.5-mL microcentrifuge tube. The supernatant was removed, and the cell pellets were fixed with a freshly made fixative solution containing (2% glutaraldehyde: 4% paraformaldehyde (v/v) in 0.2 M cacodylate buffer) at room temperature for 1 hour. Samples were stored at 4ºC until sectioning and negative staining (3% lead citrate solution, cat. 22410, Electron Microscopy Sciences). The TEM micrographs were taken with a Hitachi H-7600 Transmission Electron Microscope at the Oklahoma Medical Research Foundation (OMRF) imaging core facility in Oklahoma City, OK.

2.2.11 Agarose gel electrophoresis

Gels with 0.5% (m/v) agarose (Fisher BioReagents) and 0.5x TBE buffer (Sigma-Aldrich) were used to analyze HEP coating on AuNPs. Nanoparticle samples were concentrated to ensure visibility and (typically 10 μL/lane) then mixed with 150 mg/mL Ficoll (Research Products International) in a 4:1 ratio for loading into wells. Gels were run at 50 V for 40 min. Gel images were taken with an Azure C600 imager using visible light.

2.2.12 Quantifying HEP desorption upon exposure of HEP-coated nanoparticles to human plasma

Radioactive heparosan-modified 15-nm or 55-nm AuNPs were incubated with human plasma or 1X PBS for 12 h, 24 h, or 48 h at 37°C. After centrifugation (15,000 x*g*, 15 min for 15-nm AuNPs; 2,000 x*g*, 15 min for 55-nm AuNPs), radioactivity in the supernatants and pellets was measured with the liquid scintillation analyzer (Tri-carb 2300TR). The percentage of radioactivity is calculated using the following equation:

$$\%\ of\ radioactivity = \frac{radio\ counts\ of\ the\ pellets}{radio\ counts\ in\ the\ supernatant + radio\ counts\ in\ the\ pellets}\ x\ 100\%$$

2.2.13 Protein corona formation upon nanoparticle incubation in FBS

The protocol followed published papers [199,200]. Briefly, HEP- or PEG-modified gold nanoparticles were incubated with fetal bovine serum (FBS, ThermoFisher) at a ratio of 10 μL per cm^2 of nanoparticle surface area. This incubation was at 37℃ for 24 hours, performed in triplicate. To remove unbound FBS, three rounds of washing were performed by 500 μL of 1X PBS with 5-mM EDTA and 0.05% (v/v) Tween 20 at 18,000 x*g* for 30 min at 4℃. After the final wash, the nanoparticles were then measured by DLS and assessed with agarose gel electrophoresis as described in previous sections.

Similarly, we exposed HEP-, PEG-coated AgNPs, or liposomes to FBS, and measured the hydrodynamic diameter change by DLS.

2.2.14 Protein isolation

Samples with 50 cm^2 nanoparticle surface area were prepared for FBS incubation, followed by the incubation and washing protocol described in the previous paragraph. After the final wash, resuspend the nanoparticle pellets in the residual solution (15 μL). Next, to isolate proteins from nanoparticles, 8 μL of the 4x LDS buffer (Invitrogen) and 4 μL of the 0.5-M dithiothreitol (DTT) solution were added to the vials. The vials were then incubated at 70℃ for 60 minutes to strip the proteins bound to the surface of the nanoparticles. After the 60-minute incubation, the vials were centrifuged at 18,000 x*g* for 15 minutes to remove nanoparticles. Around 30 μL protein supernatant was collected from each tube; 6.5 μL was reserved for SDS-PAGE. The rest of the proteins were processed with clean-up to remove DTT and LDS.

2.2.15 Protein cleanup

To remove the DTT and LDS in the remaining protein solutions, the trichloroacetic acid (TCA) / acetone method from published literature was used [200]. Proteins were precipitated by the addition of 950 µL 10% w/v TCA(Sigma) in acetone (ThermoFisher) overnight at –80°C. The next day, the precipitated proteins were collected by centrifugation at 18,000 x*g* for 15 min at 4°C, and the supernatant was discarded. The pellets were first dissolved in 500 µL of 0.03% w/v sodium deoxycholate (Sigma) and then incubated on ice for 30 min after adding 100 µl of 72% (w/v) TCA. The supernatant was removed after centrifugation at 18,000 x*g*, 4°C for 15 min. The pellets were dissolved in 1 mL of acetone. The 1 mL solution was split into aliquots of 400 µL for BCA assay and 600 µL for LC-MS/MS and dried in a fume hood. The pellets were stored at -80°C until LC-MS/MS characterization.

2.2.16 SDS-PAGE for protein corona characterization

SDS-PAGE gels procedures were based on protocols from Walkey *et al.* [199,200]. We used 4-12 % NuPAGE™ Bis-Tris precast Protein Gels, 1.0 mm, 12-well (ThermoFisher) with as a PageRuler™ Plus Prestained 10-250 kDa Protein Ladder (ThermoFisher) standards in a mini gel tank (ThermoFisher) for SDS-PAGE. The 6.5-µL samples previously saved (section 11) were then mixed with 2.5 µL of the 4x LDS buffer and 1 µL of the 500-mM DTT solution and incubated for 5 minutes at 95°C. Along with 2 µL of the protein ladder, samples were then carefully injected into the wells on the gel, and the gel was run at 200 V for 55 minutes on ice. Once the gel was done, it was carefully separated from the case, and the gel was submerged in the fixing solution (10% (v/v) acetic acid (Fisher Scientific) and 40% (v/v) ethanol (PHARMCO-AAPER)) in a petri dish overnight at room temperature with gentle agitation. The next morning, the gel was rinsed with DI water and then stained by1x SYPRO™ Tangerine Protein Gel Stain according to the manufacturer's protocol for 60 minutes at room temperature with gentle agitation (wrapped in aluminum foil to avoid light). Stained gel was rinsed with DI water and imaged under Azure C600 with an excitation/emission set compatible with the stain and ladder. ImageJ (NIH) was used to analyze the intensity of each lane on the same SDS PAGE images [199].

2.2.17 Liquid Chromatography Tandem Mass Spectrometry (LC-MS/MS)

All chemicals were purchased from Sigma-Aldrich (Milwaukee, WI) unless noted otherwise. Trypsin (TPCK treated) was obtained from ThermoFisher (Rockford, IL).

The protein pellet was solubilized in 15 µL of 25-mM ammonium bicarbonate. Six M urea, 200-mM dithiothreitol, and 200-mM iodoacetamide were prepared in 25-mM ammonium bicarbonate. The protein solution was incubated with 1 µL of 6-M urea and 1 µL of 200-mM dithiothreitol for 1 h at 37°C for denaturation and reduction. Then the reduced proteins were incubated with 5 µL of 200-mM iodoacetamide for 30 minutes in the dark at room temperature for alkylation. After incubation, 5 µL of 200-mM dithiothreitol was added to the solutions followed by incubation with 3 µL of 0.1-µg/µL trypsin (prepared in 25-mM ammonium bicarbonate) at 37°C and pH 7 overnight. For both the HEP coating and PEG coating, protein digest samples containing varying coating densities were prepared in triplicate. All samples were stored at -20°C until analysis.

The LC-MS/MS work was conducted by Mulin Fang in Dr. Si Wu's lab at the department of Chemistry and Biochemistry at the University of Oklahoma. A 15-µL aliquot of the protein digest was injected onto a custom-packed C18 reverse-phase liquid chromatography (RPLC) column (75 µm i.d., 150 mm length, 2 µm C18 resin) for peptide separation. Mobile phase A was 0.1% formic acid in HPLC grade water and mobile phase B was 0.1% formic acid in acetonitrile. The flow was split to result in a flow rate of approximately 0.8 µL/min through the RPLC column. The LC gradient started with sample loading at 0% mobile phase B for 30 min, followed by an increase from 0% to 35% mobile phase B over 120 min. The mobile phase B gradient was increased to 90% over 3 min and was held constant for 5 min. Mobile phase B was then decreased to 0% over 2 min and maintained for 50 min for column re-equilibration. The eluted peptides were analyzed using an LTQ mass spectrometer (Thermo Fisher Scientific, Hanover Park, IL, USA) with a custom nano-ESI interface [201]. The heated capillary temperature

was 275°C with a spray voltage of 3.5 kV. MS scans were obtained with a normal scan rate and the m/z range was 350-1350. MS/MS scans were acquired using ITMS with collisional induced dissociation (CID) at a normalized collision energy setting of 35%. The ten most abundant precursor ions were selected for MS/MS. The AGC for MS/MS was 3E4 and the maximum ion injection time was 50 ms with 3 microscans. The column was washed between sample runs by injecting a buffer blank and running the same gradient setup.

Peptides were identified using MSGF+ to search the mass spectra from the LC-MS/MS analysis against the annotated bovine database downloaded from www.uniprot.org (proteome ID is UP000009136) [202]. A decoy database was automatically generated by MSGF+. Peptide identifications were filtered using a SpecE value cut-off of 1E-10 (i.e., the calculated FDR < 1% at the unique peptide level).

E Coli digest was used as a quality control in this LC-MS/MS experiment, and the unique peptide detected should be 1000+. The database search identified 14 proteins for the HEP coating and 14 proteins for the PEG coating with three replicates, excluding proteins identified in only a single experimental replicate. Identified proteins with relative abundance (by mass) less than 0.25% in one coating density were also excluded [200,203]. The spectral count of the same identified protein in each experimental set was normalized using the highest value. The average normalized spectral counts for the identified protein in triplicate sets are reported in Table S2 and Table S3 for the HEP and PEG coatings. The identified proteins for the HEP and PEG coatings were clustered using the "clustergram" function in MATLAB. Pearson correlation coefficient and unweighted average distance were used as a distance metric. The relative abundance of proteins in the same cluster were summed and plotted as a function of the coating densities [200].

2.2.18 BCA-based protein quantification assays

The commercial BCA (bicinchoninic acid) assay was used to quantify the protein concentration (cat. 23225, ThermoFisher). The purified protein pellets were dissolved in 40 µL of 2% (w/v) SDS dispersed in 1X PBS. 50-µL aliquots of serially diluted concentration of bovine serum albumin (BSA, Pierce) or 10 µL of each sample were placed into 96 well plates. Next, 200 µL of freshly made BCA working solution was added to each well, then incubated at 37ºC for 1 hour. Absorbance at 562 nm was measured by a plate reader (BioTek Synergy Neo2 Multi-Mode Plate Reader). The protein concentrations were calculated based on the BSA standard protein curve.

2.2.19 Cell viability tests

Cell viability assay was performed as previously described [204]. Briefly, cells were grown in 96-well plates at a density of 3.5×10^3 cells/well overnight in the presence of recommended complete media containing 10% (v/v) fetal bovine serum (cat. 16000-044, Life Technologies) and 1% (v/v) pen-strep (cat. 15140-122, Life Technologies). After overnight incubation, media was aspirated, and cells were then treated with either various doses of gold nanoparticles or PBS at a final volume of 100 µL per well. After 48 h incubation, cells were washed with PBS thrice, and the cell viability was determined using the XTT assay (2,3-Bis-(2-Methoxy-4-Nitro-5-Sulfophenyl)-2H-Tetrazolium-5-Carboxanilide, cat. 11465015001, Sigma) according to the manufacturer's protocol. The cell viability as a readout of absorbance of formazan in dimethyl sulfoxide (DMSO) at 570 nm was expressed as a percentage (%) of cells that remained live.

2.2.20 Hemolysis assays

The hemolysis assay procedures were adopted from published papers [205,206]. Briefly, 100 µL of 10% of washed human red blood cells (2% packed cells final; Innovative research) were incubated with PEG- or HEP-coated AuNPs (1 nM final in 400 µL volume of 1X PBS) at 37ºC for 3 h. Triton-X 100 and 1X PBS were used for the positive and negative controls, respectively. Blood-free samples (without incubation of human red blood cells) were also prepared to account for the intrinsic absorbance of AuNPs. After the incubation, all samples were centrifuged at 10,050 x*g* for 30 min at room temperature. A 100-µL aliquot of the supernatant was transferred into a 96 well plate, and the absorbance of hemoglobin at a wavelength of 577 nm was measured. The values of the blood-free samples were lower than the negative control, thus no interference from the AuNPs was observed. The hemolysis percentage was calculated according to the following equation:

$$\%\ hemolysis = \frac{(absorbance\ of\ sample - absorbance\ of\ blank)}{(absorbance\ of\ positive\ control - absorbance\ of\ blank)}\ \text{x}100\%$$

2.2.21 Cytokine release assay

As a measure of biocompatibility, the levels of various proteins known to be involved in stress and inflammatory reactions were analyzed after treatment with various nanoparticles. RAW 264.7 macrophages were seeded in 48-well-plates overnight (2E5 cells per well). Then either 1X PBS (control) or suspensions of 0.06-nM of 55-nm citrate-, PEG-, or HEP-AuNPs were added to cells for 24 h. The supernatants were collected and washed by centrifuging at 15,000 x*g* for 15 min twice. Aliquots of the supernatants were incubated with Mouse Cytokine Array Panel A Detection Antibody Cocktail (Proteome Profiler Mouse Cytokine Array Kit, Panel A, ARY006, R & D Systems, Minneapolis, MN 55413) for 1 h. The sample/antibody mixtures were then incubated with the array membranes overnight at 4°C. After washing, the membranes were incubated with HRP-conjugated secondary antibody for 30 min. For blotting development, 1 mL of Chemi Reagent Mix was applied to each of the membranes, followed by chemiluminescence film (BX810, Midsci, St. Louis, MO 63088) exposure for 24 h to get the optimal images. Blot images were quantified by the Quick Spot image analysis tool.

2.2.22 Nanoparticle cell uptake studies

The cell uptake protocols follow previously published procedures [194]. Briefly, human endothelial cells (HUVECs), J774A.1, and RAW 264.7 macrophages were purchased from ATCC, USA. First, a total of $3x10^5$ cells/well were seeded onto a 24-well plate and allowed to adhere overnight. The cells were washed with sterile 1x phosphate buffered saline (PBS) thrice, then 1 mL of nanoparticles (0.3 nM final) in the corresponding cell media with FBS were administered and incubated for 6 h at 37°C (5% CO_2) in a humidified tissue culture incubator.

To assess the effect of FBS on cellular uptake studies, after seeding overnight, the cells were 'cleansed' by incubating in cell media without FBS for 30 min at 37°C. Then the cells were washed with sterile 1X phosphate buffered saline (PBS) thrice, and 1 mL of 0.2-nM nanoparticles in either complete cell media or FBS-free cell media were added to cleansed cells for 6 h incubation at 37°C (5% CO_2) as above.

After incubation with nanoparticles, cells were washed with 2 mL of 1X PBS thrice to remove non-internalized nanoparticles. Purified cell samples were then digested by adding 500 µL of Aqua Regia (1-part nitric acid, 3-part hydrochloric acid, v/v) directly into the wells. After 30 min, the acid-digested samples were transferred to 1.5-mL microcentrifuge tubes and placed in a water bath at 70°C for 1 h to complete the digestion process. Samples were then allowed to cool and then diluted 40-fold into nanopure water with a final volume of 5 mL. All elemental analysis measurements for nanoparticle uptake were done using the PerkinElmer NexIon 2000 ICP-MS on the Prepfast IC Sample Introduction system at the Mass Spectrometry Facility, University of Oklahoma. To determine the average number of nanoparticles per cell, the dissolved gold signal was correlated to the magnesium signal from known cell numbers. Cell samples were then analyzed for both gold and magnesium signals. Iridium was used as an internal standard. Data was analyzed on GraphPad Prism.

2.2.23 Confocal laser scanning microscopy studies

DC 2.4 dendritic cells were seeded onto sterile glass coverslips placed into a 6 well-plate overnight with RPMI 1640 culture media supplemented with 10% fetal bovine serum and 1% Penicillin-Streptomycin. The next day cell media was removed. 0.2 nM PEG- or HEP-coated 55-nm gold nanoparticles were administrated for a 3 h incubation. Cells were washed thrice with PBS to remove noninternalized gold nanoparticles. Cells were fixed by 4% paraformaldehyde (PFA, cat# AAJ19943K2, Thermo Fisher) at room temperature for 10 minutes. Fixed cells were stained with wheat germ agglutinin CF633 (WGA, cat# 29024, Biotium) and NucBlue DAPI (cat# R37606, Thermo Fisher) according to the manufacturer's protocols to label the cell surface or the nuclei, respectively. Confocal images were taken with a 63x oil immersion objective (1.4 NA) on a ZEISS LSM 880 inverted confocal laser scanning microscope (CLSM) using photomultiplier tube (PMT) detectors with a 405-nm diode laser and a 633-nm helium-neon laser for fluorescent channels through a main beam splitter (MBS) 488/561/633 filter. The nanoparticles were imaged using light scattering principles described by Jiang *et al.* with a 561-nm diode-pumped solid-state laser and an MBS T80/R20 filter [159,207]. Light scattering intensities of the gold nanoparticles were quantified by manually drawing regions of interest around the cell membranes and measuring the integrated density in the light scattering channel on ImageJ. Typical measurements were the result of imaging 25 cells/condition.

Similarly, we studied the cellular uptake of HEP- or PEG-coated AgNPs and liposomes in RAW 264.7 macrophages. Silver and liposome nanoparticles were incubated with cells seeded in 96 well-plates. After fixing and staining, cells were scraped down and dropped on glass slides, then covered by another glass slips to image silver and liposome samples. The same confocal setup was used for AgNPs. Liposomes labeled with DiO'; DiOC18(3) (3,3'-Dioctadecyloxacarbocyanine Perchlorate) (DIO, cat# D275, ThermoFisher) were imaged using a 488-nm laser for the fluorescent channel, but the rest of the procedures were the same.

2.2.24 UV-Vis spectrophotometry-based depletion assay

We adopted a previously published protocol to obtain a maximum loading capacity of 10-kDa PEG-OPSS on 15-nm gold nanoparticles [194]. Briefly, PEGylated gold nanoparticles were centrifuged at 15,000 x*g* for 30 min. The supernatant was separated from gold nanoparticle pellets and measured at 283 nm by a UV-Vis-NIR spectrophotometer (Agilent Cary 5000). The absorbance differences between the added PEG and the supernatant were the absorbance of PEG conjugated to gold nanoparticles. We defined the absorbance of PEG conjugated to gold nanoparticles as ΔAb. The point at which ΔAb does not increase is defined as the saturation point.

2.3 Results and Discussion

2.3.1 Surface modification of nanoparticles with polysaccharide heparosan

We demonstrated in previous studies that orthopyridyl disulfide (OPSS) is an effective linker to bind OPSS-modified polymers to citrate-coated gold nanoparticles (AuNPs) [36,43]. Therefore, we covalently attached an OPSS group via an amide bond to a modified HEP polysaccharide chain containing an amine at the reducing-end terminus to form OPSS-HEP. Figure S1 depicts the chemical structure of OPSS-HEP. The qualitative characterization of the successful OPSS conjugation to HEP is shown in Figure S2. We selected 10-kDa OPSS-PEG as a comparative control for the 13-kDa OPSS-HEP to match the molecular weights of both polymers.

To modify colloidally dispersed citrate-coated AuNPs with negatively charged HEP polymers (**Figure 2.1 A**), we established two different surface modification strategies: (I) an increase in ionic strength to 0.7 M through the step-wise addition of a saline solution (salt aging method, **Figure 2.1 B**), or (II) a single-step pH reduction to pH 3 by addition of an aqueous hydrochloric acid solution (pH reduction method, **Figure 2.1 C**). We applied these two methods to increase surface coating effectiveness by reducing the electrostatic repulsion between individual HEP polymers [195,208].

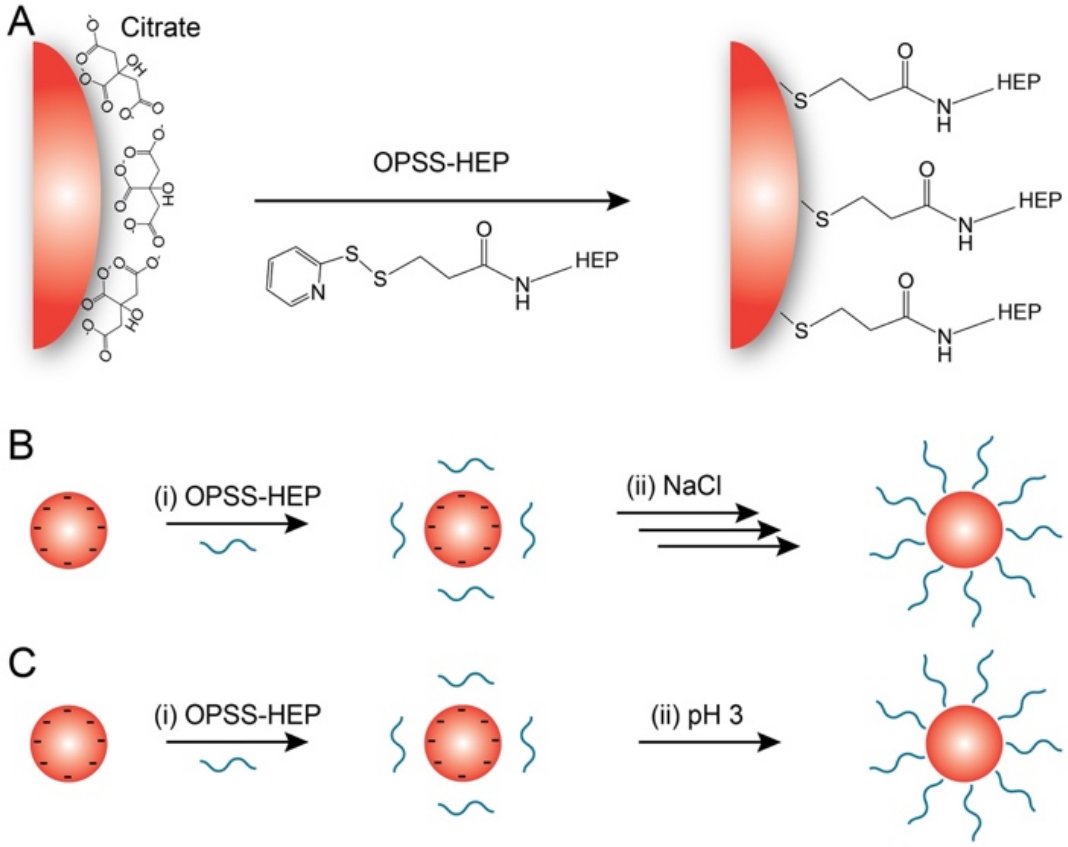

Figure 2.1: Schematic of gold nanoparticle (AuNP) surface modification with heparosan (HEP) polymers.

(A) General surface attachment strategy of OPSS-terminated HEP (OPSS-HEP). **(B)** Salt aging method: (i) OPSS-HEP is mixed with colloidally dispersed citrate-coated AuNPs. (ii) The ionic strength of the dispersion is then increased by the step-wise addition of a NaCl solution (denoted with multiple arrows). **(C)** pH method. (i) OPSS-HEP is mixed with colloidally dispersed citrate-coated AuNPs. (ii) The pH of the colloidal dispersion is subsequently decreased to ~pH 3 by the one-step addition of a hydrochloric acid solution.

To establish the feasibility of the salt aging and pH methods for the attachment of OPSS-HEP onto AuNPs, we used 15-nm AuNPs as a model nanoparticle system. These AuNPs can be synthesized reproducibly with high yield (typically >80%) and narrow size distribution (<10% deviation)[43]. As shown in Figure 2.2 A, simply mixing AuNPs with OPSS-HEP did not result in substantial increases in AuNPs hydrodynamic diameter, measured by dynamic light scattering (DLS), which is likely due to the electrostatic repulsion between individual negatively charged HEP polymers. In contrast, both salt aging and pH methods increased the AuNPs

hydrodynamic diameters similarly up to ~49 nm as a function of the amount of OPSS-HEP added per nanoparticle surface area in a coating reaction (**Figure 2.2 B**). Saturation of the surface was indicated by a plateau when maximal hydrodynamic size was achieved. These DLS results were supported qualitatively by agarose gel electrophoresis experiments, where the migration of the nanoparticles was reduced with an increase in size and HEP surface coverage (Figure S3). Transmission electron microscopy (TEM) of negative-stained nanoparticles indicated the presence of a dense surface coating layer around HEP-modified AuNPs and revealed an average increase in nanoparticle size of ~25 nm (**Figure 2.2 C-E**). This size increase is smaller than the hydrodynamic size increase observed with DLS, most likely due to a partial collapse of the polysaccharide structure during the sample dehydration process required for TEM imaging.

To determine the HEP coating efficiency on AuNPs, we prepared tritium [^{3}H] radiolabeled OPSS-HEP polymers and used liquid scintillation counting measurements to quantify the amount of HEP conjugated to AuNPs (**Figure 2.2 F-G**). As shown in Figure 2G, the maximum achievable HEP surface coating density was ~1.1 HEP/nm^2. In addition, we observed that the colloidal stability of HEP-conjugated AuNPs did not change noticeably for various storage conditions (Figure S4). Collectively, our data confirmed that both salt aging and pH methods resulted in effective and stable HEP surface coating of 15-nm AuNPs.

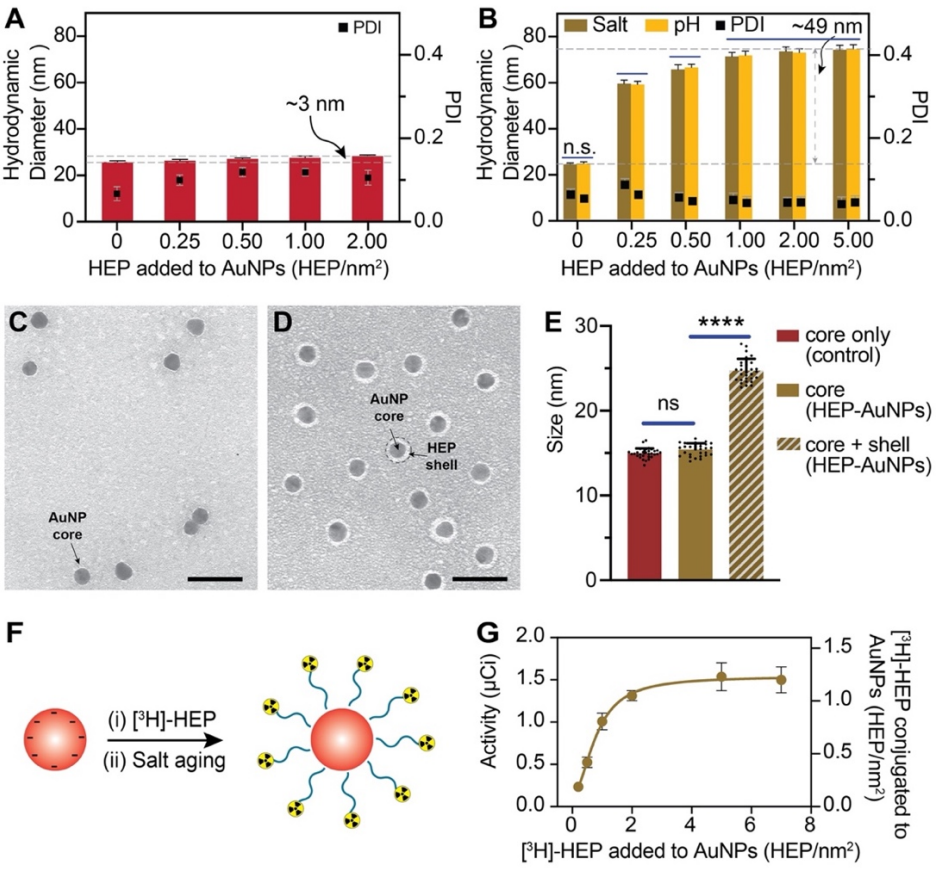

Figure 2.2: Characterization of heparosan (HEP) surface modification using 15-nm AuNPs.

(A) Dynamic light scattering (DLS) was used to measure the hydrodynamic diameter of 15-nm AuNPs after simply mixing with various amounts of HEP per nm^2 of nanoparticle surface area with vortexing (without changes in salt concentration (salt aging) or pH reduction). The increase in hydrodynamic diameter of only ~3 nm suggests that HEP did not efficiently conjugate AuNPs. Bars indicate mean ± SD (n=3). **(B)** DLS results of 15-nm AuNPs mixed with various amounts of HEP per nm^2 nanoparticle surface area and addition of saline (salt aging) or subsequent decrease in pH (pH reduction method). The increase in hydrodynamic diameter of ~49 nm suggests efficient HEP conjugation. Bars indicate mean ± SD (n=3). Statistical tests were performed by two-way ANOVA; n.s. indicates no statistically significant differences. **(C-D)** Representative TEM micrograph of 15-nm citrate-coated AuNPs with a diameter of 14.9 ± 0.6 nm (C) and HEP-AuNPs with a diameter of 24.7 ± 1.4 nm (D). Citrate-coated AuNPs (C) and HEP-AuNPs (D) were stained with 2% uranyl acetate. The light grey halo around the dark AuNP core corresponds to the coating or shell of the surface conjugated HEP. Scale bar indicates 50 nm. **(E)** Size analysis of 15 nm citrate- and HEP-AuNPs by TEM imaging. The core only is the core size of citrate-AuNPs of panel C (control; red bar). The core of HEP-AuNPs of panel D is represented by a brown bar. The diameter of the core and shell of HEP-AuNPs of panel D is represented by a slanted lined brown bar. Bars indicate mean ± SD. Statistical tests were performed by one-way ANOVA ($p<0.0001$ (****); n.s. indicates no statistically significant differences). **(F)** Schematic of AuNP surface modification with radiolabeled HEP. **(G)** Radiochemical assessment of HEP coating density: Liquid scintillation analysis was used to measure the ^3H radioactivity in comparison to coating density (the addition of [^3H]-HEP per nm^2) conjugated to 15-nm AuNPs.

Next, we expanded this surface modification strategy to larger nanoparticles to demonstrate the generalizability of our approach. As shown in Figures S5-S8, we used both surface modification methods to successfully coat 55-nm and 100-nm AuNPs with OPSS-HEP, resulting in similar overall increases in hydrodynamic diameter (~49 nm) as observed with 15-nm AuNPs. These results indicate that both surface modification strategies were functional and consistent across a wide range of nanoparticle sizes. Additionally, we found that the long-term colloidal stability of AuNPs coated with low HEP surface density (<0.1 HEP/nm^2) could be increased to over one year when using the pH method without citrate (Figure S8). In summary, both surface modification strategies allowed the successful coating of HEP polymers onto various AuNPs systems. It is worth mentioning that these surface coating strategies could be used as effective general approaches to modify nanoparticles with negatively charged polymers, which is in line with reports by Hurst *et al*. and Xu *et al*. for DNA coatings [195,208].

2.3.2 Ability of heparosan to reduce protein adsorption on nanoparticle surface

The hydrophilicity of PEG has been reported to reduce protein adsorption through repulsion between the PEGylated nanoparticle surface and serum proteins [209,210]. HEP polymers exhibit a high number of hydroxyl and amide groups ([-4-N-acetylglucosamine-α1,4-glucuronic acid-β1-]$_n$) that render the polymer overall hydrophilic. This hydrophilicity and the overall negative charge of the polysaccharide may reduce HEP polymer-protein interactions. Based on this rationale, we then hypothesized that HEP would not only enhance the colloidal stability but further reduce the serum protein adsorption onto the nanoparticle surface. To evaluate heparosan's ability to reduce protein adsorption, we exposed HEP-modified AuNPs coated with various surface densities to 100% fetal bovine serum (FBS; **Figure 2.3 A**) as a model serum [168,211,212]. We qualitatively assessed the serum protein adsorption before and after FBS incubation on 15-, 55-, or 100-nm HEP-AuNPs with two different methods: (i) by DLS via changes in hydrodynamic diameter (Figure S9), and (ii) by agarose gel shift experiments via changes in nanoparticle electrophoretic mobility (Figure S10). After the FBS exposure, nanoparticles without HEP surface modification exhibited a substantial and consistent DLS size increase of ~26 nm (**Figure 2.3 B**) and an overall reduced electrophoretic mobility (Figure S10). We did not observe significant differences in hydrodynamic diameter for AuNPs modified with >0.5 HEP/nm^2 before and after FBS incubation (**Figure 2.3 C** and Figure S9). To demonstrate the broad applicability of this HEP surface modification strategy, we additionally synthesized HEP-coated AgNPs and liposomes [160,213,214]. We observed no significant changes in hydrodynamic diameter for HEP-coated AgNPs and liposomes before and after FBS incubation indicating minimal interactions between the nanoparticle surfaces and serum proteins (Figure S11). Our findings suggest that the HEP surface modification strategy effectively minimizes serum protein adsorption onto the surfaces of various nanoparticles, i.e. AuNPs, AgNPs, and liposomes. We corroborated these findings qualitatively with sodium dodecyl sulphate-polyacrylamide gel electrophoresis (SDS-PAGE) of isolated proteins from AuNPs surfaces

(**Figure 2.3 E-F**; S12). Using a quantitative bicinchoninic acid (BCA) assay, we confirmed that the observed nanoparticle surface protein adsorption correlated inversely with increasing surface density of the HEP coating (**Figure 2.3 D**). This ability to reduce the protein adsorption of HEP-coated AuNPs was similar for AuNPs that were surface-modified with OPSS-PEG. We used PEG as a control surface modification due to PEG's widespread use in nanomedicine [8,164,215]. We summarized the physicochemical characterization results of PEG-modified AuNPs in Figure S13. Overall, our findings confirmed that the HEP surface modification effectively reduced protein adsorption onto nanoparticles, and this effect was more pronounced with increasing HEP surface coating densities similar to PEGylated nanoparticles.

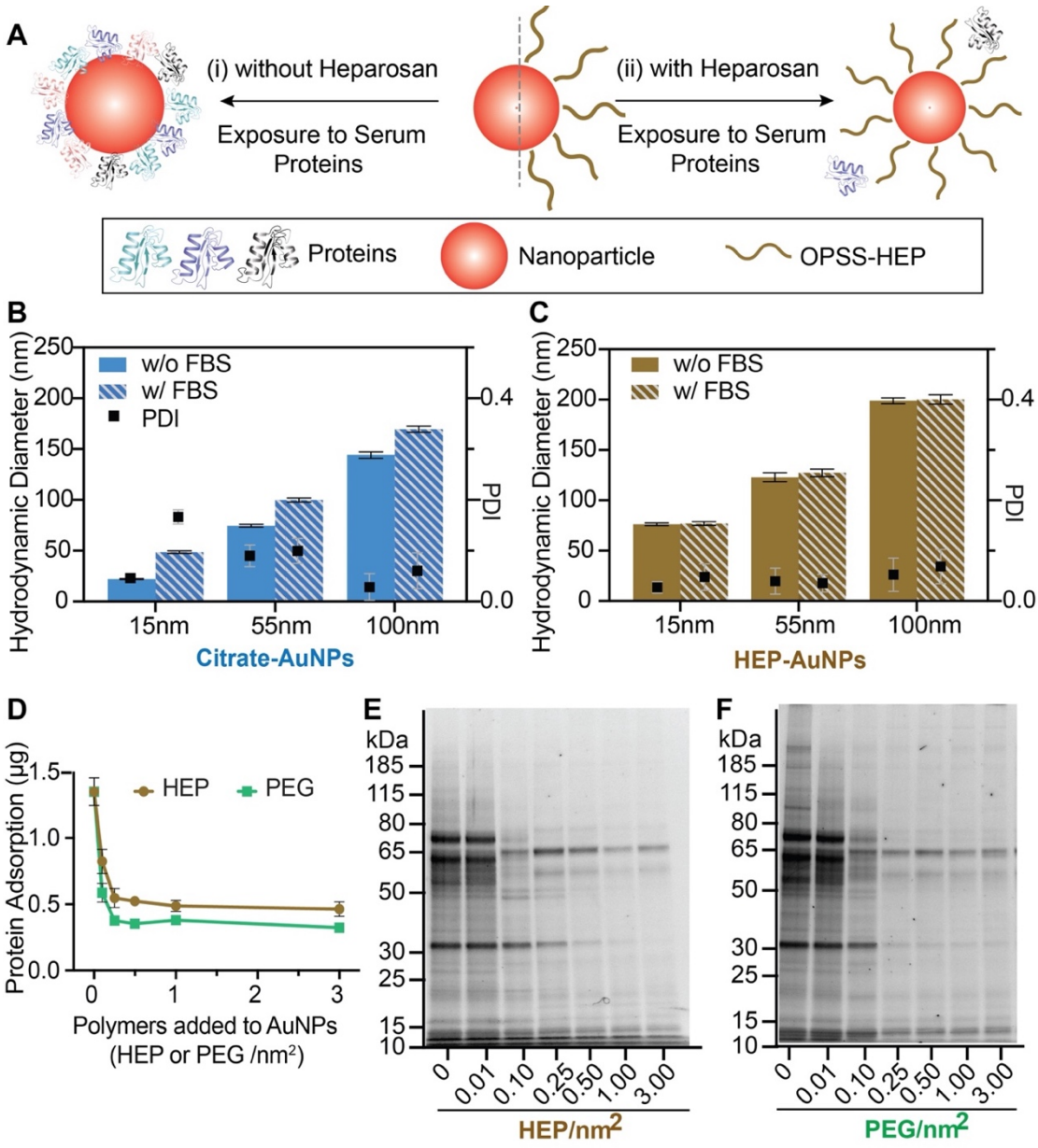

Figure 2.3: Nanoparticle surface engineering with heparosan reduces protein corona formation.

(A) Schematic representation of nanoparticle protein corona formation with and without HEP coating. **(B-C)** Dynamic light scattering (DLS) was used to compare the hydrodynamic diameter differences before and after FBS incubation (slanted lined bars stand for incubation with FBS) of citrate-coated (B; 0 HEP/nm^2) and HEP-coated (panel C)15-, 55-, or 100-nm AuNPs. Bar graphs indicate mean ± SD (n=3). Statistical tests were performed by two-way ANOVA ($p<0.0001$ (****)). **(D)** Quantitative BCA protein assay results for HEP- or PEG-coated 55-nm AuNPs created by increasing amounts of polymer added to coating reactions. Results are presented as mean ± SD (n=3). **(E-F)** SDS-PAGE showing the qualitative biomolecular composition of the adsorbed FBS protein layer on 55-nm AuNPs with various surface HEP (panel E) or PEG densities (panel F). The coating densities represent the added amount of polymers in a coating reaction per nanoparticle surface area.

2.3.3 Protein analysis of nanoparticle protein corona

Next, we used label-free LC-MS/MS to characterize the adsorbed proteins isolated from the nanoparticle surfaces (**Figure 2.4**). Table S1 summarizes the complete list of protein names, molecular weights, and known biological activities of the 16 detected protein species identified on the HEP- and PEG-coated AuNPs. The HEP and PEG surface coatings shared 12 proteins (**Figure 2.4 E**). Average spectral counts for each identified protein from HEP-AuNPs and PEG-AuNPs are reported in Tables S2 and S3, respectively. The spectral counts varied with both the densities and types of surface coating, as summarized in the corresponding heat maps (**Figure 2.4 A, C**). We performed hierarchy clustering to organize proteins into groups based on the correlation of relative abundances (**Figure 2.4 B, D**). We observed that the identified proteins presented distinct preferential surface adsorption as a function of the nanoparticle surface coating types and densities. We summarized the similarities and differences between the five protein cluster groups in a Venn diagram (**Figure 2.4 F**). Our proteomic analysis showed that changes in nanoparticle surface coating affect the types and quantities of surface-adsorbed proteins.

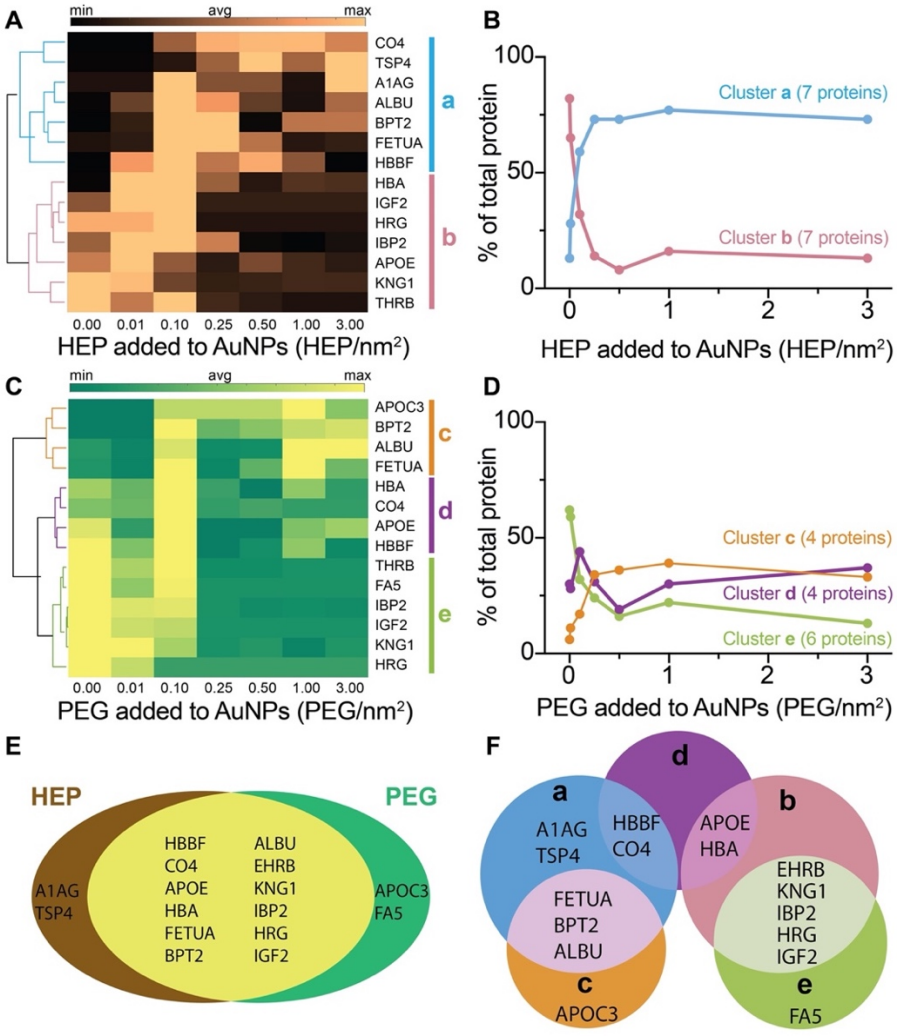

Figure 2.4: Proteomic analysis of nanoparticle protein corona by LC-MS/MS.

(A), (C) Heat maps and clustergrams of the most abundant proteins isolated from HEP- (panel A) or PEG-coated (panel C) AuNPs. The dendrogram on the left side of the heat map shows the hierarchical relationship between proteins in each row across the densities. According to the correlation in the dendrogram, proteins were clustered into groups a, b, c, d, and e (represented by colored bars on the right side of the heat maps and colored lines in the dendrograms). The average amount of each protein was calculated from three independent experimental replicates. The scale bars on the top of the heat maps stand for the relative abundance of proteins (min, avg, and max represent the minimum, average and maximum amount of proteins in the heat map, respectively). Only proteins with relative abundance larger than 0.25% were included. **(B), (D)** The number of proteins in a cluster group was reported. The data points represent proteins amount of the same cluster groups over different densities. The connections of data points show the trend of protein amount change in each cluster group along with different densities. **(E-F)** The proportional Venn diagrams of protein corona isolated from HEP- or PEG-coated 55-nm AuNPs and the clustered groups. The intersection of proteins from HEP- with PEG-coated AuNPs (panel E). Proteins from the clustered groups a, b, c, d, and e were intersected (panel F). The cluster groups a, b, c, d, e are defined in panels A and C.

2.3.4 Biological interaction of nanoparticles with cells

Considering the potential impact of the nanoparticle protein corona on biological function and toxicity, we then compared the cytotoxicity, hemolysis potential, and cytokine release profiles of HEP- or PEG-modified AuNPs (**Figure 2.5 A-B**, S14). On average, we added about five polymers/nm^2 to modify AuNPs with HEP or PEG. We evaluated the cytotoxicity for various nanoparticle doses, nanoparticle sizes, and incubation periods in different cell types (Figure S15 A-C). We did not observe any noticeable cytotoxicity at the highest nanoparticle dose tested. In addition, we did not detect any pronounced hemoglobin release upon incubation of human red blood cells with HEP- or PEG-modified nanoparticles (**Figure 2.5 B**, S15D). We analyzed the cytokine release levels in supernatants of RAW264.7 macrophages after 24 h of incubation with either citrate-, HEP-, or PEG-modified AuNPs (Figure S14). In comparison to the untreated cell control, no significant changes were observed in this panel of over three dozen cytokines, interleukins, or factors known to be involved in stress and inflammatory reactions. These results highlight the biocompatibility of HEP coatings and warrant the future investigation of HEP for safe and effective nanomedicine coatings.

Since the protein corona molecular composition is critical in governing the nanoparticles' biological fate and cellular interactions, we wondered about potential differences in cell uptake efficiencies between HEP- and PEG-modified nanoparticles. We incubated HEP-AuNPs or PEG-AuNPs with various healthy and cancerous cell lines, including J774A.1 macrophages, RAW264.7 macrophages, DC2.4 dendritic cells, HUVEC human endothelial cells, B16f10 melanoma cells, and C2C12 muscle cells. Our nanoparticle-cell incubation experiments revealed high associations of HEP-AuNPs with certain cell types of the innate immune system (Figure S16). To prove that the observed nanoparticle-cell interactions were due to the intracellular uptake of nanoparticles, we conducted confocal laser scanning microscopy (CLSM) to visualize AuNPs in a label-free manner via light scattering[207,216]. Figure

5E shows intracellular CLSM image sections, which confirmed the substantial uptake of HEP-coated AuNPs into these cells (Figure S17).

To further confirm the intracellular localization of AuNPs, we performed a gold etching experiment by exposing cells to KI/I_2 etchant, a highly effective etchant of gold. Our rationale for the etching experiment was that any externally located AuNPs, for example, AuNPs attached to the cell membrane, will dissolve during this etching treatment[40,217]. As shown in Figure S18, quantitative inductively coupled plasma mass spectrometry (ICP-MS) of cells exposed to nanoparticles revealed no notable changes in the extent of nanoparticle cell uptake after the etchant treatment. These results suggest that most AuNPs were located inside the cells in line with our CLSM images. To visualize the subcellular distribution of AuNPs, we performed transmission electron microscopy (TEM) of cells incubated with AuNPs. The TEM micrographs shown in Figure S19 reveal the localization of AuNPs in intracellular vesicles. We additionally confirmed the intracellular uptake of HEP-coated AgNPs and liposomes with CLSM (Figure S20).

We then used ICP-MS to quantify nanoparticle cellular uptake in various cell types. Compared with 55-nm PEG-AuNP, we observed up to 230-fold higher 55-nm HEP-AuNPs uptake in immune cells, including J774A.1 and RAW264.7 macrophages, as well as in DC2.4 dendritic cells (**Figure 2.5 C**). For B16f10 melanoma cells, C2C12 muscle cells, murine 4T1 breast cancer cells, and human endothelial cells (HUVEC), the uptake results of HEP-AuNPs were similar to those obtained for PEG-AuNPs. (**Figure 2.5 C**, S18, S21).

Since our previous LC-MS/MS studies revealed that HEP- and PEG-AuNPs exhibited different protein corona profiles, we wondered about the role of the protein corona in driving nanoparticle cell uptake. We performed cellular uptake experiments with and without FBS in the cell media (**Figure 2.5 D** and S22). Our results indicate that heparosan's intrinsic properties rather than the protein corona determine the observed cellular uptake efficiencies.

To investigate whether the nanoparticle size mediated the high cellular uptake of HEP-AuNPs, we incubated RAW264.7 macrophages with 15-nm AuNPs. Interestingly, we observed a 21-fold higher cell uptake for 15-nm HEP-AuNPs than 15-nm PEG-AuNPs (Figure S18). This finding confirms that relatively high cell uptake can be achieved even with small HEP-modified nanoparticles and further suggests that HEP has a specific role in driving cellular interactions. Further mechanistic studies are needed to determine how HEP-based surface modifications facilitate the internalization of nanoparticles in cells.

In summary, our data suggest that HEP-AuNPs exhibit no apparent cytotoxicity or hemolysis, and very interestingly, display relatively high cellular uptake by specific innate immune cells. There is no correlation between this high cellular uptake and the protein corona (as shown by controlled FBS incubation experiments), thus suggesting that the uptake behavior is intrinsic to the HEP polysaccharide. The high cellular uptake of HEP-coated nanoparticles may increase the effectiveness of macrophage and antigen-presenting cell targeting deliveries and therapies compared to the existing PEG-coatings. The important translational impacts for such improved behavior may include higher potency of HEP-modified nanomedicines yielding drug sparing (i.e. less active ingredient is needed and thus cost savings and more doses per manufacturing batch become available) and reduced potential side effects due to lowered bioburden. In future studies, we will investigate the mechanisms involved in the observed cellular uptake behavior of HEP-modified nanoparticles.

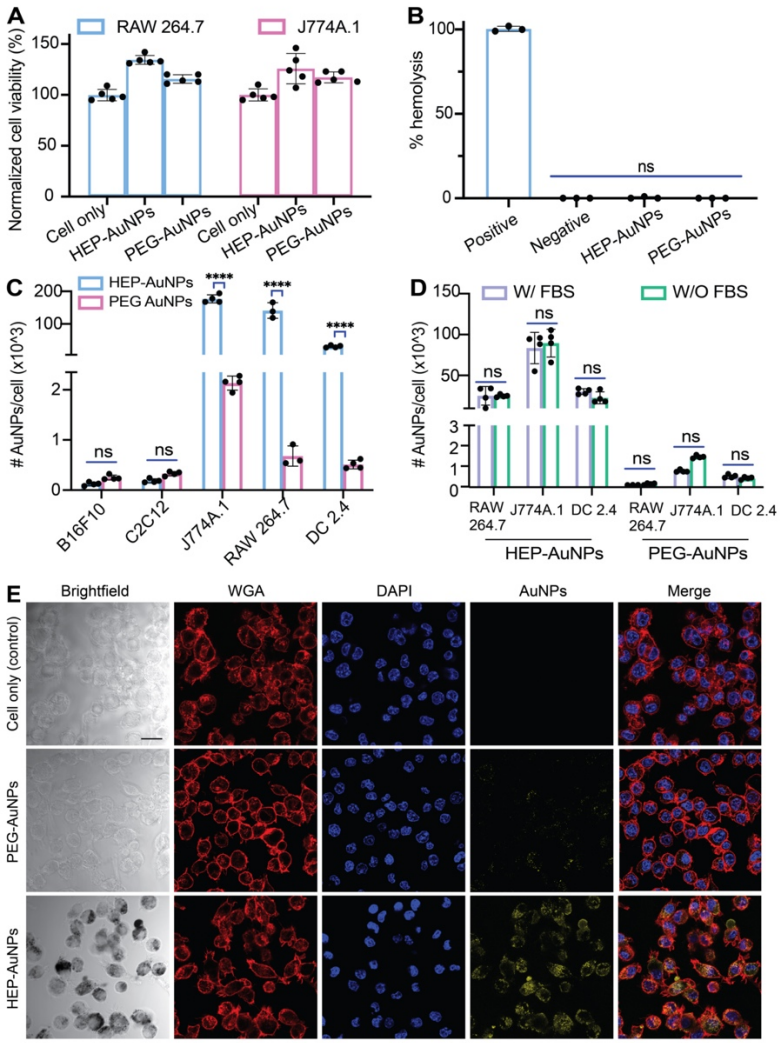

Figure 2.5: Cytotoxicity, hemolysis, and cell uptake of HEP- and PEG-modified 55-nm AuNPs.

(A) Cell viability test of RAW 264. 7 or J774A macrophages treated with 1-nM HEP-AuNPs for 48 h with control groups (cells with PEG- AuNPs or without AuNPs) by XTT assay. Bar graphs indicate mean ± SD (n=5). **(B)** Hemolysis assay of 55-nm nanoparticles (1-nM HEP- or PEG-AuNPs final). 1X PBS or 1% Triton-X 100 were used as negative and positive controls, respectively. Bar graphs indicate mean ± SD (n=3). **(C)** Cell uptake assays: HEP-AuNPs or control PEG-AuNPs were incubated with B16F10 murine melanoma, C2C12 murine muscle cells, J774A.1 murine macrophages, RAW 264.7 murine macrophages, or DC2.4 murine dendritic cells. ICP-MS was performed to quantify cell uptake of nanoparticles. About 70x, 230x, and 45x more HEP-AuNPs were internalized than PEG-AuNPs in J774A.1 macrophage, RAW 264.7 macrophage, and DC 2.4 dendric cells, respectively. Bar graphs indicate mean ± SD (n=3-4). **(D)** The effect of FBS (protein corona) on cellular uptake of HEP-AuNPs with control (PEG-AuNPs) when incubated with J774A.1 murine macrophages, RAW 264.7 murine macrophages, and DC2.4 murine dendritic cells. ICP-MS was performed to quantify nanoparticles cell uptake. No significant difference was observed with FBS-treatment as in panel C. Bar graphs indicate mean ± SD (n=3-4). **(E)** Confocal laser scanning microscopy images of HEP- and PEG-coated AuNPs incubated with DC2.4 dendritic cells for 3 h. The added coating density of HEP-AuNPs and PEG-AuNPs in this figure was ~5 polymers/nm^2. The scale bar indicates 20 μm.

2.4 Conclusion

We demonstrated that the salt aging and pH reduction methods effectively coated negatively charged HEP onto various sized AuNPs. Similar to PEG-based modifications, surface engineering of AuNPs with HEP reduced protein adsorption as a function of HEP surface density. While HEP coatings exhibited a comparable ability to reduce protein adsorption as PEG, HEP substantially enhanced cellular uptake in certain antigen-presenting cells, but not in other tested cell types from various lineages. While we observed some differences in serum protein corona profiles between HEP-AuNPs and PEG-AuNPs, we found that the high nanoparticle cell uptake was not affected by serum proteins. We further demonstrated our HEP-coating strategy's broad applicability for various inorganic and organic nanomaterials. In future studies, we will investigate the mechanisms for the enhanced cellular uptake of HEP-coated nanoparticles. This research will guide the translation of HEP-based nanoparticle surface engineering to enable nanomedicine-based immunotherapies, such as vaccines and CAR-T therapies, that safely and efficiently target immune cells.

Chapter 3 Controlling Nanoparticle Uptake in Innate Immune Cells with Heparosan Polysaccharides

3.1 Introduction

Nanoparticles are versatile devices for the delivery of biomolecules and other payloads that interact with cells of the innate immune system [218–220], the first line of defense against foreign entities and pathogens. Upon entry into the body, antigen-presenting cells of the innate immune system can recognize such invaders to elicit immune responses [220–223]. Interactions between engineered nanoparticles and immune cells can lead to immunomodulation by bridging the gap between innate immunity and adaptive immunity [176,224–227]. Therefore, understanding the nanoparticles' interaction with the innate immune system is critical for the development of safe and effective nanoparticle-based therapeutics.

In the last decade, multiple nanoparticle surface engineering strategies have been applied to target cells of the innate immune system [222,228–230]. However, the observed high levels of nanoparticle uptake are not always appropriate for clinical use due to cell or systemic toxicity [231,232]. There is a need to develop methods to control nanoparticle uptake into innate immune cells to engineer desired immune responses [176,229,233–236]. This approach has the potential to minimize undesirable side effects of nanomedicines, enabling the development of new nanoparticle-based immunomodulation, immunotherapy, and vaccine applications [176,229,233–236].

We previously demonstrated that heparosan (HEP) polysaccharide is an efficient surface engineering technology to create nanoparticles that exhibit a reduction in protein corona formation with enhanced cellular uptake properties in antigen-presenting cells [229]. In this report, we investigated the interactions between HEP-modified nanoparticles and innate immune cells mechanistically by studying the nanoparticle cellular uptake characteristics and associated

endocytosis pathways. Considering that surface properties strongly govern nanoparticle cellular uptake [231,232,237–239], we investigated the nanoparticle uptake efficiency using competition assays of various HEP structural analogs, i.e. polymers of the glycosaminoglycan (GAG) family, and by systematically varying the HEP surface coating density. Our results indicate that nanoparticle uptake in innate immune cells can we controlled over three orders of magnitude when using HEP polysaccharides. These finding may enable the development of safe and effective nanomedicines for applications in immunomodulation, immunotherapy, and vaccine research.

3.2 Materials and Methods

3.2.1 Gold nanoparticle synthesis (15-nm or 55-nm AuNPs)

A redox reaction-based bottom-up synthesis approach was used for the synthesis of 15-nm and 55-nm nanoparticles. Aqua regia was used to clean the glass reaction flasks before synthesis. Aqua regia is prepared as a 3:1 ratio of hydrochloric acid (Sigma-Aldrich, ACS reagent, 37%) and nitric acid (Sigma-Aldrich, ACS reagent, 70%).

Based on a protocol published by Turkevich et al., we synthesized 15-nm gold nanoparticles [188]. A solution of 1.0 mL of 0.102 M sodium citrate tribasic dihydrate (Sigma-Aldrich) and 98.9 mL nanopure water were prepared in aqua regia-cleaned 250-mL Erlenmeyer flask, and stirred on a hot plate at ~200 rpm. When the solution started boiling, 100 µl of 0.25 M aqueous gold (III) chloride trihydrate (Sigma-Aldrich) was added rapidly, and the stir rate increased to ~400 rpm for 7 min. During this reaction time, the color of the solution changed from purple to cherry red. After 7 min, the flask was placed on ice to quench the reaction. To prevent nanoparticle aggregation, Tween 20 (Sigma-Aldrich, Molecular Biology, Grade) was added with a final concentration of 0.01% (*v/v*) before storage at 4°C. Before use, nanoparticles were washed with 0.1% (*v/v*) Tween 20, 0.01% (*w/v*) sodium citrate tribasic dihydrate solution (NP wash buffer) thrice by centrifuging at 15,000 x*g* for 90 minutes (ThermoFisher Heraeus Multifuge X3R centrifuge). Both DLS and UV-Vis spectrophotometry were performed for nanoparticle size and concentration, separately.

To synthesize larger nanoparticles, a seed-mediated synthesis protocol from Perrault *et al*. was adopted.[189] The 15-nm seed without Tween 20 gold nanoparticles were prepared by the previously described protocol above; these 'seed' particles were transferred to a new clean flask to synthesize 55-nm AuNPs. The solutions were added and mixed in the following order at room temperature with ~400 rpm stirring: 93.7 mL nanopure water, 0.967 mL 15 mM aqueous sodium citrate tribasic dihydrate, 0.967 mL 25 mM aqueous gold (III) chloride trihydrate, 3.35 mL

citrate-stabilized 2.4 nM 15-nm gold nanoparticles (without the addition of Tween 20), and 0.967 mL 25 mM aqueous hydroquinone (Sigma-Aldrich, ReagentPlus, ≥ 99.0%). The solution turned from light pink to dark wine-red right after the addition of hydroquinone. After the overnight reaction, 1 mL 10% Tween 20 (*v/v*) was added for a final ~0.1% concentration. Nanoparticles were centrifuged at 2000 x *g* for 120 minutes and then the supernatant was discarded. Pellets were washed with 0.1% (*v/v*) Tween 20, 0.01% (*w/v*) sodium citrate tribasic dihydrate solution (NP wash buffer) thrice using centrifugation steps at 2000 x *g* for 30 minutes. The nanoparticles were dispersed in NP wash buffer, and then both concentration and hydrodynamic diameter were measured by UV-Vis spectrophotometry and DLS, respectively. The nanoparticle dispersion was stored at 4°C until further use.

3.2.2 Heparosan synthesis

As published in a previous study by our laboratories, a quasi-monodisperse 13-kDa heparosan (HEP) polysaccharide (polydispersity *Mw/Mn* 1.038 +/- 0.0046) with a reducing end amino group (HEP-NH2) was synthesized by synchronized, stoichiometrically-controlled chemoenzymatic reaction using an amine-containing acceptor, UDP-sugar donors, and PmHS enzyme as described previously.[191] This starting material was employed to create a HEP with a thiol-reactive group (HEP-OPSS) at the reducing terminus. HEP polymers were quantified using the carbazole assay with a glucuronic acid standard.[192]

The thiol-reactive dithio-pyridyl (OPSS) group was introduced into the reducing end of various HEP-NH_2 polymers using a 31- to 42-fold molar excess of *N*-succinimidyl 3-(2-pyridyldithio)propionate (SPDP) (ThermoFisher) added as 2 or 4 additions in neat DMSO; the reaction was performed with 6-6.7 mg/mL HEP-NH_2 and 30-37% DMSO solvent final in 0.1 M HEPES, pH 7.2, 5 mM EDTA, at room temperature overnight. The HEP-OPSS target was precipitated by the addition of NaCl (0.1 M final) and 4.8 volumes of isopropanol on ice for 2 hours The resulting pellet was harvested by centrifugation (1,800 x*g*, 30 min), the supernatant aspirated, and the pellet dried (3 min under vacuum or air-dried for 2.25 hours) before re-suspension in water at 4°C overnight. The HEP-OPSS was purified from small MW compounds via either strong anion exchange chromatography or by ultrafiltration.

The HEP-OPSS (~100 mg synthesis scale) was applied to a HiTrap Q strong anion exchange column (5 mL bed; GE Healthcare) equilibrated in Buffer A (10 mM NaOAc, pH 5.8) at 2 mL/min and washed with 4 column volumes (cv) of 100% buffer A. A series of linear gradient steps with NaCl elution (using B buffer = A + 1 M NaCl in steps of 10 cv of 90A:10B, 4 cv of 60A:40B, and then 1 cv of 40A:60B) removed traces of OPSS from the target. The 0.21-0.5 M NaCl fractions containing the HEP-OPSS target were pooled, precipitated with 2.5 volumes of ethanol (similar process to isopropanol employed above), the pellet suspended in

water, and stored at -20°C. Alternatively, the HEP-OPSS (~200 mg synthesis scale) target was purified by repeated ultrafiltration (6 cycles with a spin unit with 3 kDa MWCO membrane; Amicon) against water at room temperature to desalt the sample and to remove any residual SPDP. The presence of the OPSS group on the sugar chain was verified by reaction with SAMSA (a fluorescent thiol activated with base per the manufacturer's instructions; ThermoFisher) and then PAGE analysis [193]. A fluorescent band at the appropriate MW was detected, thus indicating the successful installation of the OPSS moiety onto the sugar chain as described later.

3.2.3 HEP-AuNPs prepared by the pH assisted method

The protocol was adapted and modified from a published paper from the Liu group [196]. Here, pH 3.0 HCl without citrate was used as a solvent for the heparosan and gold nanoparticle mixture. Unless specified, all HEP-AuNPs in this paper refer to 13-kDa 55-nm HEP-AuNPs synthesized by adding 5 HEP/nm^2. The calculated amount of HEP for 5 polymers/nm^2 was added and mixed with acidic water, followed by nanoparticle addition. After briefly vortexing, a 3.43 M stock of NaCl in water was added in 0.3 M NaCl increments until the final NaCl concentration reached 0.6 M. Each increment was followed by a 20 min incubation at room temperature. DLS was measured after final incubation to confirm successful HEP conjugation as determined by an increase in hydrodynamic diameter compared to control AuNPs (no addition of HEP).

3.2.4 Nanoparticle cell uptake study

This protocol was followed by previously published methods in our laboratory [194]. RAW 264.7 macrophages were purchased from ATCC. DC 2.4 were provided by Dr. Chen. First, a total of $2x10^5$ cells were seeded onto a 48-well plate and allowed to adhere overnight. The cells were washed with sterile 1X phosphate buffered saline (PBS) thrice, then 500 µl of nanoparticles in the corresponding cell media with FBS were administered and the cells were incubated for at 37°C (5% CO_2) in a humidified tissue culture incubator. Specific incubation times and nanoparticle concentrations are noted in the figure captions along with each experiment result. After incubation with nanoparticles, cells were washed with 1X PBS thrice to remove non-internalized nanoparticles.

Purified cell samples were then digested by adding 500 µl of Aqua Regia (4:1 nitric acid/ hydrochloric acid, *v/v*) directly into the wells. After 30 min, acid-digested samples were transferred to 1.5-mL microcentrifuge tubes and placed in a water bath at 70°C for 1 h to complete the digestion process. Samples were then allowed to cool and then diluted 40-fold into nanopure water with a final volume of 5 mL. All elemental analysis measurements for nanoparticle uptake were done using the PerkinElmer NexIon 2000 ICP-MS on the Prepfast IC Sample Introduction system at the Mass Spectrometry, Proteomics, and Metabolomics Core Facility, University of Oklahoma. To determine the average number of nanoparticles per cell, dissolved gold signal was correlated to the magnesium signal from known numbers of cells. Iridium was used as an internal standard. The data were analyzed on GraphPad Prism with three or four replicates.

3.2.5 Real time confocal characterization of nanoparticle cellular uptake

RAW 264.7 macrophages were seeded onto sterile glass coverslips placed into a 6 well-plate overnight with DMEM culture media supplemented with 10% FBS and 1% Penicillin-Streptomycin. The next day, cell media was removed and HEP-coated 55-nm gold nanoparticles (0.2 nM final) were administrated. Cells were stained with wheat germ agglutinin CF488A (WGA, cat# 29022, Biotium) and NucBlue Live cell Hoechst (cat# R37605, Thermo Fisher) according to the manufacture's protocols to label the cell surface or the nuclei, respectively. Confocal images were taken with a 63X oil immersion objective (1.4 NA) on a ZEISS LSM 880 inverted confocal microscope using photomultiplier tube (PMT) detectors with a 405 nm diode laser and a 488 nm argon laser for fluorescent channels through a main beam splitter (MBS) 488/561/633 filter. The nanoparticles were imaged using light scattering principles described by Jiang et al [159,207] with a 561 nm diode-pumped solid-state laser and an MBS T80/R20 filter.

3.2.6 Confocal characterization of nanoparticle cellular uptake in fixed cells

Similarly, RAW 264.7 macrophages or DC 2.4were seeded onto sterile glass coverslips placed into a 6 well-plate overnight with DMEM culture media supplemented with 10% fetal bovine serum and 1% Penicillin-Streptomycin. The next day cell media was removed. Cells were pretreated with inhibitors for 1 hour. Next, 0.2 nM HEP-coated 55-nm gold nanoparticles were administrated for 4.5 h in the presence of inhibitors. Cells were washed thrice with 1X PBS to remove noninternalized gold nanoparticles. Cells were fixed by 4% paraformaldehyde (PFA, cat# AAJ19943K2, Thermo Fisher) at room temperature for 10 minutes. Fixed cells were stained with wheat germ agglutinin CF488A (WGA, cat# 29022, Biotium) and NucBlue fix cell DAPI (cat# R37606, Thermo Fisher) according to the manufacture's protocols to label the cell surface or the nuclei, respectively. Confocal images were taken as described above.

3.2.7 Transmission electron microscopy (TEM) imaging of AuNPs inside of cells

For TEM imaging, we adapted a previously published method [240]. Cells were seeded in 6-well plates ($1x10^6$ cells/well) and incubated overnight. Either 0.3 nM PEG- or HEP-AuNPs were incubated with RAW 264.7 macrophages and DC 2.4 cells for 3 h, 6 h, and 24 h. After incubation, uninternalized AuNPs were removed by washing with 1X PBS thrice. RAW cells were scraped off the wells and collected by centrifugation (500 xg, 5 min, 25ºC) into a 1.5 mL Eppendorf tube; DC 2.4 were removed from wells by trypsin-mediated release, and collected into a 1.5 mL tube by centrifugation. The supernatants were removed, and the cell pellets were fixed with freshly made EM-grade glutaraldehyde/paraformaldehyde (2% and 4% final in 0.2 M cacodylate buffer) at room temperature for 1 hour. Samples were then stored at 4 ºC until sectioning and staining (3% lead citrate solution, cat. 22410, Electron Microscopy Sciences). TEM images were taken by a Hitachi H-7600 Transmission Electron Microscope at Oklahoma Medical Research Foundation (OMRF) in Oklahoma City, OK.

3.2.8 Energy dependent temperature and transport inhibition experiment

Cells ($1.5x10^5$ cells/well) were seeded in 48-well plates overnight to allow adherence. To investigate the effect of low temperature on cellular uptake, cells were incubated at 4ºC for 1 h, then 0.1 nM 55-nm 13 kDa HEP-AuNPs were added for another 1.5 h incubation at 4ºC. Parallel plates of cells were incubated at 37ºC for the control.

To investigate the chemical endocytic inhibitors' effect on cellular uptake, we followed the method published by Okuyama et al. [241]. Cells were seeded in 48-well plates overnight, then next day inhibitors were added to cells for 1 h. Then 0.1 nM of 55-nm 13 kDa HEP-AuNPs were added to cells for 1.5 h in the continued presence of inhibitors. Cells without any inhibitors were used as a control.

3.2.9 HEP structural analog competition experiment

Cells ($1.5x10^5$ cells/well) were seeded in 48-well plates overnight to allow adherence. To investigate the inhibition effect of HEP structural analogs, the next day, competitors were added to cells for 1 h incubation. Then, 0.1 nM of 55-nm 13 kDa HEP-AuNPs were added to cells for another 2.5 h incubation (3.5 h and 0.05 nM for dose-response experiment) in the presence of inhibitors. Parallel plates of cells were incubated at 37ºC for the control. 3.2.10 Cytokine release assay

3.2.10 Multivalent nanoparticle cell interaction

Our previously published pH-assisted conjugation method was used for coating HEP to AuNPs [240]. A concentration of HEP polymers calculated to obtain a defined coating density was first added into pH 3 nanopure water, then 55-nm AuNPs were added. The hydrodynamic diameter and zeta potential were measured by DLS after the final incubation, HEP-AuNPs were then purified by three cycles with washing nanopure water using centrifugation at 2,000 x*g* at 4 ºC for 30 min. Then, PEG-OPSS was added at a level of 7 PEG/nm^2 particle were added to the HEP-AuNPs to backfill any empty surface that was not covered by HEP polymer. AuNPs were washed thrice with nanopure water to remove free PEG and HEP before DLS characterization of hydrodynamic diameter and zeta potential. images. Blot images were quantified by the Quick Spot image analysis tool.

3.3 Results and Discussion

3.3.1 Uptake behavior of heparosan (HEP) modified nanoparticles over time

In Figure S23, we demonstrated that HEP-coated gold nanoparticles (HEP-AuNPs) efficiently target antigen-presenting cells, such as macrophages and dendritic cells, which is consistent with our previous findings [229]. In this study, DC 2.4 dendritic cells and RAW 264.7 macrophages were used as model innate immune cells for further the following studies. As shown under the light micrographs in Figures 3.1 A and S24, HEP-AuNPs incubated with DC 2.4 dendritic cells and RAW 264.7 exhibited a time-dependent nanoparticle uptake behavior, as evidenced by a progressively darker color upon brightfield imaging over time. We quantified the nanoparticle cellular uptake in RAW 264.7 (**Figure 3.1 B**) and DC 2.4 (Figure S25) by inductively coupled plasma mass spectrometry (ICP-MS) and observed that the nanoparticle uptake per cell increased over time, plateauing at ~12 h post incubation. These results indicate that innate immune cells exhibit a time-dependent cellular internalization process of HEP-coated nanoparticles.

To further validate the time-dependent cellular internalization, we performed confocal laser scanning microscopy (CLSM) to monitor the nanoparticle uptake behavior in real-time in RAW 264.7 up to 7 h post-incubation (**Figure 3.1 C-D**, S26). The HEP-coated AuNPs (yellow color) were imaged in a label-free manner via nanoparticle light scattering and were mainly present surrounding or at the cell membrane surface after 1 h of incubation [229,242]. Strong intracellular nanoparticle signals were detected at 4.5 h, 5 h, and 7 h time points post incubation. To corroborate the intracellular localization, we subsequently visualized the spatial distribution of nanoparticles in RAW 264.7 at 3 h, 6 h, and 24 h (**Figure 3.1 E** and S27) and DC 2.4 cells at 3 h and 24 h (Figure S28) post incubation by transmission electron microscopy (TEM). We observed that the HEP-AuNPs were present in intracellular vesicles and discovered that some nanoparticles were able to escape from these intracellular vesicles to access the cytoplasm

(**Figure 3.1 E** and S29). Our findings reveal that the cellular uptake of HEP-AuNPs in RAW 264.7 macrophages and DC 2.4 dendritic cells is time-dependent with a majority of internalized nanoparticles present in intracellular vesicles and a smaller fraction of nanoparticles accessing the cytoplasm.

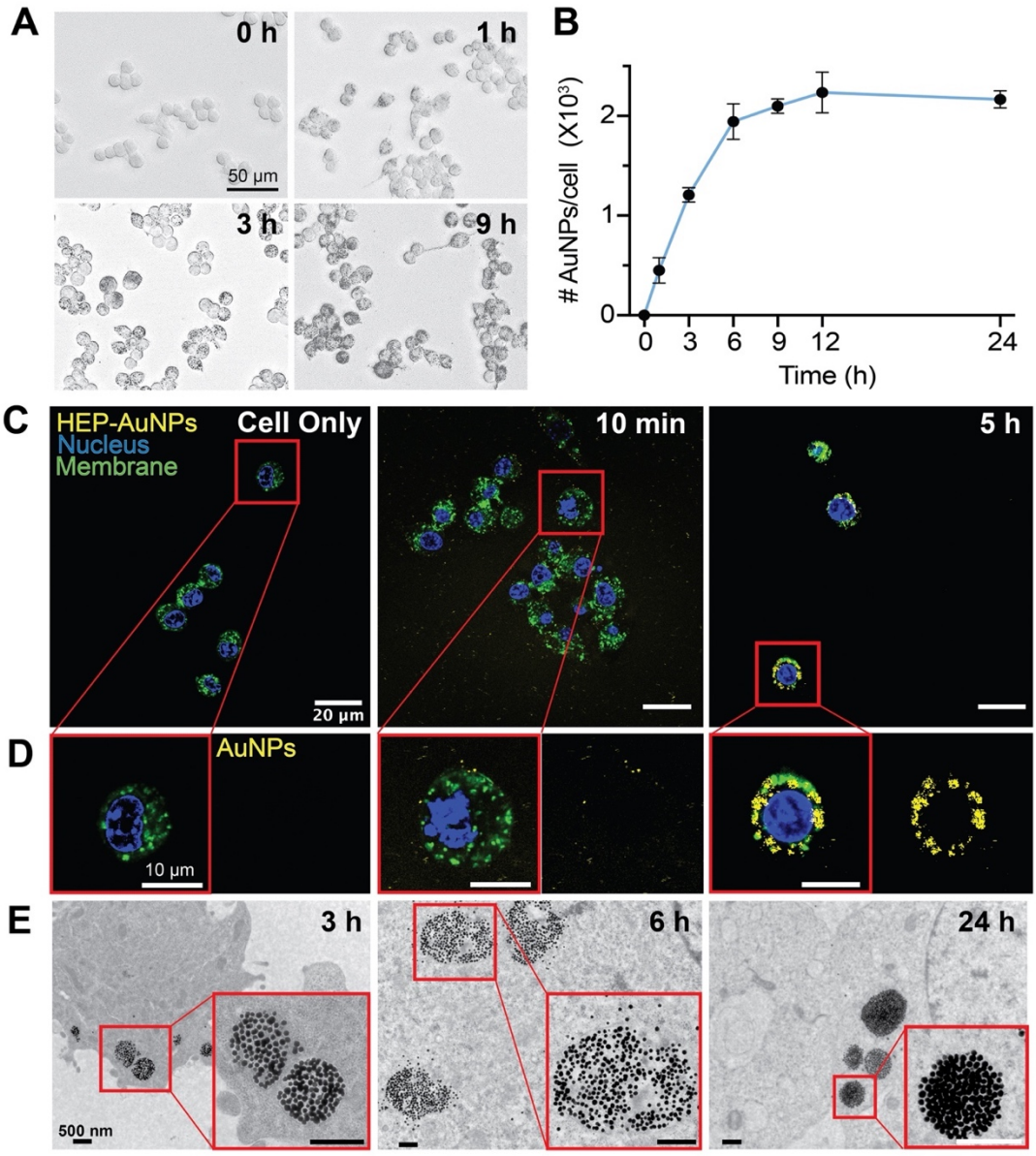

Figure 3.1: The cellular uptake of heparosan (HEP) modified gold nanoparticles (AuNPs) is time-dependent.

(A) Representative bright-field light micrographs of HEP-AuNPs internalization in RAW 264.7 macrophages before ICP-MS characterization at 0 h, 1 h, 3 h, and 9 h. 0.05 nM 55-nm HEP-AuNPs were used (scale bar, 50 µm). **(B)** ICP-MS was used to analyze the uptake of 0.05 nM 55-nm HEP-AuNPs in RAW 264.7 macrophages. The data points indicate the mean and standard deviation (n = 3-4). **(C)** Selective real-time confocal laser scanning microscopy (CLSM) imaging of HEP-AuNP internalization in living RAW 264.7 macrophages. 0.2 nM 55-nm HEP-AuNPs were used (scale bar, 20 µm). **(D)** A representative individual cell image was selected from panel C. The gold nanoparticle channel was extracted from the left panel (right panel; scale bar, 10 µm). **(E)** Transmission electron micrographs of 0.2 nM 55-nm HEP-AuNP internalization in RAW 264.7 after 3 h, 6 h, and 24 h incubation. High-resolution photographs of the selected field are shown at the bottom right-hand corners (scale bar, 500 nm).

3.3.2 HEP-AuNPs cellular internalization through the energy-dependent endocytic pathways

Since the HEP-AuNPs were found in intracellular vesicles, we hypothesized that these nanoparticles may enter cells via endocytosis by one or more energy-dependent uptake pathways [243,244]. To discern which uptake pathways were involved, we carried out a systematic endocytosis inhibition study in RAW 264.7 macrophages. First, we confirmed that the uptake was indeed facilitated via energy-dependent endocytosis by exposing the cells to known non-specific endocytosis inhibition conditions, i.e low temperature (4ºC), or 0.1% w/v sodium azide [245–247]. We found that the cellular uptake of HEP-AuNPs was reduced by ~89% and ~22% when NPs were incubated at 4ºC (**Figure 3.2 B** and S30) or treated with sodium azide, respectively (**Figure 3.2 C** and S30), confirming an energy dependent nanoparticle uptake process.

Next, we screened specific endocytosis pathways using established chemical inhibitors (**Table 3.1**) that more selectively block certain uptake pathways using concentrations from published literature reports (**Figure 3.2 A**). The innate immune cells were pre-incubated for 1 h with the endocytosis, then the nanoparticles were added and incubated with the cells for an additional 1.5 h. The cells were imaged using a light microscope and the nanoparticle uptake was quantified by ICP-MS over time (**Figure 3.2 D** and S30-31). The ICP-MS results revealed that the inhibition efficiencies of nanoparticle cellular uptake were ~73%, 12%, 24%, or 8% for chlorpromazine, chloroquine, cytochalasin D, or imipramine, respectively (**Figure 3.2 D**). Under our study conditions, chlorpromazine was the most effective agent. As shown in Figures 3.2 D and S30-31, no reduction in nanoparticle cellular uptake was observed when the cells were treated with the inhibitors N-ethylmaleimide (NEM), Filipin, Dynasore, or 5-(*N*-ethyl-*N*-isopropyl) amiloride (EIPA). However, our findings suggest that HEP-AuNPs primarily enter the model innate immune cells through both clathrin-mediated endocytosis and macropinocytosis/phagocytosis pathways.

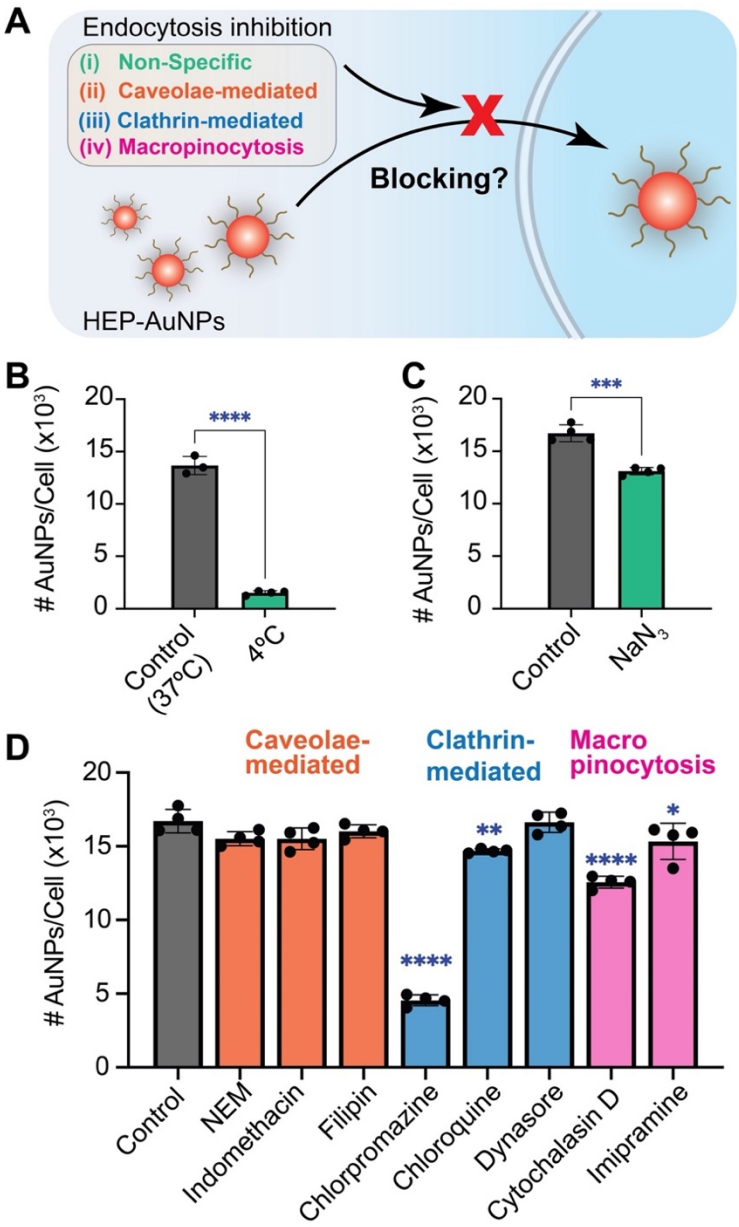

Figure 3.2: HEP-coated nanoparticles enter cells through endocytosis.

(A) Schematic representation of the uptake pathway study: (i) non-specific endocytosis inhibition to determine whether nanoparticle cellular uptake is energy dependent. (ii-iv) Specific endocytosis inhibitors for studying (ii) caveolae-mediated endocytosis, (iii) clathrin-mediated endocytosis, and (iv) macropinocytosis/phagocytosis. **(B-D)** ICP-MS quantification of the nanoparticle cellular uptake in RAW 264.7 macrophages at 4ºC **(B)**, in the presence of ATPase inhibitor sodium azide **(C)**, or chemical endocytosis inhibitors of caveolae-mediated endocytosis, clathrin-mediated endocytosis, and macropinocytosis/phagocytosis **(D)**. Gold NPs modified with 13-kDa HEP (at 0.2 nM) were used as control without inhibitors at 37ºC (histograms indicate mean ± SD (n=3-4); statistical tests used one-way ANOVA ($p<0.0001$ (****); $p<0.0021$ (**); $p<0.0332$ (*)).

Table 3.1: Summary of endocytosis inhibitors

Inhibitors	Mechanism of Action*	Function*	Condition/ Concentration	Ref.
Low temperature	Lowers metabolism	Non-specific endocytosis	4ºC	[245]
Sodium Azide (NaN_3)	Decreases ATP by inhibiting glycolysis	Non-specific endocytosis	0.1% w/v	[248]
N-ethylmaleimide (NEM)	Inactivates the ATPase	Caveolae-mediated endocytosis	0.3 µg/mL	[249–251]
Indomethacin	Increases [arachidonate] to prevent plasmalemmal vesicle formation	Caveolae-mediated and clathrin-dependent endocytosis	10 µg/mL	[252]
Filipin	Removes cholesterol from the plasma membrane	Caveolae-mediated and clathrin independent endocytosis	5 µg/mL	[253]
Chlorpromazine (CPZ)	Unknown (AP2 inhibition?)	Clathrin-mediated endocytosis	10 µg/mL	[252,253]
Chloroquine	Rho GTPase inhibition	Clathrin-mediated endocytosis	30 µg/mL	[254]
Dynasore	Blocks GTPase activity of dynamin	Clathrin-mediated endocytosis	25 µg/mL	[255]
Cytochalasin D (CD)	Depolymerizes F-actin	Macropinocytosis and phagocytosis	1 µg/mL	[255,256]
Imipramine	Inhibits the ruffling of plasma membranes	Macropinocytosis	10 µg/mL	[257]
Amiloride (EIPA)	Inhibits Na^+ channels and Na^+/H^+ exchange, F-action reorganization, pseudopodia retraction	Macropinocytosis and phagocytosis	10 or 20 µg/mL	[258]

*Information on the mechanism of action and function was adopted in part from reviews by Sheth et al., Rennick et al., and Almeida et al. [258–260].

3.3.3 HEP-AuNPs cellular internalization through clathrin-mediated endocytosis and macropinocytosis/phagocytosis

As schematically shown in Figure 3.3 A, chlorpromazine inhibits clathrin-mediated endocytosis while cytochalasin D inhibits macropinocytosis/phagocytosis [259,261]. These agents were the most effective HEP-AuNP uptake inhibitors in our screening experiments (**Figure 3.2**). To assess the dose response of the inhibitory effect and the cell toxicity of these two agents, we performed systematic dose escalation studies. Based on previous screening and published cell viability data [262–264], the dose ranges were selected as 0-31.4 μM and 0-3.9 μM for chlorpromazine and cytochalasin D, respectively. The cell viability assays confirmed that these inhibitor doses were not cytotoxic under the tested conditions (**Figure 3.3 B-C**). Using ICP-MS analysis, we quantified the inhibitory effects for nanoparticle uptake in RAW264.7 macrophages to be ~70% (chlorpromazine) and ~51% (cytochalasin D), respectively (**Figure 3.3 B-C**). Furthermore, the light micrographs showed an obvious reduction in light extinction for cells, consistent with a decrease in nanoparticle cellular uptake (Figure S32-33). Additionally, notably reduced cellular uptake by chlorpromazine (23.5 μM) and Cytochalasin D (3.0 μM) in RAW 264.7 was confirmed by CLSM imaging (**Figure 3.3 D**). Reduced nanoparticle intensity signals were observed in the cell groups treated with the inhibitors compared to the groups without the inhibitors (**Figure 3.3 D**).

To test whether the HEP-coated nanoparticles could enter cells through clathrin-mediated endocytosis and macropinocytosis/phagocytosis in other cell lines, we conducted similar inhibition experiments in DC 2.4 dendritic cells. As shown in Figures S34, both chlorpromazine and cytochalasin D reduced HEP-AuNP uptake by ~77% in DC 2.4 dendritic cells. Additionally, we co-incubated chlorpromazine and cytochalasin D inhibitors with cells to test if there was any synergistic inhibitory effect. However, co-incubation of these two inhibitors showed ~71% inhibitory effect, thus a significant synergistic inhibition was not observed with this inhibitor combination. This finding from DC 2.4 cells was corroborated by the co-

incubation of inhibitors in RAW 264.7 (Figure S35). No significant cytotoxicity of the inhibitors was observed at these tested doses (Figure S36). Our results indicate that in the immune cell types we tested, uptake of HEP-AuNPs occurs in a time dependent manner and involves both clathrin-mediated endocytosis and macropinocytosis/phagocytosis.

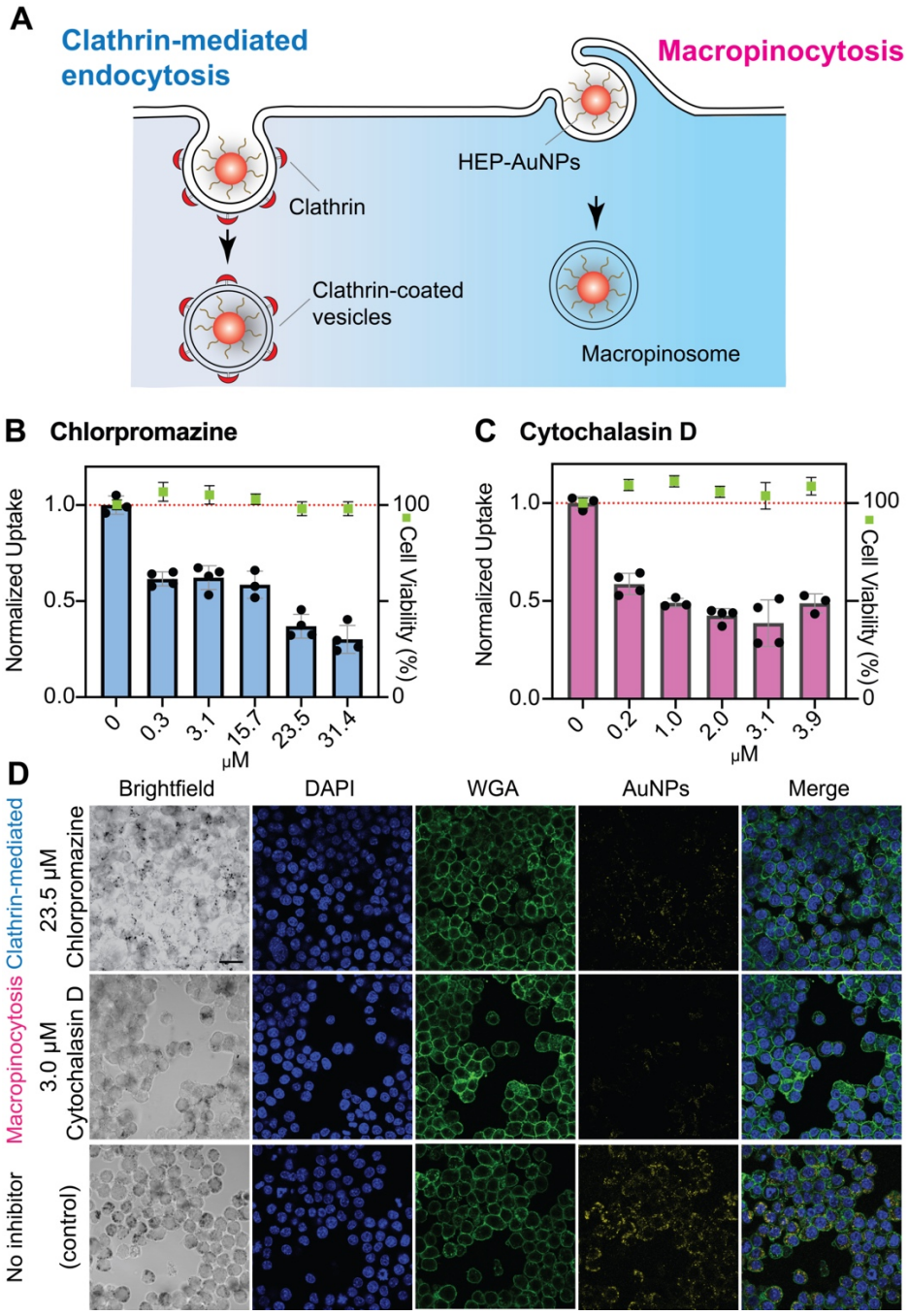

Figure 3.3: HEP-coated nanoparticles enter cells through clathrin-mediated endocytosis and macropinocytosis/phagocytosis.

(A) Schematic representation of HEP-AuNPs uptake through clathrin-mediated endocytosis or macropinocytosis/phagocytosis. **(B-C)** ICP-MS was used to quantify the nanoparticle cellular uptake in RAW 264.7 macrophages upon inhibition with different concentrations of chlorpromazine (**B**; clathrin-mediated endocytosis) and cytochalasin D (**C**; macropinocytosis/phagocytosis). Histograms indicate mean ± SD (n=3-4). The statistical analysis of groups with competitors showed $p<0.0001$ compared to the no-competitor group using one-way ANOVA. **(D)** Confocal laser scanning micrographs of nanoparticle uptake in the presence of endocytosis inhibitors chlorpromazine or cytochalasin D along with non-inhibition control group.

3.3.4 Controlling HEP-AuNPs cellular uptake by structural analogs of HEP

Our experiments strongly suggest that clathrin-mediated endocytosis plays an important role in the cellular uptake of HEP-AuNPs, indicating that cell surface receptors may facilitate the cell uptake. We wondered whether various structural analogs of HEP, the glycosaminoglycans including heparin, hyaluronan (HA), chondroitin sulfates (CS), could interact with cell surface receptors to compete with and thereby reduce the uptake of HEP-AuNPs (**Figure 3.4 A**).

To address this question, we first pre-incubated RAW 264.7 macrophages systematically with a library of HEP structural analogs (**Table 3.2**), and then added HEP-AuNPs to the cells. To quantify the nanoparticles' cellular interactions, we performed quantitative ICP-MS (**Figure 3.4 B** and Figures S37-38) and corroborated the results qualitatively with light microscopy (**Figure 3.4 C-E**, S37 and S39). The ICP-MS and microscopy data both revealed that CS A (i.e. CS with mostly C4-sulfo isomers) was most effective at reducing the cellular uptake (~ 43%) of HEP-AuNPs compared with the 'no-competitor' group. We observed 15% weak inhibition by CS C (i.e. CS with mostly C6-sulfo isomers) and 18% inhibition of heparin (i.e. the anticoagulant drug that is a highly sulfated HEP); no significant competition with the remaining structural analogs was observed (**Figure 3.4 B**, S37-38). The result that HEP itself was not a good competitor (either the high molecular weight 169-kDa HEP or the 13-kDa HEP used for the nanoparticle coating) is puzzling, but reproducible. We speculate that the multivalent interactions of the HEP-AuNPs with cells were too strong to be effectively competed by a 'monovalent' free HEP chain.

We next investigated whether the CS A inhibitory effect of HEP-AuNP uptake was due to a potential toxicity effect of the CS A preparation, which was extracted from mammalian source. We observed that the CS A material did not affect cell viability at the working concentrations employed in this study (**Figures 3.4 C-E**, S37, S39-41).

Next, we expanded the structural analog competition study to DC 2.4 dendritic cells. Since the previous study demonstrated that CS A significantly reduced uptake of the HEP-AuNPs in RAW 264.7 macrophages, we pre-incubated CS A with the DC 2.4 cells for 1 h, then added the nanoparticles for an additional 2.5-h incubation. The competition effect was then quantified by ICP-MS and corroborated with light microscopy (Figures S41-42). Non-cytotoxic doses of CS A resulted in a lower nanoparticle uptake as quantified by ICP-MS, and fewer nanoparticles were visible than in the no-competitor group using light microscopy (Figures S41-42).

We further assessed the competition effect of CS A as a function of time and concentration at noncytotoxic levels. The CS A agent showed a significant competition effect of HEP-AuNPs' cellular uptake as confirmed by light microscopy and ICP-MS quantification (Figures S43-46 and **Figures 3.4 F-G**). The inhibitory effect of 1 mg/mL CS A persisted throughout time (**Figure 3.4 F**). At 2 mg/mL, CS A suppressed cellular uptake of HEP-AuNPs up to 9-fold, according to our inhibitory dose-response curve (IC_{50} of 0.5 mg/mL, **Figure 3.4 G**). The GAG analog competition experiments imply that CS A can substitute as a ligand for HEP for the internalization receptor, but its identity remains unknown.

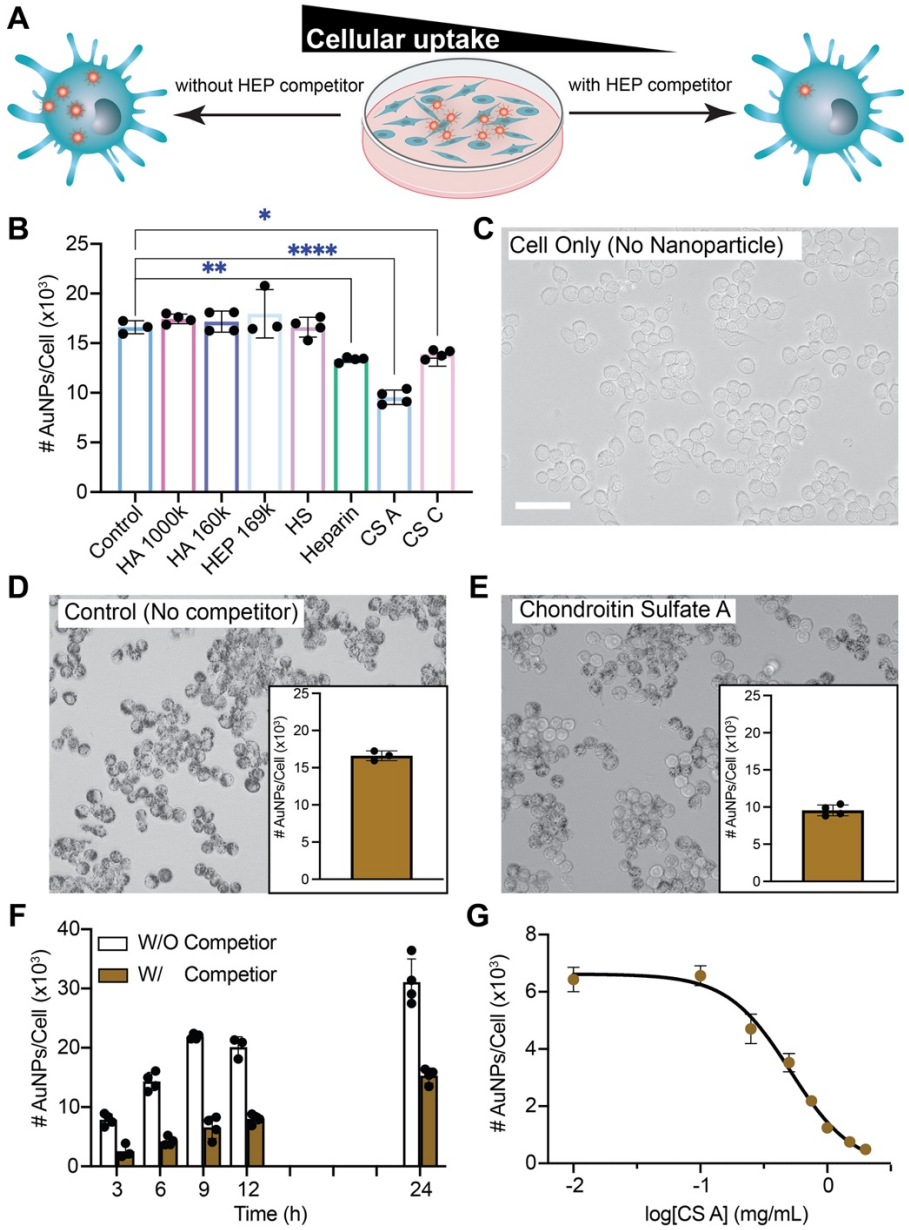

Figure 3.4: Evaluation of structural HEP analogs as competitors for HEP-coated nanoparticle uptake.

(A) Schematic illustration of experimental hypothesis. **(B)** ICP-MS was used to quantify the cellular uptake of HEP-AuNPs in the presence of HEP structural analogs: 0.1 mg/mL 1,000 kDa-HA, 160-kDa HA, 169-kDa HEP, heparin sulfate (HS), or heparin, and 1 mg/mL chondroitin sulfate A (CS A) or chondroitin sulfate C (CS C). The graphs indicate mean ± SD (n=3-4). Statistical tests were performed using one-way ANOVA ($p<0.0001$ (****); $p<0.0021$ (**); $p<0.0332$ (*); n.s. indicates no statistically significant differences). **(C-E)** Representative bright-field light micrographs of cellular HEP-AuNPs uptake in the presence of competitors before ICP-MS analysis. The inserted bar graphs are the ICP/MS quantitative analysis of the nanoparticle uptake of samples in the light micrographs. The bars indicate mean ± SD (n=3-4). (scale bar, 50 μm). **(F-G)** ICP-MS was used to quantify the CS A competition effect of HEP-AuNPs cellular uptake over time (F; 1 mg/mL CSA was used) and various concentration (G). The graphs indicate mean ± SD (n=3-4).

Table 3.2: Summary of structural analogs of HEP for competition experiments

GAG or Sugar	Average Molecular Weight (kDa)	Surface Receptors (Not all inclusive)	Major Repeat Structure	Similarity with Heparosan	Difference from Heparosan	Ref
Heparosan	43.8; 169		[GlcA]-4-beta-[GlcNAc]-4-alpha	-	-	
Hyaluronic acid (HA)	160; 1,000	CD 44; LYVE-1; HARE; Stabilin-1	[GlcA]-3-beta-[GlcNAc]-4-beta	same sugar composition and charge density	different glycosidic linkages	182,265,266
Heparan Sulfate	~12.9	Fibroblast growth factor receptor	[GlcA]-[6OS-GlcNAc/GlcNS]	same backbone	~1-2 sulfates per repeat	267,268
Heparin	~16.6	G6b; Fibroblast growth factor receptor; FGF2	[2S-IdoA/GlcA]-[6OS-GlcNS]	similar backbone	~3 sulfates per repeat; some GlcA epimer, IdoA	266,267,269,270
Chondroitin Sulfate A (CS A)	~19.5	CD 44	[GlcA]-3-beta-[4S-GalNAc]-4-beta	GAG family	GalNAc instead of GlcNAc; different glycosidic linkages; 1 sulfate per repeat.	267,268,271–273
Chondroitin Sulfate B (CS B)	~21		[2S-GlcA/IdoA]-3-beta-[4,6S-GalNAc]-4-beta	GAG family	GalNAc instead of GlcNAc; different glycosidic linkages; ~2 sulfate per repeat.	274
Chondroitin Sulfate C (CS C)	~45	CD 44	[GlcA]-3-beta-[6S-GalNAc]-4-beta	GAG family	GalNAc instead of GlcNAc; different glycosidic linkages; 1 sulfate per repeat.	2

Chondroitin Sulfate D (CS D)	~39		[2S-GlcA]-3-beta-[6S-GalNAc]-4-beta	GAG family	GalNAc instead of GlcNAc; different glycosidic linkages; ~2 sulfate per repeat.	[275]
Chondroitin Sulfate E (CS E)	~140	Contactin-1	[GlcA]-3-beta-[4,6S-GalNAc]-4-beta	GAG family	GalNAc instead of GlcNAc; different glycosidic linkages; ~2 sulfate per repeat.	[275,276]
Unsulfated chondroitin	~100-200		[GlcA]-3-beta-[GalNAc]-4-beta	GAG family; same charge density	GalNAc instead of GlcNAc	
GlcNAc(*N*-acetyl-glucosamine)	0.221	-	-	monosaccharide component	-	[277]

3.3.5 Controlling HEP-AuNPs cellular uptake by varying surface HEP density

Next, we examined if the substantial cellular uptake of HEP-AuNPs is due to a multivalent nanoparticle/receptor interaction by investigating the effect of HEP coating level (i.e. surface density) on internalization. Since uncoated AuNPs are prone to substantial protein corona formation that may affect cellular interactions [8,36,43,278–280], we used a backfilling strategy to cover the entire uncoated nanoparticles surface with poly(ethylene glycol), PEG, after the initial HEP-coating step (**Figure 3.5 A** and S23). PEG is known to minimize non-specific protein adsorption on nanoparticle surfaces and is used in the clinic [240,281]. The coating process was characterized by measuring the hydrodynamic diameter and zeta potential using DLS before and after back-filling with PEG. The data show that with HEP added at 0.5 HEP/ nm^2 and greater, there was no significant difference in the hydrodynamic diameter or the zeta potential values after PEG backfilling. At the added densities of less than 0.5 HEP/ nm^2, the hydrodynamic diameter and the zeta potential increased with the addition of PEG, indicating that the AuNPs were successfully backfilled (Figure S47 and S49 A-B). These results confirmed that fully surface-coated AuNPs with various HEP densities were generated successfully.

Next, we exposed these HEP/PEG-AuNPs with various HEP coating densities to RAW macrophages and evaluated the uptake efficiency of HEP-AuNPs as a function of HEP densities qualitatively by light microscopy and quantitatively by ICP-MS (**Figure 3.5 B-E** and S49 C-D). The gradual nanoparticles accumulation as HEP surface density increased was observed under a light microscope and showed that the nanoparticle cellular uptake efficiency is HEP surface density-dependent (**Figure 3.5 C-E** and S48-49 D). This relationship was further corroborated by ICP-MS quantification; the nanoparticle cellular uptake can be controlled by more than 3 orders of magnitude via varying the HEP surface density (**Figure 3.5 B** and S49 C). Overall, our results suggest that the multivalent interactions strengthen with an increase in HEP surface density, leading to higher HEP-AuNP cell uptake. Manipulating the surface HEP coating density could provide a strategy for controlled delivery of nanoparticles to immune cells.

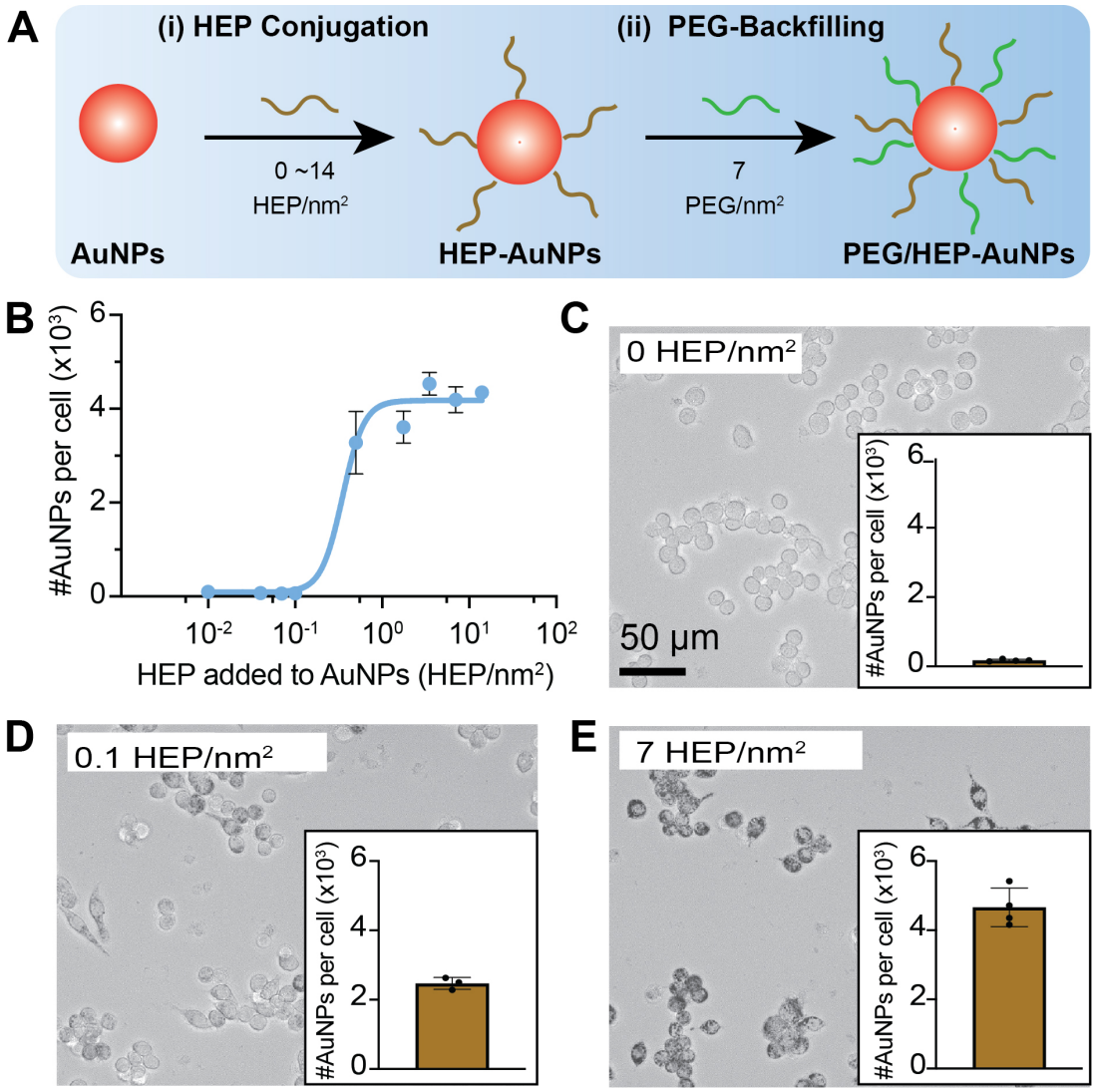

Figure 3.5: Surface coating of HEP provides multivalent ligands for strong nanoparticles and cell interaction.

(A) Schematic representation of the process of generating various HEP/PEG ligand densities of NPs. HEP polymers were added to AuNPs with theoretical surface densities ranging from 0 to 14 HEP/nm^2 using the pH-assisted method (i). A second conjugation step was followed with the addition of a constant addition quantity (7 PEG/nm^2) of poly[ethylene glycol] (PEG) to generate HEP/PEG-AuNPs (ii). The addition of PEG was used to backfill the surface of AuNPs that was not covered by HEP. **(B)** The uptake efficiency was measured as a function of surface HEP density by ICP-MS. Nanoparticle concentration was adjusted to 0.06 nM for comparison. The data points indicate mean ± SD (n=3-4). **(C-E)** Representative bright-field light micrographs of HEP/PEG-AuNPs in cells before ICP-MS analysis. NPs were observed as dark substances with accumulation in cells as the increasing HEP surface densities. The inserted bar graphs display the quantitative ICP/MS detection of nanoparticle uptake of cells shown in the light micrographs. The data points indicate mean ± SD (n=3-4). Scale bar: 50 μ

3.4 Conclusion

In the current work, we studied the cellular uptake behaviors and pathways of HEP-AuNPs in innate immune cells, i.e. macrophages and dendritic cells antigen-presenting cells. Our study demonstrates that HEP-AuNPs are taken up by these cells in a time-dependent manner and are internalized into intracellular vesicles through both clathrin-mediated endocytosis and macropinocytosis/phagocytosis with some fraction of internalized nanoparticles accessing the cytoplasm. The nanoparticle cellular uptake is strongly affected by the HEP surface density, and we found that this nanoparticle uptake can be controlled over three orders of magnitude through surface coating densities engineering. These control strategies of HEP-AuNP cellular uptake lay the groundwork for the future development nanoparticles as safe, effective, and efficient delivery systems for improved immunotherapies.

Chapter 4 Summary and future directions

We demonstrated the successful coating of polysaccharide heparosan (HEP) on inorganic nanoparticles of various materials and sizes by the salt aging and pH-assisted conjugation method and organic nanoparticles by post-insertion. Similar to PEG-based modifications, surface engineering of HEP on nanoparticles exhibited a comparable ability to reduce protein adsorption. HEP coating can substantially enhance cellular uptake in specific antigen-presenting cells but not in other tested cell types. We further discovered the HEP-AuNPs uptake in the antigen presenting cells is time-dependent and involves clathrin-mediated endocytosis and macropinocytosis/phagocytosis. Additionally, we controlled nanoparticle cellular uptake in antigen-presenting cells by utilizing structural analog competition and changing surface HEP density. Future studies will investigate the applications of HEP-based nanoparticle surface engineering in immunotherapies, such as vaccines, immunomodulation, and CAR-T therapies.

References

(1) Publicly Available Specification. Terminology for Nanomaterials. *British Standards Institute, London* **2007**.

(2) Li, N.; Georas, S.; Alexis, N.; Fritz, P.; Xia, T.; Williams, M. A.; Horner, E.; Nel, A. A Work Group Report on Ultrafine Particles (American Academy of Allergy, Asthma & Immunology): Why Ambient Ultrafine and Engineered Nanoparticles Should Receive Special Attention for Possible Adverse Health Outcomes in Human Subjects. *J. Allergy Clin. Immunol.* **2016**, *138* (2), 386–396. https://doi.org/10.1016/j.jaci.2016.02.023.

(3) Santos, A. C.; Morais, F.; Simões, A.; Pereira, I.; Sequeira, J. A. D.; Pereira-Silva, M.; Veiga, F.; Ribeiro, A. Nanotechnology for the Development of New Cosmetic Formulations. *Expert Opin Drug Deliv* **2019**, *16* (4), 313–330. https://doi.org/10.1080/17425247.2019.1585426.

(4) Hajba, L.; Guttman, A. The Use of Magnetic Nanoparticles in Cancer Theranostics: Toward Handheld Diagnostic Devices. *Biotechnology Advances* **2016**, *34* (4), 354–361. https://doi.org/10.1016/j.biotechadv.2016.02.001.

(5) Liu, Y.; Bhattarai, P.; Dai, Z.; Chen, X. Photothermal Therapy and Photoacoustic Imaging via Nanotheranostics in Fighting Cancer. *Chem Soc Rev* **2019**, *48* (7), 2053–2108. https://doi.org/10.1039/c8cs00618k.

(6) Hochella, M. F.; Mogk, D. W.; Ranville, J.; Allen, I. C.; Luther, G. W.; Marr, L. C.; McGrail, B. P.; Murayama, M.; Qafoku, N. P.; Rosso, K. M.; Sahai, N.; Schroeder, P. A.; Vikesland, P.; Westerhoff, P.; Yang, Y. Natural, Incidental, and Engineered Nanomaterials and Their Impacts on the Earth System. *Science* **2019**, *363* (6434). https://doi.org/10.1126/science.aau8299.

(7) Mills, N. L.; Miller, M. R.; Lucking, A. J.; Beveridge, J.; Flint, L.; Boere, A. J. F.; Fokkens, P. H.; Boon, N. A.; Sandstrom, T.; Blomberg, A.; Duffin, R.; Donaldson, K.; Hadoke, P. W. F.; Cassee, F. R.; Newby, D. E. Combustion-Derived Nanoparticulate Induces the Adverse Vascular Effects of Diesel Exhaust Inhalation. *Eur Heart J* **2011**, *32* (21), 2660–2671. https://doi.org/10.1093/eurheartj/ehr195.

(8) Narum, S. M.; Le, T.; Le, D. P.; Lee, J. C.; Donahue, N. D.; Yang, W.; Wilhelm, S. Chapter 4 - Passive Targeting in Nanomedicine: Fundamental Concepts, Body Interactions, and Clinical Potential. In *Nanoparticles for Biomedical Applications*; Chung, E. J., Leon, L., Rinaldi, C., Eds.; Micro and Nano Technologies; Elsevier, 2020; pp 37–53. https://doi.org/10.1016/B978-0-12-816662-8.00004-7.

(9) Sindhwani, S.; Syed, A. M.; Ngai, J.; Kingston, B. R.; Maiorino, L.; Rothschild, J.; MacMillan, P.; Zhang, Y.; Rajesh, N. U.; Hoang, T.; Wu, J. L. Y.; Wilhelm, S.; Zilman, A.; Gadde, S.; Sulaiman, A.; Ouyang, B.; Lin, Z.; Wang, L.; Egeblad, M.; Chan, W. C. W. The Entry of Nanoparticles into Solid Tumours. *Nature Materials* **2020**, 1–10. https://doi.org/10.1038/s41563-019-0566-2.

(10) Mohammed, Y. H.; Holmes, A.; Haridass, I. N.; Sanchez, W. Y.; Studier, H.; Grice, J. E.; Benson, H. A. E.; Roberts, M. S. Support for the Safe Use of Zinc Oxide Nanoparticle Sunscreens: Lack of Skin Penetration or Cellular Toxicity after Repeated Application in Volunteers. *J. Invest. Dermatol.* **2019**, *139* (2), 308–315. https://doi.org/10.1016/j.jid.2018.08.024.

(11) Albanese, A.; Tang, P. S.; Chan, W. C. W. The Effect of Nanoparticle Size, Shape, and Surface Chemistry on Biological Systems. *Annu. Rev. Biomed. Eng.* **2012**, *14* (1), 1–16. https://doi.org/10.1146/annurev-bioeng-071811-150124.

(12) Akaighe, N.; Maccuspie, R. I.; Navarro, D. A.; Aga, D. S.; Banerjee, S.; Sohn, M.; Sharma, V. K. Humic Acid-Induced Silver Nanoparticle Formation under

Environmentally Relevant Conditions. *Environ. Sci. Technol.* **2011**, *45* (9), 3895–3901. https://doi.org/10.1021/es103946g.
(13) Glover, R. D.; Miller, J. M.; Hutchison, J. E. Generation of Metal Nanoparticles from Silver and Copper Objects: Nanoparticle Dynamics on Surfaces and Potential Sources of Nanoparticles in the Environment. *ACS Nano* **2011**, *5* (11), 8950–8957. https://doi.org/10.1021/nn2031319.
(14) Wilhelm, S.; Hirsch, T.; Patterson, W. M.; Scheucher, E.; Mayr, T.; Wolfbeis, O. S. Multicolor Upconversion Nanoparticles for Protein Conjugation. *Theranostics* **2013**, *3* (4), 239–248. https://doi.org/10.7150/thno.5113.
(15) Zheng, Y.; Lee, P. W.; Wang, C.; Thomas, L. D.; Stewart, P. L.; Steinmetz, N. F.; Pokorski, J. K. Freeze-Drying To Produce Efficacious CPMV Virus-like Particles. *Nano Lett.* **2019**, *19* (3), 2099–2105. https://doi.org/10.1021/acs.nanolett.9b00300.
(16) Guo, B.; Zebda, R.; Drake, S. J.; Sayes, C. M. Synergistic Effect of Co-Exposure to Carbon Black and Fe2O3 Nanoparticles on Oxidative Stress in Cultured Lung Epithelial Cells. *Part Fibre Toxicol* **2009**, *6*, 4. https://doi.org/10.1186/1743-8977-6-4.
(17) Andriyanov, A. V.; Koren, E.; Barenholz, Y.; Goldberg, S. N. Therapeutic Efficacy of Combining Pegylated Liposomal Doxorubicin and Radiofrequency (RF) Ablation: Comparison between Slow-Drug-Releasing, Non-Thermosensitive and Fast-Drug-Releasing, Thermosensitive Nano-Liposomes. *PLoS ONE* **2014**, *9* (5), e92555. https://doi.org/10.1371/journal.pone.0092555.
(18) Elsaesser, A.; Howard, C. V. Toxicology of Nanoparticles. *Advanced Drug Delivery Reviews* **2012**, *64* (2), 129–137. https://doi.org/10.1016/j.addr.2011.09.001.
(19) Muhr, V.; Wilhelm, S.; Hirsch, T.; Wolfbeis, O. S. Upconversion Nanoparticles: From Hydrophobic to Hydrophilic Surfaces. *Acc. Chem. Res.* **2014**, *47* (12), 3481–3493. https://doi.org/10.1021/ar500253g.
(20) Elci, S. G.; Jiang, Y.; Yan, B.; Kim, S. T.; Saha, K.; Moyano, D. F.; Yesilbag Tonga, G.; Jackson, L. C.; Rotello, V. M.; Vachet, R. W. Surface Charge Controls the Suborgan Biodistributions of Gold Nanoparticles. *ACS Nano* **2016**, *10* (5), 5536–5542. https://doi.org/10.1021/acsnano.6b02086.
(21) Poon, W.; Zhang, Y.-N.; Ouyang, B.; Kingston, B. R.; Wu, J. L. Y.; Wilhelm, S.; Chan, W. C. W. Elimination Pathways of Nanoparticles. *ACS Nano* **2019**, *13* (5), 5785–5798. https://doi.org/10.1021/acsnano.9b01383.
(22) Liu, J.; Feng, X.; Wei, L.; Chen, L.; Song, B.; Shao, L. The Toxicology of Ion-Shedding Zinc Oxide Nanoparticles. *Crit. Rev. Toxicol.* **2016**, *46* (4), 348–384. https://doi.org/10.3109/10408444.2015.1137864.
(23) Sun, D.; Zhang, W.; Mou, Z.; Chen, Y.; Guo, F.; Yang, E.; Wang, W. Transcriptome Analysis Reveals Silver Nanoparticle-Decorated Quercetin Antibacterial Molecular Mechanism. *ACS Appl Mater Interfaces* **2017**, *9* (11), 10047–10060. https://doi.org/10.1021/acsami.7b02380.
(24) El-Rafie, H. M.; Hamed, M. A.-A. Antioxidant and Anti-Inflammatory Activities of Silver Nanoparticles Biosynthesized from Aqueous Leaves Extracts of Four Terminalia Species. *Adv. Nat. Sci: Nanosci. Nanotechnol.* **2014**, *5* (3), 035008. https://doi.org/10.1088/2043-6262/5/3/035008.
(25) Holmes, A. M.; Song, Z.; Moghimi, H. R.; Roberts, M. S. Relative Penetration of Zinc Oxide and Zinc Ions into Human Skin after Application of Different Zinc Oxide Formulations. *ACS Nano* **2016**, *10* (2), 1810–1819. https://doi.org/10.1021/acsnano.5b04148.
(26) Rivera Gil, P.; Oberdörster, G.; Elder, A.; Puntes, V.; Parak, W. J. Correlating Physico-Chemical with Toxicological Properties of Nanoparticles: The Present and the Future. *ACS Nano* **2010**, *4* (10), 5527–5531. https://doi.org/10.1021/nn1025687.

(27) Pankhurst, Q.; Hautot, D.; Khan, N.; Dobson, J. Increased Levels of Magnetic Iron Compounds in Alzheimer's Disease. *JAD* **2008**, *13* (1), 49–52. https://doi.org/10.3233/JAD-2008-13105.
(28) Maher, B. A.; Ahmed, I. A. M.; Karloukovski, V.; MacLaren, D. A.; Foulds, P. G.; Allsop, D.; Mann, D. M. A.; Torres-Jardón, R.; Calderon-Garciduenas, L. Magnetite Pollution Nanoparticles in the Human Brain. *Proc Natl Acad Sci USA* **2016**, *113* (39), 10797–10801. https://doi.org/10.1073/pnas.1605941113.
(29) Khatri, M.; Bello, D.; Gaines, P.; Martin, J.; Pal, A. K.; Gore, R.; Woskie, S. Nanoparticles from Photocopiers Induce Oxidative Stress and Upper Respiratory Tract Inflammation in Healthy Volunteers. *Nanotoxicology* **2013**, *7* (5), 1014–1027. https://doi.org/10.3109/17435390.2012.691998.
(30) Aktepe, N.; Kocyigit, A.; Yukselten, Y.; Taskin, A.; Keskin, C.; Celik, H. Increased DNA Damage and Oxidative Stress among Silver Jewelry Workers. *Biol Trace Elem Res* **2015**, *164* (2), 185–191. https://doi.org/10.1007/s12011-014-0224-0.
(31) Chanan-Khan, A.; Szebeni, J.; Savay, S.; Liebes, L.; Rafique, N. M.; Alving, C. R.; Muggia, F. M. Complement Activation Following First Exposure to Pegylated Liposomal Doxorubicin (Doxil): Possible Role in Hypersensitivity Reactions. *Ann. Oncol.* **2003**, *14* (9), 1430–1437. https://doi.org/10.1093/annonc/mdg374.
(32) Munger, M. A.; Radwanski, P.; Hadlock, G. C.; Stoddard, G.; Shaaban, A.; Falconer, J.; Grainger, D. W.; Deering-Rice, C. E. In Vivo Human Time-Exposure Study of Orally Dosed Commercial Silver Nanoparticles. *Nanomedicine* **2014**, *10* (1), 1–9. https://doi.org/10.1016/j.nano.2013.06.010.
(33) Donahue, N. D.; Acar, H.; Wilhelm, S. Concepts of Nanoparticle Cellular Uptake, Intracellular Trafficking, and Kinetics in Nanomedicine. *Advanced Drug Delivery Reviews* **2019**, *143*, 68–96. https://doi.org/10.1016/j.addr.2019.04.008.
(34) Pan, Y.; Neuss, S.; Leifert, A.; Fischler, M.; Wen, F.; Simon, U.; Schmid, G.; Brandau, W.; Jahnen-Dechent, W. Size-Dependent Cytotoxicity of Gold Nanoparticles. *Small* **2007**, *3* (11), 1941–1949. https://doi.org/10.1002/smll.200700378.
(35) Bozich, J. S.; Lohse, S. E.; Torelli, M. D.; Murphy, C. J.; Hamers, R. J.; Klaper, R. D. Surface Chemistry, Charge and Ligand Type Impact the Toxicity of Gold Nanoparticles to Daphnia Magna. *Environ. Sci.: Nano* **2014**, *1* (3), 260–270. https://doi.org/10.1039/C4EN00006D.
(36) Lee, J. C.; Donahue, N. D.; Mao, A. S.; Karim, A.; Komarneni, M.; Thomas, E. E.; Francek, E. R.; Yang, W.; Wilhelm, S. Exploring Maleimide-Based Nanoparticle Surface Engineering to Control Cellular Interactions. *ACS Appl. Nano Mater.* **2020**. https://doi.org/10.1021/acsanm.9b02541.
(37) Fröhlich, E. The Role of Surface Charge in Cellular Uptake and Cytotoxicity of Medical Nanoparticles. *Int J Nanomedicine* **2012**, *7*, 5577–5591. https://doi.org/10.2147/IJN.S36111.
(38) Sukhanova, A.; Bozrova, S.; Sokolov, P.; Berestovoy, M.; Karaulov, A.; Nabiev, I. Dependence of Nanoparticle Toxicity on Their Physical and Chemical Properties. *Nanoscale Res Lett* **2018**, *13* (1), 44. https://doi.org/10.1186/s11671-018-2457-x.
(39) Tripathy, N.; Hong, T.-K.; Ha, K.-T.; Jeong, H.-S.; Hahn, Y.-B. Effect of ZnO Nanoparticles Aggregation on the Toxicity in RAW 264.7 Murine Macrophage. *Journal of Hazardous Materials* **2014**, *270*, 110–117. https://doi.org/10.1016/j.jhazmat.2014.01.043.
(40) Albanese, A.; Chan, W. C. W. Effect of Gold Nanoparticle Aggregation on Cell Uptake and Toxicity. *ACS Nano* **2011**, *5* (7), 5478–5489. https://doi.org/10.1021/nn2007496.

(41) Zhao, X.; Ng, S.; Heng, B. C.; Guo, J.; Ma, L.; Tan, T. T. Y.; Ng, K. W.; Loo, S. C. J. Cytotoxicity of Hydroxyapatite Nanoparticles Is Shape and Cell Dependent. *Archives of Toxicology* **2013**, *87* (6), 1037–1052. https://doi.org/10.1007/s00204-012-0827-1.
(42) Wang, J.; Chen, H.-J.; Hang, T.; Yu, Y.; Liu, G.; He, G.; Xiao, S.; Yang, B.; Yang, C.; Liu, F.; Tao, J.; Wu, M. X.; Xie, X. Physical Activation of Innate Immunity by Spiky Particles. *Nature Nanotechnology* **2018**, *13* (11), 1078–1086. https://doi.org/10.1038/s41565-018-0274-0.
(43) Dai, Q.; Wilhelm, S.; Ding, D.; Syed, A. M.; Sindhwani, S.; Zhang, Y.; Chen, Y. Y.; MacMillan, P.; Chan, W. C. W. Quantifying the Ligand-Coated Nanoparticle Delivery to Cancer Cells in Solid Tumors. *ACS Nano* **2018**, *12* (8), 8423–8435. https://doi.org/10.1021/acsnano.8b03900.
(44) Wilhelm, S.; Tavares, A. J.; Dai, Q.; Ohta, S.; Audet, J.; Dvorak, H. F.; Chan, W. C. W. Analysis of Nanoparticle Delivery to Tumours. *Nature Reviews Materials* **2016**, *1* (5), 1–12. https://doi.org/10.1038/natrevmats.2016.14.
(45) Tsoi, K. M.; MacParland, S. A.; Ma, X.-Z.; Spetzler, V. N.; Echeverri, J.; Ouyang, B.; Fadel, S. M.; Sykes, E. A.; Goldaracena, N.; Kaths, J. M.; Conneely, J. B.; Alman, B. A.; Selzner, M.; Ostrowski, M. A.; Adeyi, O. A.; Zilman, A.; McGilvray, I. D.; Chan, W. C. W. Mechanism of Hard-Nanomaterial Clearance by the Liver. *Nature Materials* **2016**, *15* (11), 1212–1221. https://doi.org/10.1038/nmat4718.
(46) Du, B.; Yu, M.; Zheng, J. Transport and Interactions of Nanoparticles in the Kidneys. *Nature Reviews Materials* **2018**, *3* (10), 358–374. https://doi.org/10.1038/s41578-018-0038-3.
(47) Tahover, E.; Patil, Y. P.; Gabizon, A. A. Emerging Delivery Systems to Reduce Doxorubicin Cardiotoxicity and Improve Therapeutic Index: Focus on Liposomes. *Anticancer Drugs* **2015**, *26* (3), 241–258. https://doi.org/10.1097/CAD.0000000000000182.
(48) Westerhoff, P.; Atkinson, A.; Fortner, J.; Wong, M. S.; Zimmerman, J.; Gardea-Torresdey, J.; Ranville, J.; Herckes, P. Low Risk Posed by Engineered and Incidental Nanoparticles in Drinking Water. *Nat Nanotechnol* **2018**, *13* (8), 661–669. https://doi.org/10.1038/s41565-018-0217-9.
(49) Zhu, S.; Gong, L.; Li, Y.; Xu, H.; Gu, Z.; Zhao, Y. Safety Assessment of Nanomaterials to Eyes: An Important but Neglected Issue. *Adv Sci (Weinh)* **2019**, *6* (16). https://doi.org/10.1002/advs.201802289.
(50) Liou, S.-H.; Tsou, T.-C.; Wang, S.-L.; Li, L.-A.; Chiang, H.-C.; Li, W.-F.; Lin, P.-P.; Lai, C.-H.; Lee, H.-L.; Lin, M.-H.; Hsu, J.-H.; Chen, C.-R.; Shih, T.-S.; Liao, H.-Y.; Chung, Y.-T. Epidemiological Study of Health Hazards among Workers Handling Engineered Nanomaterials. *J Nanopart Res* **2012**, *14* (8), 878. https://doi.org/10.1007/s11051-012-0878-5.
(51) Ye, L.; Yong, K.-T.; Liu, L.; Roy, I.; Hu, R.; Zhu, J.; Cai, H.; Law, W.-C.; Liu, J.; Wang, K.; Liu, J.; Liu, Y.; Hu, Y.; Zhang, X.; Swihart, M. T.; Prasad, P. N. A Pilot Study in Non-Human Primates Shows No Adverse Response to Intravenous Injection of Quantum Dots. *Nature Nanotech* **2012**, *7* (7), 453–458. https://doi.org/10.1038/nnano.2012.74.
(52) Qiao, H.; Liu, W.; Gu, H.; Wang, D.; Wang, Y. *The Transport and Deposition of Nanoparticles in Respiratory System by Inhalation*. Journal of Nanomaterials. https://www.hindawi.com/journals/jnm/2015/394507/ (accessed 2020-03-18). https://doi.org/10.1155/2015/394507.
(53) Zhang, H.; Ji, Z.; Xia, T.; Meng, H.; Low-Kam, C.; Liu, R.; Pokhrel, S.; Lin, S.; Wang, X.; Liao, Y.-P.; Wang, M.; Li, L.; Rallo, R.; Damoiseaux, R.; Telesca, D.; Mädler, L.; Cohen, Y.; Zink, J. I.; Nel, A. E. Use of Metal Oxide Nanoparticle Band

Gap to Develop a Predictive Paradigm for Oxidative Stress and Acute Pulmonary Inflammation. *ACS Nano* **2012**, *6* (5), 4349–4368. https://doi.org/10.1021/nn3010087.
(54) Adamcakova-Dodd, A.; Stebounova, L. V.; Kim, J. S.; Vorrink, S. U.; Ault, A. P.; O'Shaughnessy, P. T.; Grassian, V. H.; Thorne, P. S. Toxicity Assessment of Zinc Oxide Nanoparticles Using Sub-Acute and Sub-Chronic Murine Inhalation Models. *Part Fibre Toxicol* **2014**, *11*, 15. https://doi.org/10.1186/1743-8977-11-15.
(55) Lin, Y.; Hu, C.; Chen, A.; Feng, X.; Liang, H.; Yin, S.; Zhang, G.; Shao, L. Neurotoxicity of Nanoparticles Entering the Brain via Sensory Nerve-to-Brain Pathways: Injuries and Mechanisms. *Arch. Toxicol.* **2020**. https://doi.org/10.1007/s00204-020-02701-w.
(56) Choi, H. S.; Ashitate, Y.; Lee, J. H.; Kim, S. H.; Matsui, A.; Insin, N.; Bawendi, M. G.; Semmler-Behnke, M.; Frangioni, J. V.; Tsuda, A. Rapid Translocation of Nanoparticles from the Lung Airspaces to the Body. *Nat Biotechnol* **2010**, *28* (12), 1300–1303. https://doi.org/10.1038/nbt.1696.
(57) Raftis, J. B.; Miller, M. R. Nanoparticle Translocation and Multi-Organ Toxicity: A Particularly Small Problem. *Nano Today* **2019**, *26*, 8–12. https://doi.org/10.1016/j.nantod.2019.03.010.
(58) Dominguez-Medina, S.; Kisley, L.; Tauzin, L. J.; Hoggard, A.; Shuang, B.; D. S. Indrasekara, A. S.; Chen, S.; Wang, L.-Y.; Derry, P. J.; Liopo, A.; Zubarev, E. R.; Landes, C. F.; Link, S. Adsorption and Unfolding of a Single Protein Triggers Nanoparticle Aggregation. *ACS Nano* **2016**, *10* (2), 2103–2112. https://doi.org/10.1021/acsnano.5b06439.
(59) Deng, Z. J.; Liang, M.; Monteiro, M.; Toth, I.; Minchin, R. F. Nanoparticle-Induced Unfolding of Fibrinogen Promotes Mac-1 Receptor Activation and Inflammation. *Nat Nanotechnol* **2011**, *6* (1), 39–44. https://doi.org/10.1038/nnano.2010.250.
(60) Saptarshi, S. R.; Duschl, A.; Lopata, A. L. Interaction of Nanoparticles with Proteins: Relation to Bio-Reactivity of the Nanoparticle. *Journal of Nanobiotechnology* **2013**, *11* (1), 26. https://doi.org/10.1186/1477-3155-11-26.
(61) Neagu, M.; Piperigkou, Z.; Karamanou, K.; Engin, A. B.; Docea, A. O.; Constantin, C.; Negrei, C.; Nikitovic, D.; Tsatsakis, A. Protein Bio-Corona: Critical Issue in Immune Nanotoxicology. *Arch. Toxicol.* **2017**, *91* (3), 1031–1048. https://doi.org/10.1007/s00204-016-1797-5.
(62) Nel, A.; Xia, T.; Mädler, L.; Li, N. Toxic Potential of Materials at the Nanolevel. *Science* **2006**, *311* (5761), 622–627. https://doi.org/10.1126/science.1114397.
(63) Cedervall, T.; Lynch, I.; Lindman, S.; Berggård, T.; Thulin, E.; Nilsson, H.; Dawson, K. A.; Linse, S. Understanding the Nanoparticle-Protein Corona Using Methods to Quantify Exchange Rates and Affinities of Proteins for Nanoparticles. *Proc. Natl. Acad. Sci. U.S.A.* **2007**, *104* (7), 2050–2055. https://doi.org/10.1073/pnas.0608582104.
(64) Linse, S.; Cabaleiro-Lago, C.; Xue, W.-F.; Lynch, I.; Lindman, S.; Thulin, E.; Radford, S. E.; Dawson, K. A. Nucleation of Protein Fibrillation by Nanoparticles. *PNAS* **2007**, *104* (21), 8691–8696. https://doi.org/10.1073/pnas.0701250104.
(65) Akhavan, O.; Ghaderi, E. Toxicity of Graphene and Graphene Oxide Nanowalls Against Bacteria. *ACS Nano* **2010**, *4* (10), 5731–5736. https://doi.org/10.1021/nn101390x.
(66) Chen, K. L.; Bothun, G. D. Nanoparticles Meet Cell Membranes: Probing Nonspecific Interactions Using Model Membranes. *Environ. Sci. Technol.* **2014**, *48* (2), 873–880. https://doi.org/10.1021/es403864v.
(67) Leifert, A.; Pan, Y.; Kinkeldey, A.; Schiefer, F.; Setzler, J.; Scheel, O.; Lichtenbeld, H.; Schmid, G.; Wenzel, W.; Jahnen-Dechent, W.; Simon, U. Differential HERG Ion Channel Activity of Ultrasmall Gold Nanoparticles. *Proceedings of the National*

Academy of Sciences **2013**, *110* (20), 8004–8009. https://doi.org/10.1073/pnas.1220143110.
(68) Fu, P. P.; Xia, Q.; Hwang, H.-M.; Ray, P. C.; Yu, H. Mechanisms of Nanotoxicity: Generation of Reactive Oxygen Species. *Journal of Food and Drug Analysis* **2014**, *22* (1), 64–75. https://doi.org/10.1016/j.jfda.2014.01.005.
(69) Abdal Dayem, A.; Hossain, M. K.; Lee, S. B.; Kim, K.; Saha, S. K.; Yang, G.-M.; Choi, H. Y.; Cho, S.-G. The Role of Reactive Oxygen Species (ROS) in the Biological Activities of Metallic Nanoparticles. *Int J Mol Sci* **2017**, *18* (1). https://doi.org/10.3390/ijms18010120.
(70) Xia, T.; Kovochich, M.; Brant, J.; Hotze, M.; Sempf, J.; Oberley, T.; Sioutas, C.; Yeh, J. I.; Wiesner, M. R.; Nel, A. E. Comparison of the Abilities of Ambient and Manufactured Nanoparticles To Induce Cellular Toxicity According to an Oxidative Stress Paradigm. *Nano Lett.* **2006**, *6* (8), 1794–1807. https://doi.org/10.1021/nl061025k.
(71) Zorov, D. B.; Juhaszova, M.; Sollott, S. J. Mitochondrial Reactive Oxygen Species (ROS) and ROS-Induced ROS Release. *Physiological Reviews* **2014**, *94* (3), 909–950. https://doi.org/10.1152/physrev.00026.2013.
(72) Pelaz, B.; Alexiou, C.; Alvarez-Puebla, R. A.; Alves, F.; Andrews, A. M.; Ashraf, S.; Balogh, L. P.; Ballerini, L.; Bestetti, A.; Brendel, C.; Bosi, S.; Carril, M.; Chan, W. C. W.; Chen, C.; Chen, X.; Chen, X.; Cheng, Z.; Cui, D.; Du, J.; Dullin, C.; Escudero, A.; Feliu, N.; Gao, M.; George, M.; Gogotsi, Y.; Grünweller, A.; Gu, Z.; Halas, N. J.; Hampp, N.; Hartmann, R. K.; Hersam, M. C.; Hunziker, P.; Jian, J.; Jiang, X.; Jungebluth, P.; Kadhiresan, P.; Kataoka, K.; Khademhosseini, A.; Kopeček, J.; Kotov, N. A.; Krug, H. F.; Lee, D. S.; Lehr, C.-M.; Leong, K. W.; Liang, X.-J.; Ling Lim, M.; Liz-Marzán, L. M.; Ma, X.; Macchiarini, P.; Meng, H.; Möhwald, H.; Mulvaney, P.; Nel, A. E.; Nie, S.; Nordlander, P.; Okano, T.; Oliveira, J.; Park, T. H.; Penner, R. M.; Prato, M.; Puntes, V.; Rotello, V. M.; Samarakoon, A.; Schaak, R. E.; Shen, Y.; Sjöqvist, S.; Skirtach, A. G.; Soliman, M. G.; Stevens, M. M.; Sung, H.-W.; Tang, B. Z.; Tietze, R.; Udugama, B. N.; VanEpps, J. S.; Weil, T.; Weiss, P. S.; Willner, I.; Wu, Y.; Yang, L.; Yue, Z.; Zhang, Q.; Zhang, Q.; Zhang, X.-E.; Zhao, Y.; Zhou, X.; Parak, W. J. Diverse Applications of Nanomedicine. *ACS Nano* **2017**, *11* (3), 2313–2381. https://doi.org/10.1021/acsnano.6b06040.
(73) McShan, D.; Ray, P. C.; Yu, H. Molecular Toxicity Mechanism of Nanosilver. *Journal of Food and Drug Analysis* **2014**, *22* (1), 116–127. https://doi.org/10.1016/j.jfda.2014.01.010.
(74) Tsoi, K. M.; Dai, Q.; Alman, B. A.; Chan, W. C. W. Are Quantum Dots Toxic? Exploring the Discrepancy Between Cell Culture and Animal Studies. *Acc. Chem. Res.* **2013**, *46* (3), 662–671. https://doi.org/10.1021/ar300040z.
(75) Chen, N.; He, Y.; Su, Y.; Li, X.; Huang, Q.; Wang, H.; Zhang, X.; Tai, R.; Fan, C. The Cytotoxicity of Cadmium-Based Quantum Dots. *Biomaterials* **2012**, *33* (5), 1238–1244. https://doi.org/10.1016/j.biomaterials.2011.10.070.
(76) Derfus, A. M.; Chan, W. C. W.; Bhatia, S. N. Probing the Cytotoxicity Of Semiconductor Quantum Dots. *Nano Lett* **2004**, *4* (1), 11–18. https://doi.org/10.1021/nl0347334.
(77) Hauck, T. S.; Anderson, R. E.; Fischer, H. C.; Newbigging, S.; Chan, W. C. W. In Vivo Quantum-Dot Toxicity Assessment. *Small* **2010**, *6* (1), 138–144. https://doi.org/10.1002/smll.200900626.
(78) Nishanth, R. P.; Jyotsna, R. G.; Schlager, J. J.; Hussain, S. M.; Reddanna, P. Inflammatory Responses of RAW 264.7 Macrophages upon Exposure to Nanoparticles: Role of ROS-NFκB Signaling Pathway. *Nanotoxicology* **2011**, *5* (4),

502–516. https://doi.org/10.3109/17435390.2010.541604.
(79) Son, Y.; Cheong, Y.-K.; Kim, N.-H.; Chung, H.-T.; Kang, D. G.; Pae, H.-O. Mitogen-Activated Protein Kinases and Reactive Oxygen Species: How Can ROS Activate MAPK Pathways? *J Signal Transduct* **2011**, *2011*. https://doi.org/10.1155/2011/792639.
(80) Walter, P. L.; Kampkötter, A.; Eckers, A.; Barthel, A.; Schmoll, D.; Sies, H.; Klotz, L.-O. Modulation of FoxO Signaling in Human Hepatoma Cells by Exposure to Copper or Zinc Ions. *Arch. Biochem. Biophys.* **2006**, *454* (2), 107–113. https://doi.org/10.1016/j.abb.2006.08.016.
(81) Frame, M. C. Src in Cancer: Deregulation and Consequences for Cell Behaviour. *Biochimica et Biophysica Acta (BBA) - Reviews on Cancer* **2002**, *1602* (2), 114–130. https://doi.org/10.1016/S0304-419X(02)00040-9.
(82) Nyga, A.; Hart, A.; Tetley, T. D. Importance of the HIF Pathway in Cobalt Nanoparticle-Induced Cytotoxicity and Inflammation in Human Macrophages. *Nanotoxicology* **2015**, *9* (7), 905–917. https://doi.org/10.3109/17435390.2014.991430.
(83) Weidemann, A.; Johnson, R. S. Biology of HIF-1 α. *Cell Death & Differentiation* **2008**, *15* (4), 621–627. https://doi.org/10.1038/cdd.2008.12.
(84) Angelé-Martínez, C.; Nguyen, K. V. T.; Ameer, F. S.; Anker, J. N.; Brumaghim, J. L. Reactive Oxygen Species Generation by Copper(II) Oxide Nanoparticles Determined by DNA Damage Assays and EPR Spectroscopy. *Nanotoxicology* **2017**, *11* (2), 278–288. https://doi.org/10.1080/17435390.2017.1293750.
(85) Manke, A.; Wang, L.; Rojanasakul, Y. Mechanisms of Nanoparticle-Induced Oxidative Stress and Toxicity. *BioMed Research International* **2013**, *2013*, 1–15. https://doi.org/10.1155/2013/942916.
(86) Campisi, L.; Cummings, R. J.; Blander, J. M. Death-Defining Immune Responses After Apoptosis. *Am J Transplant* **2014**, *14* (7), 1488–1498. https://doi.org/10.1111/ajt.12736.
(87) Frank, D.; Vince, J. E. Pyroptosis versus Necroptosis: Similarities, Differences, and Crosstalk. *Cell Death & Differentiation* **2019**, *26* (1), 99–114. https://doi.org/10.1038/s41418-018-0212-6.
(88) Wang, Q.; Wang, Y.; Ding, J.; Wang, C.; Zhou, X.; Gao, W.; Huang, H.; Shao, F.; Liu, Z. A Bioorthogonal System Reveals Antitumour Immune Function of Pyroptosis. *Nature* **2020**, *579* (7799), 421–426. https://doi.org/10.1038/s41586-020-2079-1.
(89) Bergström, K.; Holmberg, K.; Safranj, A.; Hoffman, A. S.; Edgell, M. J.; Kozlowski, A.; Hovanes, B. A.; Harris, J. M. Reduction of Fibrinogen Adsorption on PEG-Coated Polystyrene Surfaces. *J. Biomed. Mater. Res.* **1992**, *26* (6), 779–790. https://doi.org/10.1002/jbm.820260607.
(90) Banerjee, I.; Pangule, R. C.; Kane, R. S. Antifouling Coatings: Recent Developments in the Design of Surfaces That Prevent Fouling by Proteins, Bacteria, and Marine Organisms. *Advanced Materials* **2011**, *23* (6), 690–718. https://doi.org/10.1002/adma.201001215.
(91) Ingen-Housz-Oro, S.; Pham-Ledard, A.; Brice, P.; Lebrun-Vignes, B.; Zehou, O.; Reitter, D.; Ram-Wolff, C.; Dupin, N.; Bagot, M.; Chosidow, O.; Beylot-Barry, M. Immediate Hypersensitivity Reaction to Pegylated Liposomal Doxorubicin: Management and Outcome in Four Patients. *Eur J Dermatol* **2017**, *27* (3), 271–274. https://doi.org/10.1684/ejd.2017.2986.
(92) Szebeni, J.; Simberg, D.; González-Fernández, Á.; Barenholz, Y.; Dobrovolskaia, M. A. Roadmap and Strategy for Overcoming Infusion Reactions to Nanomedicines. *Nat Nanotechnol* **2018**, *13* (12), 1100–1108. https://doi.org/10.1038/s41565-018-0273-1.
(93) Szebeni, J. Complement Activation-Related Pseudoallergy: A Stress Reaction in

Blood Triggered by Nanomedicines and Biologicals. *Molecular Immunology* **2014**, *61* (2), 163–173. https://doi.org/10.1016/j.molimm.2014.06.038.
(94) Ishida, T.; Wang, X.; Shimizu, T.; Nawata, K.; Kiwada, H. PEGylated Liposomes Elicit an Anti-PEG IgM Response in a T Cell-Independent Manner. *J Control Release* **2007**, *122* (3), 349–355. https://doi.org/10.1016/j.jconrel.2007.05.015.
(95) Wang, X.; Ishida, T.; Kiwada, H. Anti-PEG IgM Elicited by Injection of Liposomes Is Involved in the Enhanced Blood Clearance of a Subsequent Dose of PEGylated Liposomes. *Journal of Controlled Release* **2007**, *119* (2), 236–244. https://doi.org/10.1016/j.jconrel.2007.02.010.
(96) Shimizu, T.; Mima, Y.; Hashimoto, Y.; Ukawa, M.; Ando, H.; Kiwada, H.; Ishida, T. Anti-PEG IgM and Complement System Are Required for the Association of Second Doses of PEGylated Liposomes with Splenic Marginal Zone B Cells. *Immunobiology* **2015**, *220* (10), 1151–1160. https://doi.org/10.1016/j.imbio.2015.06.005.
(97) Mohamed, M.; Abu Lila, A. S.; Shimizu, T.; Alaaeldin, E.; Hussein, A.; Sarhan, H. A.; Szebeni, J.; Ishida, T. PEGylated Liposomes: Immunological Responses. *Sci Technol Adv Mater* **2019**, *20* (1), 710–724. https://doi.org/10.1080/14686996.2019.1627174.
(98) Kozma, G. T.; Mészáros, T.; Vashegyi, I.; Fülöp, T.; Örfi, E.; Dézsi, L.; Rosivall, L.; Bavli, Y.; Urbanics, R.; Mollnes, T. E.; Barenholz, Y.; Szebeni, J. Pseudo-Anaphylaxis to Polyethylene Glycol (PEG)-Coated Liposomes: Roles of Anti-PEG IgM and Complement Activation in a Porcine Model of Human Infusion Reactions. *ACS Nano* **2019**, *13* (8), 9315–9324. https://doi.org/10.1021/acsnano.9b03942.
(99) Chen, F.; Wang, G.; Griffin, J. I.; Brenneman, B.; Banda, N. K.; Holers, V. M.; Backos, D. S.; Wu, L.; Moghimi, S. M.; Simberg, D. Complement Proteins Bind to Nanoparticle Protein Corona and Undergo Dynamic Exchange in Vivo. *Nature Nanotechnology* **2017**, *12* (4), 387–393. https://doi.org/10.1038/nnano.2016.269.
(100) Moghimi, S. M.; Simberg, D. Complement Activation Turnover on Surfaces of Nanoparticles. *Nano Today* **2017**, *15*, 8–10. https://doi.org/10.1016/j.nantod.2017.03.001.
(101) Povsic, T. J.; Lawrence, M. G.; Lincoff, A. M.; Mehran, R.; Rusconi, C. P.; Zelenkofske, S. L.; Huang, Z.; Sailstad, J.; Armstrong, P. W.; Steg, P. G.; Bode, C.; Becker, R. C.; Alexander, J. H.; Adkinson, N. F.; Levinson, A. I. Pre-Existing Anti-PEG Antibodies Are Associated with Severe Immediate Allergic Reactions to Pegnivacogin, a PEGylated Aptamer. *Journal of Allergy and Clinical Immunology* **2016**, *138* (6), 1712–1715. https://doi.org/10.1016/j.jaci.2016.04.058.
(102) Ganson, N. J.; Povsic, T. J.; Sullenger, B. A.; Alexander, J. H.; Zelenkofske, S. L.; Sailstad, J. M.; Rusconi, C. P.; Hershfield, M. S. Pre-Existing Anti-Polyethylene Glycol Antibody Linked to First-Exposure Allergic Reactions to Pegnivacogin, a PEGylated RNA Aptamer. *J. Allergy Clin. Immunol.* **2016**, *137* (5), 1610-1613.e7. https://doi.org/10.1016/j.jaci.2015.10.034.
(103) Finkelman, F. D. Anaphylaxis: Lessons from Mouse Models. *Journal of Allergy and Clinical Immunology* **2007**, *120* (3), 506–515. https://doi.org/10.1016/j.jaci.2007.07.033.
(104) Zhang, P.; Sun, F.; Liu, S.; Jiang, S. Anti-PEG Antibodies in the Clinic: Current Issues and beyond PEGylation. *Journal of Controlled Release* **2016**, *244*, 184–193. https://doi.org/10.1016/j.jconrel.2016.06.040.
(105) Yang, Q.; Jacobs, T. M.; McCallen, J. D.; Moore, D. T.; Huckaby, J. T.; Edelstein, J. N.; Lai, S. K. Analysis of Pre-Existing IgG and IgM Antibodies against Polyethylene Glycol (PEG) in the General Population. *Anal Chem* **2016**, *88* (23), 11804–11812. https://doi.org/10.1021/acs.analchem.6b03437.
(106) Ju, Y.; Lee, W. S.; Kelly, H. G.; Pilkington, E. H.; Wragg, K. M.; Subbarao, K.;

Nguyen, T. H. O.; Rowntree, L. C.; Allen, L. F.; Bond, K.; Williamson, D. A.; Truong, N. P.; Plebanski, M.; Kedzierska, K.; Mahanty, S.; Caruso, F.; Wheatley, A. K.; Juno, J. A.; Kent, S. J. Anti-PEG Antibodies Boosted in Humans by SARS-CoV-2 Lipid Nanoparticle MRNA Vaccine. medRxiv January 10, 2022, p 2022.01.08.22268953. https://doi.org/10.1101/2022.01.08.22268953.

(107) Erdeljic Turk, V. Anaphylaxis Associated with the MRNA COVID-19 Vaccines: Approach to Allergy Investigation. *Clin Immunol* **2021**, *227*, 108748. https://doi.org/10.1016/j.clim.2021.108748.

(108) Sellaturay, P.; Nasser, S.; Ewan, P. Polyethylene Glycol–Induced Systemic Allergic Reactions (Anaphylaxis). *The Journal of Allergy and Clinical Immunology: In Practice* **2021**, *9* (2), 670–675. https://doi.org/10.1016/j.jaip.2020.09.029.

(109) Chen, B.-M.; Cheng, T.-L.; Roffler, S. R. Polyethylene Glycol Immunogenicity: Theoretical, Clinical, and Practical Aspects of Anti-Polyethylene Glycol Antibodies. *ACS Nano* **2021**, *15* (9), 14022–14048. https://doi.org/10.1021/acsnano.1c05922.

(110) Chang, C.-J.; Chen, C.-H.; Chen, B.-M.; Su, Y.-C.; Chen, Y.-T.; Hershfield, M. S.; Lee, M.-T. M.; Cheng, T.-L.; Chen, Y.-T.; Roffler, S. R.; Wu, J.-Y. A Genome-Wide Association Study Identifies a Novel Susceptibility Locus for the Immunogenicity of Polyethylene Glycol. *Nat Commun* **2017**, *8* (1), 522. https://doi.org/10.1038/s41467-017-00622-4.

(111) Bigini, P.; Gobbi, M.; Bonati, M.; Clavenna, A.; Zucchetti, M.; Garattini, S.; Pasut, G. The Role and Impact of Polyethylene Glycol on Anaphylactic Reactions to COVID-19 Nano-Vaccines. *Nat. Nanotechnol.* **2021**, 1–3. https://doi.org/10.1038/s41565-021-01001-3.

(112) DeAngelis, P. L. Heparosan, a Promising 'Naturally Good' Polymeric Conjugating Vehicle for Delivery of Injectable Therapeutics. *Expert Opinion on Drug Delivery* **2015**, *12* (3), 349–352. https://doi.org/10.1517/17425247.2015.978282.

(113) Chen, E.; Chen, B.-M.; Su, Y.-C.; Chang, Y.-C.; Cheng, T.-L.; Barenholz, Y.; Roffler, S. R. Premature Drug Release from Polyethylene Glycol (PEG)-Coated Liposomal Doxorubicin *via* Formation of the Membrane Attack Complex. *ACS Nano* **2020**, acsnano.9b07218. https://doi.org/10.1021/acsnano.9b07218.

(114) Yang, Q.; Lai, S. K. Anti-PEG Immunity: Emergence, Characteristics, and Unaddressed Questions. *Wiley Interdisciplinary Reviews: Nanomedicine and Nanobiotechnology* **2015**, *7* (5), 655–677. https://doi.org/10.1002/wnan.1339.

(115) Abu Lila, A. S.; Kiwada, H.; Ishida, T. The Accelerated Blood Clearance (ABC) Phenomenon: Clinical Challenge and Approaches to Manage. *J Control Release* **2013**, *172* (1), 38–47. https://doi.org/10.1016/j.jconrel.2013.07.026.

(116) Afantitis, A.; Melagraki, G.; Isigonis, P.; Tsoumanis, A.; Danai Varsou, D.; Valsami-Jones, E.; Papadiamantis, A.; Ellis, L.-Jayne. A.; Sarimveis, H.; Doganis, P.; Karatzas, P.; Tsiros, P.; Liampa, I.; Lobaskin, V.; Greco, D.; Serra, A.; Anneli Sofia Kinaret, P.; Aliisa Saarimäki, L.; Grafström, R.; Kohonen, P.; Nymark, P.; Willighagen, E.; Puzyn, T.; Rybinska-Fryca, A.; Lyubartsev, A.; Alstrup Jensen, K.; Gerit Brandenburg, J.; Lofts, S.; Svendsen, C.; Harrison, S.; Maier, D.; Tamm, K.; Jänes, J.; Sikk, L.; Dusinska, M.; Longhin, E.; Rundén-Pran, E.; Mariussen, E.; El Yamani, N.; Unger, W.; Radnik, J.; Tropsha, A.; Cohen, Y.; Leszczynski, J.; Ogilvie Hendren, C.; Wiesner, M.; Winkler, D.; Suzuki, N.; Hyun Yoon, T.; Choi, J.-S.; Sanabria, N.; Gulumian, M.; Lynch, I. NanoSolveIT Project: Driving Nanoinformatics Research to Develop Innovative and Integrated Tools for in Silico Nanosafety Assessment. *Computational and Structural Biotechnology Journal* **2020**. https://doi.org/10.1016/j.csbj.2020.02.023.

(117) Furxhi, I.; Murphy, F.; Mullins, M.; Poland, C. A. Machine Learning Prediction of

Nanoparticle in Vitro Toxicity: A Comparative Study of Classifiers and Ensemble-Classifiers Using the Copeland Index. *Toxicology Letters* **2019**, *312*, 157–166. https://doi.org/10.1016/j.toxlet.2019.05.016.

(118) Oh, E.; Liu, R.; Nel, A.; Gemill, K. B.; Bilal, M.; Cohen, Y.; Medintz, I. L. Meta-Analysis of Cellular Toxicity for Cadmium-Containing Quantum Dots. *Nat Nanotechnol* **2016**, *11* (5), 479–486. https://doi.org/10.1038/nnano.2015.338.

(119) Kolanjiyil, A. V.; Kleinstreuer, C.; Kleinstreuer, N. C.; Pham, W.; Sadikot, R. T. Mice-to-Men Comparison of Inhaled Drug-Aerosol Deposition and Clearance. *Respiratory Physiology & Neurobiology* **2019**, *260*, 82–94. https://doi.org/10.1016/j.resp.2018.11.003.

(120) Ha, M. K.; Trinh, T. X.; Choi, J. S.; Maulina, D.; Byun, H. G.; Yoon, T. H. Toxicity Classification of Oxide Nanomaterials: Effects of Data Gap Filling and PChem Score-Based Screening Approaches. *Scientific Reports* **2018**, *8* (1), 1–11. https://doi.org/10.1038/s41598-018-21431-9.

(121) Leong, H. S.; Butler, K. S.; Brinker, C. J.; Azzawi, M.; Conlan, S.; Dufés, C.; Owen, A.; Rannard, S.; Scott, C.; Chen, C.; Dobrovolskaia, M. A.; Kozlov, S. V.; Prina-Mello, A.; Schmid, R.; Wick, P.; Caputo, F.; Boisseau, P.; Crist, R. M.; McNeil, S. E.; Fadeel, B.; Tran, L.; Hansen, S. F.; Hartmann, N. B.; Clausen, L. P. W.; Skjolding, L. M.; Baun, A.; Ågerstrand, M.; Gu, Z.; Lamprou, D. A.; Hoskins, C.; Huang, L.; Song, W.; Cao, H.; Liu, X.; Jandt, K. D.; Jiang, W.; Kim, B. Y. S.; Wheeler, K. E.; Chetwynd, A. J.; Lynch, I.; Moghimi, S. M.; Nel, A.; Xia, T.; Weiss, P. S.; Sarmento, B.; das Neves, J.; Santos, H. A.; Santos, L.; Mitragotri, S.; Little, S.; Peer, D.; Amiji, M. M.; Alonso, M. J.; Petri-Fink, A.; Balog, S.; Lee, A.; Drasler, B.; Rothen-Rutishauser, B.; Wilhelm, S.; Acar, H.; Harrison, R. G.; Mao, C.; Mukherjee, P.; Ramesh, R.; McNally, L. R.; Busatto, S.; Wolfram, J.; Bergese, P.; Ferrari, M.; Fang, R. H.; Zhang, L.; Zheng, J.; Peng, C.; Du, B.; Yu, M.; Charron, D. M.; Zheng, G.; Pastore, C. On the Issue of Transparency and Reproducibility in Nanomedicine. *Nature Nanotechnology* **2019**, *14* (7), 629–635. https://doi.org/10.1038/s41565-019-0496-9.

(122) Hussain, S. M.; Hess, K. L.; Gearhart, J. M.; Geiss, K. T.; Schlager, J. J. In Vitro Toxicity of Nanoparticles in BRL 3A Rat Liver Cells. *Toxicol In Vitro* **2005**, *19* (7), 975–983. https://doi.org/10.1016/j.tiv.2005.06.034.

(123) Lee, J.; Lilly, G. D.; Doty, R. C.; Podsiadlo, P.; Kotov, N. A. In Vitro Toxicity Testing of Nanoparticles in 3D Cell Culture. *Small* **2009**, *5* (10), 1213–1221. https://doi.org/10.1002/smll.200801788.

(124) Kumar, G.; Degheidy, H.; Casey, B. J.; Goering, P. L. Flow Cytometry Evaluation of in Vitro Cellular Necrosis and Apoptosis Induced by Silver Nanoparticles. *Food and Chemical Toxicology* **2015**, *85*, 45–51. https://doi.org/10.1016/j.fct.2015.06.012.

(125) Lewinski, N.; Colvin, V.; Drezek, R. Cytotoxicity of Nanoparticles. *Small* **2008**, *4* (1), 26–49. https://doi.org/10.1002/smll.200700595.

(126) Trouiller, B.; Reliene, R.; Westbrook, A.; Solaimani, P.; Schiestl, R. H. Titanium Dioxide Nanoparticles Induce DNA Damage and Genetic Instability In Vivo in Mice. *Cancer Research* **2009**, *69* (22), 8784–8789. https://doi.org/10.1158/0008-5472.CAN-09-2496.

(127) Evans, B. C.; Nelson, C. E.; Yu, S. S.; Beavers, K. R.; Kim, A. J.; Li, H.; Nelson, H. M.; Giorgio, T. D.; Duvall, C. L. Ex Vivo Red Blood Cell Hemolysis Assay for the Evaluation of PH-Responsive Endosomolytic Agents for Cytosolic Delivery of Biomacromolecular Drugs. *J Vis Exp* **2013**, No. 73. https://doi.org/10.3791/50166.

(128) Elsabahy, M.; Wooley, K. L. Cytokines as Biomarkers of Nanoparticle Immunotoxicity. *Chem Soc Rev* **2013**, *42* (12), 5552–5576.

https://doi.org/10.1039/c3cs60064e.
(129) Kirchner, C.; Liedl, T.; Kudera, S.; Pellegrino, T.; Muñoz Javier, A.; Gaub, H. E.; Stölzle, S.; Fertig, N.; Parak, W. J. Cytotoxicity of Colloidal CdSe and CdSe/ZnS Nanoparticles. *Nano Lett.* **2005**, *5* (2), 331–338. https://doi.org/10.1021/nl047996m.
(130) Wörle-Knirsch, J. M.; Pulskamp, K.; Krug, H. F. Oops They Did It Again! Carbon Nanotubes Hoax Scientists in Viability Assays. *Nano Lett.* **2006**, *6* (6), 1261–1268. https://doi.org/10.1021/nl060177c.
(131) Lynch, I.; Dawson, K. A.; Linse, S. Detecting Cryptic Epitopes Created by Nanoparticles. *Sci. STKE* **2006**, *2006* (327), pe14–pe14. https://doi.org/10.1126/stke.3272006pe14.
(132) Zhao, J.; Riediker, M. Detecting the Oxidative Reactivity of Nanoparticles: A New Protocol for Reducing Artifacts. *J Nanopart Res* **2014**, *16* (7). https://doi.org/10.1007/s11051-014-2493-0.
(133) Balke, J.; Volz, P.; Neumann, F.; Brodwolf, R.; Wolf, A.; Pischon, H.; Radbruch, M.; Mundhenk, L.; Gruber, A. D.; Ma, N.; Alexiev, U. Visualizing Oxidative Cellular Stress Induced by Nanoparticles in the Subcytotoxic Range Using Fluorescence Lifetime Imaging. *Small* **2018**, *14* (23), e1800310. https://doi.org/10.1002/smll.201800310.
(134) Schrand, A. M.; Rahman, M. F.; Hussain, S. M.; Schlager, J. J.; Smith, D. A.; Syed, A. F. Metal-Based Nanoparticles and Their Toxicity Assessment. *WIREs Nanomedicine and Nanobiotechnology* **2010**, *2* (5), 544–568. https://doi.org/10.1002/wnan.103.
(135) Rajkumar, K. S.; Kanipandian, N.; Thirumurugan, R. Toxicity Assessment on Haemotology, Biochemical and Histopathological Alterations of Silver Nanoparticles-Exposed Freshwater Fish Labeo Rohita. *Appl Nanosci* **2016**, *6* (1), 19–29. https://doi.org/10.1007/s13204-015-0417-7.
(136) Yang, Y.; Qin, Z.; Zeng, W.; Yang, T.; Cao, Y.; Mei, C.; Kuang, Y. Toxicity Assessment of Nanoparticles in Various Systems and Organs. *Nanotechnology Reviews* **2017**, *6* (3), 279–289. https://doi.org/10.1515/ntrev-2016-0047.
(137) Hoshyar, N.; Gray, S.; Han, H.; Bao, G. The Effect of Nanoparticle Size on in Vivo Pharmacokinetics and Cellular Interaction. *Nanomedicine (Lond)* **2016**, *11* (6), 673–692. https://doi.org/10.2217/nnm.16.5.
(138) Bobo, D.; Robinson, K. J.; Islam, J.; Thurecht, K. J.; Corrie, S. R. Nanoparticle-Based Medicines: A Review of FDA-Approved Materials and Clinical Trials to Date. *Pharm. Res.* **2016**, *33* (10), 2373–2387. https://doi.org/10.1007/s11095-016-1958-5.
(139) Eftekhari, A.; Dizaj, S. M.; Chodari, L.; Sunar, S.; Hasanzadeh, A.; Ahmadian, E.; Hasanzadeh, M. The Promising Future of Nano-Antioxidant Therapy against Environmental Pollutants Induced-Toxicities. *Biomedicine & Pharmacotherapy* **2018**, *103*, 1018–1027. https://doi.org/10.1016/j.biopha.2018.04.126.
(140) Buchman, J. T.; Hudson-Smith, N. V.; Landy, K. M.; Haynes, C. L. Understanding Nanoparticle Toxicity Mechanisms To Inform Redesign Strategies To Reduce Environmental Impact. *Acc. Chem. Res.* **2019**, *52* (6), 1632–1642. https://doi.org/10.1021/acs.accounts.9b00053.
(141) Wilhelm, S.; Kaiser, M.; Würth, C.; Heiland, J.; Carrillo-Carrion, C.; Muhr, V.; Wolfbeis, O. S.; Parak, W. J.; Resch-Genger, U.; Hirsch, T. Water Dispersible Upconverting Nanoparticles: Effects of Surface Modification on Their Luminescence and Colloidal Stability. *Nanoscale* **2015**, *7* (4), 1403–1410. https://doi.org/10.1039/C4NR05954A.
(142) Wilhelm, S. Perspectives for Upconverting Nanoparticles. *ACS Nano* **2017**, *11* (11), 10644–10653. https://doi.org/10.1021/acsnano.7b07120.
(143) Rao, L.; Meng, Q.-F.; Bu, L.-L.; Cai, B.; Huang, Q.; Sun, Z.-J.; Zhang, W.-F.; Li, A.;

Guo, S.-S.; Liu, W.; Wang, T.-H.; Zhao, X.-Z. Erythrocyte Membrane-Coated Upconversion Nanoparticles with Minimal Protein Adsorption for Enhanced Tumor Imaging. *ACS Appl. Mater. Interfaces* **2017**, *9* (3), 2159–2168. https://doi.org/10.1021/acsami.6b14450.

(144) Dolez, P. I.; Bodila, N.; Lara, J.; Truchon, G. Personal Protective Equipment against Nanoparticles. *International Journal of Nanotechnology* **2009**, *7* (1), 99–117. https://doi.org/10.1504/IJNT.2010.02955.

(145) The Risks of Nanomaterial Risk Assessment. *Nature Nanotechnology* **2020**, 1–1. https://doi.org/10.1038/s41565-020-0658-9.

(146) Hansen, S. F.; Lennquist, A. Carbon Nanotubes Added to the SIN List as a Nanomaterial of Very High Concern. *Nature Nanotechnology* **2020**, *15* (1), 3–4. https://doi.org/10.1038/s41565-019-0613-9.

(147) Fadeel, B.; Kostarelos, K. Grouping All Carbon Nanotubes into a Single Substance Category Is Scientifically Unjustified. *Nature Nanotechnology* **2020**, *15* (3), 164–164. https://doi.org/10.1038/s41565-020-0654-0.

(148) Heller, D. A.; Jena, P. V.; Pasquali, M.; Kostarelos, K.; Delogu, L. G.; Meidl, R. E.; Rotkin, S. V.; Scheinberg, D. A.; Schwartz, R. E.; Terrones, M.; Wang, Y.; Bianco, A.; Boghossian, A. A.; Cambré, S.; Cognet, L.; Corrie, S. R.; Demokritou, P.; Giordani, S.; Hertel, T.; Ignatova, T.; Islam, M. F.; Iverson, N. M.; Jagota, A.; Janas, D.; Kono, J.; Kruss, S.; Landry, M. P.; Li, Y.; Martel, R.; Maruyama, S.; Naumov, A. V.; Prato, M.; Quinn, S. J.; Roxbury, D.; Strano, M. S.; Tour, J. M.; Weisman, R. B.; Wenseleers, W.; Yudasaka, M. Banning Carbon Nanotubes Would Be Scientifically Unjustified and Damaging to Innovation. *Nature Nanotechnology* **2020**, 1–3. https://doi.org/10.1038/s41565-020-0656-y.

(149) Shatkin, J. A. The Future in Nanosafety. *Nano Lett.* **2020**, *20* (3), 1479–1480. https://doi.org/10.1021/acs.nanolett.0c00432.

(150) Fadeel, B. The Right Stuff: On the Future of Nanotoxicology. *Front. Toxicol.* **2019**, *1*. https://doi.org/10.3389/ftox.2019.00001.

(151) Faria, M.; Björnmalm, M.; Thurecht, K. J.; Kent, S. J.; Parton, R. G.; Kavallaris, M.; Johnston, A. P. R.; Gooding, J. J.; Corrie, S. R.; Boyd, B. J.; Thordarson, P.; Whittaker, A. K.; Stevens, M. M.; Prestidge, C. A.; Porter, C. J. H.; Parak, W. J.; Davis, T. P.; Crampin, E. J.; Caruso, F. Minimum Information Reporting in Bio–Nano Experimental Literature. *Nature Nanotechnology* **2018**, *13* (9), 777–785. https://doi.org/10.1038/s41565-018-0246-4.

(152) Nel, A.; Xia, T.; Meng, H.; Wang, X.; Lin, S.; Ji, Z.; Zhang, H. Nanomaterial Toxicity Testing in the 21st Century: Use of a Predictive Toxicological Approach and High-Throughput Screening. *Acc. Chem. Res.* **2013**, *46* (3), 607–621. https://doi.org/10.1021/ar300022h.

(153) Watson, C.; Ge, J.; Cohen, J.; Pyrgiotakis, G.; Engelward, B. P.; Demokritou, P. High-Throughput Screening Platform for Engineered Nanoparticle-Mediated Genotoxicity Using CometChip Technology. *ACS Nano* **2014**, *8* (3), 2118–2133. https://doi.org/10.1021/nn404871p.

(154) De Simone, U.; Roccio, M.; Gribaldo, L.; Spinillo, A.; Caloni, F.; Coccini, T. Human 3D Cultures as Models for Evaluating Magnetic Nanoparticle CNS Cytotoxicity after Short- and Repeated Long-Term Exposure. *Int J Mol Sci* **2018**, *19* (7). https://doi.org/10.3390/ijms19071993.

(155) Steger-Hartmann, T.; Raschke, M. Translating in Vitro to in Vivo and Animal to Human. *Current Opinion in Toxicology* **2020**, *23–24*, 6–10. https://doi.org/10.1016/j.cotox.2020.02.003.

(156) Zink, D.; Chuah, J. K. C.; Ying, J. Y. Assessing Toxicity with Human Cell-Based In

Vitro Methods. *Trends in Molecular Medicine* **2020**. https://doi.org/10.1016/j.molmed.2020.01.008.
(157) Sindhwani, S.; Syed, A. M.; Wilhelm, S.; Glancy, D. R.; Chen, Y. Y.; Dobosz, M.; Chan, W. C. W. Three-Dimensional Optical Mapping of Nanoparticle Distribution in Intact Tissues. *ACS Nano* **2016**, *10* (5), 5468–5478. https://doi.org/10.1021/acsnano.6b01879.
(158) Sindhwani, S.; Syed, A. M.; Wilhelm, S.; Chan, W. C. W. Exploring Passive Clearing for 3D Optical Imaging of Nanoparticles in Intact Tissues. *Bioconjugate Chem.* **2017**, *28* (1), 253–259. https://doi.org/10.1021/acs.bioconjchem.6b00500.
(159) Syed, A. M.; Sindhwani, S.; Wilhelm, S.; Kingston, B. R.; Lee, D. S. W.; Gommerman, J. L.; Chan, W. C. W. Three-Dimensional Imaging of Transparent Tissues via Metal Nanoparticle Labeling. *J. Am. Chem. Soc.* **2017**, *139* (29), 9961–9971. https://doi.org/10.1021/jacs.7b04022.
(160) Syed, A. M.; MacMillan, P.; Ngai, J.; Wilhelm, S.; Sindhwani, S.; Kingston, B. R.; Wu, J. L. Y.; Llano-Suárez, P.; Lin, Z. P.; Ouyang, B.; Kahiel, Z.; Gadde, S.; Chan, W. C. W. Liposome Imaging in Optically Cleared Tissues. *Nano Lett.* **2020**, *20* (2), 1362–1369. https://doi.org/10.1021/acs.nanolett.9b04853.
(161) Merrifield, R. C.; Stephan, C.; Lead, J. R. Quantification of Au Nanoparticle Biouptake and Distribution to Freshwater Algae Using Single Cell – ICP-MS. *Environ. Sci. Technol.* **2018**, *52* (4), 2271–2277. https://doi.org/10.1021/acs.est.7b04968.
(162) Fang, R. H.; Kroll, A. V.; Gao, W.; Zhang, L. Cell Membrane Coating Nanotechnology. *Adv. Mater. Weinheim* **2018**, *30* (23), e1706759. https://doi.org/10.1002/adma.201706759.
(163) Golabchi, A.; Wu, B.; Cao, B.; Bettinger, C. J.; Cui, X. T. Zwitterionic Polymer/Polydopamine Coating Reduce Acute Inflammatory Tissue Responses to Neural Implants. *Biomaterials* **2019**, *225*, 119519. https://doi.org/10.1016/j.biomaterials.2019.119519.
(164) Lazarovits, J.; Chen, Y. Y.; Song, F.; Ngo, W.; Tavares, A. J.; Zhang, Y.-N.; Audet, J.; Tang, B.; Lin, Q.; Tleugabulova, M. C.; Wilhelm, S.; Krieger, J. R.; Mallevaey, T.; Chan, W. C. W. Synthesis of Patient-Specific Nanomaterials. *Nano Lett.* **2019**, *19* (1), 116–123. https://doi.org/10.1021/acs.nanolett.8b03434.
(165) Sang, W.; Zhang, Z.; Dai, Y.; Chen, X. Recent Advances in Nanomaterial-Based Synergistic Combination Cancer Immunotherapy. *Chem Soc Rev* **2019**, *48* (14), 3771–3810. https://doi.org/10.1039/c8cs00896e.
(166) Suk, J. S.; Xu, Q.; Kim, N.; Hanes, J.; Ensign, L. M. PEGylation as a Strategy for Improving Nanoparticle-Based Drug and Gene Delivery. *Adv. Drug Deliv. Rev.* **2016**, *99* (Pt A), 28–51. https://doi.org/10.1016/j.addr.2015.09.012.
(167) Salata, O. Applications of Nanoparticles in Biology and Medicine. *Journal of Nanobiotechnology* **2004**, *2* (1), 3. https://doi.org/10.1186/1477-3155-2-3.
(168) Walkey, C. D.; Chan, W. C. W. Understanding and Controlling the Interaction of Nanomaterials with Proteins in a Physiological Environment. *Chem Soc Rev* **2012**, *41* (7), 2780–2799. https://doi.org/10.1039/c1cs15233e.
(169) Cai, R.; Chen, C. The Crown and the Scepter: Roles of the Protein Corona in Nanomedicine. *Adv. Mater. Weinheim* **2019**, *31* (45), e1805740. https://doi.org/10.1002/adma.201805740.
(170) Aggarwal, P.; Hall, J. B.; McLeland, C. B.; Dobrovolskaia, M. A.; McNeil, S. E. Nanoparticle Interaction with Plasma Proteins as It Relates to Particle Biodistribution, Biocompatibility and Therapeutic Efficacy. *Adv Drug Deliv Rev* **2009**, *61* (6), 428–437. https://doi.org/10.1016/j.addr.2009.03.009.

(171) Monopoli, M. P.; Aberg, C.; Salvati, A.; Dawson, K. A. Biomolecular Coronas Provide the Biological Identity of Nanosized Materials. *Nat Nanotechnol* **2012**, *7* (12), 779–786. https://doi.org/10.1038/nnano.2012.207.
(172) Veronese, F. M.; Pasut, G. PEGylation, Successful Approach to Drug Delivery. *Drug Discovery Today* **2005**, *10* (21), 1451–1458. https://doi.org/10.1016/S1359-6446(05)03575-0.
(173) Larson, T. A.; Joshi, P. P.; Sokolov, K. Preventing Protein Adsorption and Macrophage Uptake of Gold Nanoparticles via a Hydrophobic Shield. *ACS Nano* **2012**, *6* (10), 9182–9190. https://doi.org/10.1021/nn3035155.
(174) Chen, L.; Hong, W.; Ren, W.; Xu, T.; Qian, Z.; He, Z. Recent Progress in Targeted Delivery Vectors Based on Biomimetic Nanoparticles. *Sig Transduct Target Ther* **2021**, *6* (1), 1–25. https://doi.org/10.1038/s41392-021-00631-2.
(175) Banda, N. K.; Mehta, G.; Chao, Y.; Wang, G.; Inturi, S.; Fossati-Jimack, L.; Botto, M.; Wu, L.; Moghimi, S. M.; Simberg, D. Mechanisms of Complement Activation by Dextran-Coated Superparamagnetic Iron Oxide (SPIO) Nanoworms in Mouse versus Human Serum. *Particle and Fibre Toxicology* **2014**, *11* (1), 64. https://doi.org/10.1186/s12989-014-0064-2.
(176) Yang, W.; Wang, L.; Mettenbrink, E. M.; DeAngelis, P. L.; Wilhelm, S. Nanoparticle Toxicology. *Annu. Rev. Pharmacol. Toxicol.* **2021**, *61* (1), 269–289. https://doi.org/10.1146/annurev-pharmtox-032320-110338.
(177) Fang, J.-L.; Beland, F. A.; Tang, Y.; Roffler, S. R. Flow Cytometry Analysis of Anti-Polyethylene Glycol Antibodies in Human Plasma. *Toxicology Reports* **2021**, *8*, 148–154. https://doi.org/10.1016/j.toxrep.2020.12.022.
(178) Sellaturay, P.; Nasser, S.; Islam, S.; Gurugama, P.; Ewan, P. W. Polyethylene Glycol (PEG) Is a Cause of Anaphylaxis to the Pfizer/BioNTech MRNA COVID-19 Vaccine. *Clinical & Experimental Allergy* **2021**, *51* (6), 861–863. https://doi.org/10.1111/cea.13874.
(179) Troelnikov, A.; Perkins, G.; Yuson, C.; Ahamdie, A.; Balouch, S.; Hurtado, P. R.; Hissaria, P. Basophil Reactivity to BNT162b2 Is Mediated by PEGylated Lipid Nanoparticles in Patients with PEG Allergy. *Journal of Allergy and Clinical Immunology* **2021**, *148* (1), 91–95. https://doi.org/10.1016/j.jaci.2021.04.032.
(180) Shimabukuro, T. T.; Cole, M.; Su, J. R. Reports of Anaphylaxis After Receipt of MRNA COVID-19 Vaccines in the US—December 14, 2020-January 18, 2021. *JAMA* **2021**, *325* (11), 1101–1102. https://doi.org/10.1001/jama.2021.1967.
(181) Nogueira, S. S.; Schlegel, A.; Maxeiner, K.; Weber, B.; Barz, M.; Schroer, M. A.; Blanchet, C. E.; Svergun, D. I.; Ramishetti, S.; Peer, D.; Langguth, P.; Sahin, U.; Haas, H. Polysarcosine-Functionalized Lipid Nanoparticles for Therapeutic MRNA Delivery. *ACS Appl. Nano Mater.* **2020**, *3* (11), 10634–10645. https://doi.org/10.1021/acsanm.0c01834.
(182) Rippe, M.; Stefanello, T. F.; Kaplum, V.; Britta, E. A.; Garcia, F. P.; Poirot, R.; Companhoni, M. V. P.; Nakamura, C. V.; Szarpak-Jankowska, A.; Auzély-Velty, R. Heparosan as a Potential Alternative to Hyaluronic Acid for the Design of Biopolymer-Based Nanovectors for Anticancer Therapy. *Biomater. Sci.* **2019**, *7* (7), 2850–2860. https://doi.org/10.1039/C9BM00443B.
(183) Wang, Z.; Dordick, J. S.; Linhardt, R. J. Escherichia Coli K5 Heparosan Fermentation and Improvement by Genetic Engineering. *Bioeng Bugs* **2011**, *2* (1), 63–67. https://doi.org/10.4161/bbug.2.1.14201.
(184) Lane, R. S.; Haller, F. M.; Chavaroche, A. A. E.; Almond, A.; DeAngelis, P. L. Heparosan-Coated Liposomes for Drug Delivery. *Glycobiology* **2017**, *27* (11), 1062–1074. https://doi.org/10.1093/glycob/cwx070.

(185) Qiu, L.; Shan, X.; Long, M.; Ahmed, K. S.; Zhao, L.; Mao, J.; Zhang, H.; Sun, C.; You, C.; Lv, G.; Chen, J. Elucidation of Cellular Uptake and Intracellular Trafficking of Heparosan Polysaccharide-Based Micelles in Various Cancer Cells. *International Journal of Biological Macromolecules* **2019**, *130*, 755–764. https://doi.org/10.1016/j.ijbiomac.2019.02.133.
(186) Chen, J.-X.; Zhang, M.; Liu, W.; Lu, G.-Z.; Chen, J.-H. Construction of Serum Resistant Micelles Based on Heparosan for Targeted Cancer Therapy. *Carbohydrate Polymers* **2014**, *110*, 135–141. https://doi.org/10.1016/j.carbpol.2014.03.084.
(187) Chen, J.-X.; Liu, W.; Zhang, M.; Chen, J.-H. Heparosan Based Negatively Charged Nanocarrier for Rapid Intracellular Drug Delivery. *International Journal of Pharmaceutics* **2014**, *473* (1), 493–500. https://doi.org/10.1016/j.ijpharm.2014.07.045.
(188) Turkevich, J.; Stevenson, P. C.; Hillier, J. A Study of the Nucleation and Growth Processes in the Synthesis of Colloidal Gold. *Discuss. Faraday Soc.* **1951**, *11* (0), 55–75. https://doi.org/10.1039/DF9511100055.
(189) Perrault, S. D.; Chan, W. C. W. Synthesis and Surface Modification of Highly Monodispersed, Spherical Gold Nanoparticles of 50−200 Nm. *J. Am. Chem. Soc.* **2009**, *131* (47), 17042–17043. https://doi.org/10.1021/ja907069u.
(190) Bastús, N. G.; Merkoçi, F.; Piella, J.; Puntes, V. Synthesis of Highly Monodisperse Citrate-Stabilized Silver Nanoparticles of up to 200 Nm: Kinetic Control and Catalytic Properties. *Chem. Mater.* **2014**, *26* (9), 2836–2846. https://doi.org/10.1021/cm500316k.
(191) Lane, R. S.; Haller, F. M.; Chavaroche, A. A. E.; Almond, A.; DeAngelis, P. L. Heparosan-Coated Liposomes for Drug Delivery. *Glycobiology* **2017**, *27* (11), 1062–1074. https://doi.org/10.1093/glycob/cwx070.
(192) Bitter, T.; Muir, H. M. A Modified Uronic Acid Carbazole Reaction. *Analytical Biochemistry* **1962**, *4* (4), 330–334. https://doi.org/10.1016/0003-2697(62)90095-7.
(193) Sismey-Ragatz, A. E.; Green, D. E.; Otto, N. J.; Rejzek, M.; Field, R. A.; DeAngelis, P. L. Chemoenzymatic Synthesis with Distinct Pasteurella Heparosan Synthases: Monodisperse Polymers and Unnatural Structures. *J. Biol. Chem.* **2007**, *282* (39), 28321–28327. https://doi.org/10.1074/jbc.M701599200.
(194) Lee, J. C.; Donahue, N. D.; Mao, A. S.; Karim, A.; Komarneni, M.; Thomas, E. E.; Francek, E. R.; Yang, W.; Wilhelm, S. Exploring Maleimide-Based Nanoparticle Surface Engineering to Control Cellular Interactions. *ACS Appl. Nano Mater.* **2020**, *3* (3), 2421–2429. https://doi.org/10.1021/acsanm.9b02541.
(195) Hurst, S. J.; Lytton-Jean, A. K. R.; Mirkin, C. A. Maximizing DNA Loading on a Range of Gold Nanoparticle Sizes. *Anal. Chem.* **2006**, *78* (24), 8313–8318. https://doi.org/10.1021/ac0613582.
(196) Zhang, X.; Servos, M. R.; Liu, J. Instantaneous and Quantitative Functionalization of Gold Nanoparticles with Thiolated DNA Using a PH-Assisted and Surfactant-Free Route. *J. Am. Chem. Soc.* **2012**, *134* (17), 7266–7269. https://doi.org/10.1021/ja3014055.
(197) Liu, L. Y.; Ma, X.-Z.; Ouyang, B.; Ings, D. P.; Marwah, S.; Liu, J.; Chen, A. Y.; Gupta, R.; Manuel, J.; Chen, X.-C.; Gage, B. K.; Cirlan, I.; Khuu, N.; Chung, S.; Camat, D.; Cheng, M.; Sekhon, M.; Zagorovsky, K.; Abdou Mohamed, M. A.; Thoeni, C.; Atif, J.; Echeverri, J.; Kollmann, D.; Fischer, S.; Bader, G. D.; Chan, W. C. W.; Michalak, T. I.; McGilvray, I. D.; MacParland, S. A. Nanoparticle Uptake in a Spontaneous and Immunocompetent Woodchuck Liver Cancer Model. *ACS Nano* **2020**, *14* (4), 4698–4715. https://doi.org/10.1021/acsnano.0c00468.
(198) Schneider, C. A.; Rasband, W. S.; Eliceiri, K. W. NIH Image to ImageJ: 25 Years of Image Analysis. *Nat. Methods* **2012**, *9* (7), 671–675.

https://doi.org/10.1038/nmeth.2089.
(199) Walkey, C. D.; Olsen, J. B.; Song, F.; Liu, R.; Guo, H.; Olsen, D. W. H.; Cohen, Y.; Emili, A.; Chan, W. C. W. Protein Corona Fingerprinting Predicts the Cellular Interaction of Gold and Silver Nanoparticles. *ACS Nano* **2014**, *8* (3), 2439–2455. https://doi.org/10.1021/nn406018q.
(200) Walkey, C. D.; Olsen, J. B.; Guo, H.; Emili, A.; Chan, W. C. W. Nanoparticle Size and Surface Chemistry Determine Serum Protein Adsorption and Macrophage Uptake. *Journal of the American Chemical Society* **2012**, *134* (4), 2139–2147. https://doi.org/10.1021/ja2084338.
(201) Fang, M.; Wang, Z.; Cupp-Sutton, K. A.; Welborn, T.; Smith, K.; Wu, S. High-Throughput Hydrogen Deuterium Exchange Mass Spectrometry (HDX-MS) Coupled with Subzero-Temperature Ultrahigh Pressure Liquid Chromatography (UPLC) Separation for Complex Sample Analysis. *Analytica Chimica Acta* **2021**, *1143*, 65–72. https://doi.org/10.1016/j.aca.2020.11.022.
(202) Kim, S.; Pevzner, P. A. MS-GF+ Makes Progress towards a Universal Database Search Tool for Proteomics. *Nature Communications* **2014**, *5* (1), 5277. https://doi.org/10.1038/ncomms6277.
(203) Griffin, N. M.; Yu, J.; Long, F.; Oh, P.; Shore, S.; Li, Y.; Koziol, J. A.; Schnitzer, J. E. Label-Free, Normalized Quantification of Complex Mass Spectrometry Data for Proteomic Analysis. *Nat Biotechnol* **2010**, *28* (1), 83–89. https://doi.org/10.1038/nbt.1592.
(204) Hossen, Md. N.; Rao, G.; Dey, A.; Robertson, J. D.; Bhattacharya, R.; Mukherjee, P. Gold Nanoparticle Transforms Activated Cancer-Associated Fibroblasts to Quiescence. *ACS Appl. Mater. Interfaces* **2019**, *11* (29), 26060–26068. https://doi.org/10.1021/acsami.9b03313.
(205) Huang, H.; Lai, W.; Cui, M.; Liang, L.; Lin, Y.; Fang, Q.; Liu, Y.; Xie, L. An Evaluation of Blood Compatibility of Silver Nanoparticles. *Scientific Reports* **2016**, *6* (1), 25518. https://doi.org/10.1038/srep25518.
(206) Dobrovolskaia, M. A.; Clogston, J. D.; Neun, B. W.; Hall, J. B.; Patri, A. K.; McNeil, S. E. Method for Analysis of Nanoparticle Hemolytic Properties in Vitro. *Nano Lett.* **2008**, *8* (8), 2180–2187. https://doi.org/10.1021/nl0805615.
(207) Wang, F.; Chen, B.; Yan, B.; Yin, Y.; Hu, L.; Liang, Y.; Song, M.; Jiang, G. Scattered Light Imaging Enables Real-Time Monitoring of Label-Free Nanoparticles and Fluorescent Biomolecules in Live Cells. *J. Am. Chem. Soc.* **2019**, *141* (36), 14043–14047. https://doi.org/10.1021/jacs.9b05894.
(208) Xu, Q.; Lou, X.; Wang, L.; Ding, X.; Yu, H.; Xiao, Y. Rapid, Surfactant-Free, and Quantitative Functionalization of Gold Nanoparticles with Thiolated DNA under Physiological PH and Its Application in Molecular Beacon-Based Biosensor. *ACS Appl. Mater. Interfaces* **2016**, *8* (40), 27298–27304. https://doi.org/10.1021/acsami.6b08350.
(209) Schöttler, S.; Becker, G.; Winzen, S.; Steinbach, T.; Mohr, K.; Landfester, K.; Mailänder, V.; Wurm, F. R. Protein Adsorption Is Required for Stealth Effect of Poly(Ethylene Glycol)- and Poly(Phosphoester)-Coated Nanocarriers. *Nature Nanotechnology* **2016**, *11* (4), 372–377. https://doi.org/10.1038/nnano.2015.330.
(210) Bernhard, C.; Bauer, K. N.; Bonn, M.; Wurm, F. R.; Gonella, G. Interfacial Conformation of Hydrophilic Polyphosphoesters Affects Blood Protein Adsorption. *ACS Appl. Mater. Interfaces* **2019**, *11* (1), 1624–1629. https://doi.org/10.1021/acsami.8b17146.
(211) Walkey, C. D.; Olsen, J. B.; Guo, H.; Emili, A.; Chan, W. C. W. Nanoparticle Size and Surface Chemistry Determine Serum Protein Adsorption and Macrophage Uptake.

J. Am. Chem. Soc. **2012**, *134* (4), 2139–2147. https://doi.org/10.1021/ja2084338.
(212) Xu, Q.; Ensign, L. M.; Boylan, N. J.; Schön, A.; Gong, X.; Yang, J.-C.; Lamb, N. W.; Cai, S.; Yu, T.; Freire, E.; Hanes, J. Impact of Surface Polyethylene Glycol (PEG) Density on Biodegradable Nanoparticle Transport in Mucus Ex Vivo and Distribution in Vivo. *ACS Nano* **2015**, *9* (9), 9217–9227. https://doi.org/10.1021/acsnano.5b03876.
(213) Donahue, N. D.; Kanapilly, S.; Stephan, C.; Marlin, M. C.; Francek, E. R.; Haddad, M.; Guthridge, J.; Wilhelm, S. Quantifying Chemical Composition and Reaction Kinetics of Individual Colloidally Dispersed Nanoparticles. *Nano Lett.* **2022**, *22* (1), 294–301. https://doi.org/10.1021/acs.nanolett.1c03752.
(214) Hossen, M. N.; Wang, L.; Chinthalapally, H. R.; Robertson, J. D.; Fung, K.-M.; Wilhelm, S.; Bieniasz, M.; Bhattacharya, R.; Mukherjee, P. Switching the Intracellular Pathway and Enhancing the Therapeutic Efficacy of Small Interfering RNA by Auroliposome. *Science Advances* **2020**. https://doi.org/10.1126/sciadv.aba5379.
(215) Sheth, V.; Wang, L.; Bhattacharya, R.; Mukherjee, P.; Wilhelm, S. Strategies for Delivering Nanoparticles across Tumor Blood Vessels. *Advanced Functional Materials* **2021**, *31* (8), 2007363. https://doi.org/10.1002/adfm.202007363.
(216) Syed, A. M.; Sindhwani, S.; Wilhelm, S.; Kingston, B. R.; Lee, D. S. W.; Gommerman, J. L.; Chan, W. C. W. Three-Dimensional Imaging of Transparent Tissues via Metal Nanoparticle Labeling. *J. Am. Chem. Soc.* **2017**, *139* (29), 9961–9971. https://doi.org/10.1021/jacs.7b04022.
(217) Zhang, Y.; Wu, J. L. Y.; Lazarovits, J.; Chan, W. C. W. An Analysis of the Binding Function and Structural Organization of the Protein Corona. *J. Am. Chem. Soc.* **2020**, *142* (19), 8827–8836. https://doi.org/10.1021/jacs.0c01853.
(218) Wilhelm, S.; Tavares, A. J.; Dai, Q.; Ohta, S.; Audet, J.; Dvorak, H. F.; Chan, W. C. W. Analysis of Nanoparticle Delivery to Tumours. *Nat Rev Mater* **2016**, *1* (5), 1–12. https://doi.org/10.1038/natrevmats.2016.14.
(219) Zhao, Z.; Ukidve, A.; Kim, J.; Mitragotri, S. Targeting Strategies for Tissue-Specific Drug Delivery. *Cell* **2020**, *181* (1), 151–167. https://doi.org/10.1016/j.cell.2020.02.001.
(220) Boraschi, D.; Italiani, P.; Palomba, R.; Decuzzi, P.; Duschl, A.; Fadeel, B.; Moghimi, S. M. Nanoparticles and Innate Immunity: New Perspectives on Host Defence. *Seminars in Immunology* **2017**, *34*, 33–51. https://doi.org/10.1016/j.smim.2017.08.013.
(221) Aroh, C.; Wang, Z.; Dobbs, N.; Luo, M.; Chen, Z.; Gao, J.; Yan, N. Innate Immune Activation by CGAMP-PC7A Nanoparticles Leads to Potent and Long-Acting Antiretroviral Response against HIV-1. *J Immunol* **2017**, *199* (11), 3840–3848. https://doi.org/10.4049/jimmunol.1700972.
(222) Liu, Y.; Hardie, J.; Zhang, X.; Rotello, V. M. Effects of Engineered Nanoparticles on the Innate Immune System. *Semin Immunol* **2017**, *34*, 25–32. https://doi.org/10.1016/j.smim.2017.09.011.
(223) La-Beck, N. M.; Gabizon, A. A. Nanoparticle Interactions with the Immune System: Clinical Implications for Liposome-Based Cancer Chemotherapy. *Frontiers in Immunology* **2017**, *8*.
(224) Donahue, N. D.; Acar, H.; Wilhelm, S. Concepts of Nanoparticle Cellular Uptake, Intracellular Trafficking, and Kinetics in Nanomedicine. *Advanced Drug Delivery Reviews* **2019**, *143*, 68–96. https://doi.org/10.1016/j.addr.2019.04.008.
(225) Beck, J. D.; Reidenbach, D.; Salomon, N.; Sahin, U.; Türeci, Ö.; Vormehr, M.; Kranz, L. M. MRNA Therapeutics in Cancer Immunotherapy. *Mol Cancer* **2021**, *20*, 69. https://doi.org/10.1186/s12943-021-01348-0.
(226) Yin, Q.; Yu, W.; Grzeskowiak, C. L.; Li, J.; Huang, H.; Guo, J.; Chen, L.; Wang, F.;

Zhao, F.; von Boehmer, L.; Metzner, T. J.; Leppert, J. T.; Chien, Y.-H.; Kuo, C. J.; Davis, M. M. Nanoparticle-Enabled Innate Immune Stimulation Activates Endogenous Tumor-Infiltrating T Cells with Broad Antigen Specificities. *Proc Natl Acad Sci U S A* **2021**, *118* (21), e2016168118. https://doi.org/10.1073/pnas.2016168118.

(227) Iwasaki, A.; Medzhitov, R. Regulation of Adaptive Immunity by the Innate Immune System. *Science* **2010**, *327* (5963), 291–295. https://doi.org/10.1126/science.1183021.

(228) Mizrahy, S.; Raz, S. R.; Hasgaard, M.; Liu, H.; Soffer-Tsur, N.; Cohen, K.; Dvash, R.; Landsman-Milo, D.; Bremer, M. G. E. G.; Moghimi, S. M.; Peer, D. Hyaluronan-Coated Nanoparticles: The Influence of the Molecular Weight on CD44-Hyaluronan Interactions and on the Immune Response. *Journal of Controlled Release* **2011**, *156* (2), 231–238. https://doi.org/10.1016/j.jconrel.2011.06.031.

(229) Yang, W.; Wang, L.; Fang, M.; Sheth, V.; Zhang, Y.; Holden, A. M.; Donahue, N. D.; Green, D. E.; Frickenstein, A. N.; Mettenbrink, E. M.; Schwemley, T. A.; Francek, E. R.; Haddad, M.; Hossen, M. N.; Mukherjee, S.; Wu, S.; DeAngelis, P. L.; Wilhelm, S. Nanoparticle Surface Engineering with Heparosan Polysaccharide Reduces Serum Protein Adsorption and Enhances Cellular Uptake. *Nano Lett.* **2022**, *22* (5), 2103–2111. https://doi.org/10.1021/acs.nanolett.2c00349.

(230) Liu, Y.; Wang, L.; Song, Q.; Ali, M.; Crowe, W. N.; Kucera, G. L.; Hawkins, G. A.; Soker, S.; Thomas, K. W.; Miller, L. D.; Lu, Y.; Bellinger, C. R.; Zhang, W.; Habib, A. A.; Petty, W. J.; Zhao, D. Intrapleural Nano-Immunotherapy Promotes Innate and Adaptive Immune Responses to Enhance Anti-PD-L1 Therapy for Malignant Pleural Effusion. *Nat Nanotechnol* **2022**, *17* (2), 206–216. https://doi.org/10.1038/s41565-021-01032-w.

(231) Ding, H.; Ma, Y. Controlling Cellular Uptake of Nanoparticles with PH-Sensitive Polymers. *Sci Rep* **2013**, *3* (1), 2804. https://doi.org/10.1038/srep02804.

(232) Bai, Y.; Xing, H.; Wu, P.; Feng, X.; Hwang, K.; Lee, J. M.; Phang, X. Y.; Lu, Y.; Zimmerman, S. C. Chemical Control over Cellular Uptake of Organic Nanoparticles by Fine Tuning Surface Functional Groups. *ACS Nano* **2015**, *9* (10), 10227–10236. https://doi.org/10.1021/acsnano.5b03909.

(233) Costa da Silva, M.; Vieira Rocha, C.; Bañobre-López, M.; Gallo, J. Stimulation and Suppression of the Innate Immune System through Nanotechnology. *ACS Appl. Nano Mater.* **2021**, *4* (3), 2303–2316. https://doi.org/10.1021/acsanm.0c03424.

(234) Cai, J.; Wang, H.; Wang, D.; Li, Y. Improving Cancer Vaccine Efficiency by Nanomedicine. *Adv. Biosys.* **2019**, *3* (3), 1800287. https://doi.org/10.1002/adbi.201800287.

(235) van Leent, M. M. T.; Priem, B.; Schrijver, D. P.; de Dreu, A.; Hofstraat, S. R. J.; Zwolsman, R.; Beldman, T. J.; Netea, M. G.; Mulder, W. J. M. Regulating Trained Immunity with Nanomedicine. *Nat Rev Mater* **2022**, 1–17. https://doi.org/10.1038/s41578-021-00413-w.

(236) Moynihan, K. D.; Opel, C. F.; Szeto, G. L.; Tzeng, A.; Zhu, E. F.; Engreitz, J. M.; Williams, R. T.; Rakhra, K.; Zhang, M. H.; Rothschilds, A. M.; Kumari, S.; Kelly, R. L.; Kwan, B. H.; Abraham, W.; Hu, K.; Mehta, N. K.; Kauke, M. J.; Suh, H.; Cochran, J. R.; Lauffenburger, D. A.; Wittrup, K. D.; Irvine, D. J. Eradication of Large Established Tumors in Mice by Combination Immunotherapy That Engages Innate and Adaptive Immune Responses. *Nat Med* **2016**, *22* (12), 1402–1410. https://doi.org/10.1038/nm.4200.

(237) Verma, A.; Stellacci, F. Effect of Surface Properties on Nanoparticle-Cell Interactions. *Small* **2010**, *6* (1), 12–21. https://doi.org/10.1002/smll.200901158.

(238) Nel, A. E.; Mädler, L.; Velegol, D.; Xia, T.; Hoek, E. M. V.; Somasundaran, P.;

Klaessig, F.; Castranova, V.; Thompson, M. Understanding Biophysicochemical Interactions at the Nano–Bio Interface. *Nature Mater* **2009**, *8* (7), 543–557. https://doi.org/10.1038/nmat2442.
(239) T. Chou, L. Y.; Ming, K.; W. Chan, W. C. Strategies for the Intracellular Delivery of Nanoparticles. *Chemical Society Reviews* **2011**, *40* (1), 233–245. https://doi.org/10.1039/C0CS00003E.
(240) Yang, W.; Wang, L.; Fang, M.; Sheth, V.; Zhang, Y.; Holden, A. M.; Donahue, N. D.; Green, D. E.; Frickenstein, A. N.; Mettenbrink, E. M.; Schwemley, T. A.; Francek, E. R.; Haddad, M.; Hossen, M. N.; Mukherjee, S.; Wu, S.; DeAngelis, P. L.; Wilhelm, S. Nanoparticle Surface Engineering with Heparosan Polysaccharide Reduces Serum Protein Adsorption and Enhances Cellular Uptake. *Nano Lett.* **2022**. https://doi.org/10.1021/acs.nanolett.2c00349.
(241) Okuyama, M.; Laman, H.; Kingsbury, S. R.; Visintin, C.; Leo, E.; Eward, K. L.; Stoeber, K.; Boshoff, C.; Williams, G. H.; Selwood, D. L. Small-Molecule Mimics of an α-Helix for Efficient Transport of Proteins into Cells. *Nat Methods* **2007**, *4* (2), 153–159. https://doi.org/10.1038/nmeth997.
(242) Donahue, N. D.; Sheth, V.; Frickenstein, A. N.; Holden, A.; Kanapilly, S.; Stephan, C.; Wilhelm, S. Absolute Quantification of Nanoparticle Interactions with Individual Human B Cells by Single Cell Mass Spectrometry. *Nano Lett.* **2022**, *22* (10), 4192–4199. https://doi.org/10.1021/acs.nanolett.2c01037.
(243) Fobian, S.-F.; Petzer, M.; Vetten, M.; Steenkamp, V.; Gulumian, M.; Cordier, W. Mechanisms Facilitating the Uptake of Carboxyl–Polythene Glycol-Functionalized Gold Nanoparticles into Multicellular Spheroids. *Journal of Pharmacy and Pharmacology* **2022**, rgac017. https://doi.org/10.1093/jpp/rgac017.
(244) Foroozandeh, P.; Aziz, A. A. Insight into Cellular Uptake and Intracellular Trafficking of Nanoparticles. *Nanoscale Research Letters* **2018**, *13* (1), 339. https://doi.org/10.1186/s11671-018-2728-6.
(245) Li, Y.; Monteiro-Riviere, N. A. Mechanisms of Cell Uptake, Inflammatory Potential and Protein Corona Effects with Gold Nanoparticles. *Nanomedicine* **2016**, *11* (24), 3185–3203. https://doi.org/10.2217/nnm-2016-0303.
(246) Gao, H.; Yang, Z.; Zhang, S.; Cao, S.; Shen, S.; Pang, Z.; Jiang, X. Ligand Modified Nanoparticles Increases Cell Uptake, Alters Endocytosis and Elevates Glioma Distribution and Internalization. *Sci Rep* **2013**, *3*, 2534. https://doi.org/10.1038/srep02534.
(247) Kou, L.; Sun, J.; Zhai, Y.; He, Z. The Endocytosis and Intracellular Fate of Nanomedicines: Implication for Rational Design. *Asian Journal of Pharmaceutical Sciences* **2013**, *8* (1), 1–10. https://doi.org/10.1016/j.ajps.2013.07.001.
(248) Reisman, B. J.; Guo, H.; Ramsey, H. E.; Wright, M. T.; Reinfeld, B. I.; Ferrell, P. B.; Sulikowski, G. A.; Rathmell, W. K.; Savona, M. R.; Plate, L.; Rubinstein, J. L.; Bachmann, B. O. Apoptolidin Family Glycomacrolides Target Leukemia through Inhibition of ATP Synthase. *Nat Chem Biol* **2022**, *18* (4), 360–367. https://doi.org/10.1038/s41589-021-00900-9.
(249) Delrot, S.; Despeghel, J.-P.; Bonnemain, J.-L. Phloem Loading in Vicia Faba Leaves: Effect of N-Ethylmaleimide and Parachloromercuribenzenesulfonic Acid on H+ Extrusion, K+ and Sucrose Uptake. *Planta* **1980**, *149* (2), 144–148. https://doi.org/10.1007/BF00380875.
(250) Li, T.; Takeoka, S. Enhanced Cellular Uptake of Maleimide-Modified Liposomes via Thiol-Mediated Transport. *IJN* **2014**, *9* (1), 2849–2861. https://doi.org/10.2147/IJN.S58540.
(251) Wenge, B.; Bönisch, H. N-Ethylmaleimide Differentially Inhibits Substrate Uptake by

and Ligand Binding to the Noradrenaline Transporter. *Naunyn-Schmied Arch Pharmacol* **2008**, *377* (3), 255–265. https://doi.org/10.1007/s00210-008-0272-0.
(252) Zhang, H.; Ding, A.; Ye, B.; Wang, Z.; Zhang, J.; Qiu, L.; Chen, J. Carbon Nitride Nanosheets for Imaging Traceable CpG Oligodeoxynucleotide Delivery. *ACS Appl. Nano Mater.* **2021**, *4* (8), 8546–8555. https://doi.org/10.1021/acsanm.1c01658.
(253) Di Marzio, L.; Marianecci, C.; Cinque, B.; Nazzarri, M.; Cimini, A. M.; Cristiano, L.; Cifone, M. G.; Alhaique, F.; Carafa, M. PH-Sensitive Non-Phospholipid Vesicle and Macrophage-like Cells: Binding, Uptake and Endocytotic Pathway. *Biochimica et Biophysica Acta (BBA) - Biomembranes* **2008**, *1778* (12), 2749–2756. https://doi.org/10.1016/j.bbamem.2008.07.029.
(254) Wolfram, J.; Nizzero, S.; Liu, H.; Li, F.; Zhang, G.; Li, Z.; Shen, H.; Blanco, E.; Ferrari, M. A Chloroquine-Induced Macrophage-Preconditioning Strategy for Improved Nanodelivery. *Sci Rep* **2017**, *7* (1), 13738. https://doi.org/10.1038/s41598-017-14221-2.
(255) Perry, J. W.; Wobus, C. E. Endocytosis of Murine Norovirus 1 into Murine Macrophages Is Dependent on Dynamin II and Cholesterol. *J Virol* **2010**, *84* (12), 6163–6176. https://doi.org/10.1128/JVI.00331-10.
(256) Kapetanovic, R.; Nahori, M.-A.; Balloy, V.; Fitting, C.; Philpott, D. J.; Cavaillon, J.-M.; Adib-Conquy, M. Contribution of Phagocytosis and Intracellular Sensing for Cytokine Production by Staphylococcus Aureus-Activated Macrophages. *Infect Immun* **2007**, *75* (2), 830–837. https://doi.org/10.1128/IAI.01199-06.
(257) Lim, E. Y.; Park, J.; Kim, Y. T.; Kim, M. J. Imipramine Inhibits Migration and Invasion in Metastatic Castration-Resistant Prostate Cancer PC-3 Cells via AKT-Mediated NF-KB Signaling Pathway. *Molecules* **2020**, *25* (20), 4619. https://doi.org/10.3390/molecules25204619.
(258) Almeida, M. S. de; Susnik, E.; Drasler, B.; Taladriz-Blanco, P.; Petri-Fink, A.; Rothen-Rutishauser, B. Understanding Nanoparticle Endocytosis to Improve Targeting Strategies in Nanomedicine. *Chemical Society Reviews* **2021**, *50* (9), 5397–5434. https://doi.org/10.1039/D0CS01127D.
(259) Sheth, V.; Wang, L.; Bhattacharya, R.; Mukherjee, P.; Wilhelm, S. Strategies for Delivering Nanoparticles across Tumor Blood Vessels. *Adv. Funct. Mater.* **2021**, *31* (8), 2007363. https://doi.org/10.1002/adfm.202007363.
(260) Rennick, J. J.; Johnston, A. P. R.; Parton, R. G. Key Principles and Methods for Studying the Endocytosis of Biological and Nanoparticle Therapeutics. *Nat. Nanotechnol.* **2021**, *16* (3), 266–276. https://doi.org/10.1038/s41565-021-00858-8.
(261) Hossen, Md. N.; Wang, L.; Chinthalapally, H. R.; Robertson, J. D.; Fung, K.-M.; Wilhelm, S.; Bieniasz, M.; Bhattacharya, R.; Mukherjee, P. Switching the Intracellular Pathway and Enhancing the Therapeutic Efficacy of Small Interfering RNA by Auroliposome. *Science Advances* **2020**, *6* (30), eaba5379. https://doi.org/10.1126/sciadv.aba5379.
(262) Francia, V.; Reker-Smit, C.; Boel, G.; Salvati, A. Limits and Challenges in Using Transport Inhibitors to Characterize How Nano-Sized Drug Carriers Enter Cells. *Nanomedicine* **2019**, *14* (12), 1533–1549. https://doi.org/10.2217/nnm-2018-0446.
(263) Tian, T.; Zhu, Y.-L.; Zhou, Y.-Y.; Liang, G.-F.; Wang, Y.-Y.; Hu, F.-H.; Xiao, Z.-D. Exosome Uptake through Clathrin-Mediated Endocytosis and Macropinocytosis and Mediating MiR-21 Delivery. *J Biol Chem* **2014**, *289* (32), 22258–22267. https://doi.org/10.1074/jbc.M114.588046.
(264) Biddeci, G.; Spinelli, G.; Massaro, M.; Riela, S.; Bonaccorsi, P.; Barattucci, A.; Di Blasi, F. Study of Uptake Mechanisms of Halloysite Nanotubes in Different Cell Lines. *Int J Nanomedicine* **2021**, *16*, 4755–4768. https://doi.org/10.2147/IJN.S303816.

(265) Jackson, D. G. Hyaluronan in the Lymphatics: The Key Role of the Hyaluronan Receptor LYVE-1 in Leucocyte Trafficking. *Matrix Biol* **2019**, *78–79*, 219–235. https://doi.org/10.1016/j.matbio.2018.02.001.
(266) *Essentials of Glycobiology*, 3rd ed.; Varki, A., Cummings, R. D., Esko, J. D., Stanley, P., Hart, G. W., Aebi, M., Darvill, A. G., Kinoshita, T., Packer, N. H., Prestegard, J. H., Schnaar, R. L., Seeberger, P. H., Eds.; Cold Spring Harbor Laboratory Press: Cold Spring Harbor (NY), 2015.
(267) Chavaroche, A. A. E.; van den Broek, L. A. M.; Eggink, G. Production Methods for Heparosan, a Precursor of Heparin and Heparan Sulfate. *Carbohydrate Polymers* **2013**, *93* (1), 38–47. https://doi.org/10.1016/j.carbpol.2012.04.046.
(268) Nikitovic, D.; Assouti, M.; Sifaki, M.; Katonis, P.; Krasagakis, K.; Karamanos, N. K.; Tzanakakis, G. N. Chondroitin Sulfate and Heparan Sulfate-Containing Proteoglycans Are Both Partners and Targets of Basic Fibroblast Growth Factor-Mediated Proliferation in Human Metastatic Melanoma Cell Lines. *The International Journal of Biochemistry & Cell Biology* **2008**, *40* (1), 72–83. https://doi.org/10.1016/j.biocel.2007.06.019.
(269) de Vet, E. C. J. M.; Newland, S. A. B.; Lyons, P. A.; Aguado, B.; Campbell, R. D. The Cell Surface Receptor G6b, a Member of the Immunoglobulin Superfamily, Binds Heparin. *FEBS Letters* **2005**, *579* (11), 2355–2358. https://doi.org/10.1016/j.febslet.2005.03.032.
(270) DeAngelis, P. L. Heparosan, a Promising 'Naturally Good' Polymeric Conjugating Vehicle for Delivery of Injectable Therapeutics. *Expert Opinion on Drug Delivery* **2015**, *12* (3), 349–352. https://doi.org/10.1517/17425247.2015.978282.
(271) Soares da Costa, D.; Reis, R. L.; Pashkuleva, I. Sulfation of Glycosaminoglycans and Its Implications in Human Health and Disorders. *Annual Review of Biomedical Engineering* **2017**, *19* (1), 1–26. https://doi.org/10.1146/annurev-bioeng-071516-044610.
(272) *Natural and Synthetic Biomedical Polymers*, First edition.; Kumbar, S., Laurencin, C., Deng, M., Eds.; Elsevier: Amsterdam ; Boston, 2014.
(273) Fujimoto, T.; Kawashima, H.; Tanaka, T.; Hirose, M.; Toyama-Sorimachi, N.; Matsuzawa, Y.; Miyasaka, M. CD44 Binds a Chondroitin Sulfate Proteoglycan, Aggrecan. *Int Immunol* **2001**, *13* (3), 359–366. https://doi.org/10.1093/intimm/13.3.359.
(274) Hirose, J.; Kawashima, H.; Swope Willis, M.; Springer, T. A.; Hasegawa, H.; Yoshie, O.; Miyasaka, M. Chondroitin Sulfate B Exerts Its Inhibitory Effect on Secondary Lymphoid Tissue Chemokine (SLC) by Binding to the C-Terminus of SLC. *Biochim Biophys Acta* **2002**, *1571* (3), 219–224. https://doi.org/10.1016/s0304-4165(02)00232-5.
(275) Zhang, Q.; Du, Y.; Chen, J.; Xu, G.; Yu, T.; Hua, X.; Zhang, J. Investigation of Chondroitin Sulfate D and Chondroitin Sulfate E as Novel Chiral Selectors in Capillary Electrophoresis. *Anal Bioanal Chem* **2014**, *406* (5), 1557–1566. https://doi.org/10.1007/s00216-013-7544-3.
(276) Mikami, T.; Yasunaga, D.; Kitagawa, H. Contactin-1 Is a Functional Receptor for Neuroregulatory Chondroitin Sulfate-E*. *Journal of Biological Chemistry* **2009**, *284* (7), 4494–4499. https://doi.org/10.1074/jbc.M809227200.
(277) Singh, B.; Maharjan, S.; Kim, Y.-K.; Jiang, T.; Islam, M. A.; Kang, S.-K.; Cho, M.-H.; Choi, Y.-J.; Cho, C.-S. Targeted Gene Delivery via N-Acetylglucosamine Receptor Mediated Endocytosis. *J Nanosci Nanotechnol* **2014**, *14* (11), 8356–8364. https://doi.org/10.1166/jnn.2014.9919.
(278) Sindhwani, S.; Syed, A. M.; Ngai, J.; Kingston, B. R.; Maiorino, L.; Rothschild, J.;

MacMillan, P.; Zhang, Y.; Rajesh, N. U.; Hoang, T.; Wu, J. L. Y.; Wilhelm, S.; Zilman, A.; Gadde, S.; Sulaiman, A.; Ouyang, B.; Lin, Z.; Wang, L.; Egeblad, M.; Chan, W. C. W. The Entry of Nanoparticles into Solid Tumours. *Nat. Mater.* **2020**, *19* (5), 566–575. https://doi.org/10.1038/s41563-019-0566-2.

(279) Wilhelm, S.; Hirsch, T.; Patterson, W. M.; Scheucher, E.; Mayr, T.; Wolfbeis, O. S. Multicolor Upconversion Nanoparticles for Protein Conjugation. *Theranostics* **2013**, *3* (4), 239–248. https://doi.org/10.7150/thno.5113.

(280) Donahue, N. D.; Francek, E. R.; Kiyotake, E.; Thomas, E. E.; Yang, W.; Wang, L.; Detamore, M. S.; Wilhelm, S. Assessing Nanoparticle Colloidal Stability with Single-Particle Inductively Coupled Plasma Mass Spectrometry (SP-ICP-MS). *Anal Bioanal Chem* **2020**, *412* (22), 5205–5216. https://doi.org/10.1007/s00216-020-02783-6.

(281) Suk, J. S.; Xu, Q.; Kim, N.; Hanes, J.; Ensign, L. M. PEGylation as a Strategy for Improving Nanoparticle-Based Drug and Gene Delivery. *Adv Drug Deliv Rev* **2016**, *99* (Pt A), 28–51. https://doi.org/10.1016/j.addr.2015.09.012.

Appendix A: List of Supporting Figures

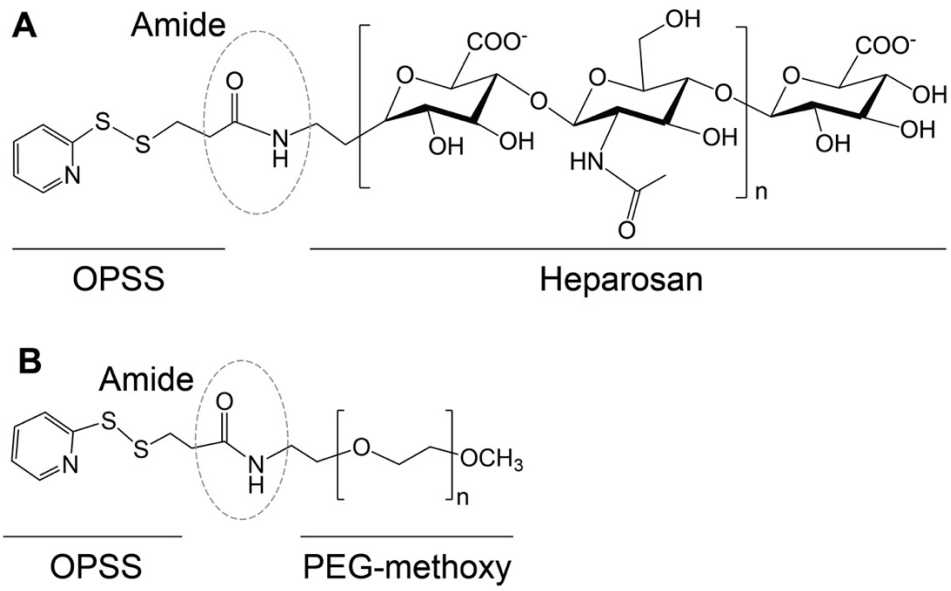

Figure S1: Chemical structure of OPSS-HEP, and OPSS-PEG.

Chemical structures of OPSS-conjugated heparosan **(A)** or OPSS-conjugated PEG **(B)**.

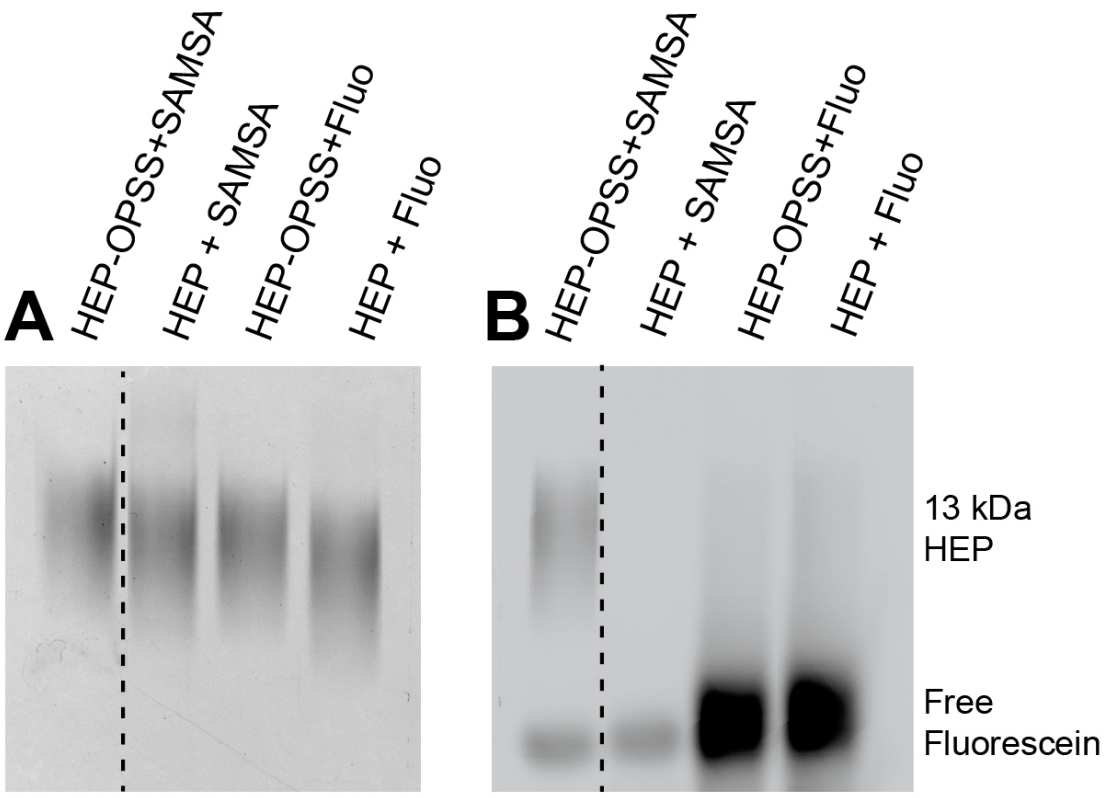

Figure S2: Characterization of the OPSS-HEP conjugation.

(A) Characterization of heparosan and its OPSS-derivative by PAGE gel. Alcian Blue-staining of the gel shows the presence of heparosan polysaccharide **(B)** Analysis of OPSS-HEP chemical reactivity via fluorescent probes: Activated SAMSA (a fluorescent group with a free thiol after deprotection) reactivity and fluorescein-5-maleimide (Fluo; a fluorescent sulfhydryl reactive reagent) reactivity were employed to qualitatively evaluate OPSS conjugation and degradation (i.e., any loss of the OPS group reveals a free thiol), respectively. The fluorescent SAMSA reaction product with OPSS-HEP aligned well with the polysaccharide bands in the Alcian blue gel, indicating that the conjugation of OPSS with HEP was effective. No fluorescent product was observed in the fluorescein-5-maleimide reactions indicating the absence of free thiol groups; therefore, no significant degradation of the OPSS-HEP was detected during handling and storage. Images are cropped and gel lanes fused as indicated with the dashed lines. Original images are available upon request.

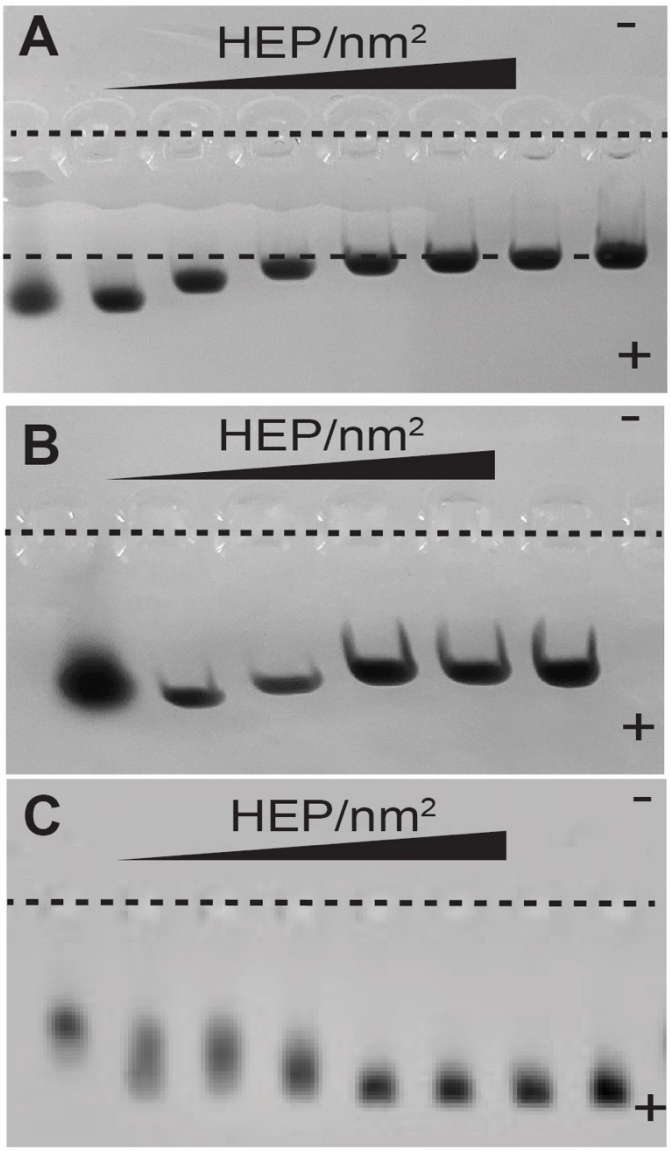

Figure S3: Agarose gel electrophoresis images of 15-nm HEP-AuNPs.

(A), (C) Agarose gel electrophoresis of heparosan-modified AuNPs by salt aging (A) or by simple mixing (C). The coating reactions contained various ratios of HEP to AuNPs ranging from 0, 0.1, 0.25, 0.5, 0.75, 1, 1.5, or 2 HEP/nm^2. The addition of HEP chains to the AuNPs slows migration, possibly due to the increase in hydrodynamic size until a plateau indicates surface saturation. **(B)** Agarose gel electrophoresis of heparosan-modified AuNPs by pH method. The surface HEP densities were 0, 0.25, 0.5, 1, 2, or 5 HEP/nm^2. The *dashed lines* indicate the position of the wells.

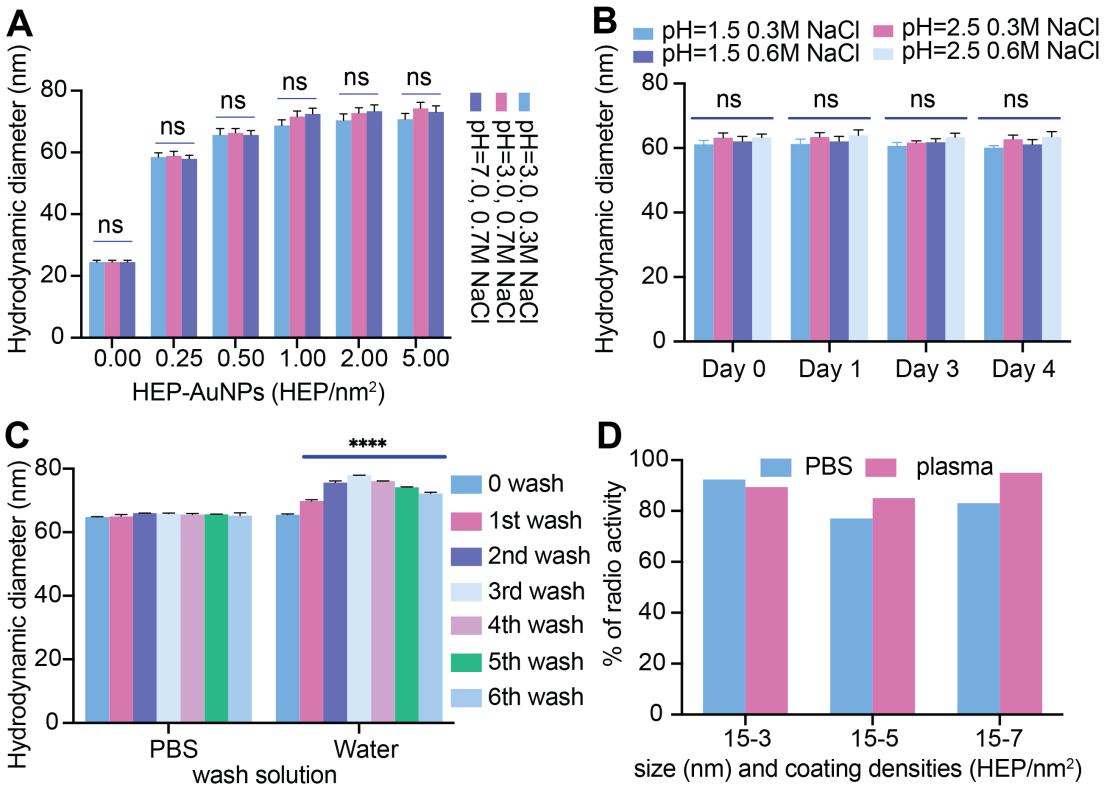

Figure S4: Nanoparticle colloidal stability of 15-nm HEP-AuNPs.

(A-B) Nanoparticle colloidal stability in buffers with different sodium chloride (NaCl) concentrations and pH (A) and over 4 days (B). **(C)** Nanoparticle colloidal stability after repeated centrifugation and washing by water and PBS. Bar graphs indicate mean ± s.d. of biological triplicates. Statistical tests were performed by Two-Way ANOVA ($p<0.0001$ (****); n.s. indicates no statistically significant differences. **(D)** Plasma challenging of radiolabeled HEP-AuNPs with different coating reaction ratios and sizes. For example, 15-3 indicates 15-nm AuNPs with calculated addition ratios of 3 HEP per nm^2 of particle surface area in the coating reaction. The incubation time for 15-3 was 12h, 15-5 was 24 hours, and 15-7 was 48 hours.

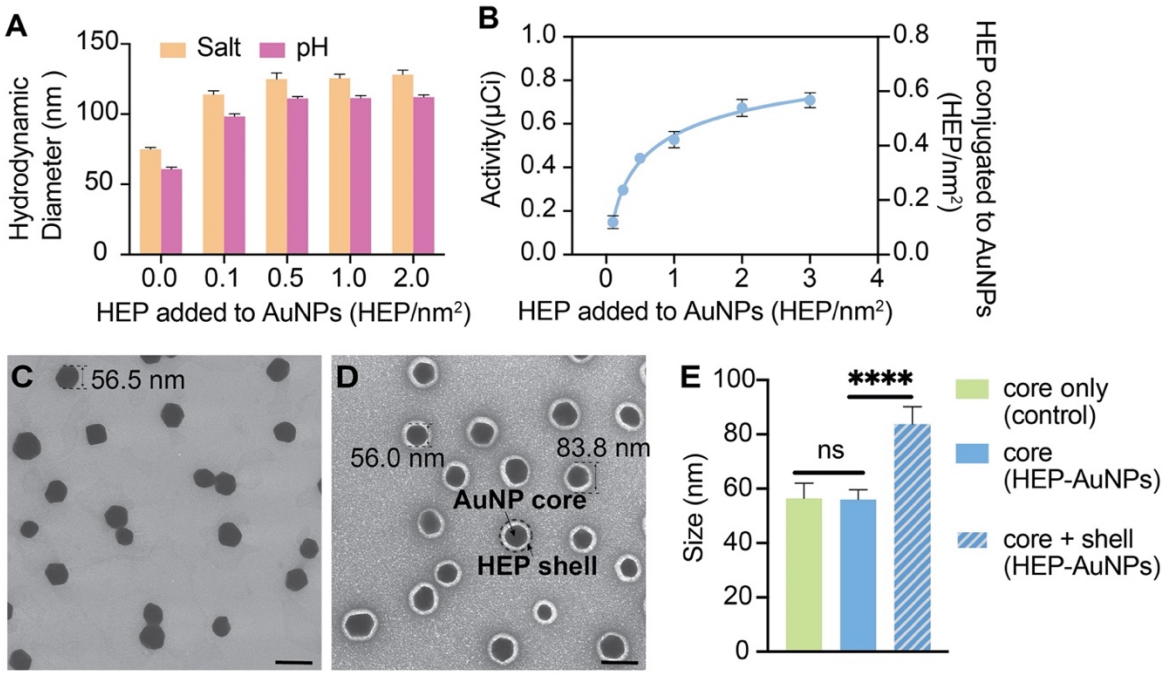

Figure S5: Physicochemical characterization of 55-nm HEP-AuNPs.

(A) Dynamic light scattering (DLS) was used to measure the hydrodynamic diameter of 55-nm AuNPs after mixing with various amounts of HEP per nm^2 of nanoparticle surface area by either the salt concentration (salt aging) or pH methods. Bars indicate mean ± SD (n=3). **(B)** Radiochemical assay of HEP incorporation onto AuNPs: Various amounts of radiolabeled heparosan were mixed with 55-nm AuNPs, and after the coating process, free HEP was washed away. The left y-axis reports the [^{3}H] radioactivity of different HEP coating levels. The right y-axis represents the actual HEP per nm^2 calculated from the specific radioactivity of [^{3}H]HEP-OPSS. **(C), (D)** Representative TEM micrograph of 55-nm citrate coated AuNPs with a diameter of 56.5 ± 5.6nm (C) and HEP-AuNPs The light grey halo or shell around the dark AuNP core (56.0 ± 3.5 nm) corresponds to surface conjugated HEP (panel D; 83.8 ± 6.5 nm) denoted here as the 'HEP shell'. **(E)** TEM micrograph image analysis of nanoparticle size. The *x*-axis labels are as follows: Core only (citrate coated AuNPs as control from panel C; green bar); Core of HEP-AuNPs from panel D (Core diameter of HEP-AuNPs in panel D; blue bar); Core + shell of HEP-AuNPs (Core and shell diameter of HEP-AuNPs from panel D; slanted lined blue bar). Bars indicate mean ± SD. Statistical tests were performed by one-way ANOVA ($p<0.0001$ (****); n.s. indicates no statistically significant differences). Scale bars denote 100 nm.

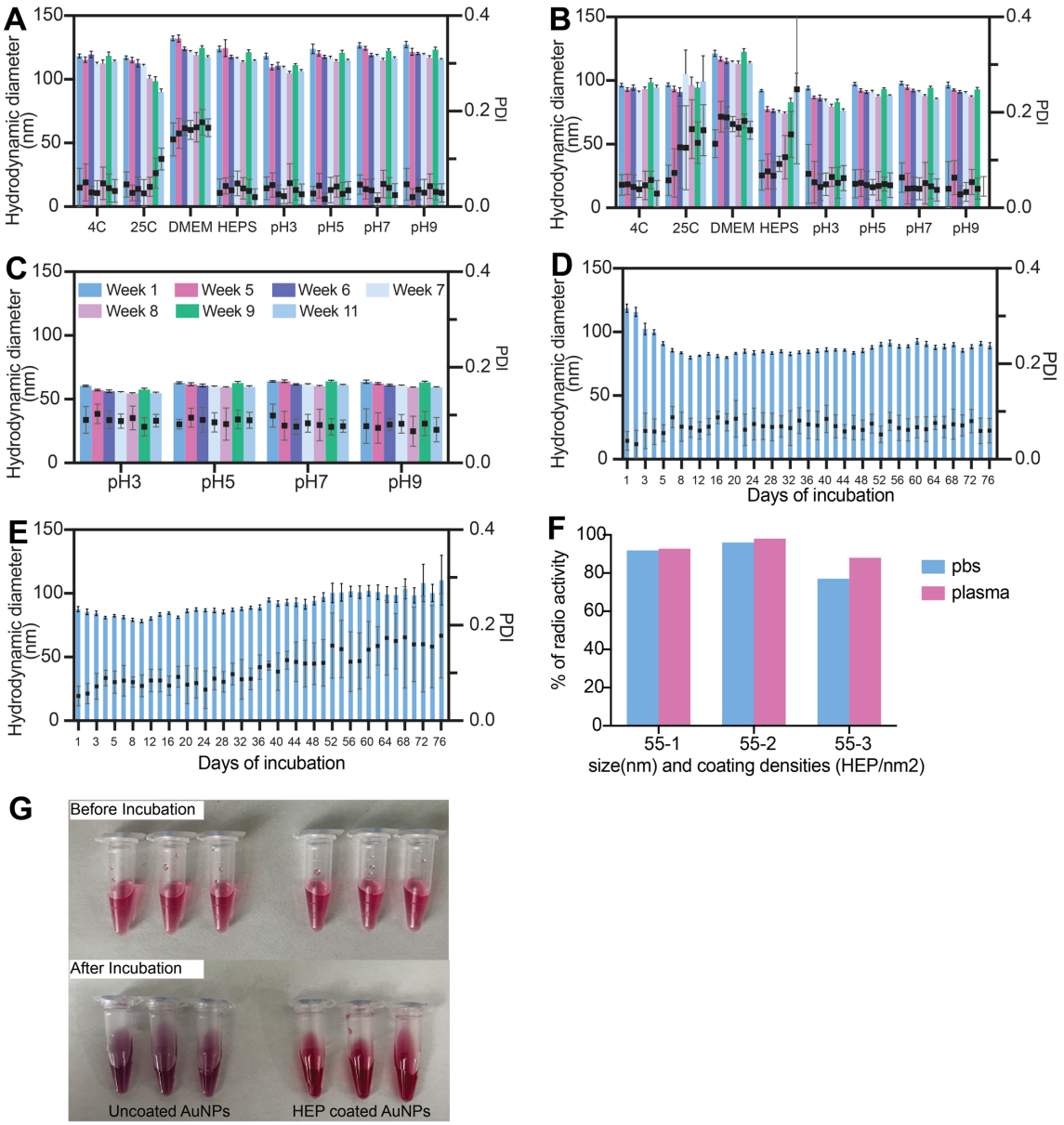

Figure S6: Nanoparticle colloidal stability of 55-nm HEP-AuNPs.

(A-C) Long-term colloidal stability of 55-nm HEP-AuNPs (A), PEG-AuNPs (B), or Citrate-AuNPs (C) under different conditions over 11 weeks. Panels A and B share the same legend as shown in Panel C. **(D- (E)** Colloidal stability of 55-nm HEP-AuNPs (D) and PEG-AuNPs (E) after FBS incubation at 37ºC for 76 days. Bars indicate mean ± SD. Dots represent the polydispersity index (PDI). **(F)** Plasma challenging of radiolabeled HEP-AuNPs with different coating densities, e.g., 5-1 indicates 55-nm AuNPs with the addition of 1 HEP per nm^2. The incubation time was 24 h. **(G)** Photographs of uncoated AuNPs (left) or HEP-coated AuNPs (right) before and after incubation in cell media without FBS. The red color indicates colloidal stability, while the blue color indicates nanoparticle aggregation.

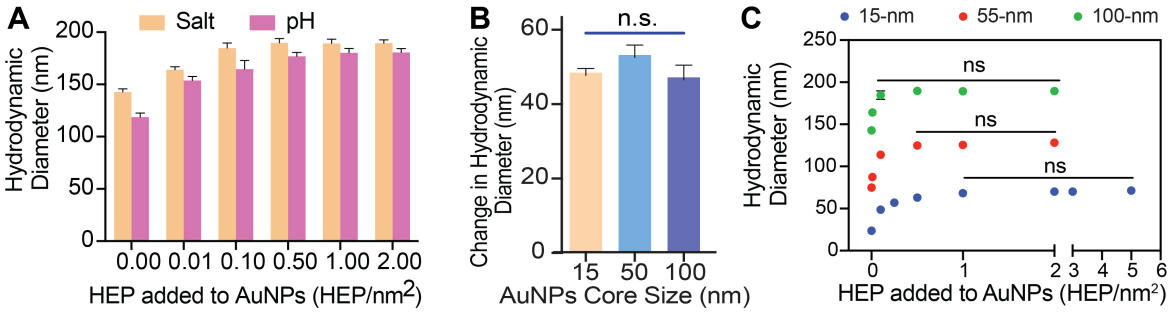

Figure S7: Characterization of 100-nm HEP-AuNPs and summary of HEP-AuNPs.

(A) Dynamic light scattering (DLS) was used to measure the hydrodynamic diameter of 100-nm AuNPs after mixing with various amounts of HEP per nm^2 of nanoparticle surface area by salt concentration (salt aging) or pH methods. Bars indicate mean ± SD (n=3). **(B)** The hydrodynamic diameter changes from 0 HEP/nm^2 to HEP saturated point (2 HEP/nm^2) calculated from dynamic light scattering data. Bars indicate mean ± SD. Statistical tests were performed by one-way ANOVA (n.s. indicates no statistically significant differences). **(C)** The saturation curves of heparosan on 15-nm, 55-nm, and 100-nm nanoparticles were measured by dynamic light scattering. Possibly due to a reduction in overall nanoparticle curvature with increasing nanoparticle size, the maximum achievable HEP surface coating densities of 15-nm, 55-nm, and 100-nm AuNPs were ~1.0 HEP/nm^2, ~0.5 HEP/nm^2, and ~0.1 HEP/nm^2, respectively. Statistical tests were performed by one-way ANOVA (n.s. indicates no statistically significant differences)

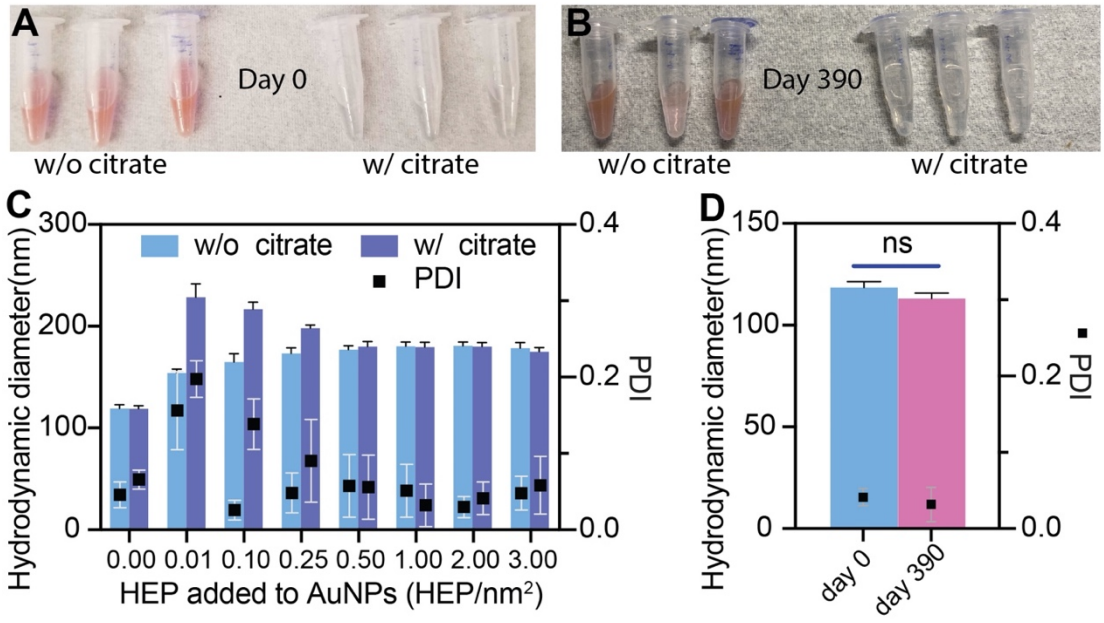

Figure S8: Optimized pH method for maintaining colloidal stability of 100-nm AuNPs modified with low HEP densities.

(A-B) Photographs of 100-nm AuNPs coated with 0.01 HEP per nm^2 using the pH method with citrate and without citrate after 0 days (A) and 390 days (B). The clear solutions indicate nanoparticle aggregation when citrate is present. **(C)** Dynamic light scattering (DLS) was used to measure the hydrodynamic diameter of 100-nm AuNPs after mixing with various amounts of HEP per nm^2 of nanoparticle surface area by pH method with citrate and without citrate. **(D)** The hydrodynamic diameter changes of HEP-AuNP with 0.01 HEP per nm^2 by pH method without citrate after 390 days. Bars indicate mean ± SD. Dots represent PDI. Statistical test was performed by unpaired T-test (n.s. indicates no statistically significant differences)

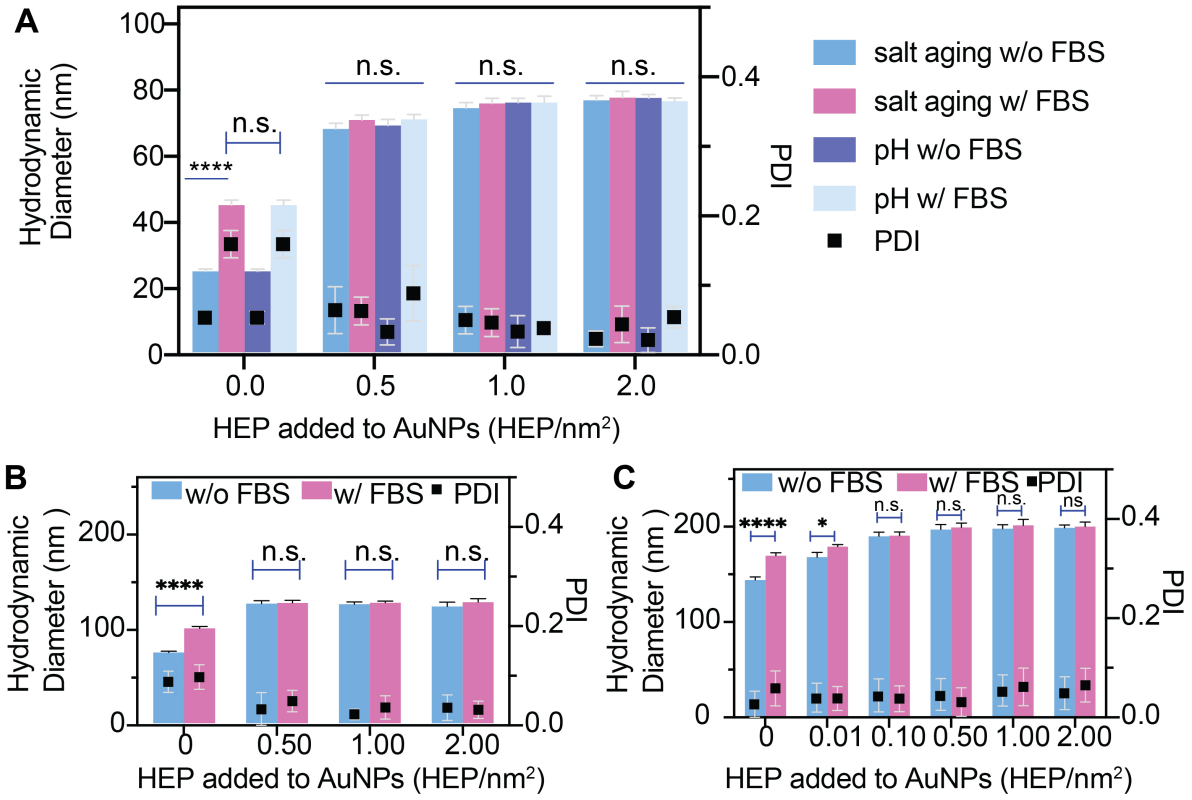

Figure S9: FBS incubation of 15-nm, 55-nm, or 100-nm HEP-AuNPs by salt aging.

(A-C) Dynamic light scattering (DLS) was used to measure the effect of FBS incubation with controls (without FBS) of AuNPs mixed with different surface HEP densities with AuNPs sizes of 15-nm (A), 55-nm (B), or 100-nm (C). The increased polydispersity index (PDI) indicates a broader nanoparticle size distribution during FBS incubation. Bar graphs indicate mean ± SD (n=3). Statistical tests were performed by one-way ANOVA ($p<0.0001$ (****); $p<0.05$(*); n.s. indicates no statistically significant differences).

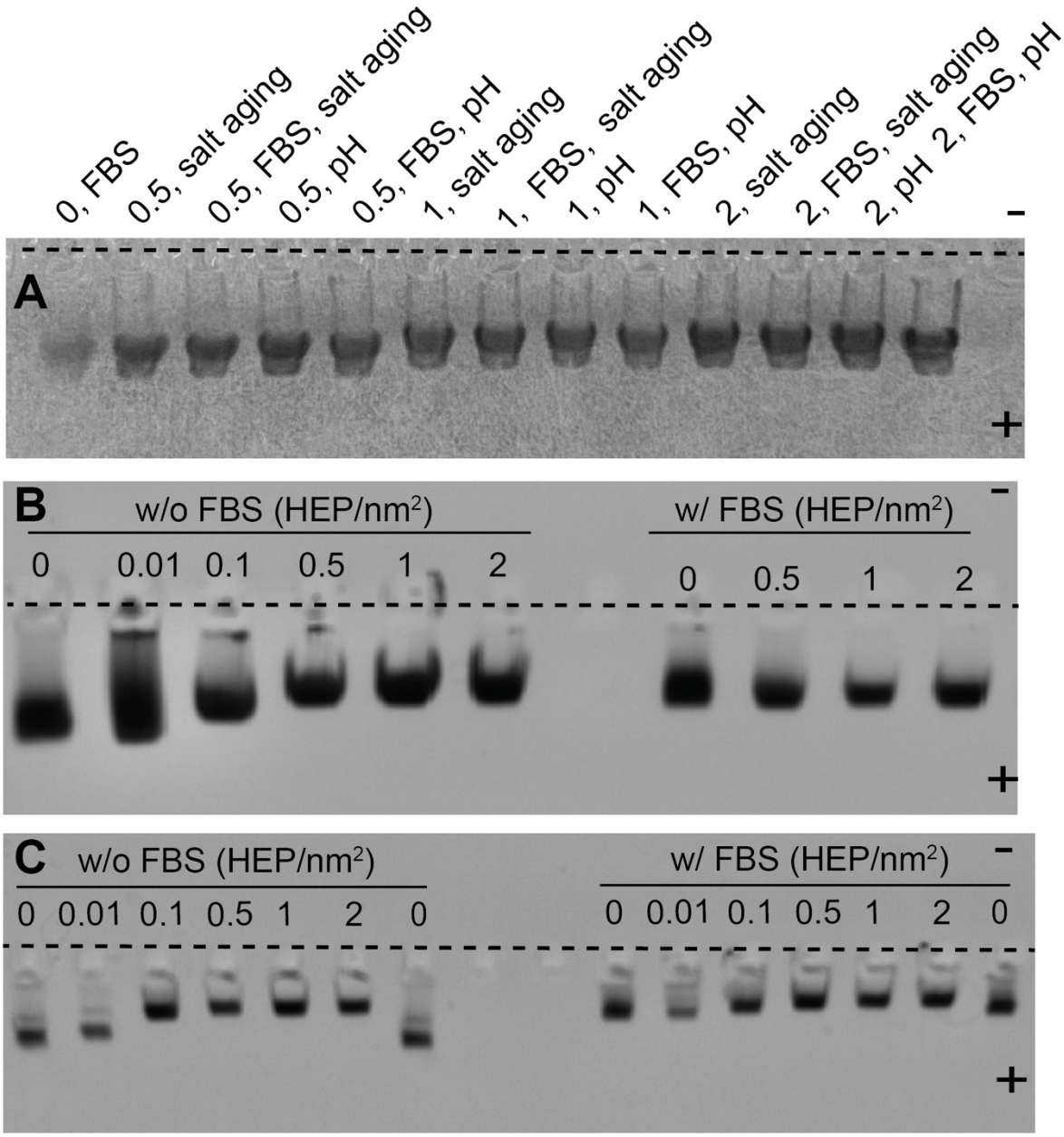

Figure S10: Agarose gel electrophoresis images of HEP-AuNPs upon FBS incubation.

(A-C) AuNPs of different sizes were compared: 15-nm (A), 55-nm (B), 100-nm (C). *Dashed lines* indicate the position of the wells.

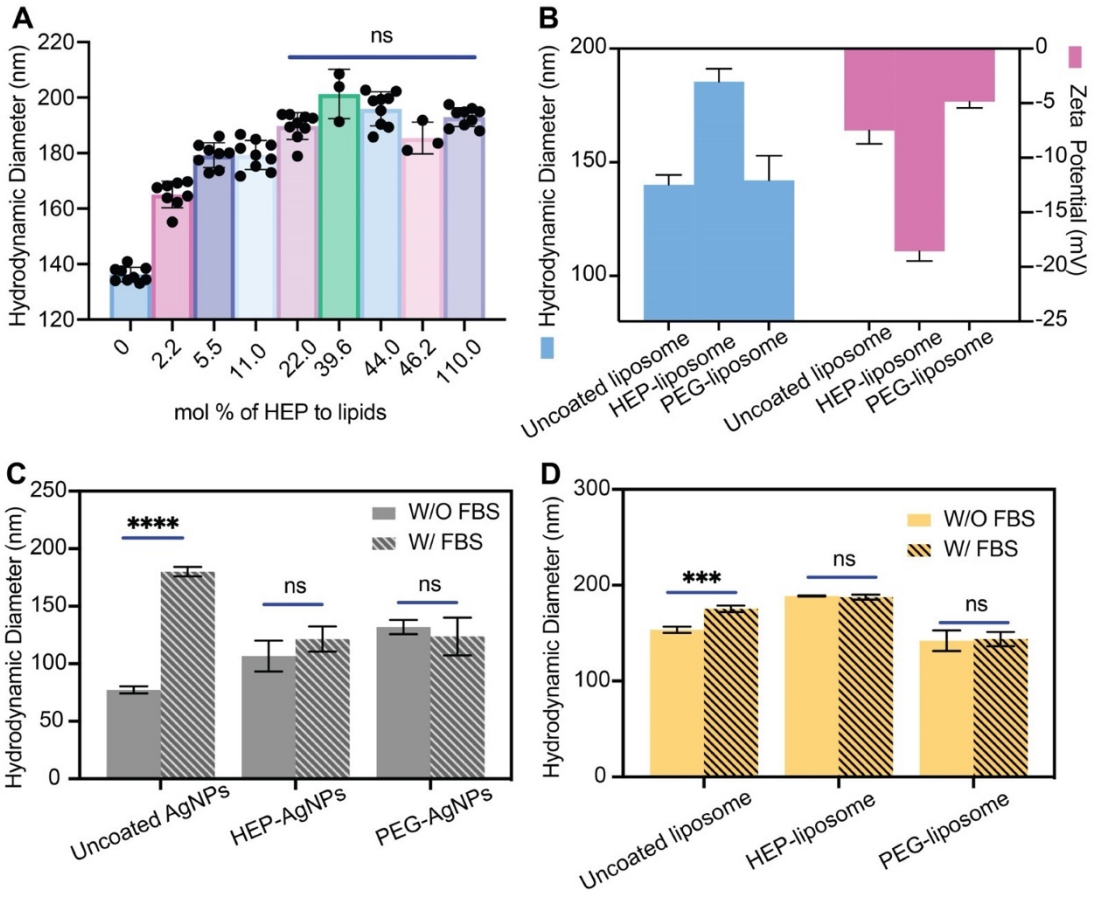

Figure S11: Heparosan coating reduces protein corona formation on silver nanoparticles and liposomes.

(A) Dynamic light scattering (DLS) was used to measure the hydrodynamic diameter of heparosan-coated liposomes with various mole percentages of HEP-dipalmitate lipid (added by post-insertional modification of pre-formed liposomes). **(B)** Hydrodynamic size and zeta potential of the uncoated liposome, HEP-liposome, or PEG-liposome preparations were measured by DLS. **(C-D)** DLS was used to compare the hydrodynamic diameter differences before and after FBS incubation (*slanted lined bars* stand for incubation with FBS) of silver nanoparticles (panel C; gray) or liposome nanoparticles (panel D; yellow). Bars indicate mean ± SD.

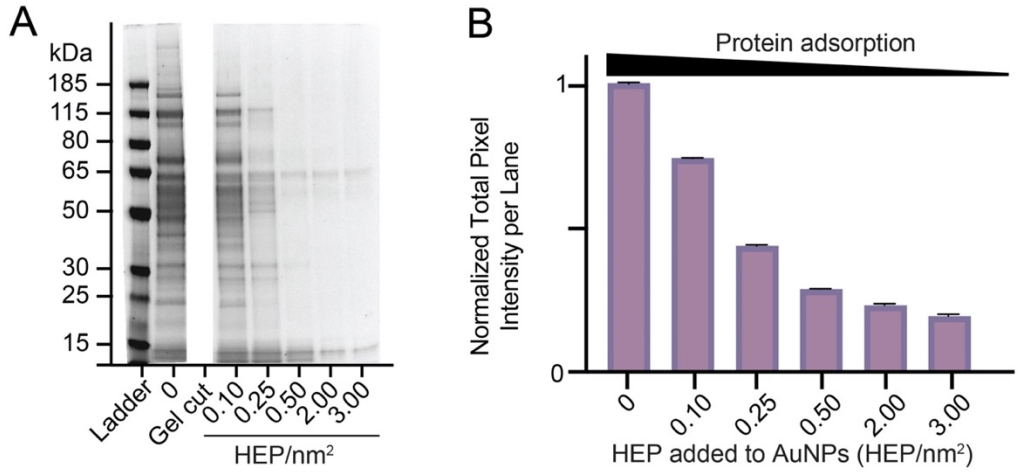

Figure S12: Heparosan coating reduces protein corona formation on 15-nm AuNPs.

(A) The qualitative molecular composition of the adsorbed FBS proteins layer on 15-nm AuNPs with various amounts of HEP in the coating reactions by SDS-PAGE gel. The lanes on the right side and left side of this image are from the same gel. **(B)** SDS-PAGE image analysis of each lane. Data points are normalized to the start point (0 HEP/nm^2). Bars indicate mean ± SD.

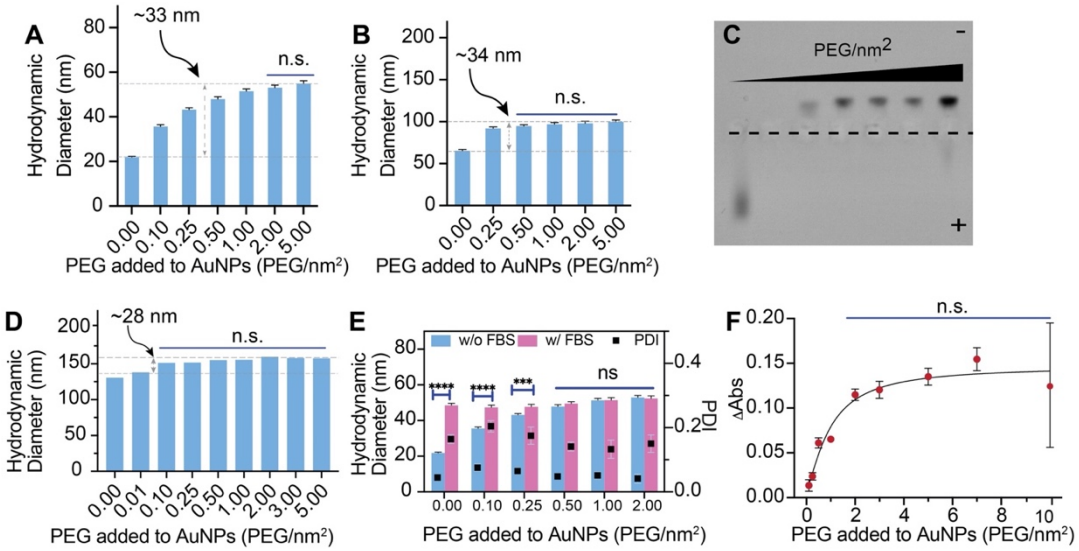

Figure S13: Physicochemical characterization of PEG-AuNPs.

(A), (B) and (D) Dynamic light scattering (DLS) was used to measure the hydrodynamic diameter of PEGylated 15-nm(A), 55-nm(B), or 100-nm AuNPs (D). Bars indicate mean ± SD (n=3). **(C)** Agarose gel electrophoresis of PEG-modified AuNPs incubation with FBS. Dashed lines indicate the position of the wells. **(E)** Dynamic light scattering (DLS) was used to measure the FBS incubation with control (without FBS) of AuNPs mixed with different surface PEG densities with AuNPs size of 15-nm. The increased polydispersity index (PDI) indicates a broader size distribution caused by FBS incubation. Bar graphs indicate mean ± SD (n=3). **(F)** An UV-Vis spectrophotometry-based depletion assay to quantify the maximum loading capacity of PEG. Statistical tests were performed by one-way ANOVA ($p<0.0001$ (****); $p<0.05$(*); n.s. indicates no statistically significant differences.

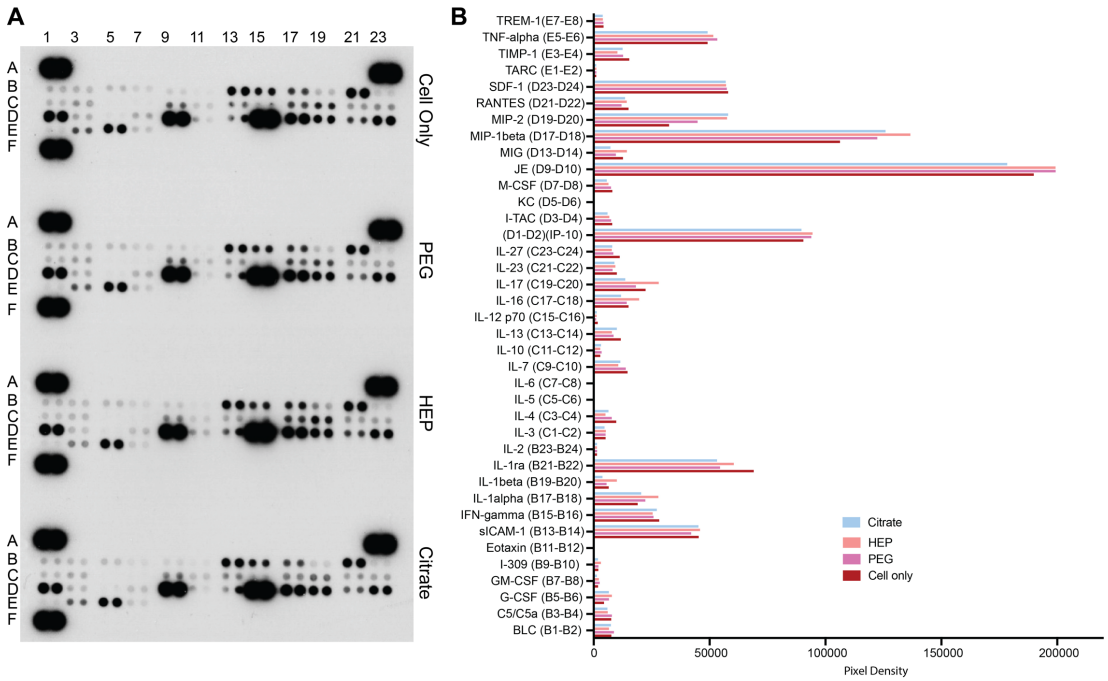

Figure S14: Assessment of cytokine release levels.

(A-B) Cytokine release levels in the supernatant of RAW 264.7 macrophages after 24 h incubation with citrate AuNPs, PEG-AuNPs, or HEP-AuNPs were determined using an array of specific antibodies (A). The signal intensities in panel A were quantified using the Quick Spot image analysis tool (B). Data points of D11-12 and D15-16 were excluded for analysis due to the interference of the nearby strong signal. A1-2, A23-24, F1-2 are reference spots; F23-24 are negative control spots.

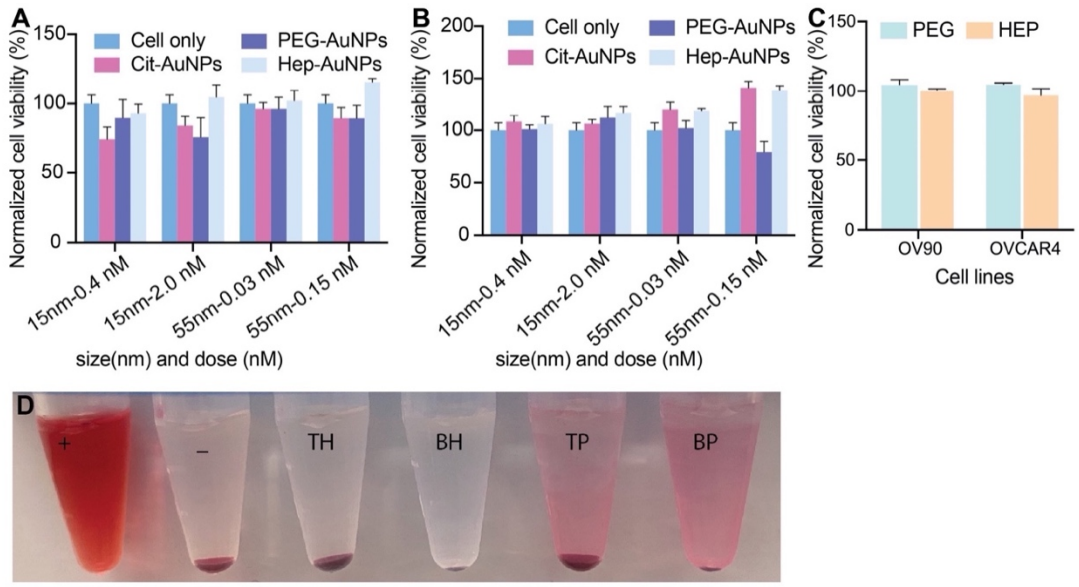

Figure S15: Cytotoxicity and hemolysis tests using HEP- or PEG-AuNPs.

(A-B) Cell viability of RAW 264.7 macrophages treated with different sizes and doses of HEP-AuNPs or PEG- AuNPs for 24 (A) and 48 (B) hours by XTT. Bar graphs indicate mean ± SD (n=5). **(C)** Cell viability test on OV90 cells and OVCAR4 cells treated with 0.1-nM HEP-AuNPs or PEG- AuNPs by XTT assay. Bar graphs indicate mean ± SD (n=5). **(D)** Photographs of AuNPs incubated with human red blood cells. From left to right: +, positive control; -, PBS negative control; TH, HEP-AuNPs with blood cells; BH, HEP-AuNPs without blood cells; TP, PEG-AuNPs with blood cells; BP, PEG-AuNPs without blood cells.

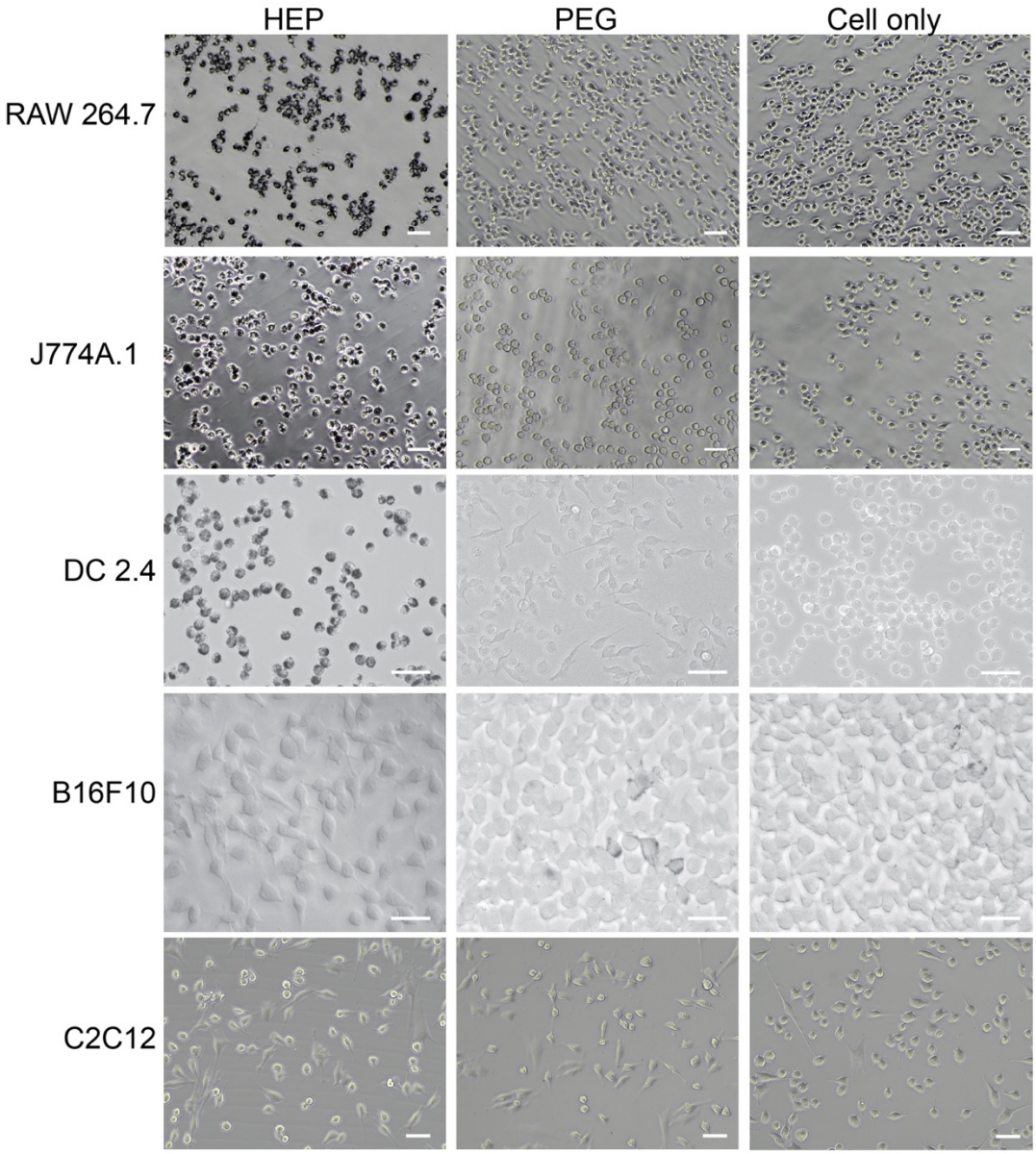

Figure S16: Light micrographs of different cell types after incubation with 55-nm HEP-AuNPs.

Either 0.2nM HEP-AuNPs or PEG-AuNPs were incubated with RAW 264.7, J774A.1 macrophages, DC2.4 dendritic cells, B16F10 melanoma, or C2C12 muscle cells for 6 hours. Cells were imaged with a brightfield light microscope after removing uninternalized AuNPs. Scale bars represent 50 μm.

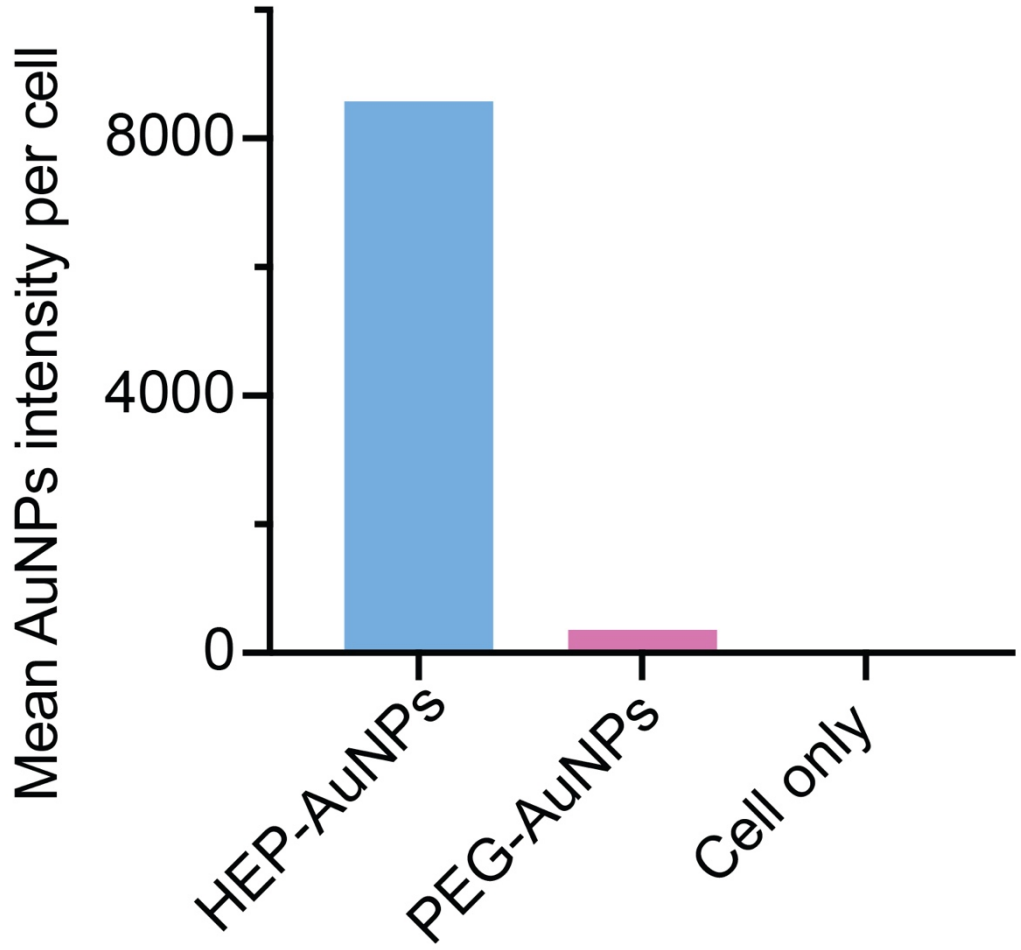

Figure S17: Quantification of the light scattering intensity of nanoparticles in cells.

Light scattering intensities of the gold nanoparticles in Figure 5 were quantified by manually drawing regions of interest around the cell membranes and measuring the integrated density in the light scattering channel on ImageJ.

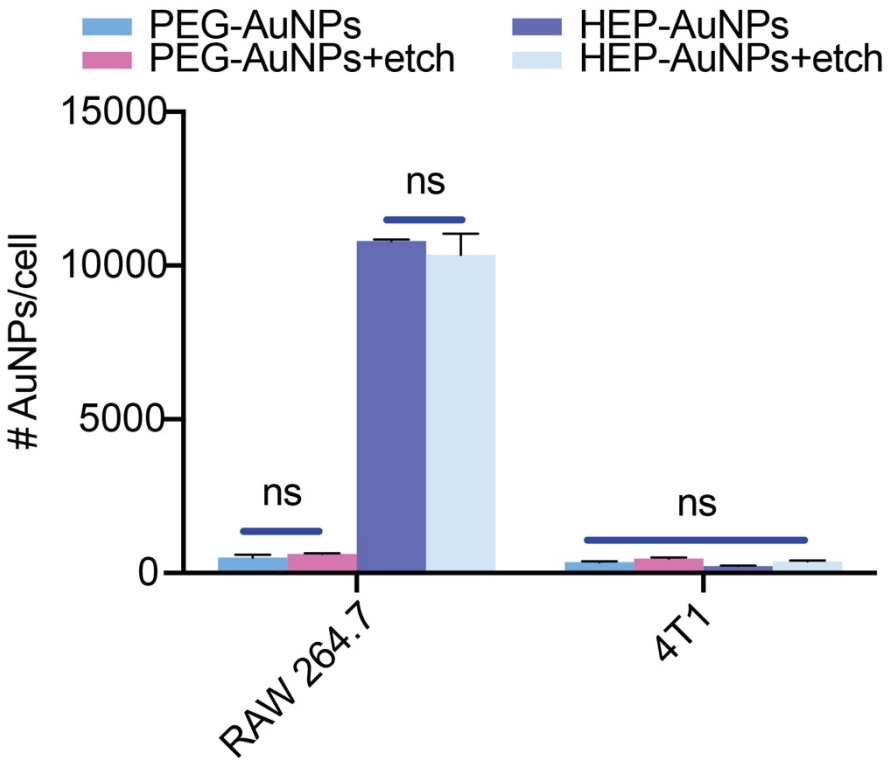

Figure S18: Cell uptake quantification of 15-nm HEP-AuNPs and PEG-AuNPs by ICP/MS in RAW 264.7 macrophages and 4T1 breast cancer cells with and without AuNPs etching.

The 15-nm HEP-AuNPs or control (PEG-AuNPs) were incubated with 4T1 murine breast cancer cells and RAW 264.7 murine macrophages. ICP-MS was performed to quantify the cell uptake of nanoparticles. Around 21x more HEP-AuNPs were internalized than PEG-AuNPs RAW 264.7 macrophage. True nanoparticle internalization was assessed by insensitivity to the KI/I_2 etchant. Bar graphs indicate mean ± SD (n=3-4).

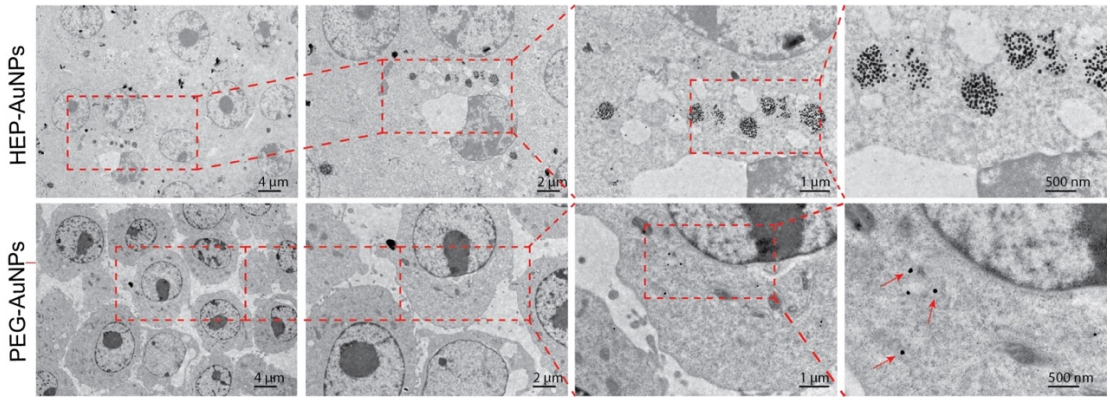

Figure S19: Transmission electron microscopy imaging of the subcellular distribution of 55-nm gold nanoparticles.

After 6 h incubation with 0.3 nM HEP- or PEG-AuNPs, the RAW 264.7 cells were collected and processed for TEM imaging. In TEM, AuNPs are observed as uniform black dots. Note that the magnification increases by ~2-fold in each panel from left to right, and the *dashed red lines* indicate the field of view selected for the next higher magnification. In the case of the less obvious signal with the PEG-coated AuNPs (lower rightmost panel), the *red arrows* indicate several individual AuNPs. The clusters of HEP-AuNPs are much more abundant.

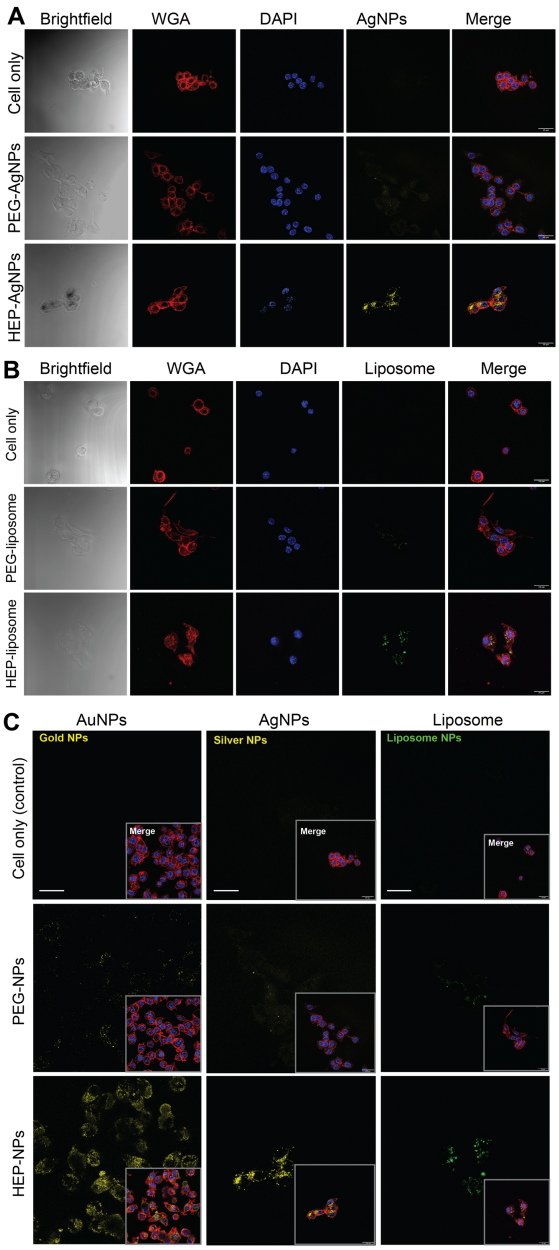

Figure S20: Cellular uptake of silver nanoparticles, liposomes, or gold nanoparticles with various coatings.

(**A-B**) Confocal laser scanning microscopy images (CLSM) of RAW 264.7 cells incubated with either silver nanoparticles (A) or liposome nanoparticles (B) for 2 h and 24 h, respectively. (**C**) CLSM images of HEP-coated gold, silver, and liposome uptake compared with nanoparticles with PEG coating and 'cell only' groups in DC 2.4 dendritic cell (gold nanoparticles) and RAW 264.7 cells (silver nanoparticles and liposomes).

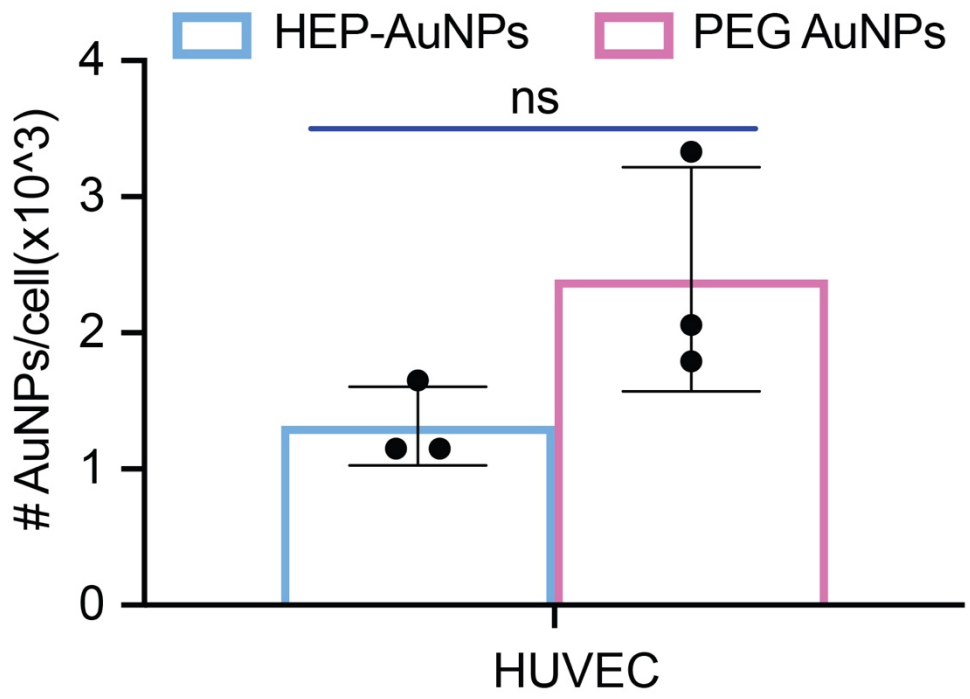

Figure S21: Cell uptake of polymer-coated 55-nm AuNPs in HUVEC endothelial cells.

Human endothelial cells were incubated with HEP-AuNPs or PEG-AuNPs. Nanoparticle cell uptake was quantified by ICP-MS. There was no difference in uptake between the two coated AuNPs. A T-test was used for statistical analysis (mean SD; n=3-4).

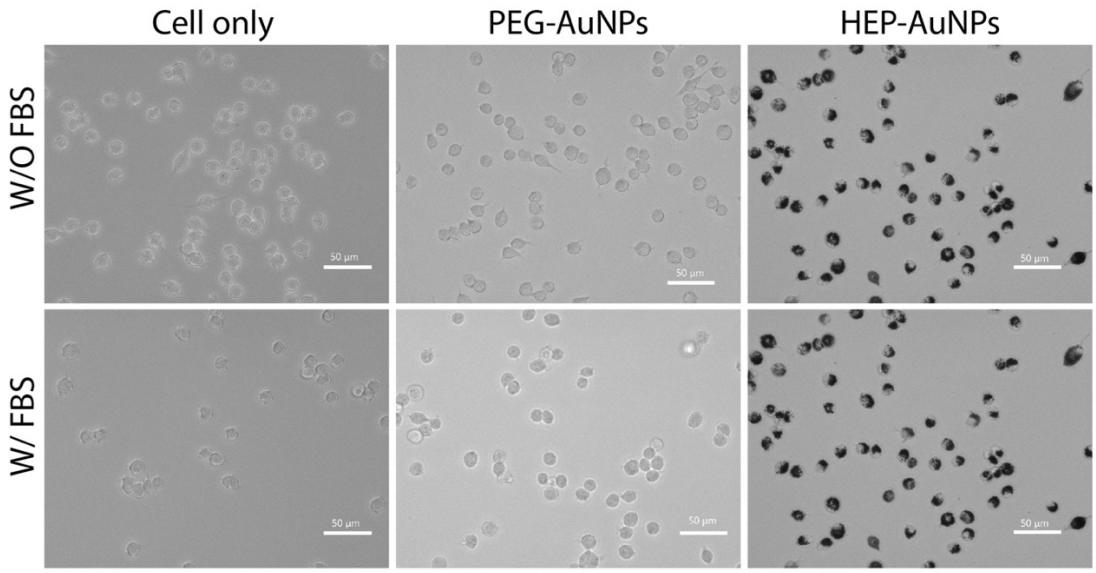

Figure S22: The effect of FBS incubation on cellular uptake.

Either 0.2nM HEP-AuNPs or PEG-AuNPs were incubated with DC 2.4 dendritic cells with or without FBS for 6 hours. Cells were imaged with a brightfield light microscope after removing uninternalized AuNPs. Scale bars represent 50 µm.

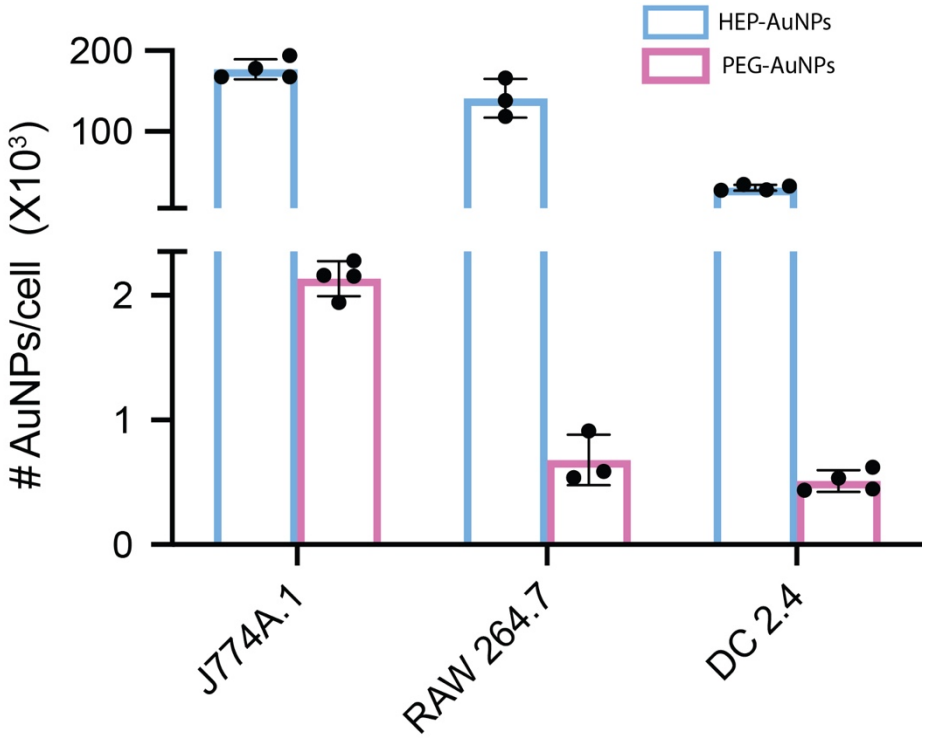

Figure S23: Cellular uptake of HEP-coated 55-nm AuNPs in J774A.1 macrophages, RAW 264.7 macrophages, and DC 2.4 dendritic cells.

The nanoparticle cell uptake was quantified by ICP-MS. About 70x, 230x, and 45x more HEP-AuNPs were internalized than PEG-AuNPs in J774A.1 macrophage, RAW 264.7 macrophage, and DC 2.4 dendric cells, respectively. Bar graphs indicate mean ± SD (n=3-4).

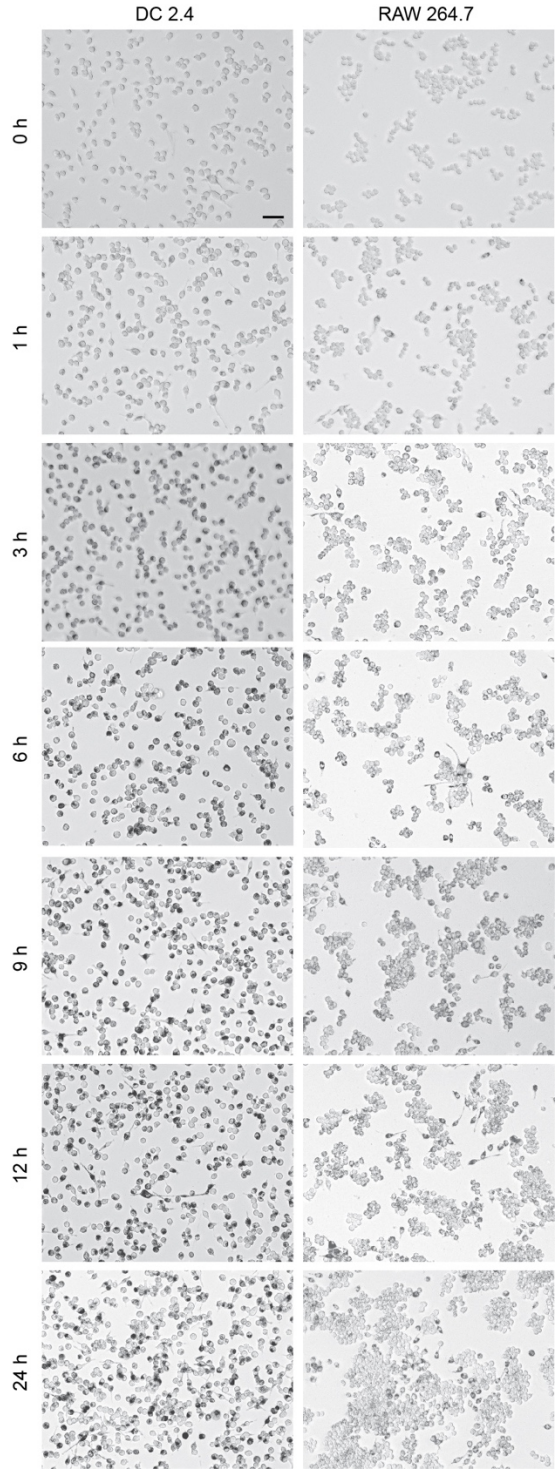

Figure S24: Light micrographs of HEP-AuNPs uptake over time.

The HEP-AuNPs (0.05 nM) were incubated with RAW 264.7 macrophages or DC 2.4 dendritic cells for 0 h, 1 h, 3 h, 6 h, 9 h, and 24 h. The cells were imaged with a bright-field light microscope after removing uninternalized AuNPs. Scale bars: 50 μm.

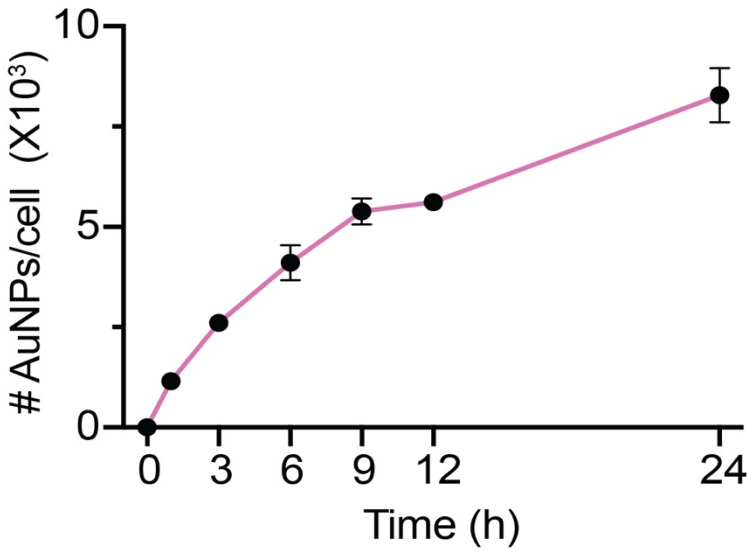

Figure S25: The cellular uptake kinetics of heparosan (HEP) modified gold nanoparticles (AuNPs) in DC 2.4 dendritic cells.

The graph shows results of ICP-MS quantification of 55-nm HEP-AuNPs cellular internalization in DC 2.4 dendritic cells at 0 h, 1 h, 3 h, 6 h, 9 h, 24 h. Data points represent mean ± SD (n = 3-4).

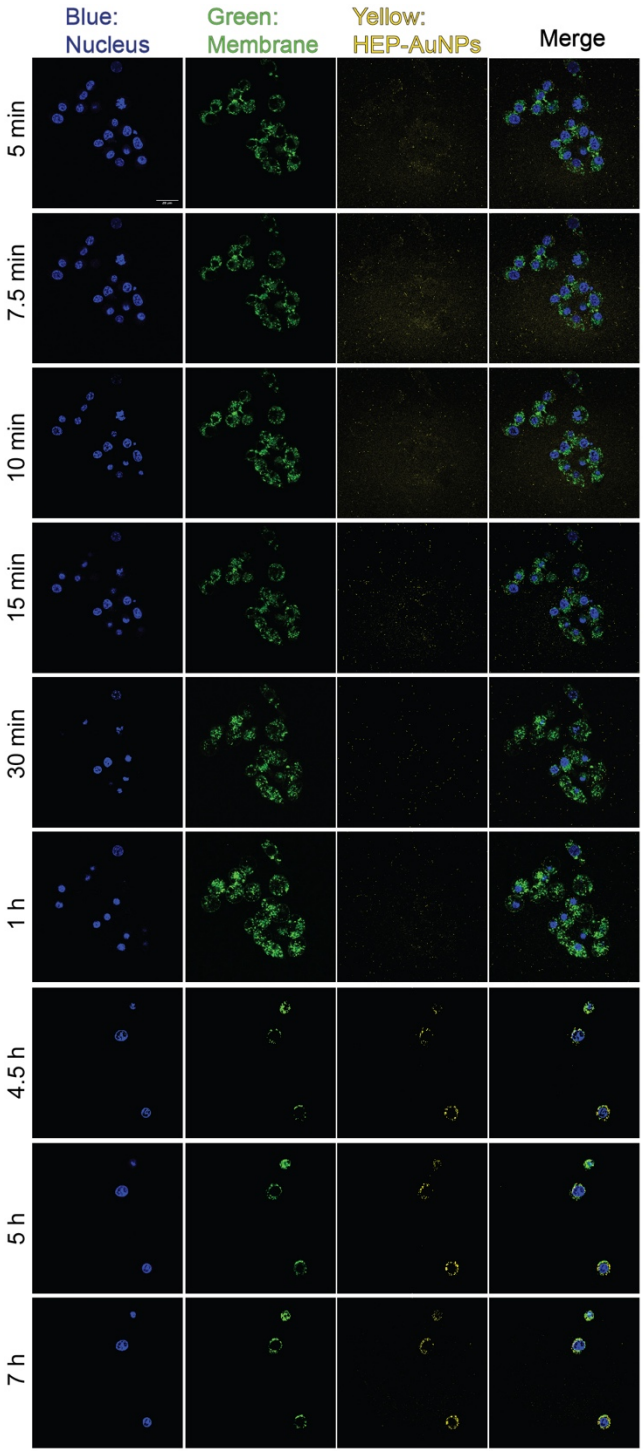

Figure S26: Confocal laser scanning micrographs of HEP-AuNPs uptake in real-time via live cell imaging.

HEP-AuNPs (0.2 nM) were incubated with RAW 264.7 macrophages for up to 7 h. Scale bar: 20 µm.

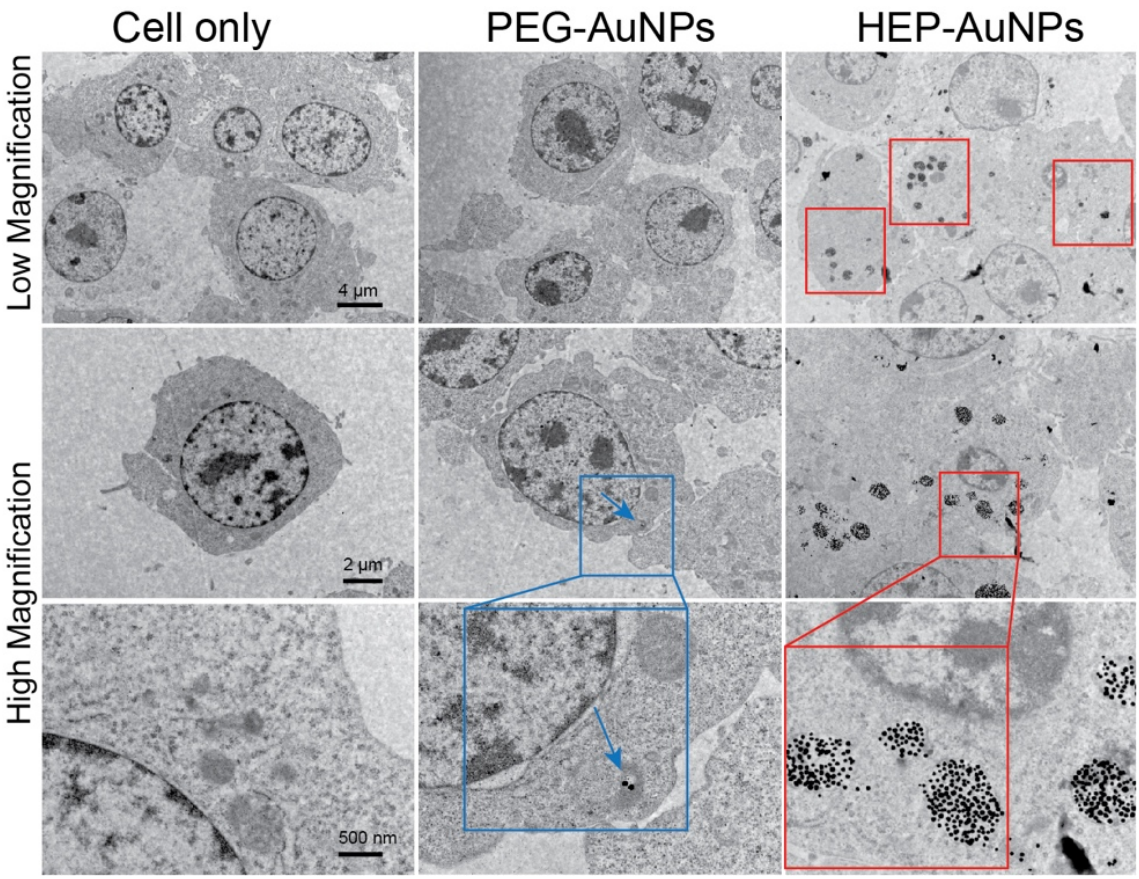

Figure S27: Internalization of heparosan (HEP) modified gold nanoparticles (AuNPs) in RAW 264.7 macrophages.

Transmission electron micrographs of 0.2 nM 55-nm HEP-AuNPs (red box) in RAW 264.7 cells after 3 h, 6 h and 24 h incubation. Control group: PEG-modified AuNPs (blue box). Note that the magnification increases by 2-fold or 4-fold in each panel from top to bottom, and the colored boxes indicate the field of view selected for the next higher magnification. In the case of the less obvious signal with the PEG-modified AuNPs (second column images, blue box), a blue arrow indicates the location of these nanoparticles.

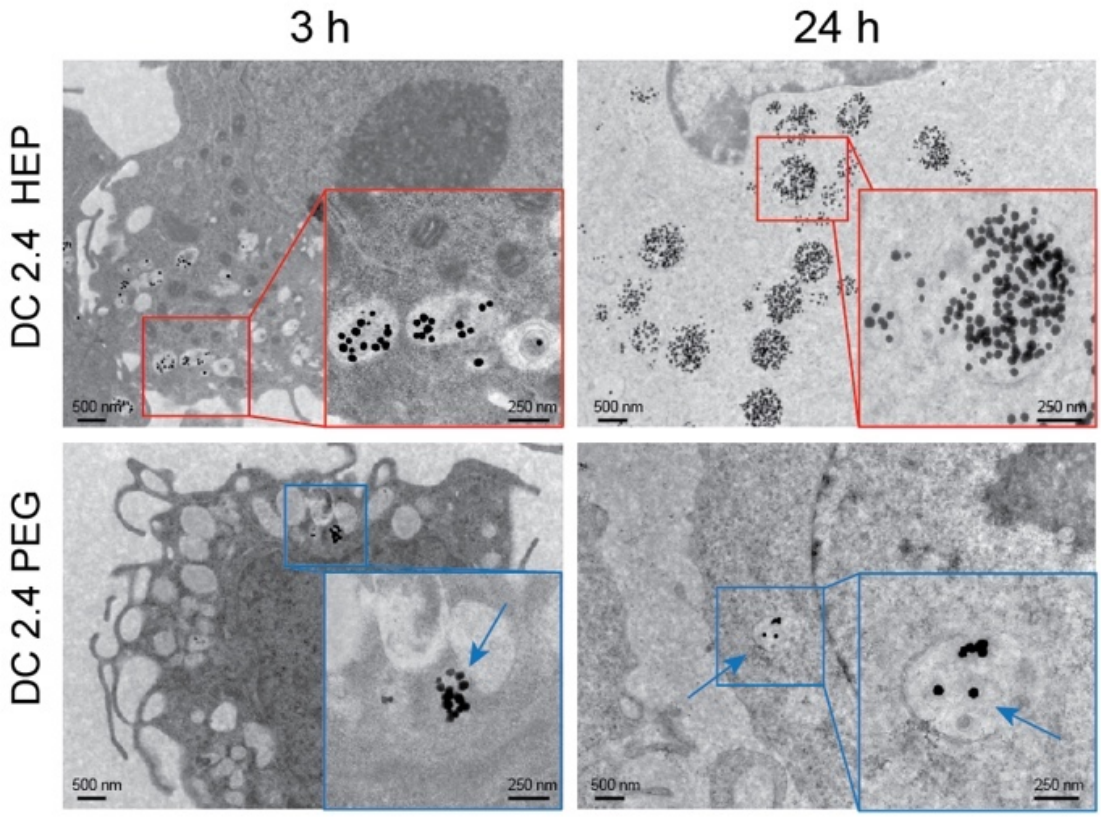

Figure S28: Internalization of heparosan (HEP) modified gold nanoparticles (AuNPs) in DC 2.4 dendritic cells.

Transmission electron microscopy images of 0.2 nM HEP-AuNPs (red box) in DC 2.4. dendritic cells after 3 h, and 24 h incubation, with PEG-AuNPs (blue box) as control. Inserts at the bottom right-hand corners show high-resolution images of selected areas.

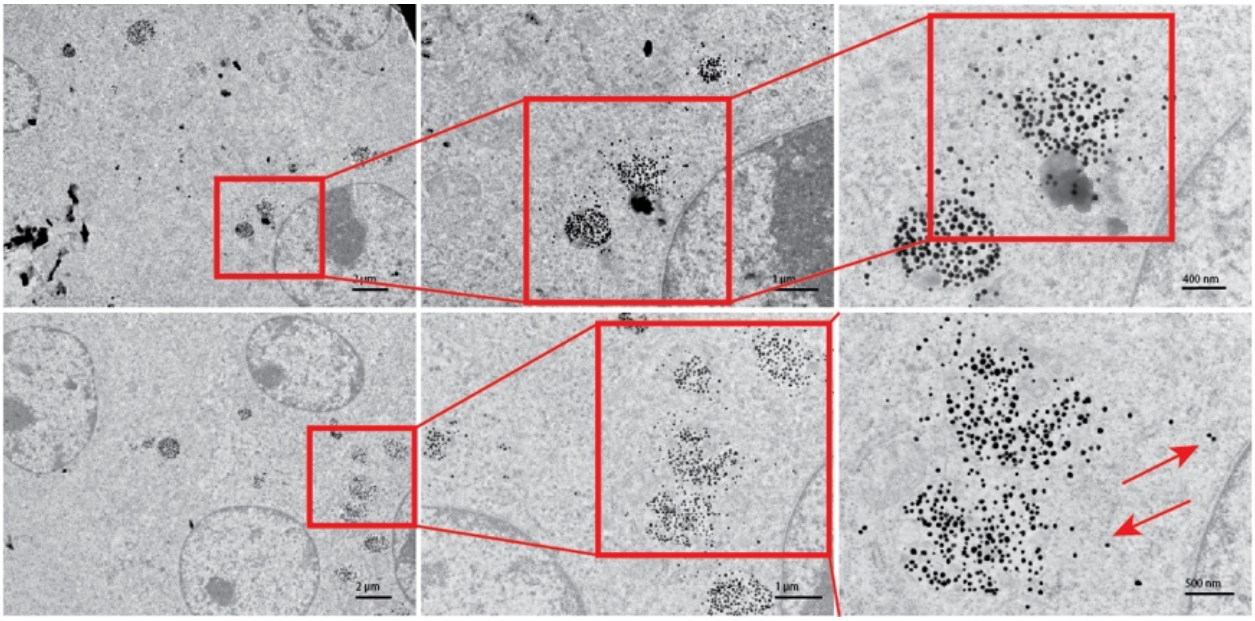

Figure S29: HEP-AuNPs escape from intracellular vesicles.

Transmission electron microscopy images of 0.2 nM 55-nm HEP-AuNPs in RAW 264.7 after 6 h incubation. Note that the magnification increases from left to right, and the red box indicates the field of view selected for the next higher magnification. The red arrows indicate examples of nanoparticles that appear outside of intracellular vesicles.

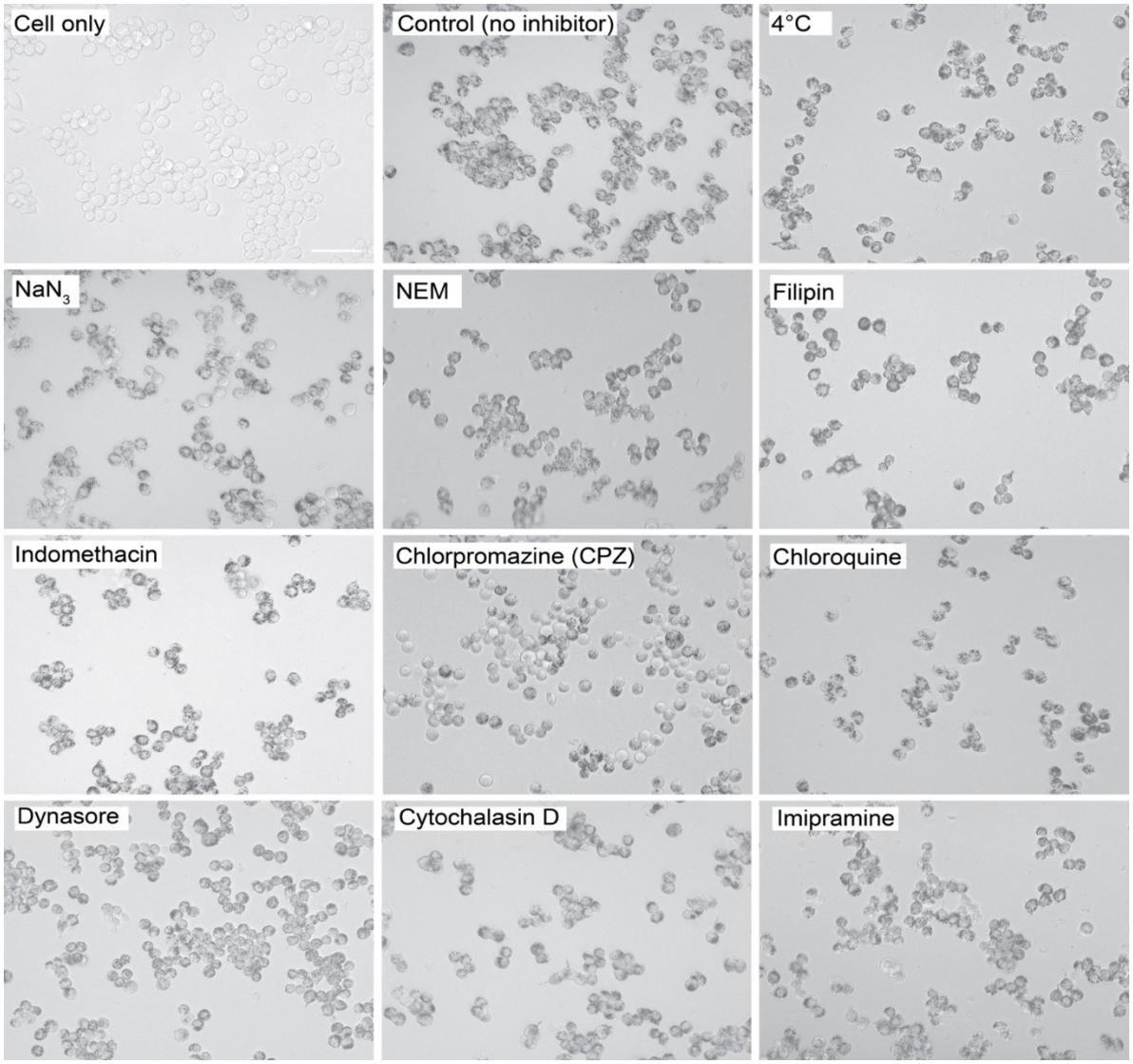

Figure S30: Light micrographs of HEP-AuNP cellular uptake at low temperature, with sodium azide, or with various other endocytic inhibitors.

Light micrographs of RAW 264.7 macrophages cellular uptake of HEP-AuNPs in the presence of endocytosis inhibitors. The cells were preincubated with inhibitors of caveolae-mediated endocytosis, clathrin-mediated endocytosis, or macropinocytosis/phagocytosis for 1 h. HEP-AuNPs were then added with another 1.5 h incubation. Scale bar: 50 μm.

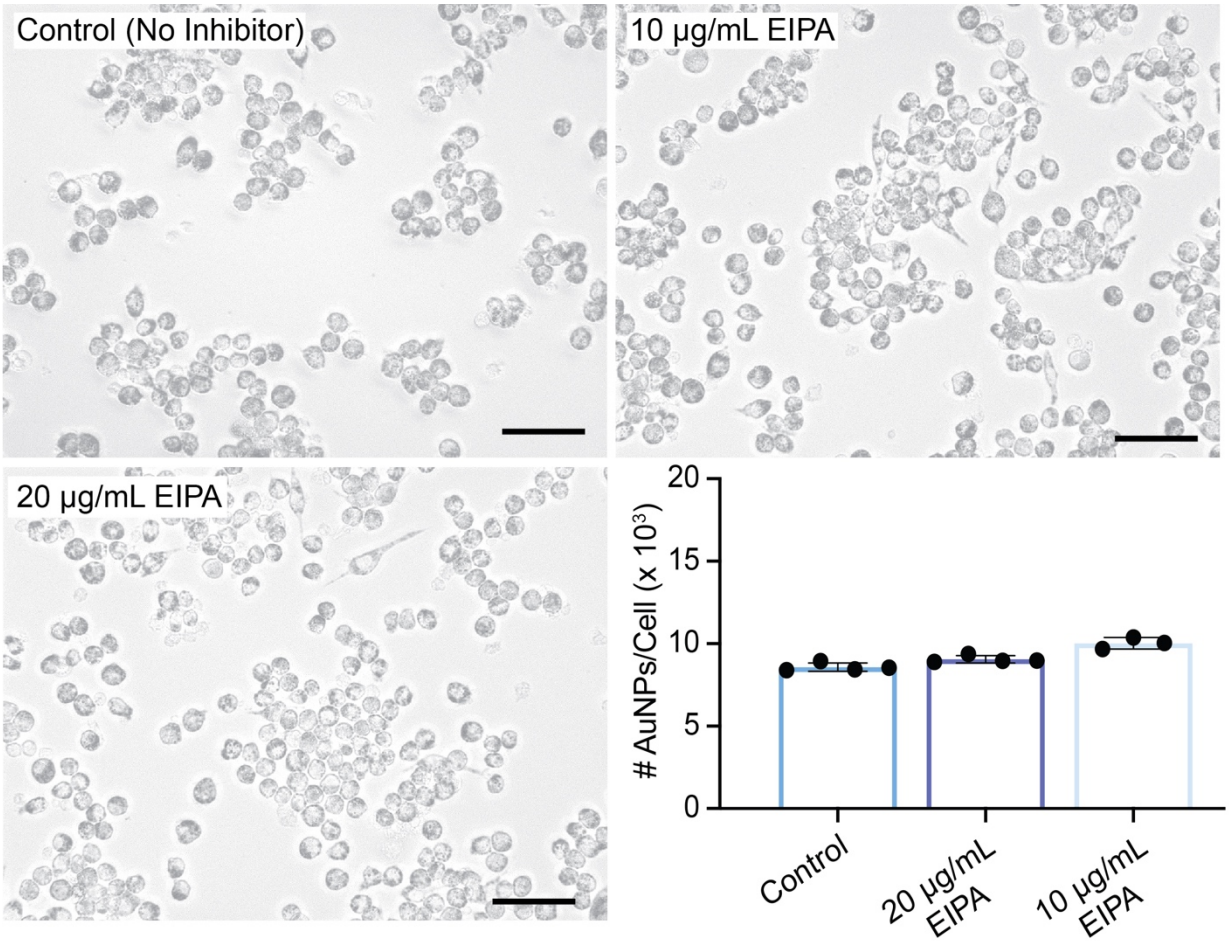

Figure S31: The lack of an inhibition effect of EIPA on 55-nm HEP-AuNP cellular internalization.

Light micrographs and ICP-MS quantification results of RAW 264.7 macrophages cellular uptake of HEP-AuNPs in the presence of 0, 10 or 20 µg/mL EIPA inhibitors. The cells were pre-treated with inhibitors for 1 h, then HEP-AuNPs were added for another 2.5 h of incubation. Scale bar: 50 µm.

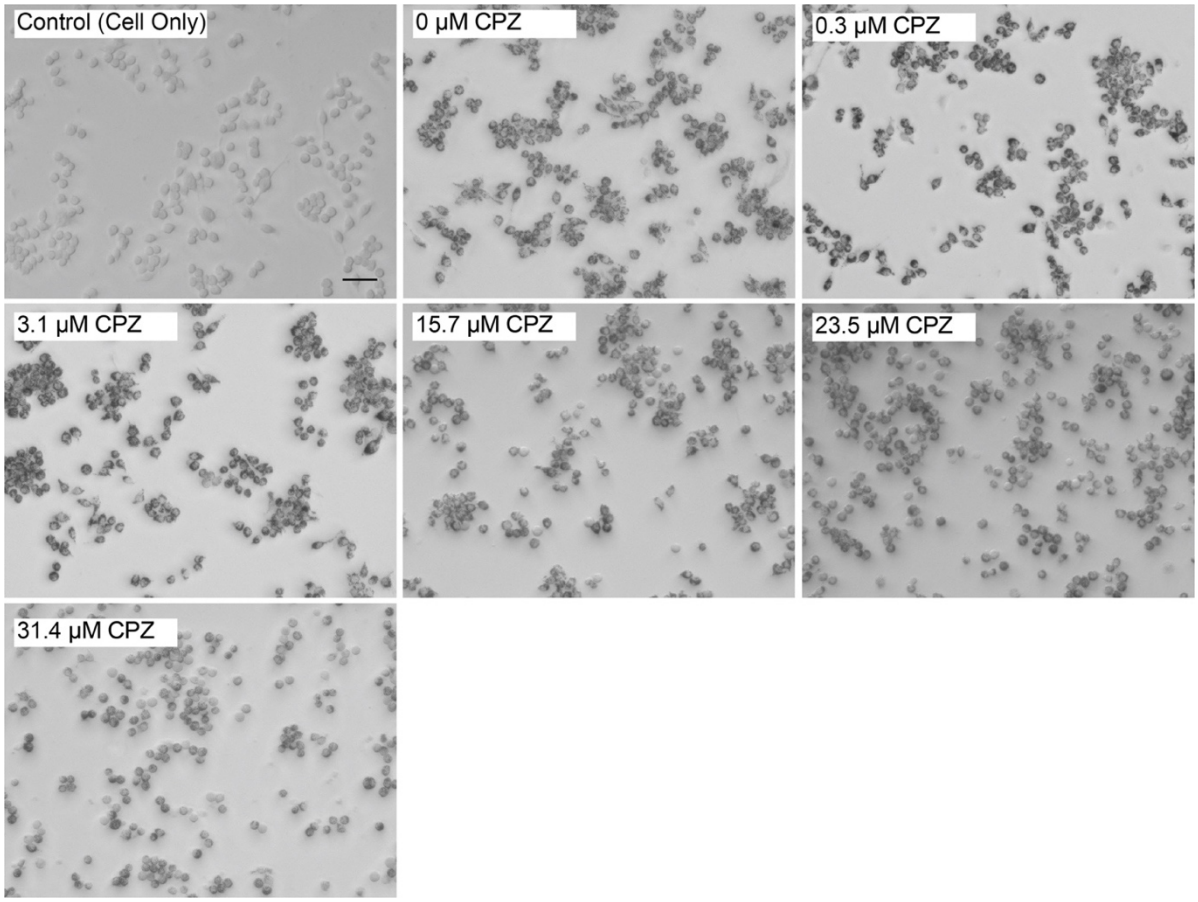

Figure S32: Light micrographs showing the effect of chlorpromazine on HEP-AuNPs cellular internalization.

Light micrographs of RAW 264.7 macrophages cellular uptake of HEP-AuNPs in the presence of 0.05, 0.1, 1, 5, 7.5, 10, or 15 µg/mL chlorpromazine (CPZ), a clathrin-mediated endocytosis inhibitor. The cells were pretreated with inhibitors for 1 h, then HEP-AuNPs were added for another 1.5 h of incubation. scale bar: 50 µm.

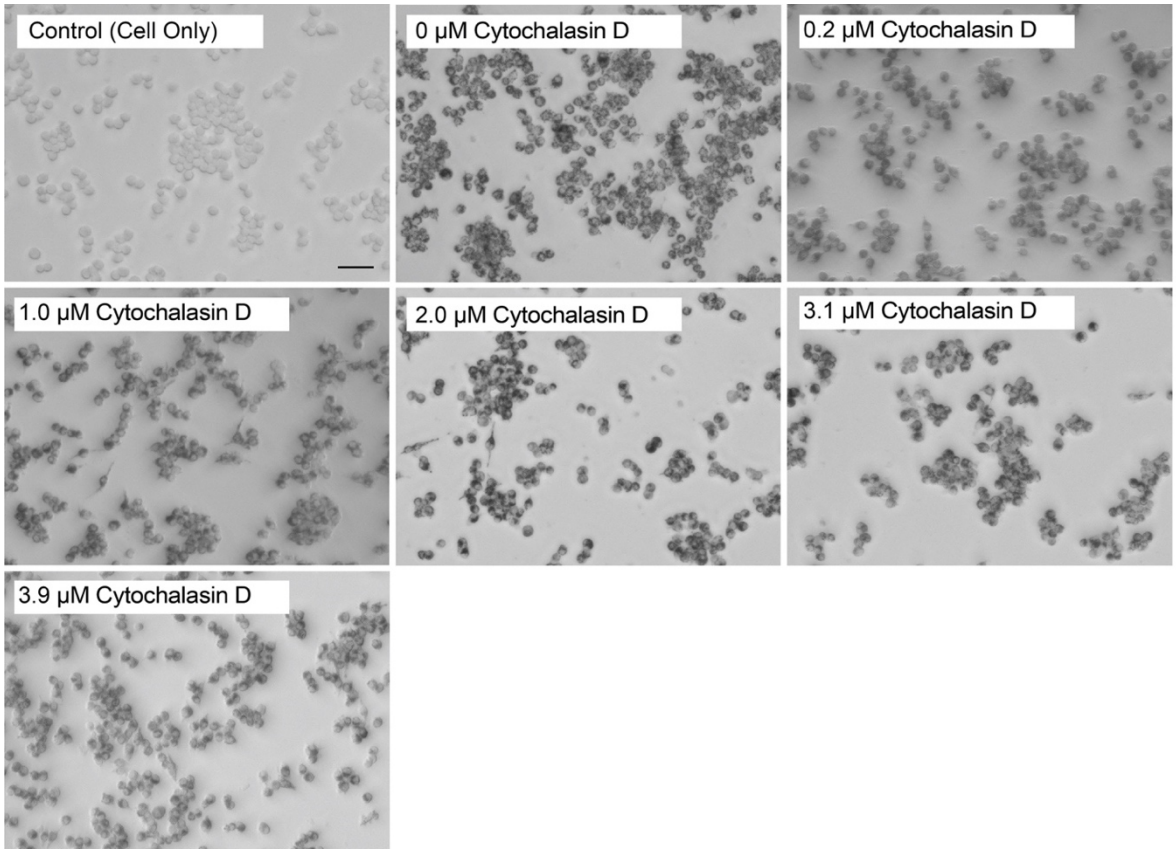

Figure S33: Light micrographs showing the inhibition effect of cytochalasin D on HEP-AuNPs cellular internalization.

Light micrographs of RAW 264.7 macrophages cellular uptake of HEP-AuNPs in the presence of 0.1, 0.5, 1, 1.5, and 2 μg/mL cytochalasin D, a macropinocytosis inhibitor. The cells were pretreated with inhibitors for 1 h, then HEP-AuNPs were added for another 1.5 h of incubation. Scale bars: 50 μm.

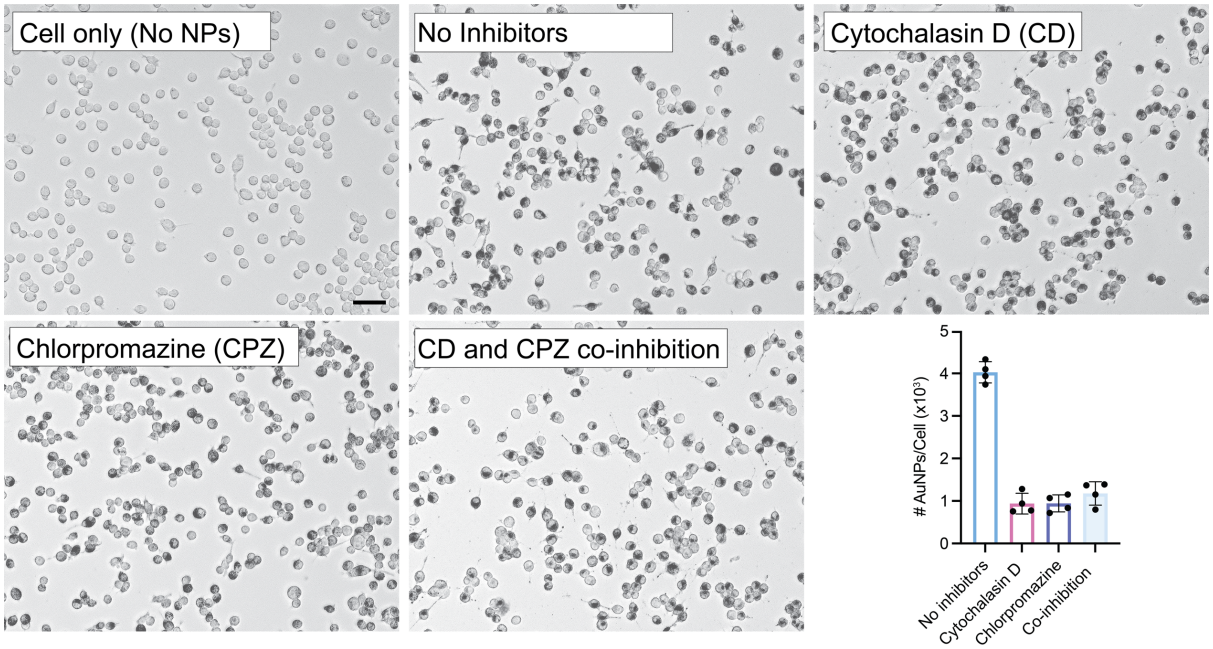

Figure S34: Light micrographs and ICP-MS results of the endocytosis inhibitor effect on DC 2.4 cells.

Light micrographs and ICP-MS results of HEP-AuNPs cellular uptake in DC 2.4 treated with an individual inhibitor (chlorpromazine or cytochalasin D) or both inhibitors (CO, co-incubation with chlorpromazine and cytochalasin D). The cells were pre-treated with inhibitors for 1 h, and then HEP-AuNPs were added for another 1.5 h of incubation. Scale bar: 50 µm. Data points in lower left corner bar graph represent mean ± SD (n = 3-4).

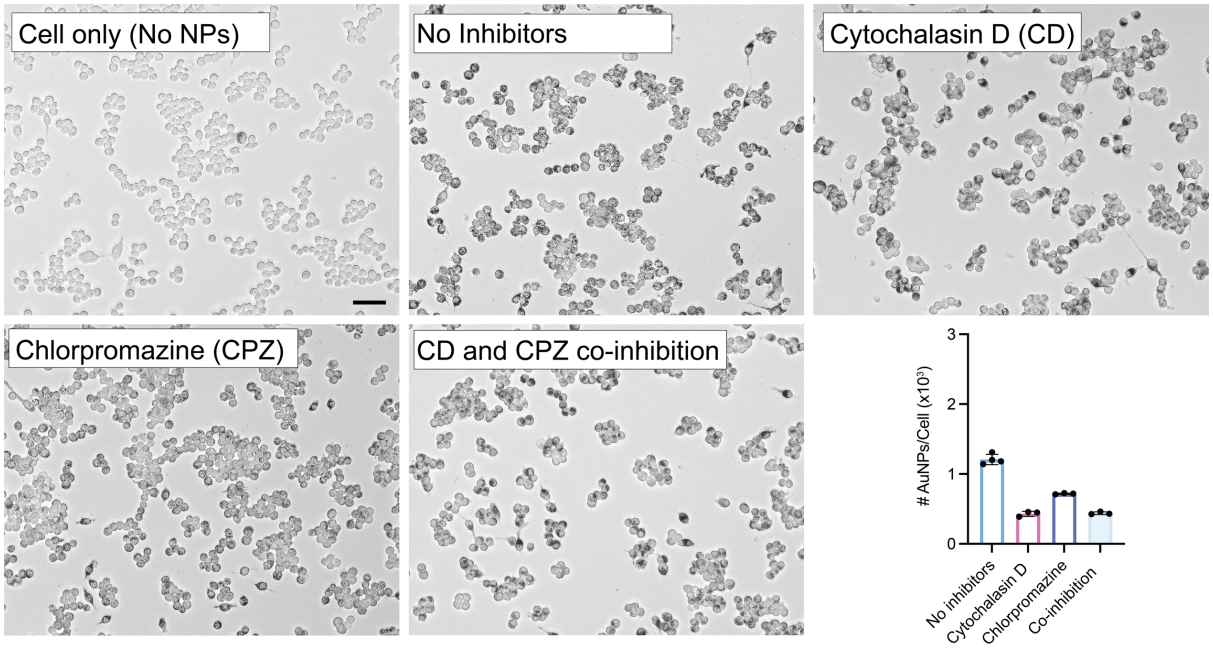

Figure S35: Light micrographs and ICP-MS results of the endocytosis inhibitor effect on RAW 264.7 cells.

Light micrographs and ICP-MS results of HEP-AuNPs cellular uptake in RAW 264.7 treated with an individual inhibitor (chlorpromazine or cytochalasin D) or both inhibitors (CO, co-incubation with chlorpromazine and cytochalasin D). The cells were pre-treated with inhibitors for 1 h, and HEP-AuNPs were added for another 1.5 h of incubation. Scale bar: 50 μm. Data points in bar graph represent mean ± SD (n = 3-4).

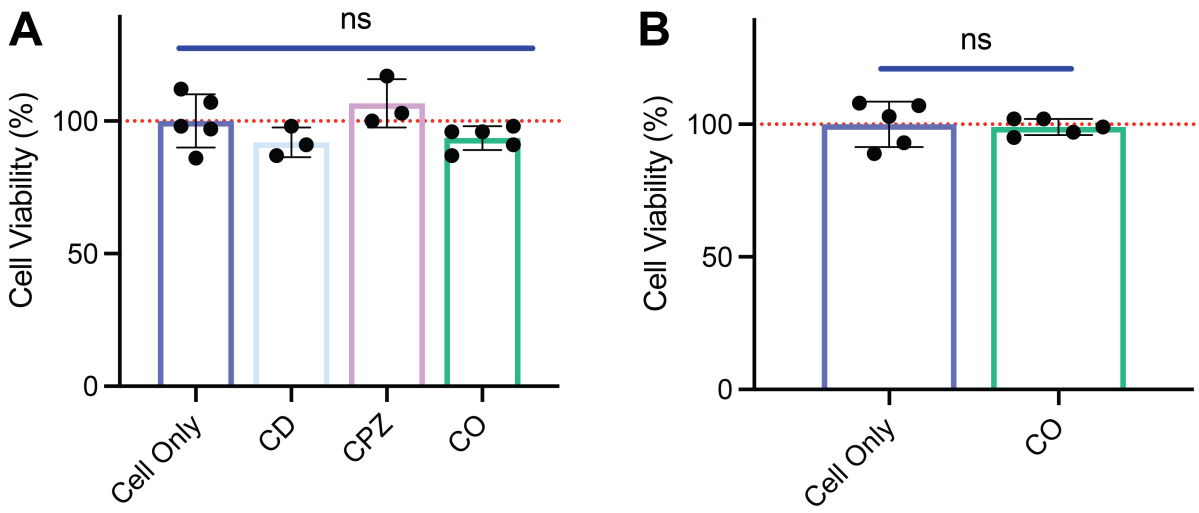

Figure S36: Cell viability of chlorpromazine and cytochalasin D in DC 2.4 and RAW 264.7 cells.

Results of XTT assays measuring the cell viability of DC 2.4 (panel A) and RAW 264.7 macrophages (panel B) treated with an individual inhibitor (chlorpromazine or cytochalasin D) or both inhibitors (CO, co-incubation with chlorpromazine and cytochalasin D). Bar graphs indicate mean ± SD (n=3-5). The cells were pre-treated with inhibitors for 1 h, then HEP-AuNPs were added for another 1.5 h of incubation. Statistical tests were performed using one-way ANOVA for panel A and an unpaired t-test for panel B (n.s. indicates no statistically significant differences).

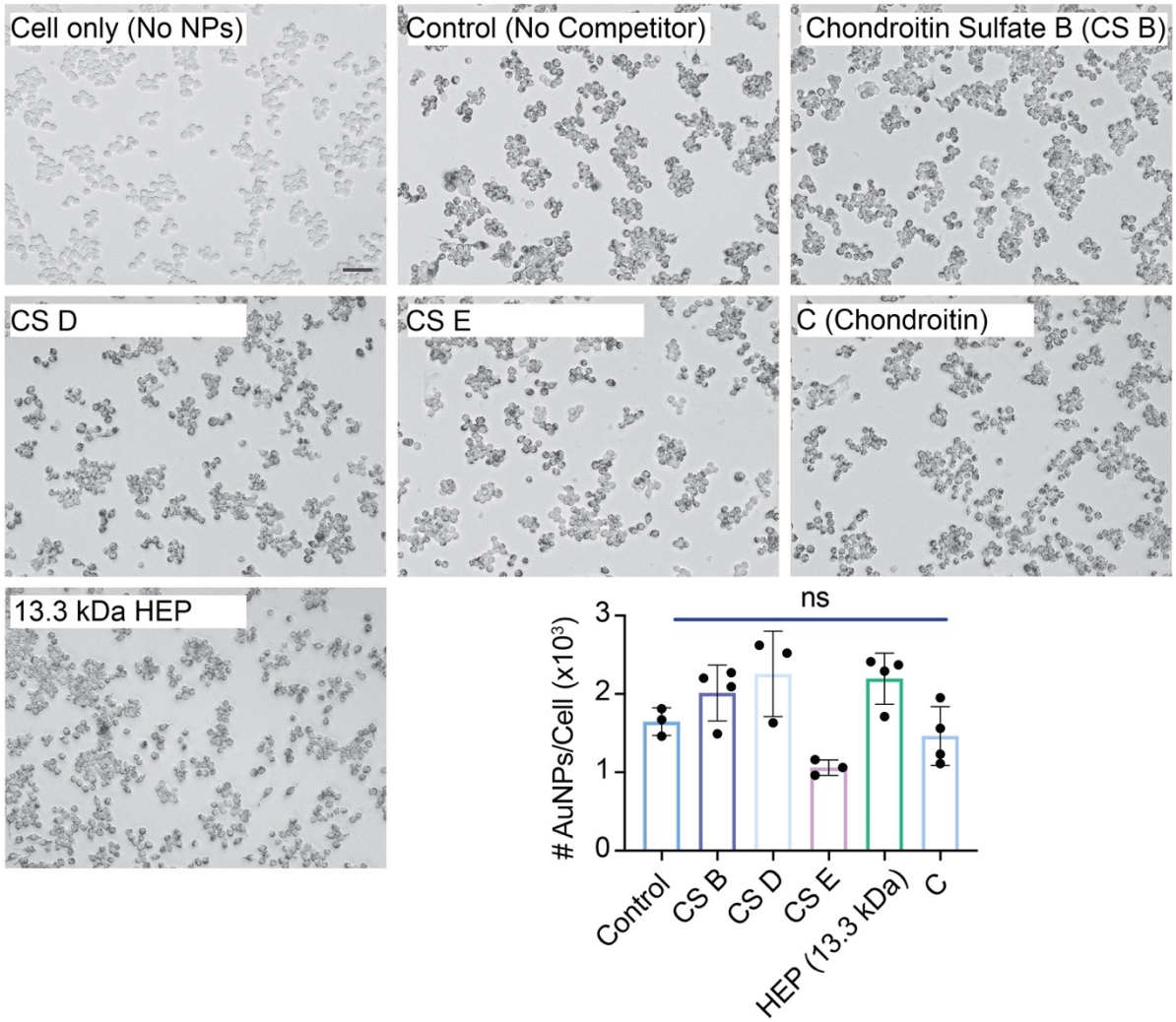

Figure S37: Light micrographs and ICP-MS results of GAG structural analogs for competition experiments using RAW 264.7 cells.

The cells were pre-incubated with competitors (1 mg/mL CS B, CS D, CS E, or Chondroitin; 0.1 mg/mL 13.3-kDa HEP) for 1 h, a concentration of 0.1 nM of 55-nm HEP-AuNPs was added into the well plates followed by another 2.5 h of incubation with cells in the presence of competitors. The nanoparticle uptake was examined with a light microscope (scale bar: 50 μm) and quantified by ICP-MS. Statistical tests were performed using one-way ANOVA (n.s. indicates no statistically significant differences). Bar graphs indicate mean ± SD (n=3-4).

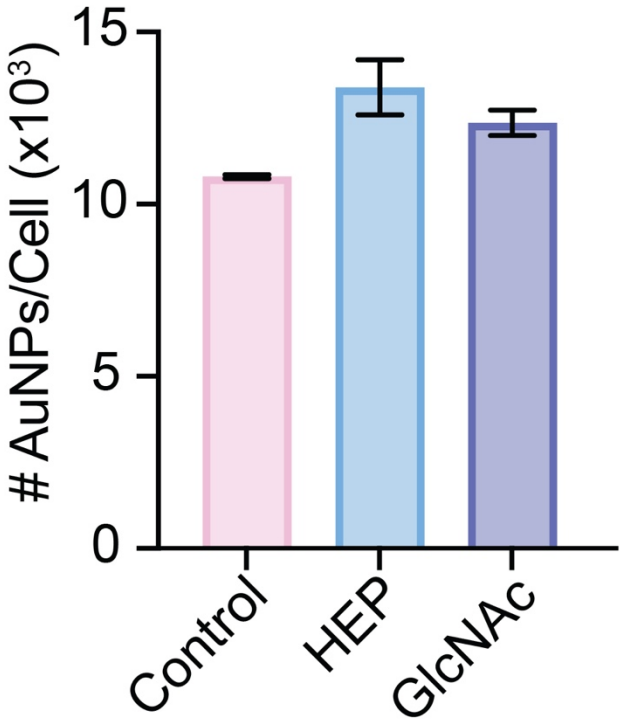

Figure S38: ICP-MS quantification of HEP-AuNPs cellular uptake in the presence of HEP or GlcNAc.

Either 1.4 mg/mL (32 μM) 43.8-kDa heparosan or 6.6 mg/mL (30 mM) N-acetyl-glucosamine (GlcNAc) were pre-incubated with RAW 264.7 for 30 min, and then 14-nm HEP-AuNPs (2.0 nM) were added for another 6 h. Bar graphs indicate mean ± SD (n=3-4).

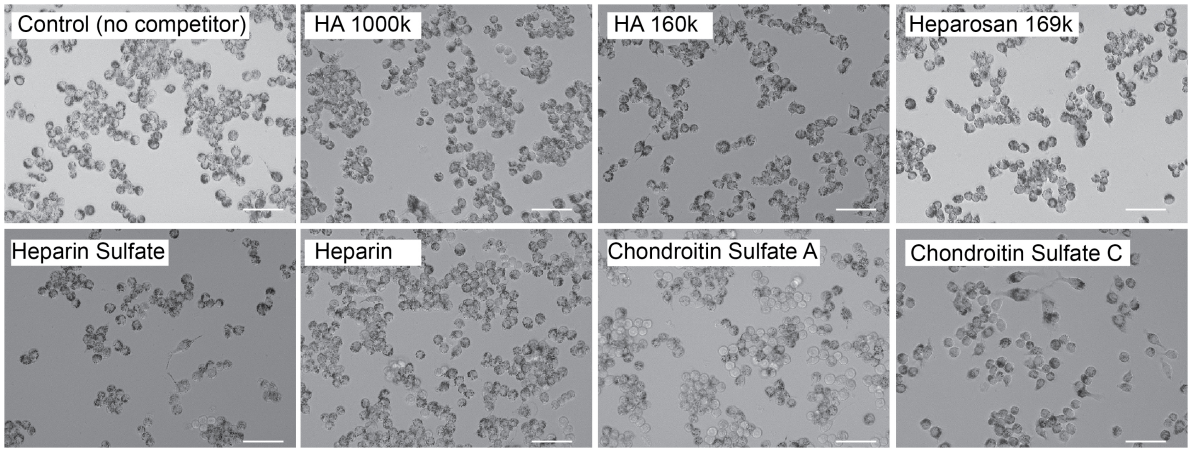

Figure S39: Light micrographs of 55-nm HEP-AuNPs uptake in RAW 264.7 cells in the presence of various GAG competitors.

Except for chondroitin sulfate A and C, which were 1 mg/mL, all competitors were dosed at 0.1 mg/mL. The competitors were preincubated with cells for 1 h, and HEP-AuNPs were added for an additional 2.5 h of incubation in the presence of the competitors. Scale bars: 50 µm.

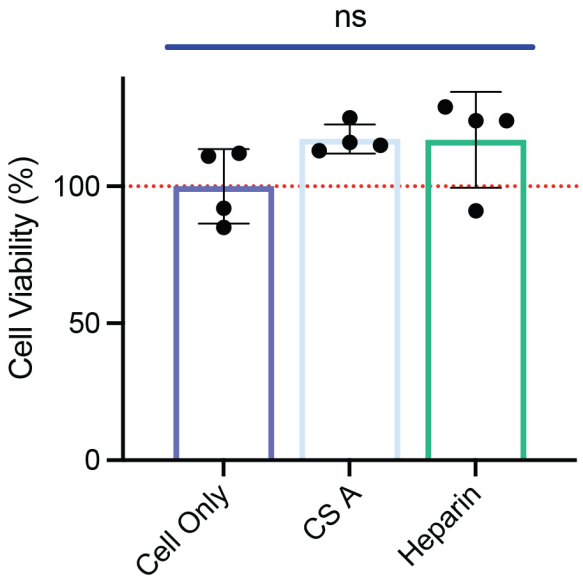

Figure S40: Cell viability of RAW 264.7 macrophages in the presence of CS A or heparin.

The XTT assay was used to test the cell viability of 1 mg/mL CS A or 0.1 mg/mL heparin. The incubation time is 3.5 h. Bar graphs indicate mean ± SD (n=4). Statistical tests were performed using one-way ANOVA (n.s. indicates no statistically significant differences).

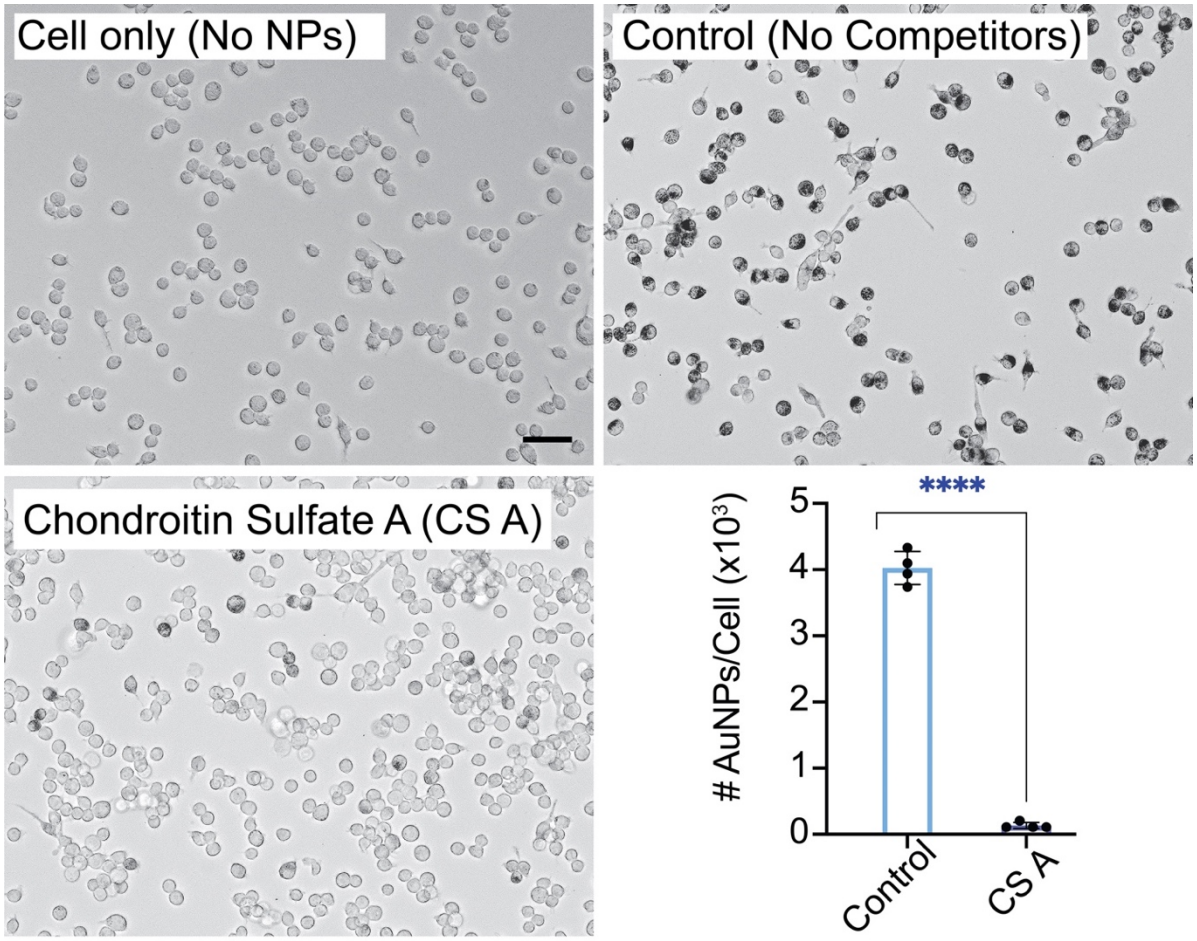

Figure S41: Light micrographs and ICP-MS results of CS A competition experiment using DC 2.4 cells.

The cells were pre-incubated with 1 mg/mL CS A for 1 h, then 55-nm HEP-AuNPs (0.1 nM) were added into the well plate followed by another 2.5 h of incubation with cells. The nanoparticle uptake was examined under the light microscope and quantified by ICP-MS. Bar graphs indicate mean ± SD (n=4). Statistical tests were performed using an unpaired t-test ($p<0.0001$ (****).

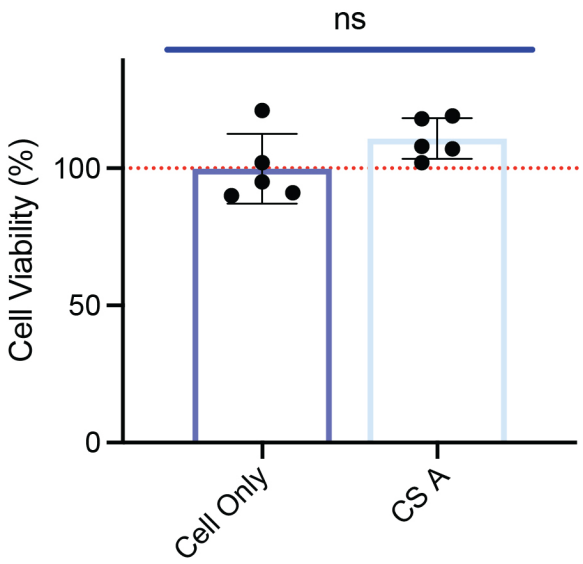

Figure S42: Effect of CS A on cell viability of DC 2.4 dendritic cells (1 mg/mL; 3.5 h).

The XTT assay was used to test the cell viability of DC 2.4 cells using 1 mg/mL CS A after 3.5 h of incubation. Bar graphs indicate mean ± SD (n=5). Statistical tests were performed using an unpaired t-test (n.s. indicates no statistically significant differences).

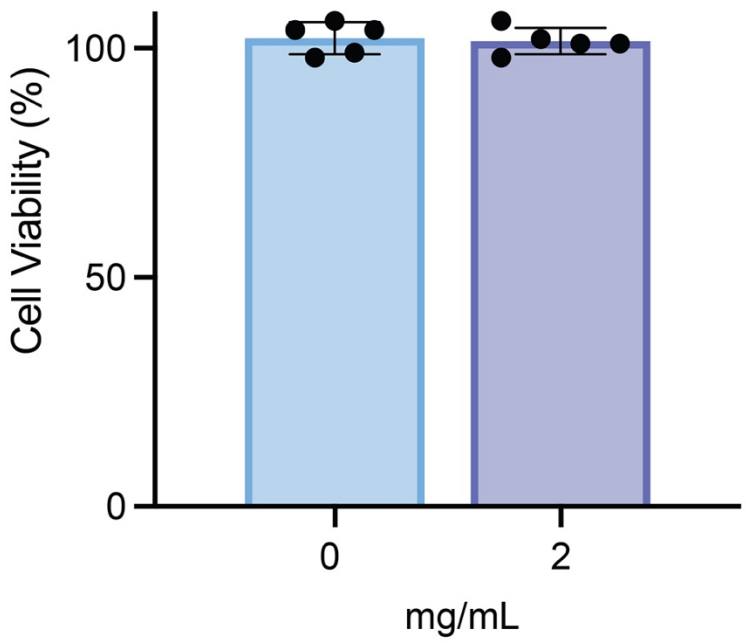

Figure S43: Effect of CS A on cell viability of DC 2.4 dendritic cells (2 mg/mL; 25 h).

The XTT assay was used to test the cell viability after treatment with 2 mg/mL CS A for 25 h. Bar graphs indicate mean ± SD (n=5).

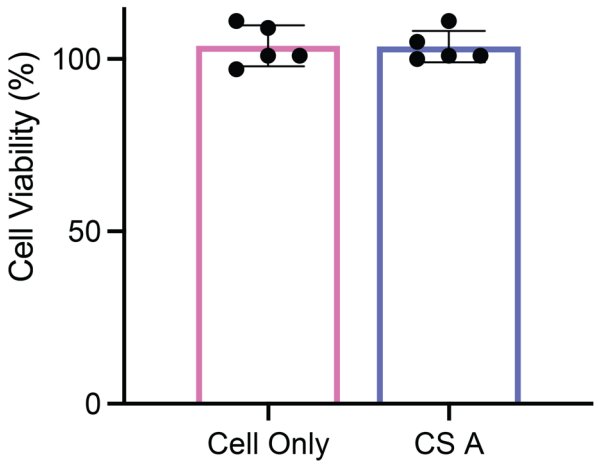

Figure S44: Effect of CS A on cell viability of DC 2.4 dendritic cells (2 mg/mL; 4.5 h).

The XTT assay was used to test the cell viability after 2 mg/mL CS A treatment for 4.5 h. Bar graphs indicate mean ± SD (n=5).

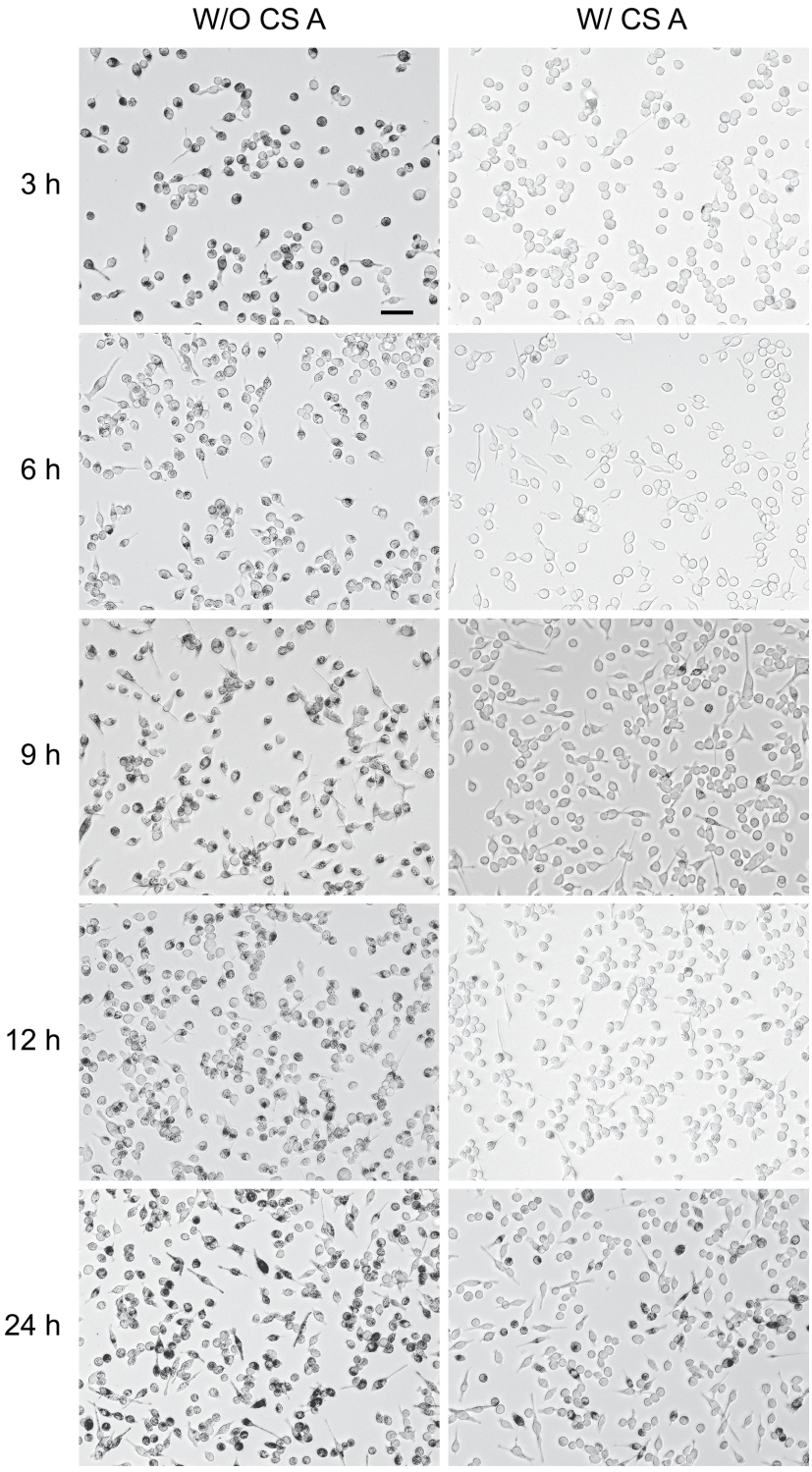

Figure S45: Light micrographs of CS A competition effect on HEP-AuNPs cellular uptake over time.

CS A (1 mg/mL) was preincubated with DC 2.4 cells for 1 h. Then, HEP-AuNPs (0.05 nM) were added for an additional 3 h, 6 h, 9 h, or 24 h of incubation. The cells were imaged by a light microscope in bright-field mode after removing uninternalized AuNPs. Scale bar: 50 µm.

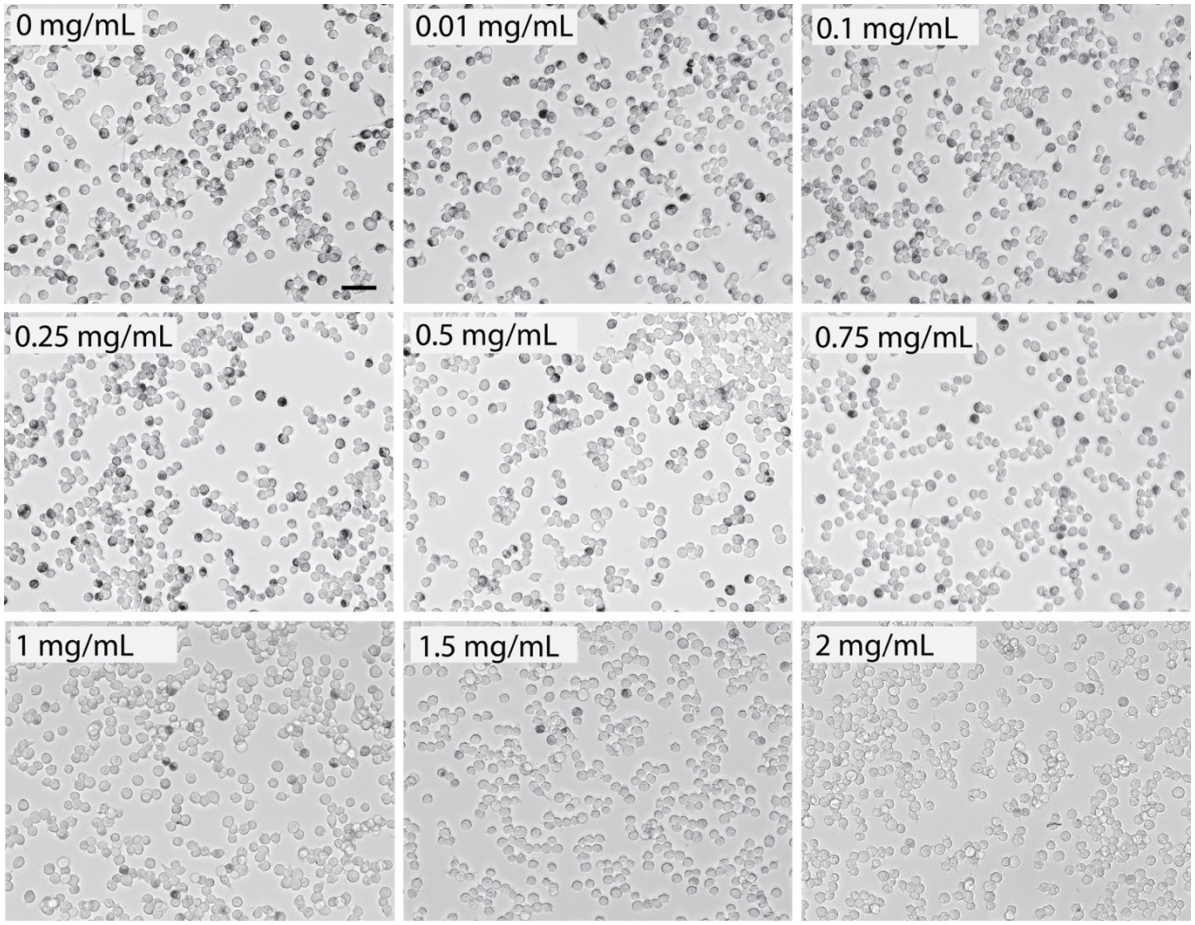

Figure S46: Light micrographs of CS A competition effect on HEP-AuNPs cellular uptake.

Various concentrations of CS A were used to pre-incubate DC 2.4 cells for 1 h. 0.05 nM HEP-AuNPs were added to DC 2.4 for 3.5 h of incubation. The cells were imaged by a light microscope in the bright-field mode after removing the uninternalized AuNPs. Scale bar: 50 μm.

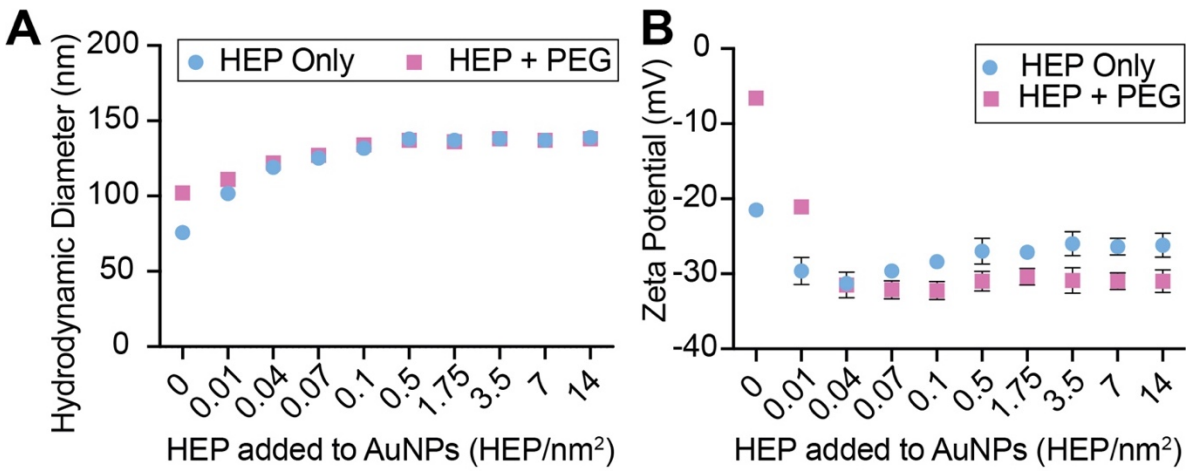

Figure S47. The physical characterization of HEP- or PEG-coated AuNPs.

(A-B) Dynamic light scattering (DLS) was used to characterize the hydrodynamic diameter (A) and zeta potential (B) of HEP/PEG AuNPs. Data points represent mean ± SD (n = 4).

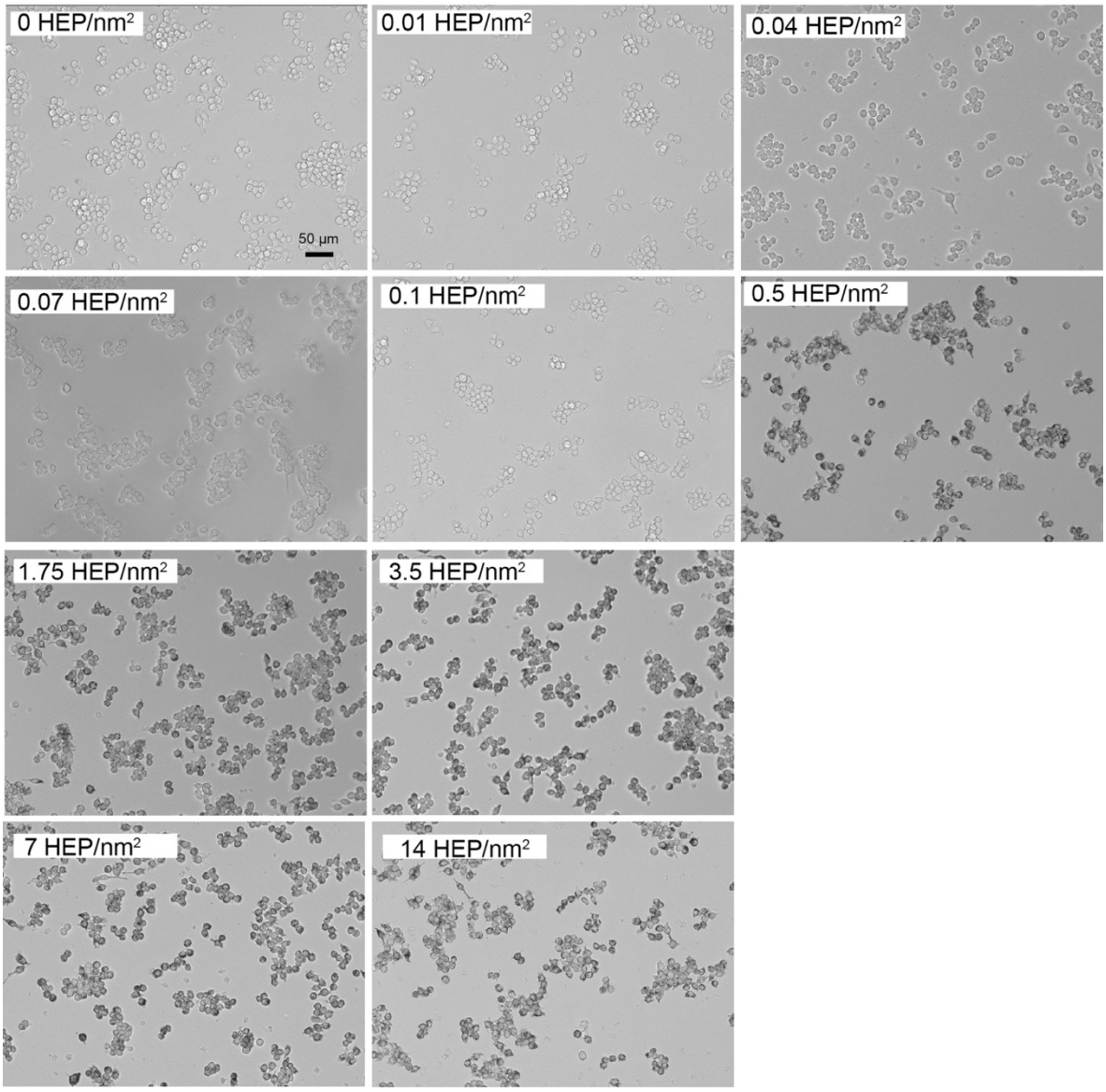

Figure S48: Light micrographs of RAW 264.7 cells incubated with AuNPs possessing different heparosan (HEP) coating densities.

Bright-field light microscope images of cells incubated with HEP-AuNPs at various HEP surface densities. The number of HEP densities in a synthesis process (as noted in the images) shows the quantity of HEP added to a coating reaction. Scale bar: 50 µm.

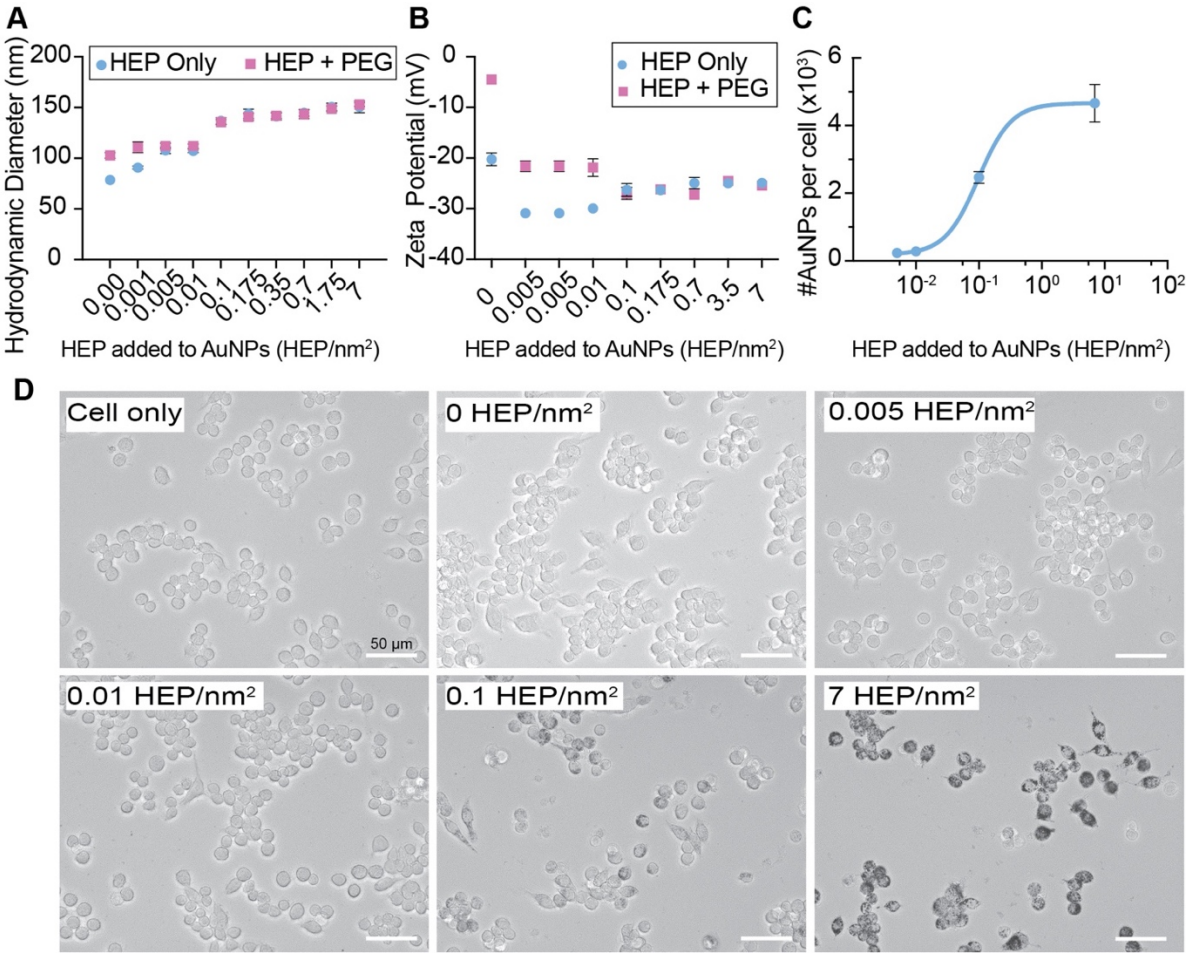

Figure S49: Effect of HEP coating density on AuNP physical parameters and RAW cell uptake.

(A-B) Dynamic light scattering (DLS) was used to characterize the hydrodynamic diameter (A) and zeta potential (B) of various HEP coating densities of AuNPs before and after the back-filling of uncoated surface area with poly(ethylene glycol), PEG. **(C)** The nanoparticle cell uptake efficiencies were measured as a function of surface HEP density by ICP-MS. All conditions were adjusted to 0.06 nM HEP-AuNPs for the uptake studies. The graphs indicate mean ± SD (n=3-4). **(D)** Selective bright-field light micrographs of different surface density HEP-coated AuNPs with RAW264.7 cells after removing the uninternalized nanoparticles before ICP-MS analysis. The number of HEP densities in a synthesis process (as noted in the images) shows the quantity of HEP added to a coating reaction. Scale bars: 50 µm.

Appendix B: List of Supporting Figures

Table S1: Summary of proteins identified from LC/MS-MS.

Abbrev	Full Name	MW[1] (Da)	Biological Process
KNG1	Kininogen-1	71,957	Blood coagulation, Hemostasis, Inflammatory response
HBBF	Hemoglobin fetal subunit beta	15,859	Oxygen transport
IBP2	Insulin-like growth factor-binding protein 2	34,015	Growth regulation
IGF2	Insulin-like growth factor II	19,682	Carbohydrate metabolism, Glucose metabolism, Osteogenesis
HBA	Hemoglobin subunit alpha	15,184	Oxygen transport
HRG	Histidine-rich glycoprotein	44,471	Blood coagulation, Fibrinolysis, Hemostasis
CO4	Complement C4	101,885	Complement pathway, Immunity, Inflammatory response, Innate immunity
BPT2	Spleen trypsin inhibitor I	10,843	Protease inhibitor, Serine protease inhibitor[2]
FA5	Coagulation factor V	248,983	Blood coagulation, Hemostasis
THRB	Prothrombin	70,506	Acute phase, Blood coagulation, Hemostasis
APOC3	Apolipoprotein C-III	10,692	Lipid degradation, Lipid metabolism, Lipid transport
APOE	Apolipoprotein E	35,980	Lipid transport, Transport
ALBU	Albumin	69,293	Cellular response to starvation, negative regulation of apoptotic process
FETUA	Alpha-2-HS-glycoprotein	38,419	Acute-phase response, negative regulation of bone mineralization, positive regulation of phagocytosis
A1AG	Alpha-1-acid glycoprotein	23182	Acute-phase response, regulation of immune system process
TSP4	Thrombospondin-4	105974	Cell adhesion, Tissue remodeling, Unfolded protein response

[1] MW: Molecular weight. [2] Molecular function.

Table S2: LC-MS/MS analysis of surface adsorbed proteins from 55-nm HEP-AuNPs.

	Spectral counts of proteins from HEP-AuNPs at different coating densities (HEP/nm^2)						
Abbrev	0	0.01	0.1	0.25	0.5	1	3
CO4	0.15	0.11	0.45	0.64	0.66	0.66	0.54
KNG1	0.76	0.46	0.10	0.00	0.01	0.03	0.02
HBA	0.28	0.64	0.78	0.45	0.32	0.37	0.36
THRB	1.00	0.42	0.77	0.09	0.03	0.00	0.00
IBP2	0.32	0.79	0.67	0.41	0.03	0.01	0.06
APOE	0.33	0.98	0.21	0.00	0.17	0.05	0.00
FETUA	0.01	0.02	0.40	0.38	0.17	0.02	0.03
HBBF	0.10	0.49	0.64	0.42	0.52	0.36	0.15
BPT2	0.21	0.32	0.69	0.69	0.27	0.48	0.49
IGF2	0.14	0.50	0.62	0.00	0.00	0.00	0.00
HRG	0.43	0.43	0.67	0.00	0.00	0.00	0.00
A1AG	0.00	0.00	0.67	0.17	0.17	0.00	0.50
ALBU	0.00	0.14	0.68	0.34	0.13	0.03	0.24
TSP4	0.00	0.00	0.07	0.30	0.64	0.31	0.81

Total spectral counts are the average of three or four independent replicates.

Table S3: LC-MS/MS analysis of surface adsorbed proteins from 55-nm PEG-AuNPs.

Abbrev	Spectral counts of proteins from PEG-AuNPs at different coating densities (PEG/nm^2)							
	0	0.01	0.1	0.25	0.5	1	3	5
KNG1	0.75	0.59	0.38	0.09	0.12	0.04	0.11	0.03
HBBF	0.57	0.30	0.67	0.04	0.12	0.34	0.10	0.10
IBP2	0.79	0.51	0.53	0.04	0.00	0.02	0.00	0.00
IGF2	1.00	0.52	0.48	0.00	0.00	0.00	0.00	0.00
HBA	0.44	0.33	0.90	0.24	0.07	0.41	0.22	0.45
HRG	0.83	0.33	0.00	0.00	0.00	0.00	0.00	0.00
CO4	0.20	0.15	1.00	0.00	0.04	0.00	0.00	0.00
BPT2	0.06	0.06	0.55	0.26	0.30	0.38	0.41	0.08
FA5	1.00	0.33	0.67	0.00	0.00	0.00	0.00	0.00
THRB	0.80	0.44	0.88	0.00	0.00	0.02	0.02	0.00
APOC3	0.08	0.17	0.50	0.50	0.50	0.67	0.42	0.42
APOE	0.53	0.19	0.77	0.07	0.06	0.33	0.39	0.09
ALBU	0.05	0.00	0.27	0.02	0.03	0.36	0.35	0.44
FETUA	0.13	0.09	0.47	0.09	0.20	0.48	0.22	0.41

Total spectral counts are the average of three or four independent replicates.

Appendix C: Abbreviations

HEP	Heparosan
PEG	Poly(ethylene glycol)
AuNPs	Gold nanoparticles
AgNPs	Silver nanoparticles
TEM	Transmission electron microscopy
CLSM	Confocal laser scanning microscopy
LC-MS/MS	Liquid chromatography tandem mass spectrometry
ICP-MS	Inductively coupled plasma mass spectrometry
MTT	Methyl tetrazolium
ALAT	Alanine aminotransferase
ALP	Alkaline phosphatase
CD	Circular dichroism
Cryo-EM	cryogenic electron microscopy
CT	X-ray computed tomography
DCFH	2′7-dichlorodihydrofluorescein
DSC	differential scanning calorimetry
FTIR	Fourier transform infrared spectroscopy
LC_{50}	Lethal concentration, 50%
LD_{50}	Lethal dose, 50%
LDH	Lactate dehydrogenase
MRI	Magnetic resonance imaging
PET	Positron emission tomography

qPCR	quantitative polymerase chain reaction
SPECT	Single-photon emission computed tomography
WST	Water-soluble tetrazolium salt
BMI	Body mass index
EDX	Energy dispersive X-ray spectroscopy
EELS	Electron energy loss spectroscopy
ELISA	Enzyme-linked immunosorbent assay
i.v.	Intravenous administration
MRI	Magnetic Resonance Imaging
N/A	Not available
8-OH-dG	8-hydroxydeoxyguanosine
ROS	Reactive oxygen species

Appendix D: List of Copyrights and Permissions

No permission is needed from Annual Reviews as an author for Chapter 1

Permission Requests link and guideline of the journal of Annual Reviews are attached below (**link:** https://www.annualreviews.org/page/about/copyright-and-permissions).

Guideline: Annual Reviews Authors: There is no need to obtain permission from Annual Reviews for the use of your own work(s). Our copyright transfer agreement provides you with all the necessary permissions. Our copyright transfer agreement provides:

> "…The nonexclusive right to use, reproduce, distribute, perform, update, create derivatives, and make copies of the work (electronically or in print) in connection with the author's teaching, conference presentations, lectures, and publications, provided proper attribution is given…"

Reuse permission for Chapter 2

Reprinted with permission from https://pubs.acs.org/doi/full/10.1021/acs.nanolett.2c00349. Copyright 2022 American Chemical Society

